

Role of Mechanics in Tactile Sensing of Shape

by

Kiran Dandekar

B. E., Mechanical Engineering
University of Poona, Pune, India, 1988

M. Tech., Mechanical Engineering
Indian Institute of Technology, Madras, India, 1990

Submitted to the Department of Mechanical Engineering
in partial fulfillment of the requirements for the degree of

Doctor of Philosophy in Mechanical Engineering

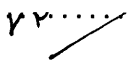
at the



MASSACHUSETTS INSTITUTE OF TECHNOLOGY

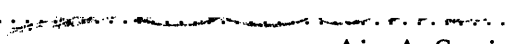
May 1995

©1995 Kiran Dandekar. All Rights Reserved.

The author hereby grants to MIT permission to reproduce and to distribute publicly paper and electronic copies of this thesis document in whole or in part.

Author..........
Department of Mechanical Engineering
May 5, 1995


Certified by..........
Dr. Mandayam A. Srinivasan
Principal Research Scientist
Thesis Supervisor

Accepted by..........
Ain A. Sonin
Chairman, Departmental Committee on Graduate Students
MASSACHUSETTS INSTITUTE
OF TECHNOLOGY

AUG 31 1995

LIBRARIES

MIT

Role of Mechanics in Tactile Sensing of Shape

by

Kiran Dandekar

Submitted to the Department of Mechanical Engineering
on May 5, 1995, in partial fulfillment of the
requirements for the degree of
Doctor of Philosophy in Mechanical Engineering

Abstract

The primary neural event in the human tactile recognition of objects is the transduction of the mechanical signals imposed on the skin into trains of nerve impulses by the mechanoreceptors embedded in the skin. Although the neural response of single mechanoreceptive afferent fibers can be electrophysiologically recorded, the *relevant stimuli* to which each class of cutaneous mechanoreceptors responds are unknown at present. To investigate the mechanics of touch, the external geometry of primate fingertips was determined and the surface deformations of human fingertips under indentation by various shaped indentors were measured *in vivo* using a videomicroscopy system. A series of two and three dimensional finite element models of the monkey and human fingertips that progressively approached the actual fingertip in geometry and material properties were developed. The models were used to simulate biomechanical and neurophysiological experiments and were validated by comparing the calculated data with empirical results. A multilayered 3-dimensional model was shown to successfully predict the experimentally observed skin surface deformations under a variety of indentors. The stress-state at typical receptor locations was calculated under various mechanical stimuli such as rectangular bars, gratings, cylinders of various radii and step shapes of varying curvature that have been used in neurophysiological experiments. Strain energy density and maximum compressive strain at the receptor location were found to be linearly related to the recorded neural discharge rate of SA-I afferents under all the mechanical stimuli and, thus, emerged as the candidate for *relevant stimuli* for the SA-I afferents. Strain energy density is a better candidate because it is a scalar that is invariant with respect to receptor orientations and is a direct measure of the distortion of the receptor. Other contributions of this thesis include exploration of the mechanistic basis of various receptor characteristics such as receptive fields and spatial acuity, a critique of common experimental techniques on the basis of underlying mechanics, and proposals for better experimental protocols. The empirically validated finite element models can now be used in predicting the surface deformations and the response of a population of mechanoreceptors to static stimulus shapes.

Doctoral Committee:

Dr. Mandayam A. Srinivasan, Chairman
Prof. Rohan Abeyaratne
Prof. Neville Hogan

Acknowledgments

I wish to thank Srini for giving me the honor of being his first student. Working with him has been a truly enriching experience for me. His insight into problems, creativity and patience has been truly remarkable. He has helped me understand the difference between being a scientist and an engineer in approaching research questions. I am grateful to my doctoral committee members Profs. Abeyaratne and Hogan for their advice during the course of the research and in the writing of this thesis.

Thanks to the TouchLab gang of my colleagues including my fellow graduate students Jyh-shing Chen, Louise Jandura, Gerald Lee Beauregard, Rogeve Gulati and Hugh Morgenbesser. The videomicroscopy setup used in the biomechanical experiments was designed and built by Jyh-shing Chen. I wish to thank him for his help in developing the hardware and software for the biomechanical experiments. Thanks to Joe Frisbie for his help along the way. Tomas Rodriguez Perez worked with me as a summer student and later as a special student and I wish to thank him for his help in the biomechanical experiments. My thanks to Fredrick Roby for his help in the surface deformation experiments. I wish to express my sense of gratitude towards all the subjects who cheerfully volunteered their time and fingertips for the advancement of science. I wish to thank Prof. LaMotte of the Yale School of Medicine for his help in obtaining fingertip replicas of monkey fingertips. I was a part of the Sensory Communications group of the Research Laboratory of Electronics during my stay at MIT. I wish to thank all the members of this group for making CBG an excellent place to be a graduate student.

Prof. Veluswami was my thesis advisor at the Indian Institute of Technology, Madras and it was because of his constant encouragement, that I applied to MIT for continuing my graduate studies. All this would not have been possible without his advice and encouragement.

The work reported here was supported by NIH grants R29-DC00625 and NS33778, ONR grant N00014-92-J-1814 and the NSF Pittsburgh Supercomputer Center grant MSS940007P.

To my mother,
Dr. Vijaya Dandekar
who is the wind beneath my wings !

Contents

1	Introduction	12
1.1	The Human Tactile Sensing System	12
1.2	The Problem	15
1.3	Thesis Overview	17
2	Background	20
2.1	The Human Fingertip	20
2.1.1	The fingertip skin	21
2.1.2	Mechanoreceptors	24
2.2	Previous Work	31
2.2.1	Attempts at modeling the fingerpad	31
2.2.2	Neurophysiological studies	32
2.3	Need for Improved Models	34
3	Research Design and Methods	37
3.1	Approach	37
3.2	The Finite Element Method	41
3.3	Mechanistic Models	42
3.3.1	Structural geometry	42
3.3.2	Material properties	43
3.3.3	Boundary conditions	45
3.4	Stimuli Applied to the Fingerpad	45
3.5	Biomechanical Verification	45
3.6	Neurophysiological Verification	46
4	Two Dimensional Models	48
4.1	Construction of the Models	48
4.2	Point Load	52
4.3	Two Point Resolution	56
4.4	Indentation by Rectangular Bars	60
4.5	Indentation by Aperiodic Gratings	62
4.5.1	The experiment	62
4.5.2	Simulations with the 8 mm diameter model	63
4.5.3	Simulations with the 16 mm diameter model	69
4.5.4	Central vs off-center receptors	79
4.5.5	Human threshold of gap discrimination	81
4.6	Indentation by Cylindrical Indentors	82
4.7	Surface Deformation Under a Line Load	89

5	Biomechanical Experiments	92
5.1	3D Reconstruction of the Primate Fingerpads	92
5.1.1	Experimental setup	93
5.1.2	Experimental protocol	94
5.1.3	Reconstruction algorithm	96
5.2	Surface Deformation of Human Fingertips <i>in vivo</i>	101
5.2.1	Experimental setup	101
5.2.2	Experimental protocol	103
5.2.3	Data analysis	107
6	3D Models	112
6.1	Construction of the Models	112
6.2	Biomechanical Verification	118
6.2.1	Surface deformation under line load	118
6.2.2	Surface deformation of human fingertips under cylindrical indentors	136
6.2.3	Force displacement relationships for human fingertips	141
6.3	Neurophysiological Verification	146
6.3.1	Indentation by rectangular bars	147
6.3.2	Indentation by cylinders	153
6.3.3	Indentation by step shapes	156
7	Discussion	172
7.1	Mechanical Behavior of Models	172
7.1.1	Effect of geometry	172
7.1.2	Effect of multiple layers	178
7.2	Comparison of the competing relevant stimuli	181
7.3	Implications	184
7.3.1	Neurophysiology	184
7.3.2	Rehabilitation	185
7.3.3	Clinical simulation tool	185
7.3.4	Virtual environments and teleoperation	185
7.3.5	Robotics	186
8	Suggestions for Future Work	187
8.1	Limitation of the Current Models	187
8.2	Neurophysiological and Psychophysical Experiments	188
8.3	Anatomical Studies	188
8.4	Receptor Silence in the Stimulus Withdrawal Phase	189
8.5	Reduced Order Model for Surface Deformations	192
A	Strain Energy Density in Plane Strain Problems	193
B	Strain calculations for finite element models with prescribed displacements	196
	References	199

List of Figures

1-1	Flow chart of events in the tactile sensing of shape	16
2-1	Cross-section through the human fingerpad	20
2-2	Cross-section of the human fingerpad skin	21
2-3	Experimental technique used in recording the response of afferent nerve fibers	25
2-4	Response of mechanoreceptors to a ramp and hold indentation	26
2-5	Tuning curves for various afferent fibers	28
2-6	Schematic of the Waterbed model (Srinivasan, 1989)	32
3-1	Black Box Approach for the problem	39
4-1	Cross-sections of the 2D finite element models	49
4-2	Finite element mesh in the 2D cylindrical model	50
4-3	Spatial filtering of sub-surface strain measures with depth for a line load on the surface	53
4-4	Receptive fields for a point load predicted by the cylindrical model	54
4-5	Strain energy density under two line loads of variable spacing	57
4-6	Intensive cues available to a human subject in a two point limen experiment	59
4-7	Indentation of the 2D models by a rectangular bar	61
4-8	Schematic of the experiment reported by Phillips and Johnson (1981a)	62
4-9	Indentation of the cylindrical model by an aperiodic grating	64
4-10	Comparison of the population response predicted by a semi-infinite model and the cylindrical model	65
4-11	Comparison of the spatial response for SA fibers recorded experimentally and predicted by the model of 8 mm diameter	67
4-12	Effect of model diameter on the load distribution under an aperiodic grating	68
4-13	Spatial response profile for an aperiodic grating with 0.5 mm bars predicted by the 16 mm diameter model	70
4-14	Spatial response for an aperiodic grating with 1.5 mm wide bars predicted by the 16 mm diameter model	71
4-15	Observed and predicted static discharge profiles for all gratings aligned along the finger ridges	72
4-16	Observed and predicted static discharge profiles for all gratings aligned across the finger ridges	75
4-17	Verification of the receptor model relating the strain measures to the dis- charge rate	76
4-18	Differences in the spatial response predicted by a central and an off-center unit	80

4-19	Shear strain at a depth of 0.75 mm for grating 4	82
4-20	Experimentally observed and predicted threshold of gap detection in humans	83
4-21	Undeformed and deformed mesh of the finite element model indented by a cylindrical indenter	84
4-22	Variation in the strain measure during stepwise indentation	85
4-23	Strain measures at a depth of 0.58 mm under various cylindrical indentors	86
4-24	Depth of indentation required to attain the constant force in solid and solid-fluid model	87
4-25	Variation in contact area and maximum pressure in the cylindrical model for indentations by cylindrical indentors	88
4-26	Comparison of observed and predicted discharge rate for indentations by cylindrical indentors	89
4-27	Deflection profiles of the skin surface under line load	90
5-1	Experimental setup for border extraction	93
5-2	Steps involved in extraction of the border from images of the fingertip replicas	96
5-3	Lateral sections of the monkey fingertip aligned at their respective orientations	97
5-4	The algorithm for reconstruction of the 3D fingertip	98
5-5	Axial cross-sections extracted from the monkey fingertip	100
5-6	Experimental setup for fingertip deformation experiments	102
5-7	Images of the undeformed and deformed human fingertip under indentation by a cylindrical indenter	104
5-8	Side view of fingertip deformations with indenter perpendicular to the finger axis	105
5-9	Axial view of fingertip deformations	106
5-10	Top view of fingertip deformations with indenter parallel to the finger axis	106
5-11	Top view of fingertip deformations with indenter perpendicular to the finger axis	107
5-12	Skin surface deformation profiles under a cylindrical indenter	108
5-13	Surface deformation profiles under a cylindrical indenter	109
5-14	Variation in contact area for cylindrical indentors	110
6-1	3D view of the monkey fingertip model	114
6-2	Three axial slices of the monkey fingertip	116
6-3	Longitudinal section of the monkey fingertip showing layers of the model	117
6-4	Undeformed and deformed mesh of the monkey fingertip under indentation by a sharp wedge	119
6-5	Contours of constant vertical displacement of the monkey fingertip under indentation by a line load	120
6-6	Undeformed and deformed mesh of the human fingertip under indentation by a sharp wedge	121
6-7	Contours of constant vertical displacement of the human fingertip under indentation by a line load	122
6-8	Surface deformation predicted by the homogeneous monkey model	123
6-9	Surface deformation predicted by the homogeneous human model	124
6-10	Effect of layer stiffness on the surface deformation	125
6-11	Surface deformation of the monkey fingertip under a line load predicted by the finite element model	128

6-12	Surface deformation of the human fingertip under a line load predicted by the finite element model	130
6-13	The comparison of the waterbed model and the "beam" model	131
6-14	Surface deformation of primate fingertips predicted by the beam model	134
6-15	Simulation of the <i>in vivo</i> indentation of the human fingertip by a cylindrical indenter	137
6-16	Undeformed and deformed meshes of the human fingertip when indented by a cylindrical indenter	138
6-17	Contours of constant vertical deformation of the human fingertip indented by a cylindrical indenter	139
6-18	Vertical displacements in the human fingertip indented by cylindrical indenter C5	140
6-19	Enlarged view of the vertical displacements in human fingertip indented by cylindrical indenter C5	141
6-20	Vertical displacement in the human fingertip indented by cylindrical indenter C2	142
6-21	Enlarged view of the vertical displacements in human fingertip indented by cylindrical indenter C2	143
6-22	The human fingerpad indented by 3 different indentors	144
6-23	The force-displacement relationship predicted by the human model	145
6-24	Indentation of the monkey model by a 1.5 mm wide rectangular bar	148
6-25	The spatial variation of strain energy density under indentation by a 1.5 mm wide bar	149
6-26	Spatial response profile for indentation by a 1.5 mm wide bar	150
6-27	Spatial response profile for indentation by a 3 mm wide bar	152
6-28	Comparison of maximum compressive strain and strain energy density in predicting spatial response profile for 3 mm wide bar	153
6-29	Predicted neural data for indentations by cylindrical indentors	154
6-30	Variation in contact area and maximum pressure under indentation by cylinders	156
6-31	Surface deformations under step 3	158
6-32	Surface deformations under step 1	159
6-33	Contact pressure on the skin under step 3	161
6-34	Contact pressure on the skin under step 1	163
6-35	Strain energy density at the receptor location under indentation by step 1	164
6-36	Strain energy density in an axial cross-section under indentation by step 5	165
6-37	Generating the spatial response profile	167
6-38	Different spatial response profiles based on the location of the receptor selected	168
6-39	The variation in contact area and maximum contact pressure as the step passes over the monkey fingertip	169
6-40	The neural response for indentation by step shapes predicted by the 3D model	170
7-1	Comparison of the 2D cylindrical model with the 3D model under indentation by a rectangular bar	173
7-2	Comparison of the stress state in an axial section of the 3d model at $z = 7.495$ and the 2D cylindrical model	175
7-3	Comparison of the stress state in an axial section of the 3d model at $z = 9.17$ and the 2D cylindrical model	177

7-4	Comparison of the stress-state in m33338 and m43338 models	179
7-5	Schematic representation of a line load imposed on a semi-infinite plane . .	182
7-6	Variation of the strain measures with respect to the orientation of the point load	183
8-1	Lumped model for mechanoreceptors	190

List of Tables

2.1	Experimentally calculated values of Young's Modulus of skin	23
2.2	Comparison of various mechanoreceptors found in the primate fingerpad.	30
2.3	Number of various peripheral afferent fibers in the primate fingertips . . .	31
4.1	Best matches between the strain measure and the neural discharge rate. . .	73
4.2	Best matches between the strain measure and the neural discharge rate for grating bars aligned across the finger ridges	74
4.3	Relevant stimuli for SA receptors: Data from gratings aligned parallel to fingertip axis	77
4.4	Relevant stimuli for SA receptors: Data from gratings aligned perpendicular to fingertip axis	78
5.1	Indentors used in the study of fingertip deformation	103

1 *Introduction*

The human tactile system is far superior than any of the man made tactile sensing systems. Humans are sensitive to touch over the entire skin as compared to localized sensory organs responsible for the sense of vision, audition, taste and smell. Humans can detect and discriminate a wide range of physical features of objects using their tactile sensing system. The details of the functioning of this system remain largely unknown at the present time. Deeper understanding of the human tactile sensing system will not only resolve the mystery behind this intricate and superior system but will also provide guidelines to scientists and engineers involved in the design and development of tactile sensing systems. Such understanding is essential in the design of tactile display systems and human-machine haptic interface used in teleoperation and virtual environments.

1.1 The Human Tactile Sensing System

Let us consider a simple thought experiment to explore the complexities involved in the human tactile sensing system. Assume that a (male) subject is blindfolded and is prevented from listening to environmental sounds by feeding white noise through earphones. He is seated in a chair and is told that there is an unknown object on the table in front of him. His task is to locate, lift and place the unknown object back on the table. A typical sequence of actions that the subject might use will consist of the following steps. Using relatively large sweeping motions of the arm, the subject would explore the workspace trying to locate the object on the table. Let us say during one such sweeps the subject touches the object with his forearm. Using this location information, the subject would next carefully move his hand so that the fingertips are in a position to explore the object in detail. In order to successfully grasp and lift the object, the subject needs to know the

dimensions, shape and weight of the object, conditions of contact and texture of the surface of the object. This information can be estimated by touching the object with one or more fingertips, pressing the fingertips onto the object, stroking the fingertips over the object with controlled motions of the hand. After getting a 'feel' for the object the next step would be to try and grasp it in the fingertips and lift it. Depending on the object, it might take a few trials for the subject to be able to lift it, manipulate it in the workspace and place it back on the table. With additional training the subject might be able to lift several objects on the table or even juggle the objects without dropping them on the table.

Picking and placing of objects, which seems like a trivial and everyday task, illustrates the various mechanisms involved in the successful exploration and manipulation of the workspace that we humans can accomplish effortlessly. Typically the sense of touch is used in combination with other senses like vision and audition in such tasks. Vision plays a very important role in exploration and manipulation tasks by providing information about the location, size and shape of the object. By blindfolding the subject and introducing white noise in the ears, sensory input from vision and audition is eliminated and the entire task is performed based on information derived from only the tactile sensing system. As can be seen in this experiment, physical contact with the object is essential to infer many of the physical properties of the object. Further, mechanical properties like compliance and viscosity or surface texture can only be estimated with relative motion of the fingertip with respect to the object with sustained contact between the fingertip and the object.

Haptics is the science that studies the sensory, motor and cognitive aspects of the hands in humans and upper extremities in primates. The tactual sensory information from the hand in contact with an object can be divided into two classes: 1) tactile information, derived from the sensors embedded in the skin within and around the contact region and 2) kinesthetic information, referring to the sense of position and motion of limbs along with the associated forces conveyed by sensory receptors in the skin around joints, joint capsules, tendons, and muscles, together with neural signals derived from the motor commands (Srinivasan, 1994). The pick and place task just described is a good example of a truly haptic task. We can broadly classify the sequence of events in the successful completion of the task in the above experiment into two phases: exploration and manipulation. Exploration is the sensory dominant phase in which well coordinated motions of the hand are used to gather information about the environment, whereas, manipulation is the motor

dominant phase where information about the object is used in changing the position or state of the object in the environment. Obviously, for successful manipulation of unknown objects, adequate exploration is a pre-requisite. In the above experiment, the subject was able to locate the object through physical contact between the object and the skin. Information from several mechano-sensitive receptors in the skin, muscle spindles and joints, can be used by the central nervous system (CNS) to detect contact with an object. Once the approximate location of the object is estimated by the brain, further exploration of the object is done using the fingertips. Fingertips have the highest innervation density of mechano-sensitive receptors and can be compared with the retinal fovea in their functional importance. Non-primate mammals who lack fingertips, rely on the perioral tissues such as lips, tongue, and snout for tactile exploration (Darian-Smith, 1984). The glabrous and readily deformable palmar side of the fingertips aids in both exploration and grasping of the objects. By coordinated motions of the various joints of the hand, the subject is able to determine the dimensions of the object. To determine the shape and mechanical properties of the object, fingertips are pressed and stroked over the object. Once the subject has an adequate understanding of the shape, dimensions, surface texture, conditions of contact and softness of the object, the subject attempts to grasp the object using two or more fingertips. This can be regarded as the transition from the sensory dominant exploration to the ensuing motor dominant manipulation phase. It should be noted that, during exploration the motor functions of the hand are used to aid in orienting the fingertips and applying the force required.

In grasping the object, the subject tries to find the optimal level of forces to be imposed by individual fingerpads, such that the object does not slip from the grip and at the same time the forces do not increase excessively to possibly damage the object. In this phase, the sensory information provided by the mechanoreceptors embedded in the skin, muscles and joints, is presumably used to control the forces exerted by the fingerpads. With time and better understanding of the object to be manipulated, the subject can optimize the forces and manipulate the object at a much faster speed and with less effort than the first trial.

Tactile sensing is the only sensory modality where sensing and manipulation are so closely linked. In auditory domain, for example, the ear which is the sensory organ is distinct from the vocal chords and the mouth which can produce auditory signals. The

human hand not only contains of mechanoreceptor populations with the associated neural mechanisms to relay sensory information to the CNS but also contains muscles and the skeletal tissues along with there neural connections to carry efferent signals from the CNS to the muscles. It is thus essential to clearly distinguish between the sensory and motor components involved in a given task, or conversely design tasks that would let us examine either of the components in isolation.

The most advanced robots put in a similar environment and given the same task would need to follow more or less the same overall procedure, but almost certainly will need several more trials if the robot is able to successfully perform the task, eventually. The reason being, although robots could be superior to humans in their motor abilities due to fast and non-fatiguing actuators, the human sensory system is far superior than any robot sensory system currently in operation, not only because of its exquisite sensitivity and remarkable spatial acuity to a variety of mechanical stimuli but also because of the higher processing in the brain.

1.2 The Problem

The sequence of events involved in human tactile sensing can be clearly understood with the help of Figure 1-1. Physical contact of the object with the fingertip is the essential first step in gathering information about the object using the tactile sense. Because of the contact, mechanical loads are imposed on the skin surface causing the fingertip to deform. All the tactile information about the object is contained in the spatio-temporal variations of the contact forces and the region of contact. At any instant of time, these loads give rise to a unique state of stress inside the fingertip in general and in the vicinity of the mechanoreceptors located below the skin in particular. The information about the object in contact with the skin on the surface, is now contained in the stress state in the fingertip. Triggered by the stress-state in the close vicinity of the mechanoreceptors, the population of mechanoreceptors responds with trains of impulses which are conveyed to the central nervous system by peripheral afferent fibers. The information about the object in contact is coded in the spatio-temporal variation of the discharge rate of the population of receptors. The neural code is processed by the brain, when the object is finally “perceived” using the tactile sense.

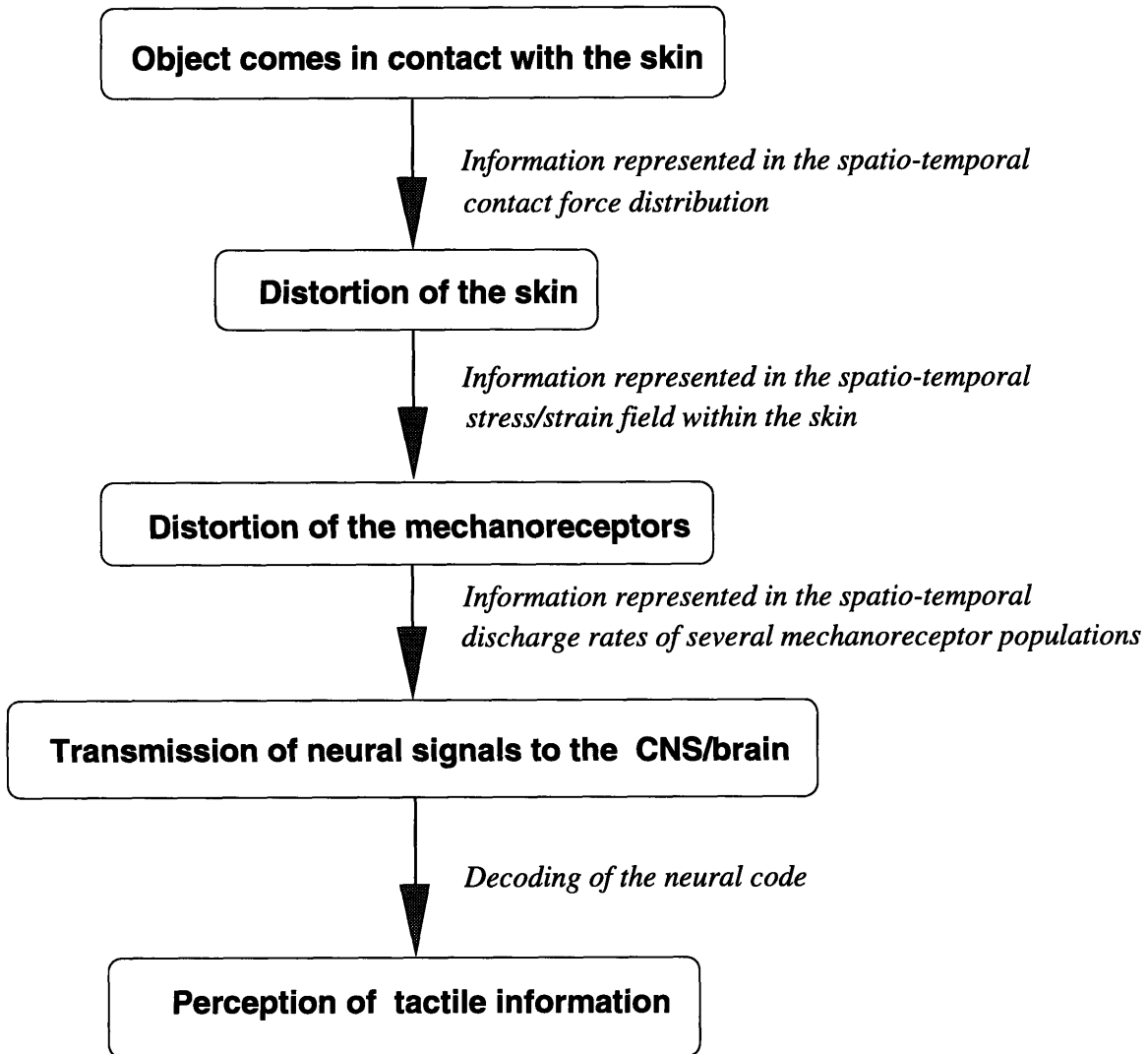


Figure 1-1: A flow chart of the series of events in the process of tactile sensing. The blocks represent the phenomenon involved and the medium in which the information is represented is shown on the right hand side.

Biomechanics of skin and subcutaneous tissues plays a fundamental role in the human tactile sense. It governs the mechanics of contact with the object, the transmission of the mechanical signals through the skin, and finally the stress state at the mechanoreceptor location that is transduced into neural signals by the mechanoreceptors. It has been hypothesized that the differences in the temporal patterns of responses among the different receptor types to the same stimulus at the skin surface are due to differences in the *relevant stimulus*, i.e., a particular combination of stresses and/or strains (and their derivatives) which triggers responses in that class of receptors (Phillips and Johnson, 1981a). Further,

the frequency of impulses emitted by a receptor is hypothesized to depend only on the local intensity of the relevant stimulus at the receptor site. Since the stress and strain fields sampled spatially and temporally by the receptor populations are directly dependent on the mechanical stimulus at the skin surface, these hypotheses offer a mechanism for the neural coding of tactile information about the object and the type of contact.

At present, the relevant stimulus for each mechanoreceptor type is largely unknown and its determination an important area of research on tactile sense. Although electrophysiological recordings of the neural signals transmitted by a single peripheral nerve fiber are possible in either a monkey or a human, the stress or strain state of the associated mechanoreceptors is not empirically observable at present. Therefore, mechanistic models of the skin and subcutaneous tissues are needed not only to generate hypotheses concerning the relevant stimuli for each class of receptors, but also to design the biomechanical, neurophysiological, and perceptual experiments that investigate the tactile sensory system. Mechanistic basis of the geometry and material properties of the fingerpad and its constituents needs to be studied to understand its relevance to the superiority of the human tactile system. The results of these studies can be used as guidelines in the design of better robotic tactile sensors. The knowledge gained from this research work will result in the better understanding of the human haptic system, which is a pre-requisite in developing better haptic interfaces, which are necessary in teleoperation and virtual environments. The deeper understanding of the biomechanics and neurophysiology involved in the human tactile system gained through this study, can be used as an clinical simulation tool for evaluation of impairments. The understanding of the mechanisms of tactile sense is beneficial in the development of tests for evaluation of tactile sensibility during diagnosis or monitoring of progress in rehabilitation, design of tactile communication devices and development of artificial sensors for prostheses.

1.3 Thesis Overview

This thesis describes a series of mechanistic models of the human and monkey fingertips. The models are analyzed using the finite element method under a variety of mechanical stimuli to simulate various biomechanical and neurophysiological experiments reported in the literature.

In Chapter 2, background information about the primate fingertip and a summary of previous work done is presented. The anatomy of the human fingertip is discussed and the reported biomechanical studies on the human skin are presented. Histological and anatomical data on the mechanoreceptors is discussed. Previous attempts at modeling the primate fingertip and various neurophysiological experiments are summarized. The limitations of the previous modeling efforts are stated and the need for better models is established.

The research design for the study described in this thesis and the methods used are discussed in Chapter 3. The approach used in solving the problem is justified. A brief description of the finite element method and the choice of finite element method as the method of choice for mechanistic analysis is explained. The issues involved in mechanistic modeling of the primate fingertip are discussed. The choice of the mechanical stimuli to be used on the models is explained and methods of performing biomechanical and neurophysiological verification of the model are described.

Chapter 4 is a description of the various two dimensional models. Starting from the semi-infinite model, a series of models approaching the primate fingertip in 2 dimensions is presented. Implications of the mechanistic analysis to biomechanical, neurophysiological and psychophysical experiments are discussed.

The biomechanical experiments performed on human subjects as a part of this thesis are described in Chapter 5. The experimental setup, the protocol of the experiments and the algorithm used in the 3D reconstruction of the fingerpads is presented. Experiments to investigate the *in vivo* surface deformation of human fingertips under indentation by cylindrical and rectangular indentors are described.

Chapter 6 is a description of the three dimensional finite element models of monkey and human fingertips based on the actual fingertip geometry. The biomechanical verification of the model is presented followed by the neurophysiological verification. The model is used in predicting results of previous neurophysiological experiments and the predicted and experimentally observed data are compared.

In Chapter 7, the significance of the work and its relevance to biomechanics, neurophysiological studies, robotics and man-machine interfaces in the virtual environment is discussed.

Chapter 8 discusses some of the enhancements that could be done to the finite element

models and several other research questions that remain unsolved are presented.

2

Background

2.1 The Human Fingertip

The human fingertip can be referred to as the “tactile fovea” to reflect its relative importance in tactile sensing. The human skin, consisting an approximate area of 2 m² in adults, is sensitive to touch at all locations in varying degrees of sensitivity and spatial acuity. Several mechanoreceptors embedded in the skin, joints, the muscle spindles, and tendons convey haptic information to the central nervous system. But primates predominantly use their fingertips in collecting tactile information from the environment because the fingertip has specialized features in geometry, mechanical constitution and the highest innervation density. Use of foveal vision to enhance visual acuity is similar to using the fingertips in tactile exploration.

The structure of the primate fingerpad is quite complex and the major macroscopic structural components that make up the fingertip are the skin, subcutaneous tissues mostly composed of fat, the bone, and the nail. Cross sectional view of a typical human fingertip

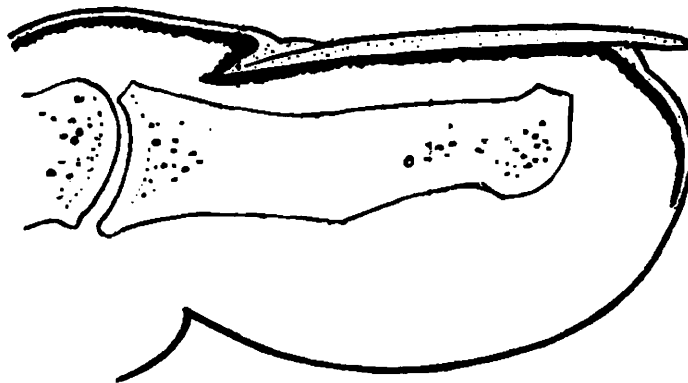


Figure 2-1: The figure shows a cross-section through the human fingerpad (O’Rahilly, 1969)

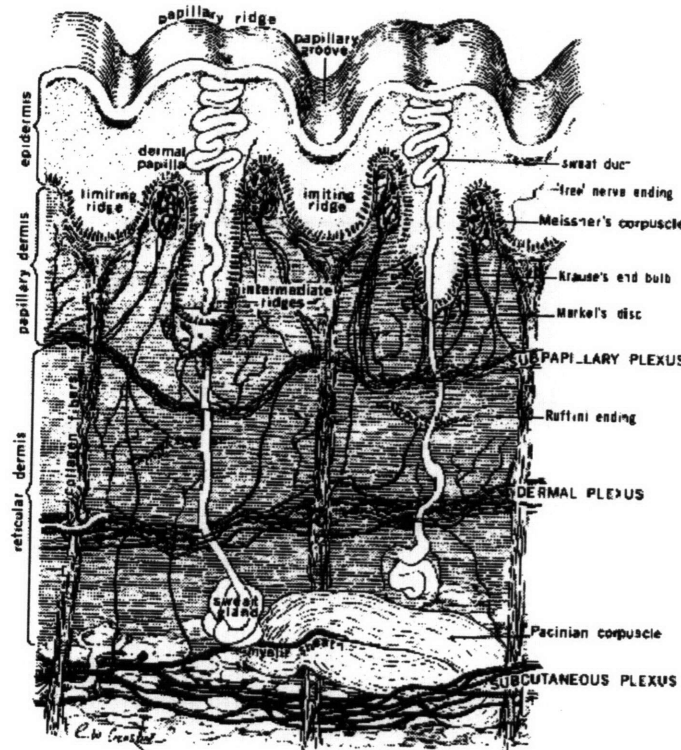


Figure 2-2: The figure shows a cross-section through the human fingerpad skin. Various layers of the skin and the location of the mechanoreceptors can be clearly seen (Jabaley, 1981).

is shown in Figure 2-1. The bone provides the structural stiffness required for effective manipulation and exploration tasks. Typical human fingerpads are about 10 to 20 mm in diameter and the length of the distal phalanx varies between 20 to 30 mm. The skin on the palmar side is glabrous (devoid of hair) and is characterized by epidermal ridges which reflect the underlying papillary ridges. These dermal striations make up the *finger prints* on the primate fingers. The relatively stiff nail on the dorsal side provides a rigid backing when the palmar side is used in exploration or manipulation tasks.

2.1.1 The fingertip skin

An enlarged schematic view of the cross-section through glabrous skin is shown in Figure 2-2. The skin can be divided into two major layers: the superficial stratified epithelium also known as the epidermis which is derived from the ectoderm and a deep vascular connective tissue layer, the dermis or corium, that is largely mesodermal in origin (O'Rahilly, 1969; Lockhart *et al.*, 1965). The epidermis is further sub-divided into layers

and the layers in the epidermis, named from dermis outwards are stratum germinativum, stratum granulosum and stratum corneum. The cells in the germinal stratum, as the name implies, keep multiplying in continuous provision for the loss of cells from the surface of epidermis. Stratum granulosum contains granules produced in chemical changes occurring within the cells as they progress to the horny keratin surface layer. The mechanical and barrier functions of the epidermis are primarily due to the horny stratum corneum, the outermost layer, made up of dead cells which are continuously cast. Epidermis is comparatively stronger than the dermis in spite of its smaller thickness (Tregear, 1966).

The dermis can be divided into the outer papillary layer, which is a close felted network of fibrous and elastic tissue connected to the epidermis by numerous papillae, and the deeper network or reticular layer which merges with the underlying superficial fascia. It is made up of networks of collagen fibers, elastin fibers, blood vessels, nerves, and lymphatics embedded in a gelatinous matrix called the ground substance (Lanir, 1987; Gibson and Kenedi, 1968). Collagen accounts for 60 to 80 percent of the dry weight of skin (about 18–30% by volume) and appears as a three-dimensional, randomly oriented network of wavy coiled fibers. Elastin accounts for about 4 percent of the dry weight of skin and as the name suggests is easily extensible. It exists as fine fibers that intertwine around collagen fibers. Reticulin fibers account for about 0.4 percent of the dry weight and because of their minute quantity have very little effect over the skin's overall mechanical properties. The ground substance matrix accounts for 70 to 90 percent of skin's volume and is the primary reason of the viscoelastic response of the skin in the low strain range.

The mechanical properties of skin are strongly dependent on species, age, sex, exposure, hydration and biological differences between individuals (Tregear, 1966; Lanir, 1987). In the same individual, the properties vary by site and orientation. There is a significant difference in properties between *in vivo* tests and *in vitro* tests due to loss of fluid and the difference in boundary conditions (Lanir, 1987). The values of Young's modulus reported by various researchers vary widely and very little data is available for *in vivo* measurements on the human fingerpad. Tregear (1966) suggests that the elastic modulus of skin is about the same range as tendons and greater than that of passive muscles. A summary of some of the reported Young's moduli for various species are tabulated in Table 2.1. There is, however, overall agreement that the skin exhibits a non-linear stress-strain relationship and is anisotropic following the same directional pattern as the Langer's lines. It is believed

	Y (MPa)	Reference
<i>In vivo</i> compression of human forehead	0.005 - 0.012	(Lanir <i>et al.</i> , 1990)
Elastin Fibers	0.6	(Fung, 1993)
Uniaxial tests on cat skin	0.689	(Veronda and Westmann, 1970)
Epidermis at 100 % relative humidity	1 – 10	(Lanir, 1987)
Human Abdominal Skin	29–100	(Tregear, 1966)
Collagen Fibers (Along the fibers)	1000	(Lanir, 1987)
Epidermis at 25-30% relative humidity	1000 – 10000	(Lanir, 1987)

Table 2.1: Values of Young's Modulus reported by various researchers. Unless otherwise specified, all tests were done on *in vitro* specimens.

that the elastin fibers are the first to be stretched, followed by the collagen fibers at higher strain levels (Lanir, 1987). The collagen fibers are several orders of magnitude stiffer than the elastin fibers resulting in a sigmoidal stress-strain curve with a sharp difference in the slope of the linear regions. The orientation of the elastin and collagen fibers, presence of finger ridges contribute to the anisotropic behavior of the human skin.

In tests for compressibility of the human skin as a whole *in vitro* (North and Gibson, 1978) and *in vivo* (von Gierke *et al.* , 1952), the ratio of the bulk to shear modulus was found to be of the order of 10^3 and 10^6 respectively. *In vivo* measurements of changes in the human fingerpad volume under indentation stimuli show that the changes are at most 5% (Srinivasan *et al.* , 1992), therefore, to a first approximation, the fingertip can be considered to be incompressible (i.e., Poisson's ratio = 0.5).

Three major classes of models have been developed for the skin: continuum, phenomenological and structural. In the continuum models, general material theories were adapted for skin and used in simulating multi-axial stress response. The phenomenological models consist of mathematical formulas describing the skin's behavior under specific schemes and some of them consist of spring and dashpot elements. In the structural models the behavior of the skin is analyzed in terms of the combined effects of its components. Lanir (1987) has compiled the various forms of constitutive equations (approximately 25 in number) proposed by different authors and it is unlikely that a common agreement will emerge in the near future. In general, the stress-strain curve for the skin usually has a concave toe region near the origin followed by a linear region at loads much below those that cause permanent damage, and is well approximated by a power law. Although skin exhibits viscoelastic properties such as rate-dependent stress-strain relations and hystere-

sis, after a few cycles of loading it settles down to a steady state response and is therefore termed "pseudoelastic" (Fung, 1981).

Skin mechanics has considerable clinical impact and the study of the structural and mechanical characteristics of skin is primarily motivated by its significance to plastic surgery (Cook, 1975; Thacker, 1976). Most of the testing has been done on excised specimens is uniaxial testing. Considering the variability in reported mechanical properties with species, location, orientation and several other environmental factors, it is clear that *in vivo* experiments on the human fingerpads are necessary to obtain mechanical properties of the fingertip as a whole and its constituents, that can be reliably used in mechanistic models. It should also be pointed out that such experiments would require sophisticated apparatus and would be quite difficult to design and perform. Some of the experiments on *in vivo* human fingertips done as a part of this thesis are described in Chapter 5.

2.1.2 Mechanoreceptors

The human skin is innervated over the entire region (covering about 1.5 to 2.0 m² in adults) by a variety of peripheral afferent nerve fibers. There are, however, differences in the type of mechanoreceptors at the end of the afferents, their location in the skin, and the innervation density of the receptors depending upon the part of the body under consideration. In this section, we shall limit our discussion to the ridged glabrous skin of human fingertip.

The geometrical features of the wavy dermo-epidermal interface and the locations of the various mechanoreceptors can be seen in Figure 2-2. Several schemes of classification of the mechanoreceptors and the afferent fiber innervating the receptor are proposed. The mechanosensitive nerve endings, also known as the receptor terminals, have been classified based various criteria, such as, their location in the skin, their morphological structure, and their sensitivity to mechanical stimuli. Receptor terminals are classified as epidermal or dermal nerve endings based on the location of the receptor in the skin. Chouchkov (1978) divides the nerve endings into un-encapsulated and encapsulated receptor terminals based on the absence or presence of a specialized capsule around the nerve terminal. The afferent fibers are classified based on their adaptive properties in response to a stepwise indentation of the most sensitive part of the fiber's receptive field (Darian-Smith, 1984; Valbo and Johansson, 1984). Salient features of the most important mechanoreceptors are

Recording the Neural Response

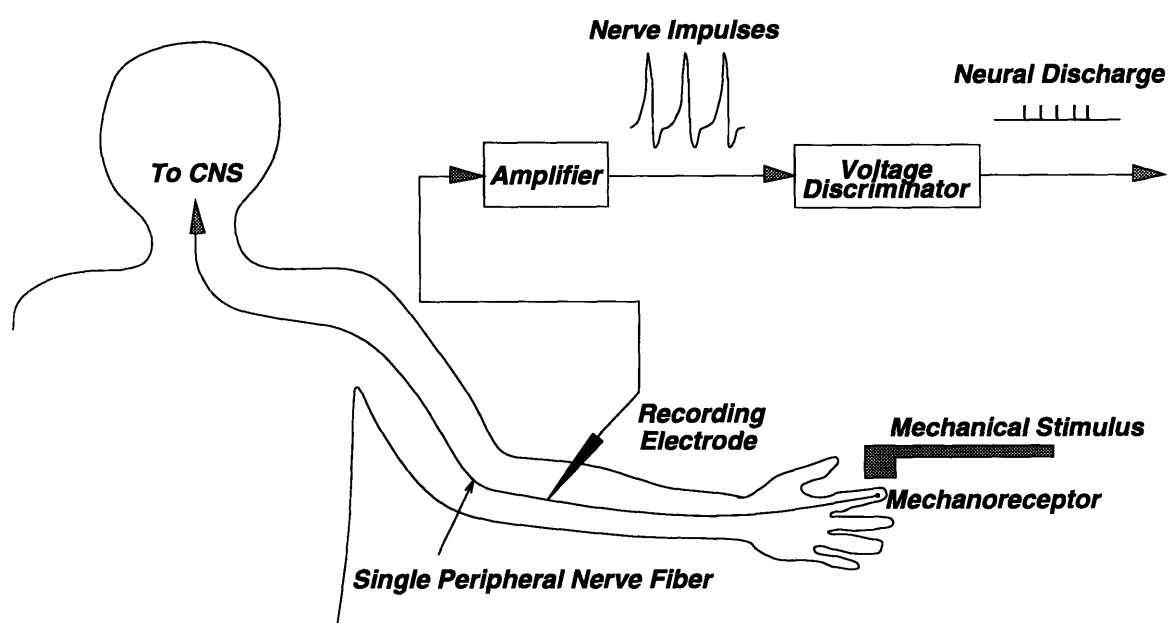


Figure 2-3: A recording electrode is used to record the action potentials from a mechanoreceptive afferent fiber in the upper or lower median and ulnar nerves of anesthetized monkeys (Srinivasan and LaMotte, 1987). An amplifier and a voltage discriminator are used to obtain the discharge rate in impulses per second (ips) for a given mechanical stimulus applied to the most sensitive spot of the afferent fiber.

listed below.

The mechanoreceptive fibers innervating the primate fingerpad are classified on the basis of the adaptive properties of the fiber in responding to stepwise indentation of the most sensitive part of the fiber's receptive field. The typical experimental setup used in this experiment is shown in Figure 2-3. A recording electrode is inserted in a mechanoreceptive afferent fiber in the upper or lower median and ulnar nerve of anesthetized monkeys. The most sensitive spot (MSS) of this unit on the surface of the fingertip skin is located using a point stimulus on the fingertip. The MSS is used as the datum in specifying the spatial location of the mechanical stimuli. The amplified signal from the afferent fiber is in the form of impulses as shown in the figure. The impulse is characterized by a rising phase followed by a falling phase, with the difference between the foot and peak potential being about 100 mV (Aidley, 1989). The voltage discriminator is used to locate the instances when a impulse are recorded and each vertical tick in the output of the voltage discriminator

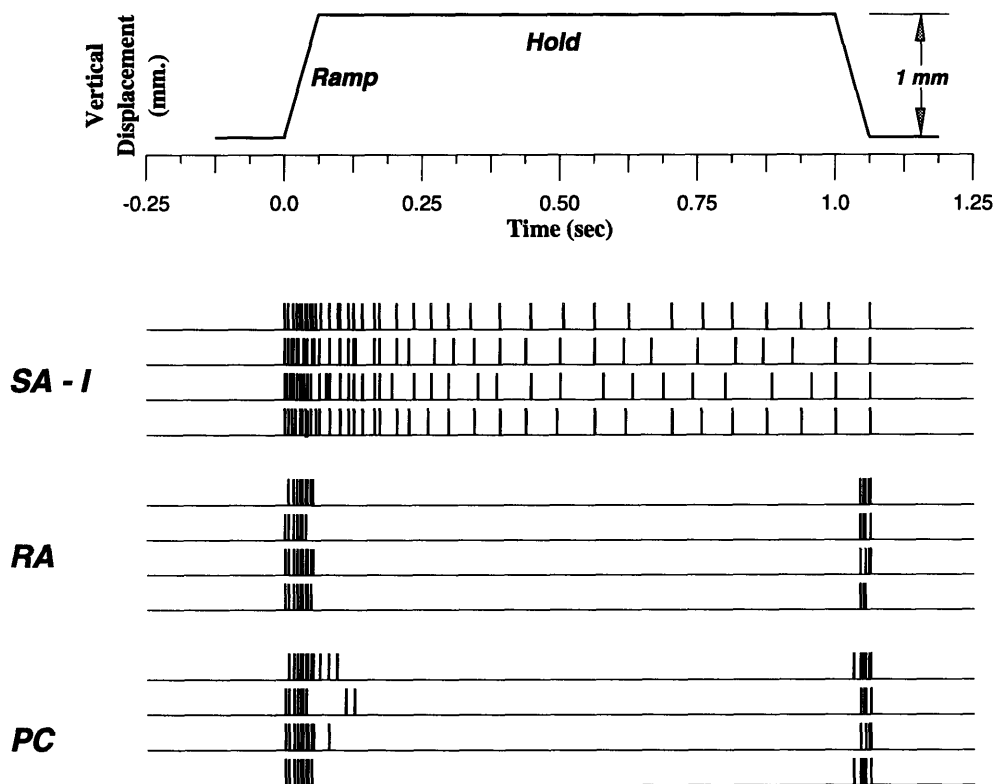


Figure 2-4: The afferent fibers are classified based on their response to a ramp and hold stimulus applied on the skin surface and shown in the top trace. The response of SA-I, RA and PC afferent fibers is schematically shown in the figure. Each vertical tick denotes a neural impulse recorded in the fiber.

indicates an impulse. The frequency of the impulses is termed as the discharge rate and is measured in impulses per second.

Figure 2-4 shows the typical ramp and hold experiment used to characterize the afferent fibers and the schematic response of the various afferent fibers. The experiment is performed as shown in Figure 2-3 and the top trace shows the ramp and hold stimulus indented into the fingerpad. Each neural impulse generated in the fiber is shown by a vertical tick on the time traces corresponding to the receptors. Three time traces for each receptive fiber are shown. The slowly adapting (SA-I) fibers respond not only at the ramp phase of the indentation but also throughout the period of sustained indentation (Darian-Smith, 1984). Microneurographic techniques of recording single-nerve fiber responses from awake humans have revealed another class of slowly adapting afferents that are primarily sensitive to skin stretch (Valbo and Hagbarth, 1968; Knibestol and Valbo, 1970; Johansson and Valbo, 1979) as are referred to as SA-II fibers. Although the response of SA-

IIs to stepwise indentation is very similar to the response of SA-Is to similar indentation, SA-IIs display a directional sensitivity to skin stretch and are frequently found either near the nail bed or near the skin creases on the digits. The rapidly adapting (RA) afferents and the fibers innervating the Pacinian corpuscles (PC) respond during the ramp phase of the indentation and during withdrawal of the stimulating probe, but do not respond during the phase of steady displacement of the skin (Darian-Smith, 1984).

Meissner's Corpuscles Meissner's corpuscles are located in the dermal papillae protruding upwards into the epidermis and are the closest to the surface of the skin among all the mechanoreceptors. The axial dimensions of these encapsulated ellipsoidal corpuscles are of the order of $100 \times 50 \mu\text{m}$ and the long axis is perpendicular to the skin surface. The afferent fiber associated with these corpuscles is of the rapidly adapting (RA) type.

Merkel Discs One of the most important un-encapsulated epidermal nerve ending in primate glabrous skin is the specialized receptor cell, the Merkel cell and the associated disk like nerve terminal. The cell is usually oval or rounded and is located in the basal layer cells of the epithelial glandular ridges in groups of 5-10. The diameter of the Merkel cells is of the order of $10 \mu\text{m}$. The afferent fiber associated with the Merkel cells is identified as the slowly adapting fiber of type I (SAI).

Ruffini Corpuscles Ruffini corpuscles are found in the sub-papillary dermis and are relatively large encapsulated structures from $500\text{--}1000 \mu\text{m}$ long, upto $200 \mu\text{m}$ in diameter in their central zone and about $30\text{--}40 \mu\text{m}$ in diameter near the poles. Their long axis typically runs parallel to the skin surface. The afferent fiber associated with these corpuscles is the slowly adapting, type II (SA-II).

Pacinian Corpuscles Pacinian corpuscles are, historically, the earliest known mechanoreceptors. They are ellipsoidal in shape and are also the largest in size amongst the mechanoreceptors. The long axis of the digital corpuscles varies from $0.3\text{--}1.5 \text{ mm}$ and the diameter from $0.2\text{--}0.7 \text{ mm}$. The corpuscle consists of a central nerve fiber, a compact inner core and a large number of membrane layers with fluid in between the layers. These are found in the deeper layers of the dermis or in the subcutaneous fat. Pacinian fibers

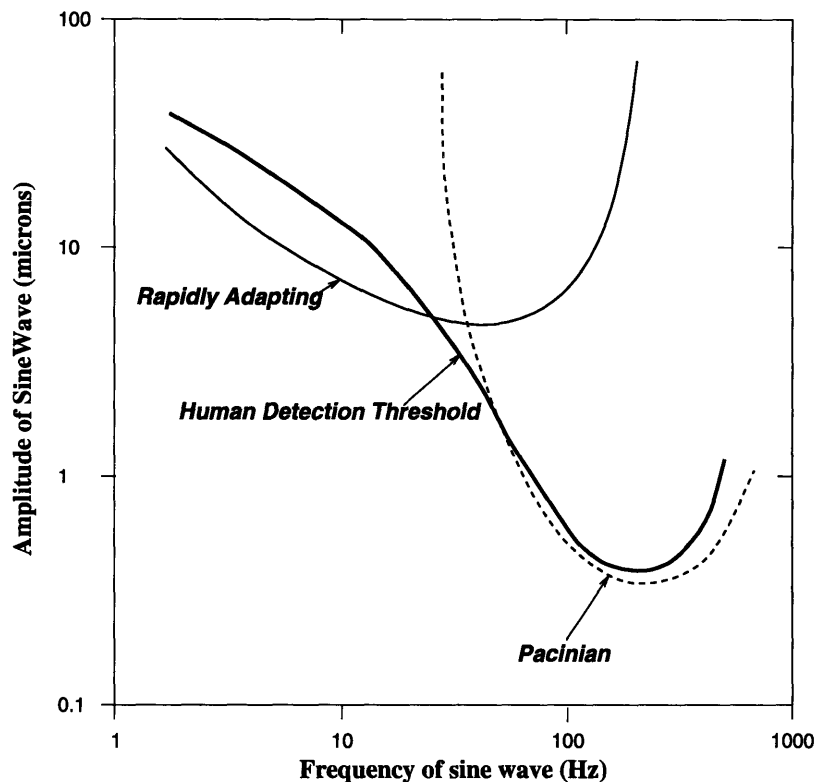


Figure 2-5: The frequency-threshold functions (“tuning curves”) for detecting vibratory stimuli applied to glabrous skin of the monkey fingerpad are shown. The thick line is the overall tuning curve, and the corresponding curves for RA and PC afferents are shown in thin solid and thin dashed line respectively. (Darian-Smith, 1984).

have low innervation density but are distinctive because of their exquisite sensitivity to vibratory stimuli.

Rapidly adapting receptors and Pacinian receptors are responsible for the detection and discrimination of vibratory stimuli. The frequency-threshold functions, also known as the tuning curves, for the monkey receptors is schematically shown in Figure 2-5. The two thin lines bound the response zone for the rapidly adapting and the Pacinian afferent fibers. The thick line indicates the detection threshold at various frequency. Although the tuning curves of rapidly adapting fibers and the pacinian afferents are similar in shape, the minimum threshold is at different frequencies and hence, the capacity of the primate to detect vibratory stimuli in the frequency range of 2-400 Hz depends on responses of both RA and PC fibers (Darian-Smith, 1984). The most sensitive region of the RA fibers is typically between 20-50 Hz, whereas, the most sensitive region of the PC fibers is 100-300 Hz. Pacinians are known to respond to vibrations of very low magnitudes, often 1 μm

or less (Mountcastle *et al.*, 1971).

Table 2.2 summarizes the structural and functional characteristics of the four main mechanoreceptors found in the primate fingertip. It can be seen that all the mechanoreceptors are rounded and smooth in shape and are located in the top 2.0 mm of the skin.

Electrophysiological recordings are possible from single peripheral afferent fibers in both monkeys and humans. The sensitivity of various fibers to a variety of mechanical stimuli is studied. The SA-I, believed to originate from Merkel cells, responds to both during ramp onset, and steady indentation by a probe. When the probe is vibrated sinusoidally at the most sensitive spot on the skin, the SA-Is are tuned (i.e. one nerve impulse per stimulus cycle) at the lowest amplitudes (about 20 μm) when the frequencies are low (less than 20 Hz). The rapidly adapting afferents (RAs) emanating from Meissner corpuscles respond to ramp onset, but are quiet during steady indentation. Their tuning threshold amplitudes (about 5 μm) are the lowest in the middle frequency range (20-50 Hz). Pacinian corpuscle fibers (PCs), while behaving similar to RAs for ramp and steady indentations, have very low tuning threshold amplitudes (about 1 μm) at high frequency ranges (100–300 Hz).

Out of the approximately 17000 fibers innervating the human hand, 56 % are rapidly adapting and the remaining 43 % are slowly adapting fibers (Valbo and Johansson, 1984). The mechanoreceptors are not uniformly distributed in the human palm and the innervation density is higher in the fingertip (distal phalanx). Table 2.3 is the comparison of innervation density of various fibers in the monkey and human fingers based on the data from Johanson and Valbo (1979). It should be noted that data for monkeys is in the terms of density, whereas, for the human data, the number of units reported.

In this thesis, neurophysiological data from SA-I type afferents is used. As the SA-Is are known to originate from the Merkel cells, the following geometrical factors are of importance: the depth of the receptors is between 0.7 and 1.0 mm from the surface of the skin; the size of the receptors is of the order of 10 μm and the inter-receptor spacing is of the order of 1 mm.

	Merkel	Ruffini	Meissner	Pacini
Location	Basal layer cells of the epithelial glandular ridges	Sub-papillary dermis	Dermal papillae protruding upward into the epidermis	Deeper layers of dermis, subcutaneous fat
Depth	0.7–1.0 mm	0.8-1.5 mm	0.5–0.7 mm	1.5 –2.0 mm
Size	10 μm	500 – 1000 μm long, 200 μm in central zone and 30-40 μm diameter near the poles	100 \times 50 μm	long axis 0.3 – 1.5 mm, diameter 0.2 – 0.7 mm
Shape	Oval or rounded	Ellipsoidal	Ellipsoidal	Ovoid
Orientation	Long axis typically perpendicular to the skin surface	Long axis typically parallel to the skin surface		
Morphological Classification	Un-encapsulated, Epidermal	Encapsulated, Dermal	Encapsulated, Dermal	Encapsulated, Dermal
Structure	Groups of 5–10 cells at a site	4–5 layers of lamellar cells covered by a basement membrane	Each fiber has a irregular discoidal form oriented at right angles to the long axis of the corpuscle	Several layers of concentrically packed lamellar cells, subcapsular space filled with fluid
Sensitivity to Stimuli	displacement and velocity	displacement and velocity	velocity	velocity
Innervating Afferent Fiber	Slowly Adapting type I (SA-I)	Slowly Adapting type II (SA-II)	Rapidly Adapting (RA)	Pacinian (PC)

Table 2.2: Comparison of various mechanoreceptors found in the primate fingerpad.

Fiber	Monkey		Human	
	Middle Phalanx	Distal Phalanx	Middle Phalanx	Distal Phalanx
Slowly Adapting	46/cm ²	134/cm ²	44	70
Rapidly Adapting	80/cm ²	178/cm ²	37	77
Pacinian	13/cm ²	13/cm ²	10	15

Table 2.3: Number of various peripheral afferent fibers in the primate fingertips. The data for monkeys is in the form of density of units, whereas, the number of units are reported for humans (Johansson and Valbo, 1979).

2.2 Previous Work

2.2.1 Attempts at modeling the fingerpad

In order to identify the relevant stimulus of SAI mechanoreceptors (Merkel Cells), Phillips and Johnson (1981a; 1981b) recorded the responses of mechanoreceptors innervating the monkey fingerpad to steady indentations by gratings with rectangular bars. To calculate the stress and strain values at typical receptor sites within the skin, they assumed the fingertip to be mechanically equivalent to a homogeneous, isotropic, incompressible and linearly elastic half-space in a state of plane stress or strain with infinitesimal deformations. In spite of such broad idealizations, maximum compressive strain profiles calculated by the models were in excellent agreement with the recorded SAI response profiles under a range of periodic and aperiodic gratings.

An alternative idealization shown in Figure 2-6 was successful in matching the measured *in vivo* skin surface deflection profiles of both monkey and human fingerpads under line loads (Srinivasan, 1989). Whereas the elastic half-space model only roughly approximated the profiles, a model of the fingertip as an elastic membrane (representing the skin) enclosing an incompressible fluid (representing the subcutaneous tissues) predicted the observed surface profiles quite accurately. This “waterbed” model, however, failed to match the variations in the responses of the receptors at different locations in the skin, owing to the uniform tension in the membrane and uniform pressure field within the fluid. If the receptors were embedded in the fluid or the membrane, all the receptors would experience the same stress state and would convey no information to infer the location of the load on the surface. Thus, the waterbed model was better for matching the available biomechanical data and the elastic half-space model was better for matching

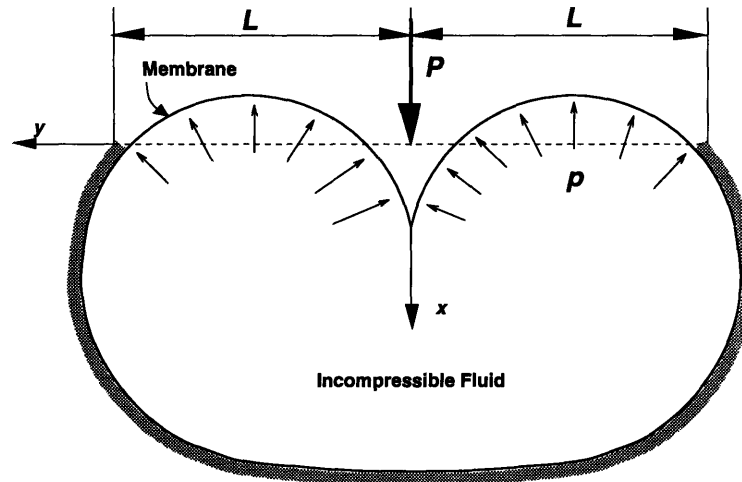


Figure 2-6: The figure shows a cross-section through the “waterbed” model of the primate fingerpad skin. The incompressible fluid is enclosed in a rigid channel. The membrane is assumed to have negligible thickness. The rest state is shown by a dashed line and the deformed state under a line load is shown by a continuous line.

receptor response profiles.

Van Doren (1987) modeled the fingertip as a infinitely wide flat medium of finite depth to investigate the mechanical response to spatiotemporal sinusoids. This model was similar to the model proposed by Phillips and Johnson (1981b) and the material was modeled as linear, homogeneous, isotropic, viscous and elastic. The results of the analysis suggested that the mechanoreceptors were responding to the normal strain in the tissue. The free parameters in the model, viz., the depth of the receptors and the thickness of the model agreed with the anatomical and physiological measurements.

Gulati and Srinivasan (1995) indented human fingertips with point, flat circular and flat plate indentors and measured the temporal force response. They proposed a lumped model consisting of a series of spring dashpots in parallel to explain the force response profiles observed experimentally. This Kelvin type model with a nonlinear spring in parallel with a sequence of piecewise linear spring-dashpot links predicted the nonlinear viscoelastic force response quite well.

2.2.2 Neurophysiological studies

As described in section 2.1.2, the mechanoreceptors in the fingertip skin have been identified, along with the afferent fibers that correspond to each receptor (Darian-Smith, 1984; Valbo and Johansson, 1984). It is possible to experimentally record from a single peripheral

afferent in monkeys and awake humans. Based on the sensitivity of the fiber to a ramp and hold indentation at its most sensitive spot, the fiber type can be identified.

In most of the neurophysiological experiments, the fingernail of the anesthetized monkey is glued to the table and the hand is restrained to limit any motions. The finger to be stimulated is held at a slightly elevated level and is not restrained in the lateral directions. Mechanical stimulators are used in applying stimuli to the fingerpad under controlled force or displacement according to the experimental protocol. By adhering to the “passive touch” protocol, where no motion of any joint in the hand is allowed, it can be ensured that the evoked response in the afferent fiber is due to the stimulus applied and not due to change in the configuration of the hand.

Single fiber recordings from SA-I afferents when the skin of their most sensitive spot is indented by rectangular bars, aperiodic rectangular gratings (Phillips and Johnson, 1981a), cylinders of various radii (Srinivasan and LaMotte, 1991; LaMotte and Srinivasan, 1993), sinusoidal shapes of varying curvature (Srinivasan and LaMotte, 1987) are reported. The evoked responses in SA and RA afferent nerve fibers when step shapes of various curvatures (LaMotte and Srinivasan, 1987a; LaMotte and Srinivasan, 1987b), a sphere, several ellipsoids (LaMotte *et al.*, 1993) and a pattern of alternating convex and concave cylindrical bars (LaMotte and Srinivasan, 1995) were pressed or stroked across the fingerpad of the anesthetized monkey have been published. To explain the questions concerning perception and neural coding of roughness or spatial resolution, precisely shaped rigid surfaces consisting of mm-sized bar gratings (Lederman and Taylor, 1972; Morley *et al.*, 1983; Phillips and Johnson, 1981a), embossed letters (Johnson and Phillips, 1981; Phillips *et al.*, 1983), or Braille dots (Lamb, 1983a; Lamb, 1983b; Darian-Smith *et al.*, 1980) have been used in neurophysiological and psychophysical experiments. The tactile sensing system is characterized by standardized measures such as the spatial resolution on the fingerpad, as measured by localization threshold of a point stimulus, which is about 0.15 mm (Loomis, 1979), whereas the two-point limen is about 1 mm (Johnson and Phillips, 1981).

Perception of shape, slip, microtexture, compliance and viscosity is investigated through several biomechanical and neurophysiological experiments. Humans can detect the presence of a 2 μm high single dot on a smooth glass plate stroked on the skin, based on the responses of rapidly adapting receptors (LaMotte and Whitehouse, 1986). Humans can also detect a 0.06 μm high grating on the plate, owing to the response of Pacinian

response fibers (LaMotte and Srinivasan, 1991). Among all the possible representations of the shapes of the objects, the surface curvature distribution seems to be the most relevant for tactile sensing (Srinivasan and LaMotte, 1991; LaMotte and Srinivasan, 1993). Slowly adapting fibers respond to both the change and rate of change of curvature of the skin surface at the most sensitive spot in their receptive fields, whereas, RAs respond only to the rate of change of curvature. Human discriminability of compliance of objects depends on whether the object has a deformable or rigid surface (Srinivasan and LaMotte, 1994). When the surface is deformable, the spatial pressure distribution within the contact region is dependent on object compliance and, hence, information from cutaneous mechanoreceptors is sufficient for discrimination of subtle differences in compliance. When the surface is rigid, kinesthetic information is necessary for discrimination, and the discriminability is much poorer than that for objects with deformable surfaces.

2.3 Need for Improved Models

The analytical model of Phillips and Johnson provided a closed form representation of the surface deformation and subsurface stress-state when the fingerpad was indented by a point load. Geometrically, the model proposed by Van Doren (1987) was different from the semi-infinite model of Phillips and Johnson only because it accounts for the finite depth of the medium. To use these idealized solutions for calculating the stress state under an arbitrary stimulus, the magnitude of the loads in the region of contact has to be known *a priori*. However, when two objects are pressed against each other, the size and shape of the region of contact and the loading in the region of contact change in a non-linear manner with increase in the depth or force of indentation (Johnson, 1985; Srinivasan and LaMotte, 1991). The analytical solution does not account for the finiteness and the curvature of the fingerpad which influence the size of the region of contact as well as the magnitude of the loads imposed on the fingertip. Irrespective of the size of the stimulus, the entire stimulus is in contact with the model if the model is flat and of infinite width. Considering the finite dimensions of the actual fingertips, the loads imposed on the skin as predicted by the semi-infinite models under finite stimuli would be different than the actual loads on the skin surface. The analytical solution does not account for the material inhomogeneities in the fingerpad and it is not trivial, if at all possible, to modify the analytical solution to

account for the inhomogeneities in the fingerpad.

The waterbed model (Srinivasan, 1989) which assumes the fingertip as being similar to a thin elastic membrane enclosing an incompressible fluid predicted skin surface deflection profiles under line loads that agreed very well with the observed profiles. However, the waterbed model leads to a uniform pressure distribution everywhere within the fluid and an identical state of stress at all points in the membrane and, therefore, is unable to explain either the reduction in the magnitude of receptor response as the stimulation location is moved farther away from the most sensitive spot of the receptor on the surface of the skin or the curvature sensitivity of SA-Is observed experimentally (Srinivasan and LaMotte, 1987). The sub-cutaneous adipose tissue exists in a semi-solid state *in vivo*, but the waterbed model does not account for any of the solid constituents of the fingerpad including the bone, which is several orders of magnitudes stiffer than the skin. The analytical solution for the waterbed model is available only for point load and commonly used loadings involving non-linear increase in contact area and load magnitudes cannot be analyzed with the available solution.

The model proposed by Gulati and Srinivasan (1995) is a lumped parameter model and is useful in predicting the force response of the entire fingerpad. It cannot predict the spatial variation of stresses or strains within the fingerpad or deformation profiles of the surface of the fingertip skin.

None of the above models can be used to predict the mechanoreceptor response to 3D stimuli like spheres and ellipsoids. Among the idealized models, the homogeneous elastic solid model was able to explain the neurophysiological data very well, while the waterbed model was better from a biomechanical viewpoint. A reliable and predictive model of the primate fingertip that can be used in the construction of the receptor population response to a given stimulus, and in the development of hypotheses for the peripheral and central coding of such diverse sensory qualities as softness or mechanical pain, has to satisfy two requirements: it should accurately model the biomechanical behavior of the fingertip and should predict the neural response observed experimentally. It is thus necessary to develop a mechanistic model that accurately represents the geometry and material properties of the primate fingerpad and a receptor model that can use the stress-state at the receptor location calculated by the mechanistic model and predict the receptor response.

On a higher level, this problem is addressed by three disjoint research communities in

their own areas of expertise. The biomechanics researchers have tested skin and bone to formulate a constitutive relationship for the materials. The neurophysiologists have performed experiments and tried to correlate the mechanical stimuli to the receptor response. The psychophysicist have tried to further our understanding of the human tactile system on similar lines as the human visual and auditory systems. Although, these studies have presented us with the knowledge of the human tactile system that we have today, the interplay of biomechanics in neurophysiological findings or the mechanistic basis of psychophysical findings have not been studied. It should be noted, that in order to undertake such inter-disciplinary studies expertise in each of the fields is necessary.

With the growing ability and need to put a human in a multi-sensory virtual environment, it is essential to have a thorough understanding of all the aspects of the human tactile system and the correlations between various factors at all levels in the process of perception. The work presented here is an attempt to model one aspect of such a multi-sensory biological system. Although the problem solved here is concerning the human tactile system, the idea can be extended to other problems where more than one area of expertise is needed to fully understand a complicated system. The idea is to identify the important components of a complicated biological system, isolate the components with dominant mechanics and dominant neurophysiological effects, model the underlying mechanics in the mechanics dominant blocks of the system, model the neurophysiology in the neurophysiology-dominant block and combine the various blocks to have one overall system that can be used to explain observed psychophysical phenomena. Having analyzed the system in blocks, it would be possible to examine the role of all the factors in a given observation.

3

Research Design and Methods

3.1 Approach

The structure of the primate fingertip is complex: from a macroscopic viewpoint, it mainly consists of two layers of skin, the epidermis and the dermis, which enclose subcutaneous tissues mostly composed of fat in a semi-liquid state together with a relatively rigid bone. When viewed as a block of material, it exhibits complex mechanical behavior such as nonlinear force-displacement relationship under indenting probes, anisotropy, and rate and time dependence. Quantitative data on the external and internal geometries of a typical fingertip, as well as the constitutive relations for the materials that make up the fingertip are unavailable at present. As discussed in Chapter 2, although some data on the *in vitro* and *in vivo* mechanical properties of the skin are available (for a review, see Cook, 1975; Thacker, 1976; Fung, 1981; Lanir, 1987; Lanir *et al.*, 1990), they have not been measured for the fingertip skin and are inappropriate for the whole primate fingertip, of which skin is one part. Furthermore, the constitutive equations and the models (for example, Danielson, 1973) that have been proposed contain a number of unknown material parameters.

At present and for the foreseeable future, a detailed model of the fingertip will have a large number of unknown geometrical and material parameters for various layers of skin and subcutaneous tissues. If they are treated as free parameters whose values are chosen such that predictions of the model match data from biomechanical and neurophysiological experiments, then the modeling process is essentially an elaborate curve-fitting procedure that does not provide any insight into the mechanistic basis of tactile sense. Alternatively, if the parameter values are arbitrarily assigned, it becomes impossible to determine the causes of success or failure of the model in explaining empirical data and to develop a

constructive procedure to improve the model. In either case, the resulting model will have too many parameters compared to the empirical data it is supposed to match or predict, while at the same time is a much simplified representation of the actual geometry and material behavior of the fingertip.

To overcome the limitations arising out of a lack of experimental data and complexity of the system, a combination of mechanistic and systems modeling can be employed. In this approach, the fingerpad with all its complexity is treated as an unknown *black box*, and the goal is to develop a *reduced order* mechanistic model that matches the empirically observed input-output relationship, without attempting to model the microscopic details of the system. The strategy here is to develop a sequence of models starting with the simplest mathematically tractable model containing a minimum number of parameters and gradually approach the actual physical structure of the primate fingerpad. This sequence is guided by agreements as well as mismatches between the model predictions and the results of biomechanical and neurophysiological experiments. The hope is that a synergistic evolution of both the models and the experiments, with each feeding information to the other, will eventually result in a fully tested realistic model and a deep understanding of the neural coding of tactile information. It should be noted that such a systems approach can be employed for mechanistic modeling of robotic tactile systems which consist of mechanoreceptors embedded in a compliant medium. The approach, however, is not limited to the analysis of tactile sensing systems, and is applicable in understanding the mechanics of any biological materials or organs.

One possible criticism of this approach in the context of tactile neural coding might be that conclusions based on simplified models are invalid in explaining experimental data from the real fingerpad. There are several responses to this criticism. First, as stated above, even detailed models of the fingerpad that take into account several layers of skin and subcutaneous tissues are quite simplistic relative to the actual biological structures. In addition, they have the problem of large number of unknown parameters. Second, a model need not and should not incorporate complexity unless it is forced to do so. Implicit in the above criticism is the assumption that the detailed geometry and material properties are of importance, which needs to be proven. For example, in the eye, although the cornea, lens, and vitreous body are structurally heterogeneous (both macro- and microscopically), they behave in concert like a simple, homogeneous lens. Radically simplified

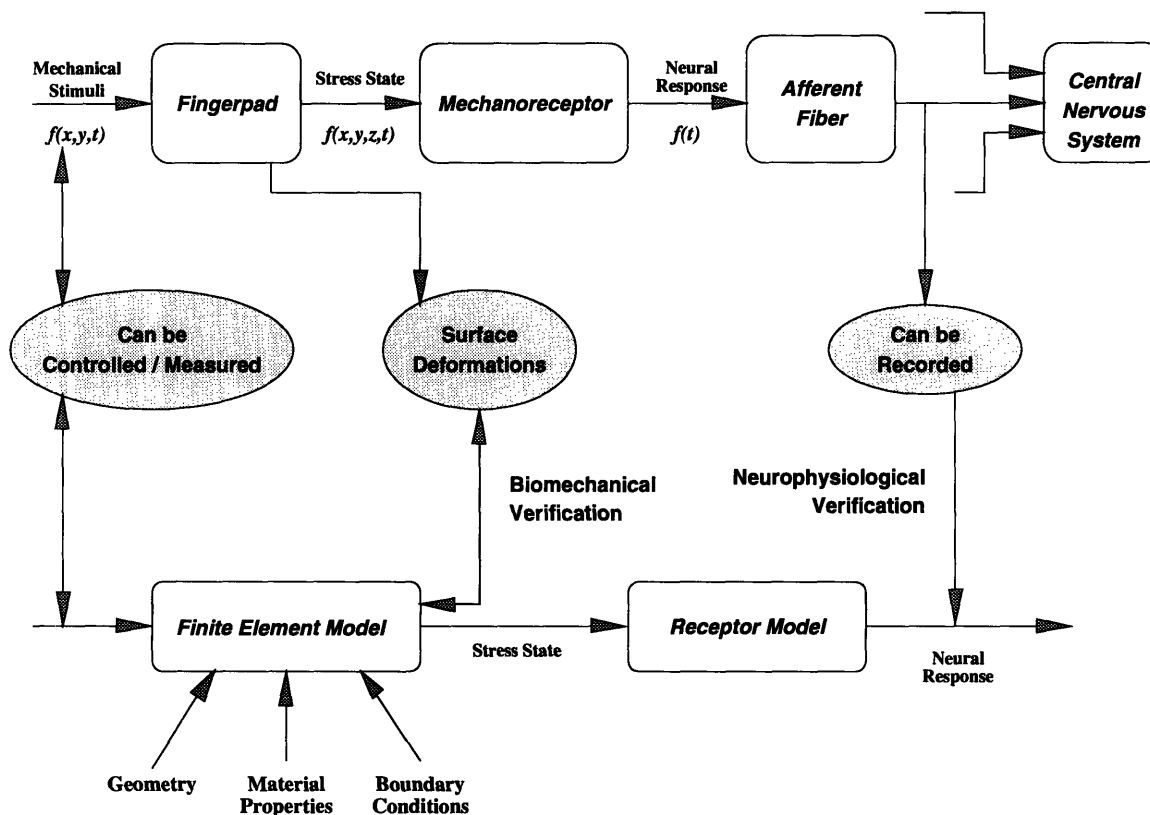


Figure 3-1: The figure shows the black-box approach used in modeling the system. The top path is the sequence of events in the actual system and the bottom path shows the proposed models.

models of the cochlea have been able to explain human auditory signal processing in the periphery (Lighthill, 1991). Similarly, it needs to be examined if the combined mechanical properties of the fingerpad and their effect on cutaneous mechanoreceptor response are simpler than that suggested by the structure of the fingerpad. Third, there are strong indications for the success of the systems approach outlined above, based on the results from extremely idealized models (Phillips and Johnson, 1981b; Srinivasan, 1989).

The top path in Figure 3-1 shows the sequence of events in the process of tactile sensing shown in Figure 1-1. During the process of contact of the fingerpad skin with the environment, loads are imposed on the skin causing it to deform. These time varying loads specified over the surface of the skin are the mechanical stimulation to the skin. These loads define a unique state of stress ($f(x, y, z, t)$) inside the fingertip skin. The mechanoreceptors responds with trains of impulses($f(t)$) in response to the stress-state in their vicinity. The central nervous system receives a temporal neural code from various afferent fibers which

is decoded to perceive the object in contact with the skin. The externally controllable or observable variables are shown in the ovals. The mechanical stimulation can be controlled and measured. Typically, if forces are prescribed, displacements can be measured and vice-versa. With the given set of mechanical loads, the surface deformations of the fingertip can be measured. Current experimental techniques allow the recording from single peripheral afferent fibers and hence the temporal neural code can be recorded and recordings for indentation by various indentors are available (see section 2.2.2).

The mechanistic behavior of the fingertip can be modeled using a mechanistic model that accurately represents the external and internal geometry of the fingerpad, the material properties of the constituents of the fingerpad and boundary conditions used in the experiments. The finite element method provides us with the flexibility required in developing a series of models with increasing degree of complexity. The finite element model can calculate the stress-state at all points in the fingertip for any set of mechanical loads imposed on the fingertip. A receptor model, that relates the stress-state in the vicinity to the neural discharge rate is used to predict the response of the mechanoreceptor to the given mechanical stimuli.

The same mechanical stimuli used in the experiment can be used in the finite element analyses. The surface deformation predicted by the finite element models can be compared with the experimentally observed data. Agreement in the experimental and predicted deformations will be used as the biomechanical check of the models. The receptor model will then be used to predict the neural discharge and the predicted discharge rate will be compared with the experimentally observed data. Agreement between the experimental and simulation results of the neural discharge will be used as a neurophysiological check. A model that satisfies both the biomechanical and neurophysiological checks can be used to generate hypotheses to be tested in future biomechanical and neurophysiological experiments.

The approach outlined above is useful for any model and for any class of receptor including slowly and rapidly adapting receptors. The goal of this thesis, however, is to explain the common features of the SA responses to diverse spatially and temporally complex stimuli. While individual SA responses might have idiosyncrasies that depend on the details of the local heterogeneity in the neighborhood of the receptor (for example, variations in local micro-mechanics of the receptor, dermis, and epidermis, together with

complex connections to the underlying fat pad), the common features of the class of SAs would only depend on globally common structures. As the empirical information about these materials of the fingertip and the computational capabilities increase with time, the models presented here serve as the essential foundations for further refinement.

3.2 The Finite Element Method

An analysis technique that can be used for mechanistic analyses of the fingertip models subjected to a variety of loadings has to be selected. The analytical solutions proposed earlier (section 2.2.1) are very specific in nature and are valid only with the modeling assumptions and loading used in the particular case. The approach in this thesis is to develop a series of models with increasing complexity and, thus, it is necessary to choose a analytical tool for mechanistic analysis which allows freedom in definition of the geometry, the boundary conditions, material properties, and the specification of the mechanical loading.

Finite element method is based on the concept of dividing the material continuum into number of small elements, each of which can have a distinct set of mechanistic properties. These elements are joined together subject to continuity requirements in the process known as assembly and each element contributes to the overall mechanistic properties of the body. The conditions of compatibility and equilibrium are satisfied in the assembly of elements and the solution of the underlying differential equations of equilibrium respectively. Boundary conditions can be specified at any point in the model and loads can be imposed either to model the prescribed displacement or the prescribed force experimental paradigm. Realistic interaction of the fingerpad with other rigid or compliant objects, with no prior knowledge of the area of contact and loading in the region of contact, can be modeled by using a step-wise iterative algorithm. Both static and dynamic analysis can be performed on the models, thereby making it possible to study slowly adapting as well as rapidly adapting mechanoreceptors. The geometry of the fingerpad and the constitutive relationships of the materials are independent inputs to the finite element model and hence each of these factors can be refined irrespective of each other. Vendor supplied codes are available to solve the finite element problems thereby eliminating the need to develop computer programs for the stress analysis involved in contact of objects with the

fingerpad.

The finite element method, thus, offers the required flexibility in modeling of geometry, material properties of the constituents, and simulating real life loadings as necessary for realistic modeling of the fingerpad.

3.3 Mechanistic Models

As shown in Figure 3-1, information about the geometry, the material properties and boundary conditions is required in the development of the mechanistic model. In considering the series of models, refinement in each of the three factors is possible. No *in vivo* biomechanical data for the human fingerpads is available and considering the variability in the reported *in vivo* and *in vitro* data from different sources (see Table 2.1), refinement in the material properties of the fingertip constituents should be attempted only when reliable *in vivo* biomechanical data becomes available. Accurate external geometry of the primate fingertips can be obtained from experiments described in Chapter 5 and some internal data can be obtained from published literature. The specification of the boundary conditions depends on the experiment being simulated and can be modeled accurately depending on the geometry of the model and the size of the mesh on the surface of the model.

3.3.1 Structural geometry

A logical starting point was the semi-infinite 2D model, which was useful in comparing the numerical solution with the analytical solution. The model geometry was refined in two-dimensions starting from the semi-infinite medium. The assumption of infiniteness was removed next and a finite-flat model was constructed. The curvature of the finger was accounted for by modeling the fingertip as a cylinder. Monkey and human fingertips were modeled as cylinders of 8 mm and 16 mm diameter respectively, which closely approximate the actual size of the monkey and human fingertips respectively. The cylindrical models were refined further by including a stiff concentric bone of realistic dimensions (2 mm diameter). A three dimensional model was considered next. The external geometry of monkey and human fingertips was accurately obtained by using an experimental setup described in Chapter 5. The shape of the internal bone was calculated from X-Ray images

of the primate fingertips. It was thus possible to study the effects of various geometrical factors affecting the stress-state at the mechanoreceptor location and its neural response.

3.3.2 Material properties

As described in 2.1.1, the skin is non-linear, anisotropic, visco-elastic in its mechanical response and exhibits variation in properties in the same individual by site and orientation. The *in vivo* data required to accurately model the fingertip skin is not available due to difficult experimental procedures (Lanir, 1987). The question then is how to model the fingertip skin in predicting its *in vivo* mechanical response, in the absence of reliable experimental data. The various aspects involved in the modeling are discussed below.

Homogeneity Observations by Cauna (1954) and an inspection of video images of deformed skin cross-section obtained by Vierck (n.d.) support the conclusion that, from a mechanistic viewpoint, it is enough to consider the skin as being composed of two layers and ignore the sub-layers of the epidermis and dermis. Each of the layers is clearly not homogeneous because its fibrous, cellular, vascular and granular components. In practical problems, we are interested in specimens which are orders of magnitude larger than any of the components of the skin and hence each layer of the skin can be considered as statistically homogeneous for a first analysis. The size of the Merkel cells (approx. 10 μm , see section 2.1.2) is several orders of magnitudes smaller than the size of the fingertip and its constituents. It is, therefore, valid to approximate the receptor as a point. Thus the stress-state at the mechanoreceptor is equivalent to the stress-state at its point location. In the two dimensional problems, the model was considered homogeneous. In the cylindrical model with bone, the bone was modeled as several orders of magnitude stiffer than the rest of the fingertip. The 3D models were meshed with the possibility of assigning unique stiffnesses to the various layers of the skin, but each of the layers were considered homogeneous. In the rest of the thesis, a model is referred to as *homogeneous* if all the elements have the same Young's modulus. A multilayered model, or a model with a stiff bone is referred to as *non-homogeneous*.

Stress-Strain Relationship Based on the available data, the stress-strain relationship of the skin is both nonlinear and anisotropic (section 2.1.1). In the absence of reliable *in vivo*

data for the human fingertip, the skin was modeled as linear and isotropic for the first analysis. As the constitutive relationship and geometry definition are independent inputs to the finite element model, the same geometrical model can be analyzed with non-linear stress-strain relationships as and when data becomes available. The decision of refinement of the material models was also be governed by the matches or mismatches between the model predictions and the experimentally observed data. The parameters needed for the complete specification of the material behavior in a linear isotropic material are the Young's modulus and the Poisson's ratio. It can be shown that for homogeneous finite element models if the loading is specified in terms of prescribed displacements, the strains are independent of the Young's modulus. The complete proof is given in Appendix B. The Young's Modulus was chosen arbitrarily for the homogeneous 2D models and for multi-layered models, the ratio of Young's moduli of different layers was specified.

Compressibility No experimental data on ν for fingerpad materials is available at present. There is, however, overall agreement that skin and soft tissues are nearly incompressible ($\nu \approx 0.5$). No experimental data on ν for fingerpad materials is available at present. The value of ν was chosen to be as close as possible to 0.5, i.e., 0.48. Any higher value caused numerical instabilities in the finite element solution of the plane strain models. Some of the 2D plane strain models were checked with $\nu = 0.499$, using hybrid formulation and found no significant difference in the results was found for a variety of loadings.

Viscoelasticity Skin is a viscoelastic tissue and the stress-strain relations are rate-dependent and exhibit considerable hysteresis (Lanir, 1987). For all the stimuli used in neurophysiological and biomechanical experiments data was recorded after the transients settle down. Thus the experimental data considered here is always "*pseudostatic*". The mechanistic problems to simulate the pseudostatic loading are, hence, static in nature. It is, thus, not necessary to model the viscoelasticity of the fingerpad. Since we are interested in biomechanical events of the time scale of a few minutes, the complexities of cell migration (about 25-50 μm per day (Quilliam, 1978)) can be ignored at present.

3.3.3 Boundary conditions

In typical biomechanical and neurophysiological experiments (LaMotte and Srinivasan, 1987a; Phillips and Johnson, 1981a), the fingernail is glued to the table to prevent any motion of the fingertip. This condition is simulated by suppressing all the degrees of freedom for the nodes that define the nail. Thus, all the degrees of freedom were suppressed at the nodes spanning the bottom boundary of the finite square model, and a third of the boundary at the bottom of the cylindrical models. All the degrees of freedom of the nodes defining the fingernail in the 3D model were suppressed.

3.4 Stimuli Applied to the Fingerpad

The stimuli to be applied to the fingertip are governed by the availability of published data from biomechanical and neurophysiological experiments. Using the finite element method, it is possible to impose loads that specify prescribed displacement as well as prescribed force. Based on the availability of published data and the biomechanical experiments on human subjects, the models were indented with single line loads, two point loads, rectangular bars of various widths, aperiodic gratings, cylindrical indentors of various diameters and step shapes of varying curvatures, under prescribed displacement and prescribed force protocols.

3.5 Biomechanical Verification

Considering the blackbox approach outlined in Figure 3-1, the mechanics of the system can be considered to be adequately modeled if the experimentally observed and analytically predicted surface deformations under similar mechanical loadings are identical. It should be noted that the biomechanical and neurophysiological components of the system are separated and, therefore, two different checks are necessary to evaluate the model. Due to the opacity of the fingerpad, the deformation of subsurface points cannot be observed. It would be a very important verification if it would be possible to measure the area of contact between the indenter and the fingertip when the indenter is pressed against the finger with prescribed force. These experiments are difficult to design, but if data from such experiments is available, it should be used in the biomechanical verifications.

Srinivasan (1989) indented human and monkey fingertips with a sharp wedge and observed the surface deformations. The finite element models will be subjected to a similar line load and the surface deformations will be calculated. The experimentally observed surface deformation profiles under line load were compared with the predictions of the model and the material parameters adjusted depending on the matches or mismatches between the two. The same material parameters will be used in predicting the surface deformation profiles under different mechanical stimuli, such as cylindrical indentors and the surface deformation profiles compared to check the predictive ability of the model. The model with the material parameters fixed, was indented by a series of indentors for which the force of indentation was available for various depths of indentation. The observed and predicted force displacement relations were compared.

3.6 Neurophysiological Verification

Monkeys are used as experimental models for physiological mechanisms in humans since the morphological types of mechanoreceptors (Chouchkov, 1978; Halata, 1975), the innervation density in the glabrous skin (Darian-Smith and Kennis, 1980; Darian-Smith, 1984), and the sensory capacities to detect and discriminate vibratory stimuli (LaMotte and Mountcastle, 1975; Mountcastle *et al.*, 1972) are similar for the two species. It is thus possible to relate the neurophysiological results obtained from the experiments on monkeys to the biomechanical and psychophysical results obtained from experiments on human subjects.

At typical receptor locations (known from published histological studies), profiles of various components of stresses and strains under some of the stimuli listed above were obtained. Using a methodology similar to that outlined by Phillips and Johnson (Phillips and Johnson, 1981b) a linear relationship of the following form was used to relate the stress-state at the receptor location to the neural discharge rate of the receptor.

$$R(x, y, z; t) = K_1[S(x, y, z; t) - S_1] + K_2\left[\frac{\partial S(x, y, z; t)}{\partial t} - S_2\right] + E(x, y, z; t) \quad (3.1)$$

where,

- $R(x, y, z; t)$ = discharge rate of a receptor located at a depth of x from the surface with y and z being the other two coordinates and t being time
- $S(x, y, z; t)$ = a candidate relevant stimulus in terms of, say, a strain component at receptor location (x, y, z) and time t
- $\frac{\partial S(x, y, z; t)}{\partial t}$ = Rate of change of S over time
- K_1, K_2 = sensitiveness constants
- S_1, S_2 = threshold constants.
- $E(x, y, z; t)$ = Error at time t , between the model predictions for a receptor located at (x, y, z) and neurophysiological data

For steady state response of SA-Is under static stimuli, there is no dependence on t , and K_2 will be taken to be zero. Then, for a given skin surface location (y, z) , only the three receptor parameters, x , K_1 and S_1 are unknown and are constant for a receptor, regardless of which stimulus is applied to the skin surface. Therefore, they are determined by fitting the recorded spatial neural response profiles under all the stimuli to the corresponding calculated candidate stimulus $S(x, y, z)$ profiles such that the squared error between the two profiles is minimized. The candidate stimulus that provides good fits over diverse stimulus conditions is judged as the relevant stimulus for that receptor.

4

Two Dimensional Models

The development of two dimensional models is the first step in the constructing a series of models of the primate fingertip that approach the actual fingertip. In this chapter, the construction and analyses of various two dimensional models is discussed. The construction of the models, including the choice of external and internal geometry, material properties and boundary conditions is explained. The results of the analysis of the models under simple mechanical stimuli including point load, two point loads of variable separation and rectangular bars are presented. The various biomechanical, neurophysiological and psychophysical implications of the mechanistic analysis are discussed. In order to investigate the role of mechanics in tactile spatial resolution, the experiment reported by Phillips and Johnson (1981a) is simulated using the two dimensional cylindrical models and the strain measures that are most likely the relevant stimuli to the slowly adapting afferents are identified. Validity of using the spatial response constructed from a single fiber recording as equivalent to the true population response is discussed. The correlation between the object curvature and experimentally observed and predicted neural discharge is examined by simulating the indentation of the models by several cylindrical indentors of varying curvatures. The observed and predicted surface deformation profiles under a single line load for various 2D models are compared.

4.1 Construction of the Models

The uniform cross-sections of a sequence of four models composed of isotropic, incompressible, and linear elastic media are as shown in Figure 4-1. As discussed in Chapter 3, the effect of refining the geometry on the state of stress in the vicinity of the mechanoreceptors will be examined, while maintaining the other variables in the model including

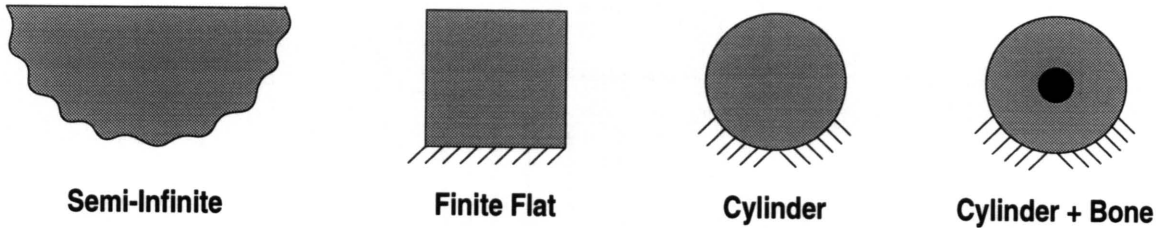


Figure 4-1: Cross-sections of each of the four models composed of an incompressible elastic material and assumed to satisfy plane strain conditions. The finite square model was 8 mm × 8 mm in size. The homogeneous cylinder and cylinder with bone had an external diameter of 8 mm and the diameter of the central rigid bone was 2 mm.

material properties constant.

The availability of analytical solutions to a line load acting upon a semi-infinite linear elastic medium (Timoshenko and Goodier, 1982) provides a means of verifying the finite element calculations. This solution was also the basis of calculations done by Phillips and Johnson (1981b) in their half-space model of the monkey fingertip. Therefore, a model with a large rectangular cross-section was analyzed first and the numerical solution was compared with the analytical solution. Model dimensions of 40mm × 18mm containing 8-noded plane strain isoparametric elements were sufficient to match the analytical results in the region of interest. The next step was to remove the assumption of semi-infiniteness and model the finger as a finite medium. The second model was of square cross-section (8 mm × 8 mm), with dimensions comparable to the actual monkey fingerpad. To account for the effects of curvature of the central cylindrical region of typical monkey fingertips (distal phalanx), the next refinement was to model the fingertip as a cylinder of 8 mm diameter, with and without a central rigid bone of 2 mm diameter. To simulate the fingernail which is very stiff relative to the soft tissues and is typically glued to a rigid support in biomechanical and neurophysiological experiments, all the degrees of freedom were suppressed at the nodes spanning the bottom boundary of the finite square model, and a third of the boundary at the bottom of the cylindrical models. In this chapter we mainly focus on the results of the cylindrical model with bone.

Figure 4-2 shows the mesh in the 2D cylindrical model with bone consisting of 8 noded plain strain elements. The top part of the model corresponds to the volar surface of the fingerpad, where stimuli are applied. In the monkey fingerpad skin, Merkel cell receptors associated with SAI fibers are embedded at a depth of about 0.5 mm to 1.0 mm from the

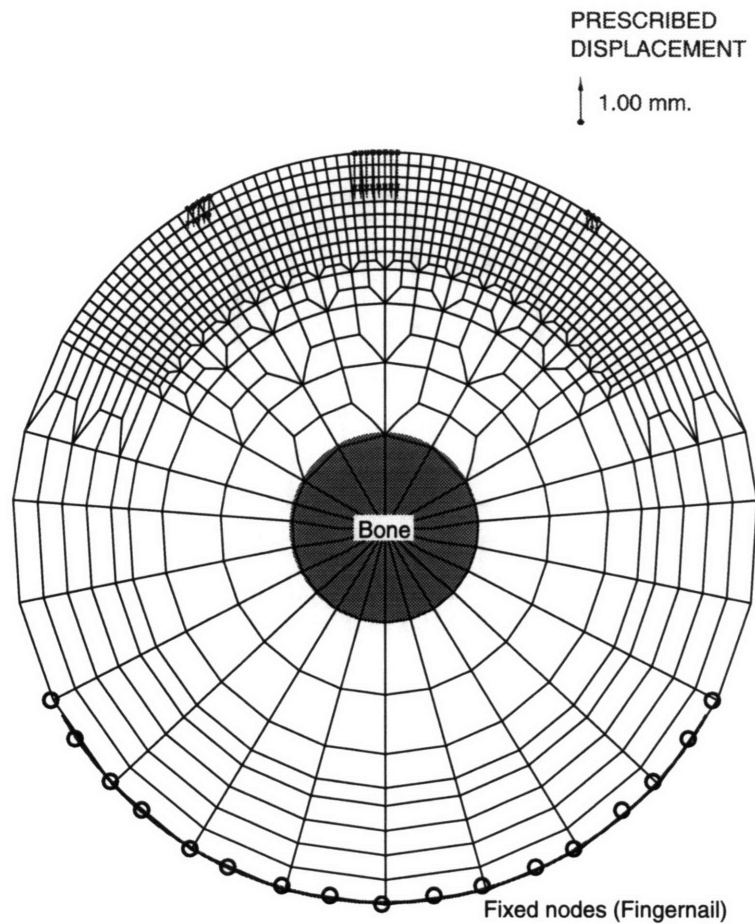


Figure 4-2: Cross-section of the cylindrical model with bone is shown. The nodes on the lower third of the circumference are constrained to simulate a concentric fingernail of anatomically correct dimensions, which is modeled to be rigid relative to the soft tissues. Displacements or forces can be prescribed on the top surface as shown. The top layer of the skin has a large number of elements where finer spatial resolution is sought. The element size is increased away from the top to reduce the computational effort.

surface and the receptor spacing is of the order of 1.0 mm. In order to have sufficient spatial resolution in calculating strains at typical receptor locations, square elements of 0.125 mm sides in the top 1.0 mm thick layer of the model, and 3×3 integration points within each element were used, resulting in an effective spatial resolution of about 0.05 mm in this region. The element size was gradually increased for deeper locations from the top surface as shown in Figure 4-2. This helped to reduce the size of the problem, thereby reducing the computational effort. The aspect ratio of the elements was maintained as close to 1.0 as possible by using layers of transition elements. The stiff nail is simulated by constraining

all the degrees of freedom of the bottom third of the circumference of the cylindrical model as shown in the figure. The same transition scheme was used in all the other models, thereby maintaining high spatial resolution in the region of interest.

The structural complexity of the primate fingertip and the variability in the mechanical properties of the fingertip reported in the literature are summarized in section 2.1.1. For reasons discussed in section 3.3.2 on page 43, for this first analysis, the fingertip was assumed to be homogeneous and the material was assumed to be linear elastic and isotropic, which required the specification of only the Young's modulus and the Poisson's ratio. If the prescribed loading and boundary conditions are in terms of displacements, it can be shown that for a homogeneous model under infinitesimal deformations, the strains are independent of the Young's modulus (see Appendix B). Thus, no specific value of the Young's modulus was needed to be assumed in the calculations. Various *in vivo* and *in vitro* measurements of compressibility of the skin summarized in section 2.1.1 indicate that the fingertip can be considered almost incompressible and, therefore, to a first approximation, the fingertip can be considered to be incompressible (i.e., Poisson's ratio = 0.5). Loading was confined to indentations by line loads and long bars that have been used as stimuli in previous biomechanical and neurophysiological experiments. Considering the approximately cylindrical structure of the fingertip (axial dimension larger than the lateral dimensions) and the loading that does not vary with length, we can consider all the 2D cross-sections of the fingertip to be in the same condition, and the finite element model to be representing the typical cross-section. Therefore, plane strain approximations (Timoshenko and Goodier, 1982) are valid in the analyses of these models. Finite element models of incompressible materials in plane strain require special care in the formulation. The mixed displacement-pressure (u-p) formulation which treats pressure as an independent nodal variable in addition to the displacements (Sussman and Bathe, 1987) was used and a Poisson's ratio of 0.48 was chosen. A subsequent analysis of some of the cases were done using a hybrid formulation which allowed the Poisson's ratio to be as high as 0.499, but no significant differences were found in the results. Since the loads are static and the recorded receptor responses that need to be correlated with the stress or strain measures are generally steady, the viscoelastic behavior of the fingerpad was not taken into account for this initial analysis.

The ADINA finite element software together with custom written codes for prepro-

cessing and generating the elements was used. The cylindrical model had 856 plane strain isoparametric elements and 2633 nodes. The resulting stiffness matrix had 838,200 elements and had a mean half-bandwidth of 161. The solution time for a static problem with prescribed loads on the DEC3100 was about 140 cpu seconds excluding pre-processing and post-processing. The same problem could be solved in about 12 cpu seconds on the MIT CRAY-XMP supercomputer. The solution for problems solved with the large displacement formulation and contact problems, which rely on iterative solutions, required substantially higher CPU time. The semi-infinite model had 3190 elements and 10,859 nodes. Depending on the model size and the computational effort involved in the simulation, a DEC3100, DEC 5000, workstation or the MIT CRAY X-MP supercomputer was used to perform the finite element analyses.

4.2 Point Load

Since the emission of neural impulses by the receptors is due to the opening of ionic channels caused by mechanical strains, the state of strain at receptor locations is important in predicting the receptor response. Shown in Figure 4-3 are three possible candidates for the relevant stimulus to SAI mechanoreceptive afferents. They have been calculated using the cylindrical model with bone subjected to a single line load imposed on the surface at the horizontal location 0.0. Each strain measure is evaluated at three depths in the region where the receptors are known to be located. For each of the components, the deeper the location, the more blurred is the spatial distribution. This illustrates the spatial low-pass filtering of the mechanical signals by the elastic medium and shows that the quality of information about the spatial variation of the surface stimulus decreases with increases in the depth of receptor locations. It should be noted that the stresses corresponding to the strain measures shown here are similar in form. The rest of the stress and strain components are not shown due to the lack of their promise as relevant stimuli for the receptor response. For the three other models described above, although the magnitudes of the stresses and strains at a given location are different for a given line load, the general spatial profile of each component is approximately the same as the corresponding one for the cylindrical model. Various strain measures are compared for a rectangular bar indenting the various models in Figure 4-7.

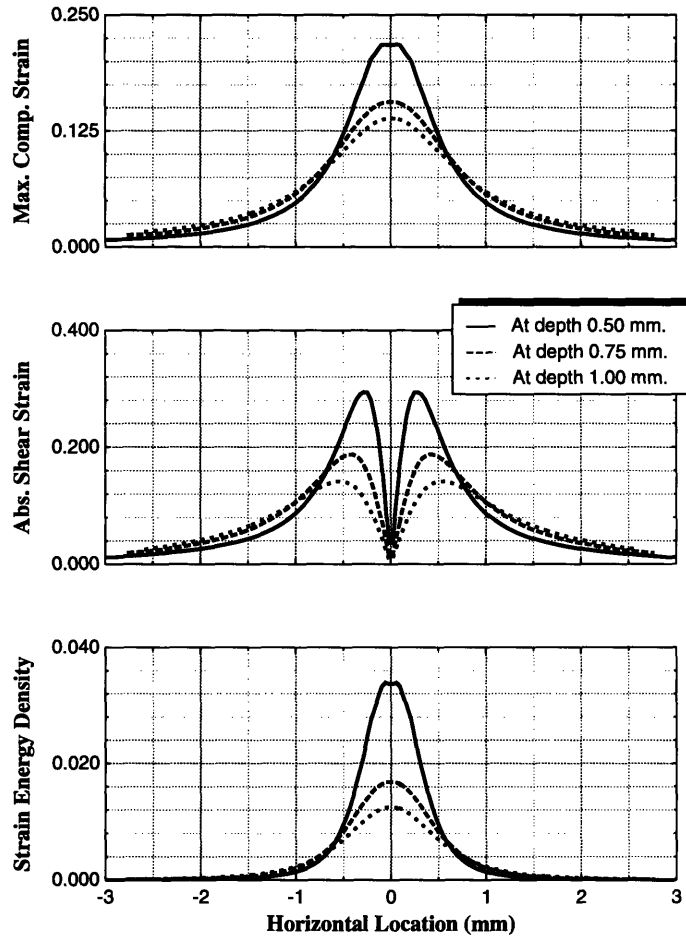


Figure 4-3: Spatial distribution of sub-surface strain measures under a line load applied normally to the cylinder model surface at the horizontal location 0.0. Distributions are calculated at three possible depths from the surface in the region where mechanoreceptors are typically located. Calculated profiles are shown as continuous traces since the data points are only 0.05 mm apart.

For a given receptor depth, the degree of blurring of the strain energy density distribution is less than that of the maximum compressive strain (Srinivasan and Dandekar, 1991). This is to be expected since, for the plane strain models composed of an incompressible material, it can be shown that the strain energy density is proportional to the square of the magnitude of maximum compressive strain (See appendix A). Therefore, for a given stimulus force distribution acting on the skin surface and receptor locations within the skin, the contrast in the neural code based on strain energy density is much higher than that based on maximum compressive strain. The distinct differences in the three component distributions indicates that if a fine enough probe (say, 0.2 mm dia.) is used in neurophysiological experiments, the spatial response profiles of the SAI and RAI

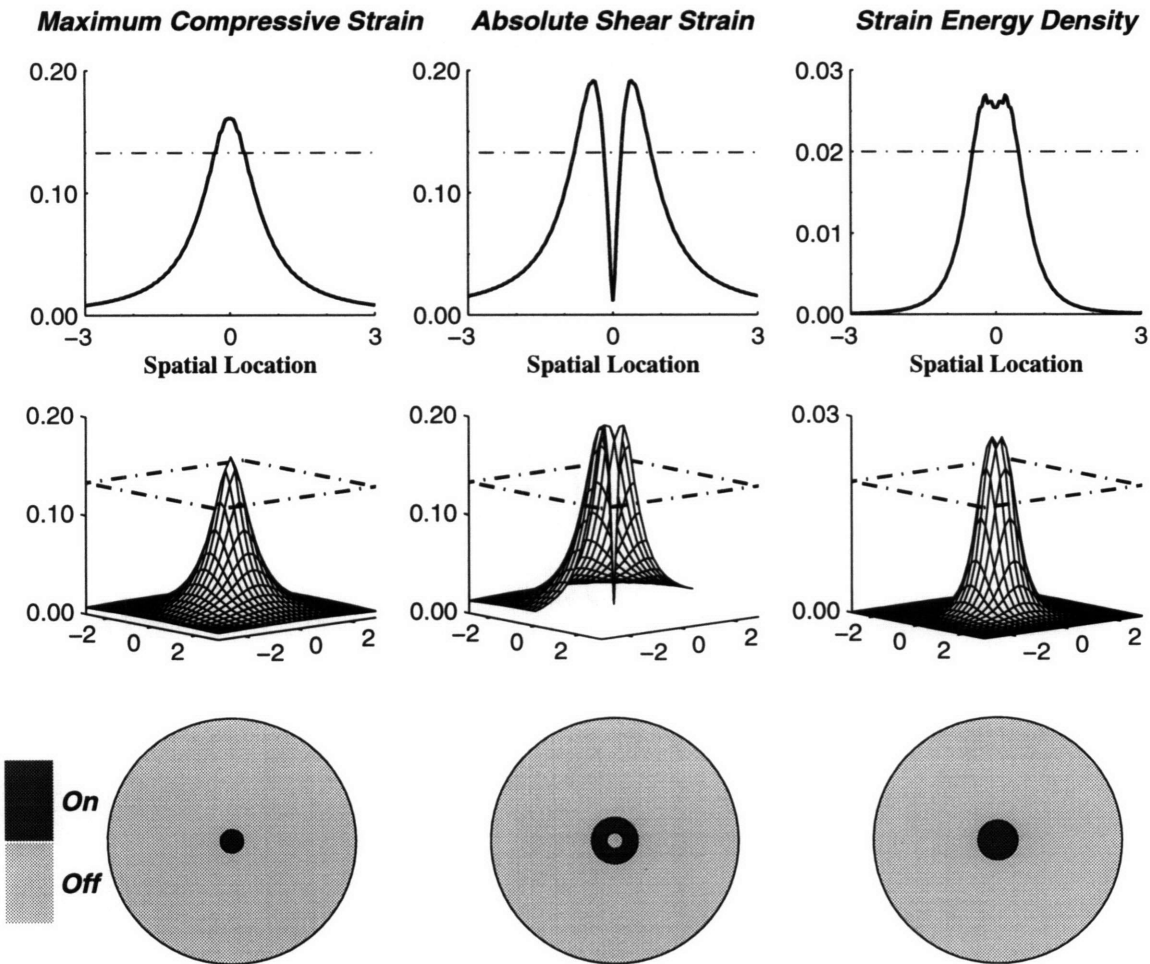


Figure 4-4: Receptive fields predicted by the candidate relevant stimuli. The top trace shows the spatial variation of the strain measure at a depth of 0.75 mm. The horizontal line is the threshold value used in plotting the receptive fields, which are shown in the bottom panel.

fibers might enable the determination of their respective relevant stimuli.

The shape and size of the receptive field is commonly used as an indicator of the spatial resolution of a mechanoreceptor. Receptive fields for an indentation by a point load can be experimentally mapped on the skin by using von Frey hairs. The receptive fields of SAs and RAs are mostly circular or oval shaped corresponding to circular areas of 2–8 mm diameters (Johansson and Vallbo, 1983; Johansson, 1978). They exhibit smaller receptive fields than PCs and hence are responsible high spatial acuity in the fingertips to low frequency mechanical stimuli.

Figure 4-4 shows how receptive fields of SA afferents for indentation by a point load can be predicted using the three candidate relevant stimuli considered in Figure 4-3. The

top panel shows the spatial variation in the strain measures at a depth of 0.75 mm when the skin is indented by a point load to a depth of 1 mm at the spatial location 0.0 mm and hence are identical to the traces of the three strain measures at a depth of 0.75 mm shown in Figure 4-3. If the receptor response is completely governed by the relevant stimulus, then a threshold value for the appropriate strain measure will determine the response threshold of the receptor. Specifically, if the magnitude of the relevant stimulus is less than the threshold, the receptor will not respond. The dash-dot line in the top trace is an arbitrarily assumed threshold value for the particular strain measure. It can be observed, that although there is a difference in the form of the spatial variations of the strain measures, because of the symmetry of the loading and geometry of the model, the variations are symmetric about the point of application of the point load. The strain profile shown in the top trace is predicted in the plane of the 2D model considered here. If we assume the same profile to be true for a depth of 0.75 mm in the all vertical planes containing the line load, then we can reconstruct the strain measures at all the points at a depth of 0.75 mm from the skin. Such reconstructed strain measures, with the spatial dimensions on the X and Y axis and the strain measure on the Z axis, are shown in the middle panel. The line representing the threshold value now takes the form of a plane shown bounded by the dash-dot lines. Let A and B be two points on the skin surface, such that A is exactly at the spatial location 0.0 and B is anywhere within a few millimeters from A . We will assume that the state of stress at the receptor below B , when the fingertip is indented by a point load on the skin at A is the same at the state of stress at the receptor below the point A when the fingertip is indented by a point load on the skin at point B . This would be the case for a semi-infinite model, but this is a reasonable approximation for the case of 2D cylindrical model, since we are restricting the discussion to a centrally located single point load and two points A and B are a short distance apart compared to the fingertip diameter. Now, the strain profile predicted in the middle panels can also be interpreted at the magnitude of the strain measure at the receptor location below point A , when a single point load is applied at various spatial locations on the skin surface, plotted with respect to the spatial location of the load. This is the predicted strain measures in a typical neurophysiological experiment involving indentation of the surface of the fingertip with a point load (von Frey monofilament). A receptor located below point A , will produce a neural response only if the magnitude of the relevant stimulus is higher than the threshold

value. Receptive fields for the candidate relevant stimuli based on the assumed threshold values are shown in the bottom panel of Figure 4-4. The receptors would respond with trains of impulses if the point load is applied in the "On" region shown shaded dark and will be silent if the point load is applied in the "Off" region shown in light gray.

It can be seen that maximum compressive strain predicts a circular receptive field, with the center of the circle being the most sensitive spot. Strain energy density predicts a similar receptive field with a circular region centered directly above the receptor as the region in which the receptor would respond. The receptive field predicted by absolute shear strain is peculiar because of its annular shape. This means that if the receptor is triggered by the absolute shear strain in its vicinity, it would not respond to a point load stimulus directly above the receptor on the skin, but would respond in an annulus around the receptor. The diameter of the OFF circle in the receptive field for absolute shear strain is about 0.3 mm. Since the diameters of the probes that have been used in the determination of receptive fields for peripheral afferents are greater than 0.3 mm (Johansson and Valbo (1983) used a probe of was 0.4 mm. dia.), they would be unable to detect the central off region. Experiments with much finer probes are necessary to empirically determine this center-surround phenomenon and if absolute shear strain is the relevant stimulus for any of the receptor classes (Srinivasan and Dandekar, 1991).

The analysis above shows that for a given material of the fingertip, the stress state at a receptor location is governed by 1) the loading on the skin surface specified by the probe contact area as well as the direction and magnitude of force or depth of indentation, and 2) the depth of the receptor below the skin surface and its relevant stimulus. Since the predicted receptive field shape and size are directly dependent on this stress-state, they are functions of all the above factors that influence the stress state at the receptor location. Therefore, the size of the receptive field can be an indicator of the spatial resolution of a fiber only when the factors defining the loading on the skin surface are adequately controlled.

4.3 Two Point Resolution

The spatial resolution of the tactile sensory system can be determined by stimulating the skin with two sharp probes at variable distances apart. It is usually measured as the

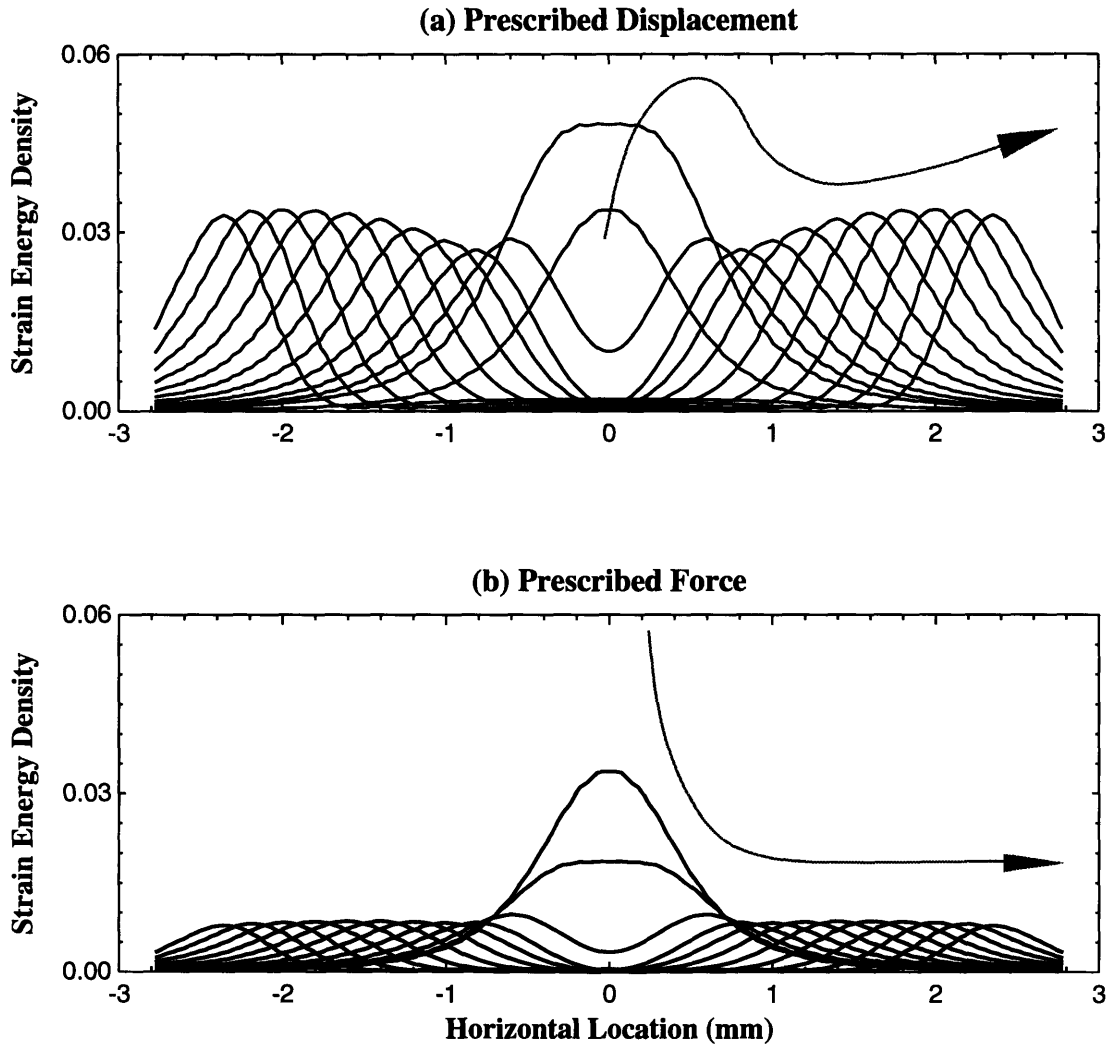


Figure 4-5: Spatial distribution of strain energy density for a pair of equal vertical point loads applied on the 2D section of the cylinder model and spaced at variable distances apart. (a) Prescribed displacement: the depth of indentation under each load is kept constant for the succession of load spacings. (b) Prescribed force: each force is kept constant for the succession of load spacings. The traces for the single load case (i.e., zero load spacing) are identical in (a) and (b).

minimum distance between the two probes for them to be perceived as distant (Johnson and Phillips, 1981; Dellon, 1981). Although the stimuli are applied by hand in clinical settings, more precise experiments can be performed using a tactile stimulator capable of indenting the fingertip with two probes at required distance apart. The loading can either be specified as prescribed displacements, where the probes would be indented into the fingerpad to a prescribed depth, or as prescribed force, where the probes would be

indented into the fingerpad till the prescribed force is achieved at each probe. To simulate the two conditions, the two point loads on the 2D model cross-section were modeled as prescribed displacements or prescribed forces each of which were maintained constant for all the load spacings. The corresponding strain energy density distributions at a depth of 0.75 mm are shown in Figure 4-5, such that for the single load (i.e, zero spacing) the solutions are identical in (a) and (b). In the prescribed displacement case, as the load spacing increases from zero, the peak value of strain energy density increases at first, then decreases sharply, followed by a gradual increase till it attains a steady value. On the other hand, in the prescribed force case, the peak value monotonically decreases and settles down to a steady value at a load spacing much smaller than the corresponding one in the prescribed displacement case.

The explanation for the difference stems from the fact that surface displacement due to each load spreads (semi-width of about 2 mm) much wider than the corresponding sub-surface strain energy distribution at the depth of interest (semi-width of about 1 mm for depths 0.5 to 1.0 mm) (Srinivasan and Dandekar, 1994a). In the prescribed force case, the principle of superposition implies that as the load spacing is increased from zero, the sub-surface strain profiles under each load remain the same for load separation distances greater than the full width of the strain distribution for a single load of the same magnitude. However, in the prescribed displacement case, the magnitudes of applied force (and consequently the strain distribution) do not reach steady values until the load separation distance is equal to the full width of the surface displacement distribution for one of those forces.

The results of a psychophysical experiment to determine the spatial acuity would be more accurate if the stimuli are such that the subject has to base his or her responses only on spatial information. In the case of the two point discrimination experiment, this would imply that the design of the experiment should be such that, ideally, no intensive cues should be available to the subject. The spatial cue in this case is the distance between the two loads, whereas, the intensive cue is the magnitude of the relevant stimulus at the receptor location. For a given load separation, the maximum strain energy density is extracted from Figure 4-5 and is plotted as a function of half separation of the loads in Figure 4-6, for force controlled and displacement controlled experiments. The variation in the maximum strain energy density represents the intensity information available to

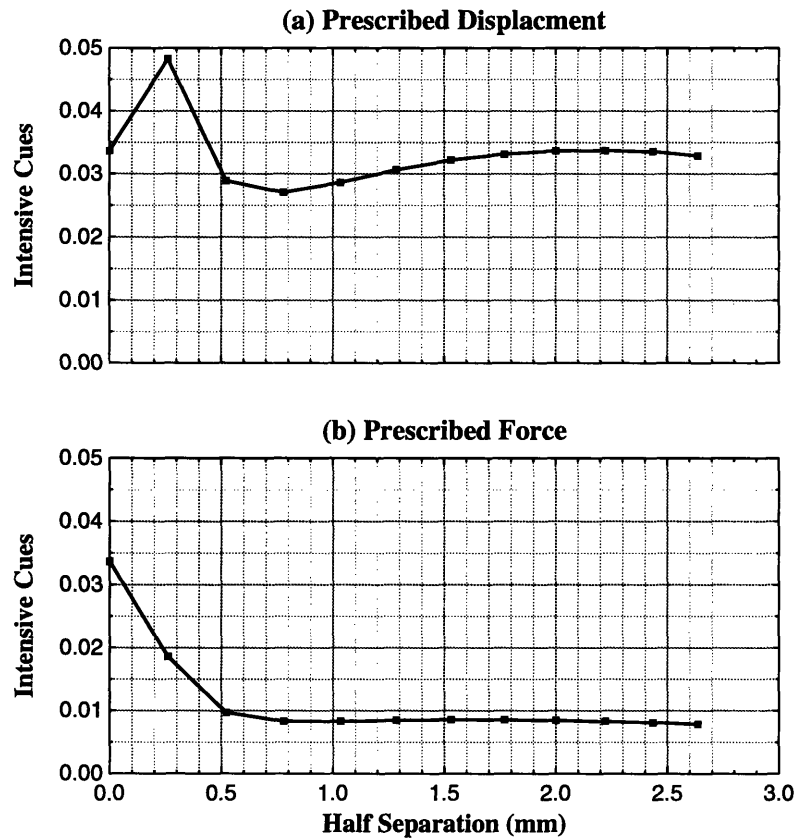


Figure 4-6: Intensive cues available to a subject when two point loads are imposed under different experimental protocols. The maximum strain energy density at a depth of 0.75 mm for two line loads spaced variable distance apart (Figure 4-5) is plotted versus the half separation between the loads. The figure shows that in experiments done under force control (top panel) the intensity information settles to a constant value at a lower value load separation than the prescribed displacement case.

the subject at each load separation. It can be seen from Figure 4-6 that, in the prescribed displacement case the intensive cues continue to vary with the load separation, whereas, the intensive cues settle down to a constant value at a separation of 1.6 mm for the prescribed force case. If the separation between the loads is more than 1.6 mm, then there are no intensive cues available to the subject if the experiment is performed with prescribed forces, whereas, the subject could base his or her responses either on the intensive or the spatial information if the experiments are done with prescribed displacements.

An implication of the mechanics of the fingertip to the neural coding of two-point stimuli is that when the loads are between about 1.5 mm to 4 mm apart, the discrimi-

nation between two load pairs may be based on intensity information in the case when displacements are kept the same for the pairs, but is based on purely spatial information when forces are kept the same. Therefore it is better to use force control in testing humans for spatial acuity using two point stimuli, than the displacement control that is typically employed due to the simplicity in the design and control of the experimental setup.

4.4 Indentation by Rectangular Bars

Rectangular bar is one of the simplest shape used in the study of tactile coding and neural representation of shape. Geometrically, the edges of a bar present a singularity in the curvature. Mechanistically, a question of considerable interest is the effect of model geometry on strains at receptor locations which, in turn, are related to neural response. The results for the four models indented to a depth of 1 mm by a 1.5 mm wide rectangular bar are shown in Figure 4-7. The surface loads imposed by the bars are shown along with the three strain measures at 0.75 mm depth. For each model, the intensity of the surface pressure is very high under the edge of the bar relative to the pressure at the center of the bar. The spatial distribution of the three strain measures shown are essentially low-pass filtered versions of the surface pressure distribution. The extent of the filtering depends on the model as well as the particular strain measure. For example, among the models, all the strain measures for the finite square case have superior contrast between the edges and the center of the bar, and the absolute shear strain has the best contrast among the strain measures for each model. Therefore, if a robot tactile sensing system needs to be designed to detect edges, the models predict that the best performance would be achieved by shear strain sensors. Strain energy density can be considered a measure of distortion in almost incompressible medium. A comparison of the strain energy profiles of the three models show that for the same stimulus, the distortion at the receptor location as measured by the strain energy density is the highest in the cylindrical model with bone. The effect of adding a stiff bone to the homogeneous cylindrical model can be seen in the increase in the maximum loads imposed and the accentuation of the strain energy density profile between the cylindrical model and the cylindrical model with bone.

The cylindrical model best approximates the geometry of the actual fingerpad as it accounts for both the finiteness and the curvature of the fingerpad. The cylindrical model

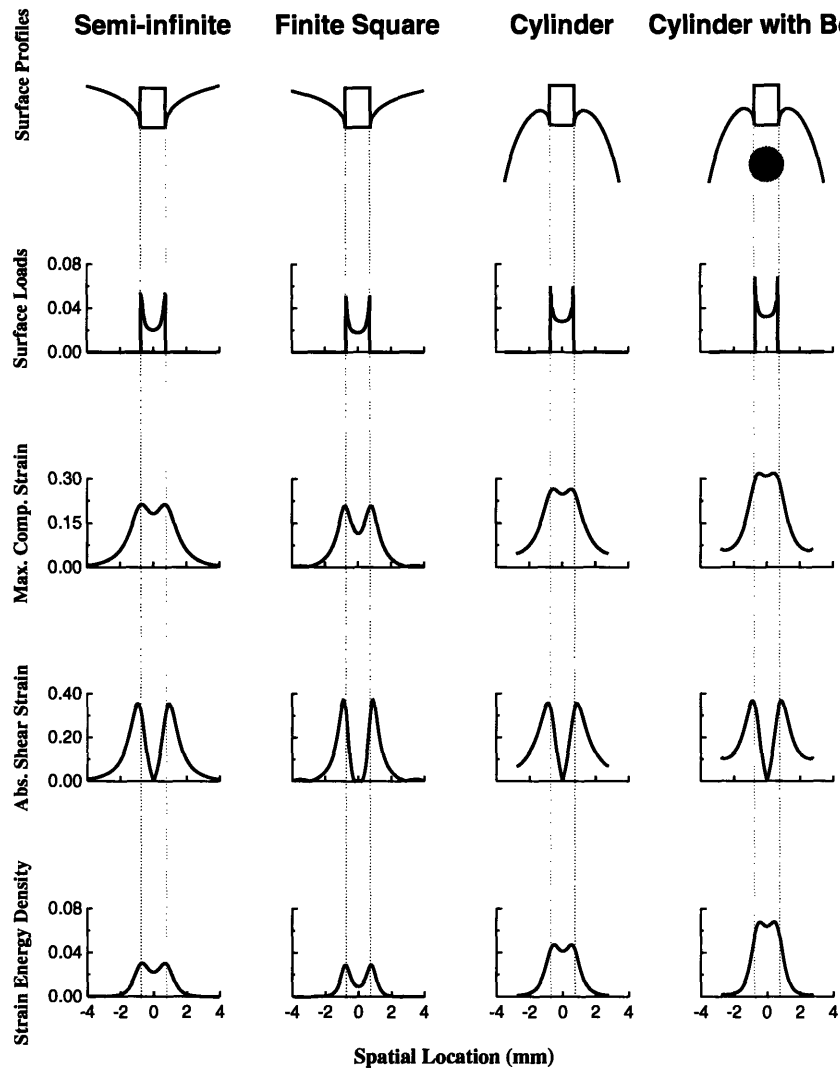


Figure 4-7: Vertical indentation of each model by a 1.5 mm wide rectangular bar to a depth of 1 mm. Calculated spatial distributions of surface deflection and surface loads, as well as maximum compressive strain, absolute value of shear strain, and strain energy density at 0.75 mm depth are shown.

with bone models the material inhomogeneity by considering the effects of a comparatively rigid bone in the rather compliant fingertip. The effect of finiteness of the model and curvature of the cross-section on the predicted stress state is studied using the single bar indenter as described above. For all the further simulations the cylindrical model with bone is used unless otherwise specified.

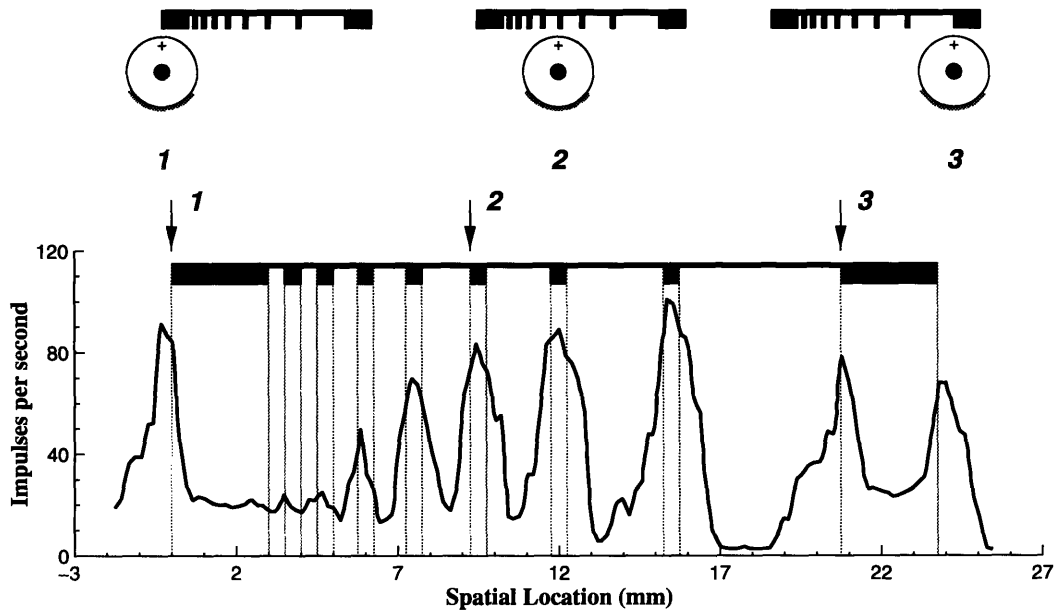


Figure 4-8: Three different positions of the grating indenting the monkey finger are shown in the top panel. The spatial response profile shown in the bottom panel is generated by plotting the neural response recorded for each indentation versus the spatial location of the grating for that indentation (Phillips and Johnson, 1981a).

4.5 Indentation by Aperiodic Gratings

4.5.1 The experiment

Neurophysiological experiments probing the primate tactile sensing system typically consist of recording the response of one peripheral nerve fiber at a time, but the responses from the population of receptors activated by a stimulus are needed to decipher the neural code for that stimulus. By carefully designing the sequential stepping of rectangular gratings across a fiber's most sensitive spot (MSS) on the skin surface, Phillips and Johnson (1981a) succeeded in reconstructing a hypothetical population response from the response of a single fiber. The schematic of the experiment is shown in Figure 4-8. During each indentation the grating indented the skin by 1.0 mm for 1 second while the fiber response was recorded. Between indenting the grating was raised free of the skin and moved laterally by 200 μm at right angle to the grating bars. The grating bars were oriented either parallel to the skin ridges (along the axis of the finger) or perpendicular to the skin ridges (perpendicular to the axis of the finger). Figure 4-8 shows the construction of the *spatial response profile* by plotting the recorded receptor response with respect to the spatial location

of the grating. If it is assumed that there exists a sheet of identical and uniformly placed receptors inside the finger and if the surface of the fingertip is modeled as a semi-infinite plane, then the *spatial response* can be considered to be an accurate representation of the population response of the mechanoreceptors. Clearly, both the assumptions required for the idealized model are not true and, hence, the spatial response was considered to be a first order approximation of the population response in the absence of experimental data and advanced mechanistic models.

4.5.2 Simulations with the 8 mm diameter model

The finite element models described here, however, are not subject to experimental limitations such as recording from a single fiber. They are able to simulate the mechanistic aspects of both the population response for a single stimulus or the response of a single fiber to multiple stimuli. Simulations of the sequential indentations of the cylindrical model with bone by all the gratings used by Phillips and Johnson (1981a) were carried out and the spatial sub-surface strain distributions for each indentation of the gratings were calculated. Figure 4-9 shows the results of one indentation to a depth of 1 mm into the skin with an aperiodic grating composed of 1.5 mm wide bars. The spatial variation of the surface load, maximum compressive strain, shear strain, and strain energy density at a depth of 0.75 mm, which corresponds to the typical Merkel cell receptor locations in primates, is shown. Only a few bars are in contact with the cylindrical finger during any one indentation, as contrasted with contact with all the bars in the case of the semi-infinite model. Owing to the surface curvature and finite extent of the cylindrical model, the loads imposed on the model and consequently the spatial distribution of various strain measures caused by an indentation of a grating are significantly different from the semi-infinite model used by Phillips and Johnson (1981b) as shown in Figure 4-10. The difference in the loads imposed for indentation by the same grating, on the semi-infinite and the cylindrical models are shown in the top trace in Figure 4-10. As the gratings are indented with a prescribed displacement, the total force imposed on the models is not the same. As only a few bars come in contact with the cylindrical model, the area over which the force acts is also different in the two models. The spatial response predicted by the semi-infinite model is the same for any spatial location of the grating since the model has infinite width. In the case of the cylindrical model only the bars in the close vicinity

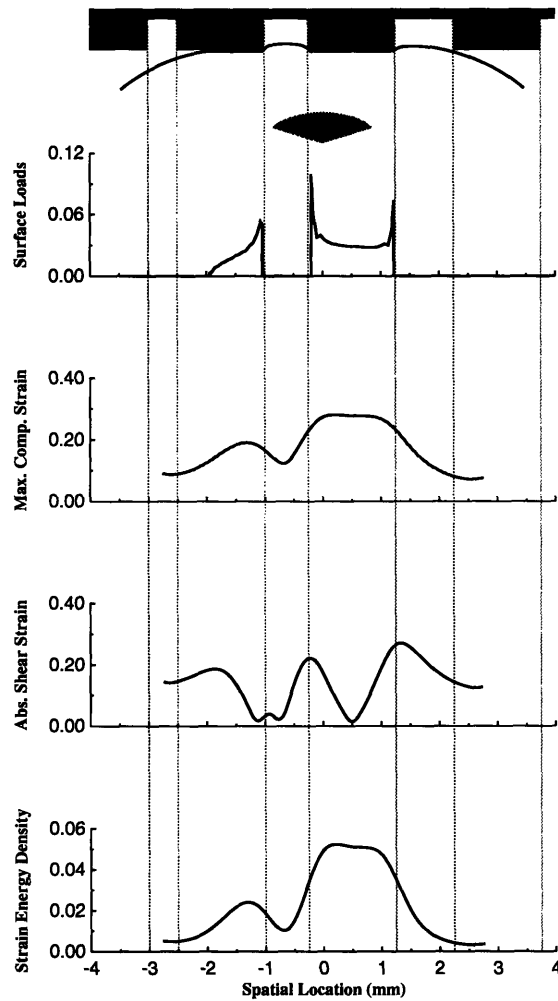


Figure 4-9: Indentation of the cylindrical model with bone by an aperiodic grating with 1.5 mm bars. Shown at the top is the deformed surface of the cylinder cross-section under the grating. A portion of the bone is shown shaded. The spatial distributions of surface loads, maximum compressive strain, absolute shear strain, and strain energy density at a depth of 0.75 mm from the surface are shown.

of the MSS affect the stress state in the vicinity of the mechanoreceptor and is strongly dependent on the spatial location of the grating. The population response and the spatial response predicted by the cylindrical model are not identical because of the finiteness and the surface curvature of model.

In order to identify the relevant stimulus (i.e., the strain component or combination at a receptor location that is coded into neural response) for the SA-Is, simulations of the stepping of aperiodic gratings across the fingerpad as done by Phillips and Johnson (1981a)

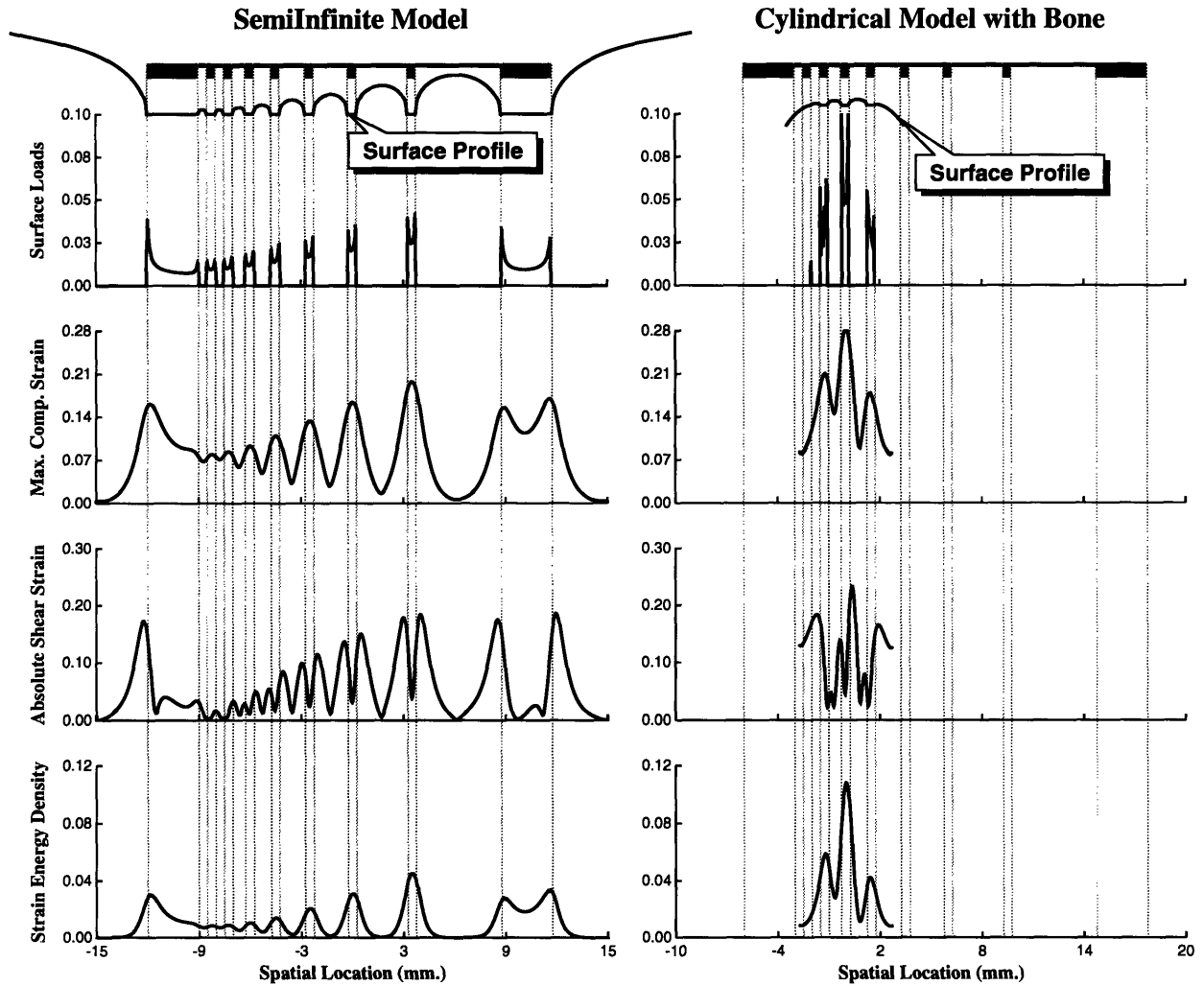


Figure 4-10: The surface deformation profiles along with the maximum compressive strain, absolute shear strain and strain energy density at a depth of 0.75 mm predicted by the semi-infinite and cylindrical models under indentation by an aperiodic grating with 0.5 mm bars are shown.

were carried out on the cylindrical model with bone. This was accomplished by performing finite element analyses of each indentation of a grating (as in Figure 4-9) in a sequence of about 150 indentations, where position of the grating relative to the fingerpad was shifted laterally by $200 \mu\text{m}$ for successive indentations. A strain measure of interest (e.g., maximum compressive strain) at a fixed receptor locations within the fingerpad were extracted from the calculations for each indentation and plotted as a function of the horizontal location of the receptor relative to a fixed point on the grating to obtain

the spatial profile for the strain measure. Spatial profiles of various strain measures were compared with the experimentally observed SAI spatial response profiles and the goodness of fit was examined. In order to correlate the two, a linear relationship between the neural discharge rate and the strain measures was assumed (Srinivasan and Dandekar, 1994a). It was of the form,

$$d_i = a\epsilon_i + b \quad (4.1)$$

where,

d_i is the experimentally recorded response at spatial location i , and
 ϵ_i is the calculated strain measure at spatial location i .

The constants a and b were determined by maximizing the goodness of fit measured as the variance ratio R^2 .

$$R^2 = \frac{\sum d_i^2 - \sum e_i^2}{\sum d_i^2}$$

where,

e_i is the difference in the experimentally recorded response and the calculated strain measure at location i .

An R^2 value of 1.0 indicates a perfect match in the experimental data and model predictions.

Such *spatial profiles* of maximum compressive strain, absolute shear strain, and strain energy density are shown in Figure 4-11 for a receptor located on the central longitudinal section of the model at 0.75 mm depth from the skin surface. The *spatial response profile* of an SAI from the experiments of Phillips and Johnson (1981a) is superimposed on each of the strain profiles for comparison. It can be observed from Figure 4-11 that the calculated strains at a fixed location under an individual bar of the grating depend on the spacing of the neighboring bars when two or more bars are in contact with the fingerpad. In the aperiodic gratings used, the width of all the bars is the same and only the gap between the bars is varied. The variations in the experimentally observed and predicted responses agree for the closely spaced bars but the finite element calculations predict almost identical strain states under each of the three rightmost bars which have the largest gaps between them. When the gaps are less than 1.5 mm, the strain state of the receptor is influenced

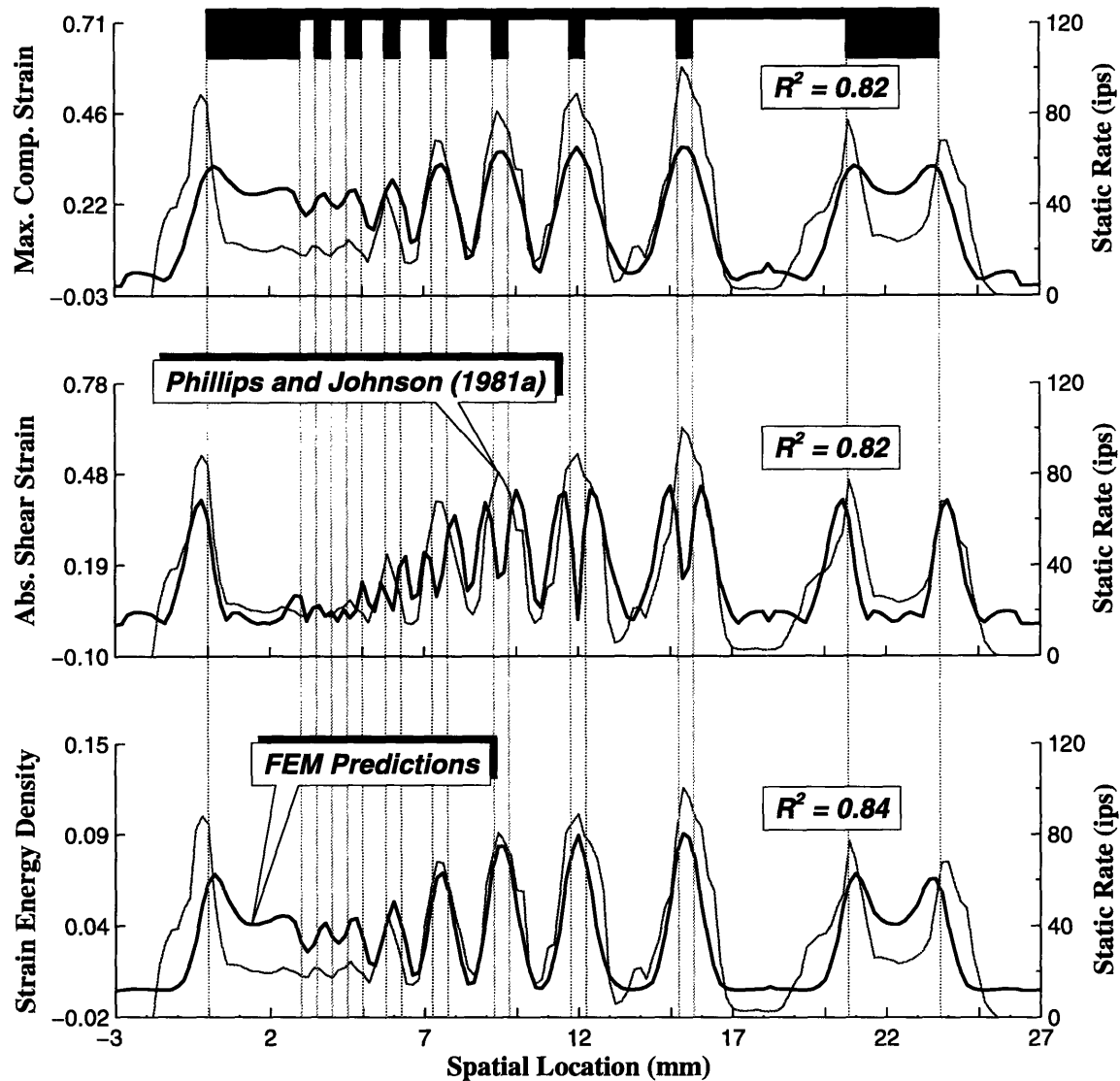


Figure 4-11: Comparison of experimentally recorded SA-I fiber spatial response profile (Phillips and Johnson, 1981a) with spatial profiles of maximum compressive strain, absolute shear strain, and strain energy density calculated using the 8 mm diameter cylindrical model with bone. The stimulus is an aperiodic grating with 0.5 mm wide bars. The model predictions are shown as thicker traces superimposed on the experimentally recorded receptor response rate profile obtained with the bars aligned along the finger ridges (parallel to the axis of the finger).

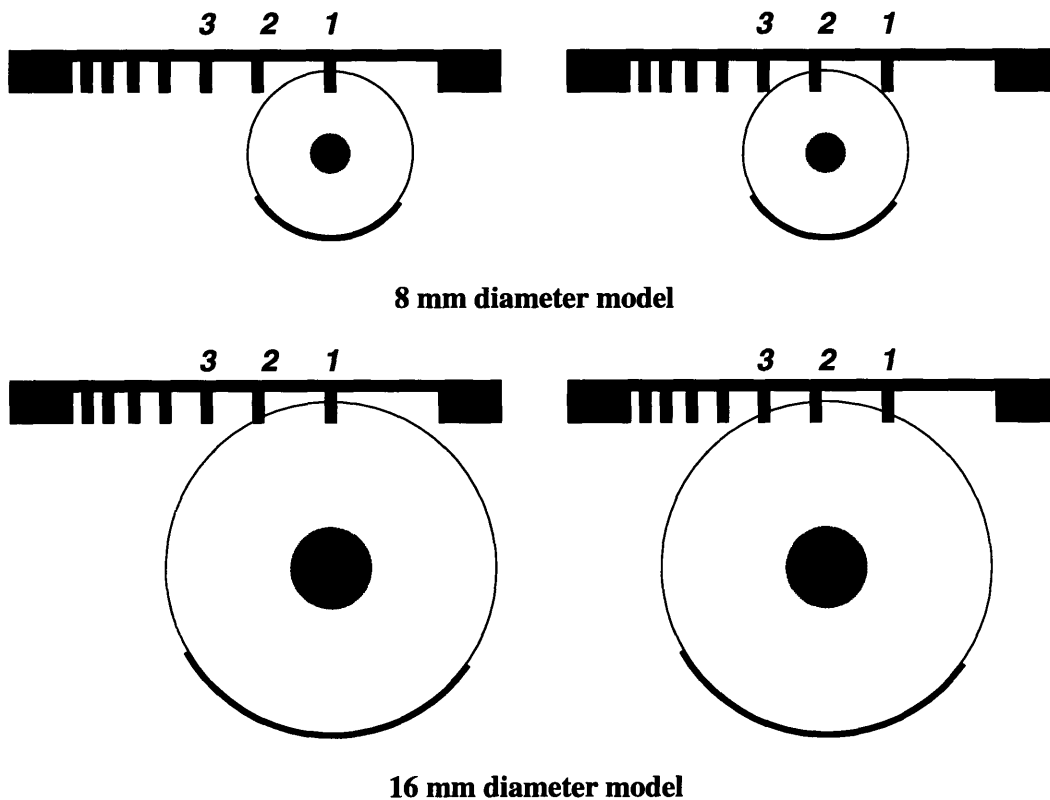


Figure 4-12: The effect of model diameter on the number of bars that can come in contact with the model is illustrated. In all the figures, the grating is shown indented to 1 mm into the fingerpad. The left figures show that for bar 1 near the center of the model, the loads imposed are almost identical. The right figures show that for bar 2 near the center, bar 1 and 3 also contact the 16 mm diameter model because its larger diameter, making the prescribed loading different than the 8 mm model for the same spatial location of the grating.

by the contacting bars neighboring the one directly above the receptor. This is true for all other stress-state measures including principal stresses and strain.

One of the unknowns in the simulation is the diameter of the monkey fingertip used in the actual experiment. The species used by Phillips and Johnson (1981a) was *Macaca nemestrina* whereas the value of 8 mm for the diameter is based on actual measurements obtained from *Macaca fascicularis*. Considering the biological variability, it is likely that the diameter of the fingertip used in the experiment might not be 8 mm. This hypotheses is examined in Figure 4-12 which is drawn to scale and shows the grating with 0.5 mm bars indenting 8 mm and 16 mm diameter fingers. In the left panels the rightmost bar (#1) is above the center of the fingertip and there is no significant difference in loading between 8 mm and 16 mm models as bar #2 barely touches the 16 mm model. But the comparison of

indentation when bar 2 is above the center of the 8 and 16 mm models reveals the difference in loading imposed on the two models, as shown on the right in Figure 4-12. Due to the higher curvature of the 8 mm model, the neighboring bars 1 and 3 barely touch the model, whereas in the 16 mm model both bars 1 and 3 indent the fingertip. This explains why the response to bars 1 and 2 is identical in the 8 mm model and establishes the need to simulate the experiment on a fingertip of diameter greater than 8 mm.

4.5.3 Simulations with the 16 mm diameter model

The same experiment was simulated using the 16 mm diameter model and the the predicted and experimentally observed spatial response profiles for gratings with 0.5 mm and 1.5 mm bars are shown in Figures 4-13 and 4-14 respectively. It can be observed that the response for the two rightmost bars is not identical as was the case for 8 mm diameter model. Consequently, the goodness of fit is better than the 8 mm model.

All the various strain measures including normal, shear and principal stresses and strains and strain energy density were compared with the experimentally observed spatial response. The finite element models predict the stress state throughout the model and hence depth of the receptor can be introduced as a free parameter in the fitting process. The depth of the receptor was allowed to vary between 0.5 and 1.0 mm which are the typical location of the Merkel cells. The scale and threshold values (a and b from Equation 4.1) were chosen to maximize the goodness of fit. The model diameter was treated as a variable that could vary between 8 mm and 16 mm and the strain measures corresponding to intermediate diameters were obtained by linear interpolation of the results from 8 mm and 16 mm diameter models. Figure 4-15 shows the best fits obtained for all the gratings used in the experiment when the grating bars were aligned parallel to the finger ridges and the axis of the finger. The filled traces are the finite element predictions and the thick line is the data from Phillips and Johnson (1981a). An excellent agreement between the experimental and finite element results is clearly evident, establishing the validity of the linear receptor model proposed (Srinivasan and Dandekar, 1994b).

Table 4.1 is the tabulated representation of the results of the examination of all the strain measures as candidates to be the relevant stimulus for SA receptors. The best, second best and the worst candidates are listed for each grating along with the goodness of the fit in R^2 , the depth of the receptor, and the diameter of the model. Strain energy density is among

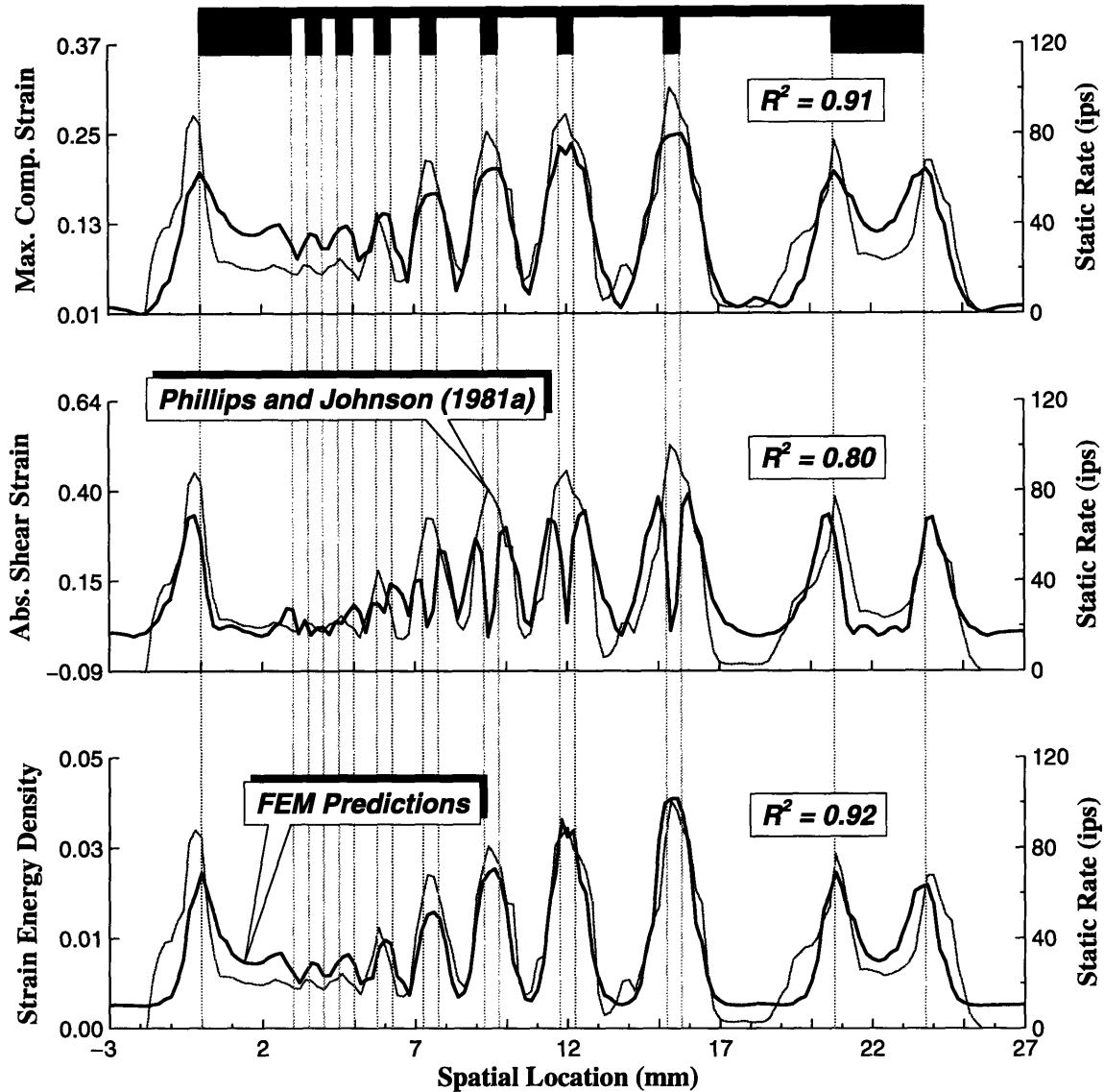


Figure 4-13: Comparison of experimentally recorded SA-I fiber spatial response profile (Phillips and Johnson, 1981a) with spatial profiles of maximum compressive strain, absolute shear strain, and strain energy density calculated using the 16 mm diameter cylindrical model with bone. The stimulus is an aperiodic grating with 0.5 mm wide bars. The model predictions are shown as thicker traces superimposed on the experimentally recorded receptor response obtained with the bars aligned along the finger ridges (parallel to the finger axis).

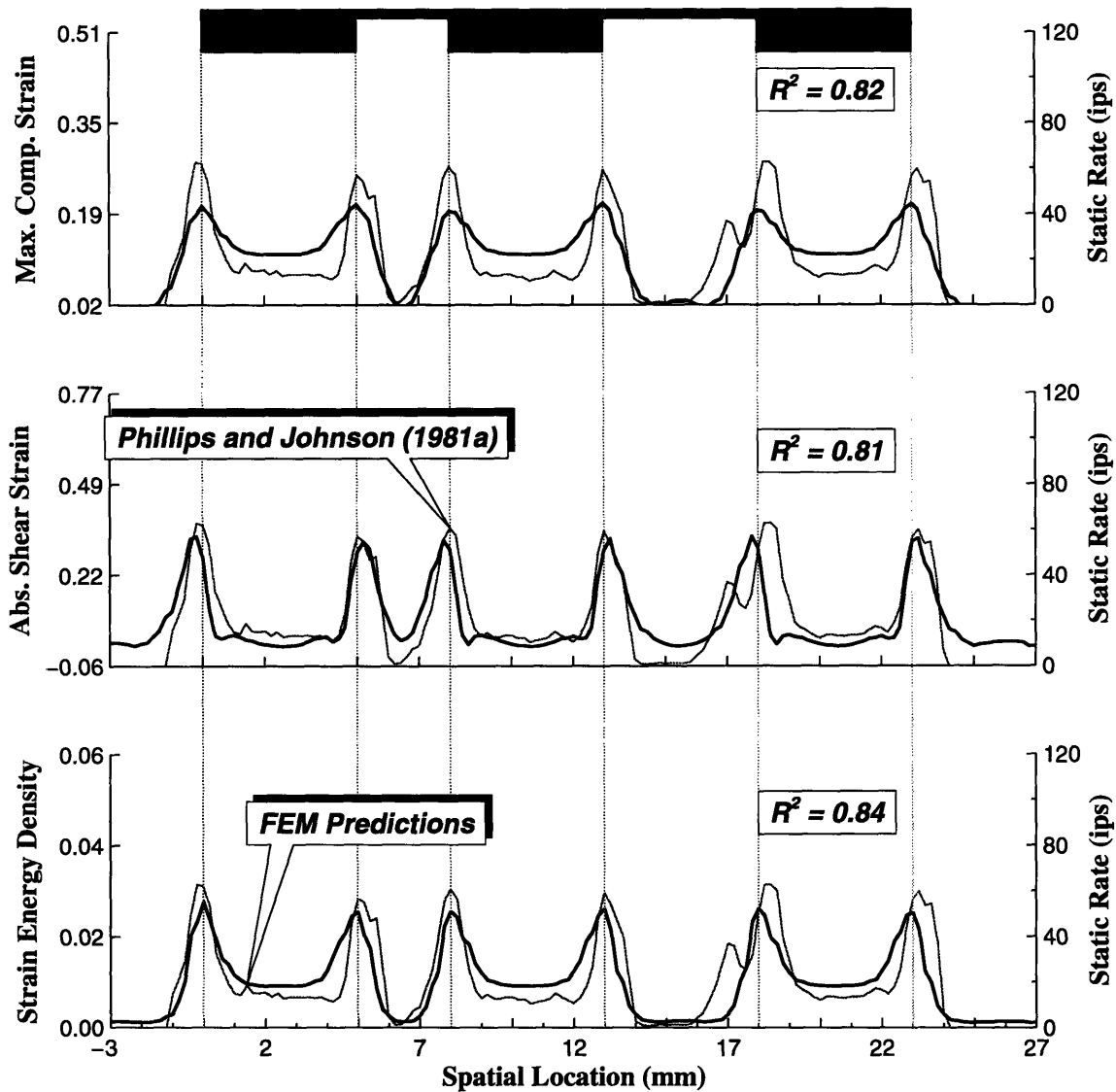


Figure 4-14: Comparison of experimentally recorded SA-I fiber spatial response profile (Phillips and Johnson, 1981a) with spatial profiles of maximum compressive strain, absolute shear strain, and strain energy density calculated using the 16 mm diameter cylindrical model with bone. The stimulus is an aperiodic grating with 5.0 mm wide bars. The model predictions are shown as thicker traces superimposed on the experimentally recorded receptor response obtained with the bars aligned along the finger ridges (parallel to the finger axis).

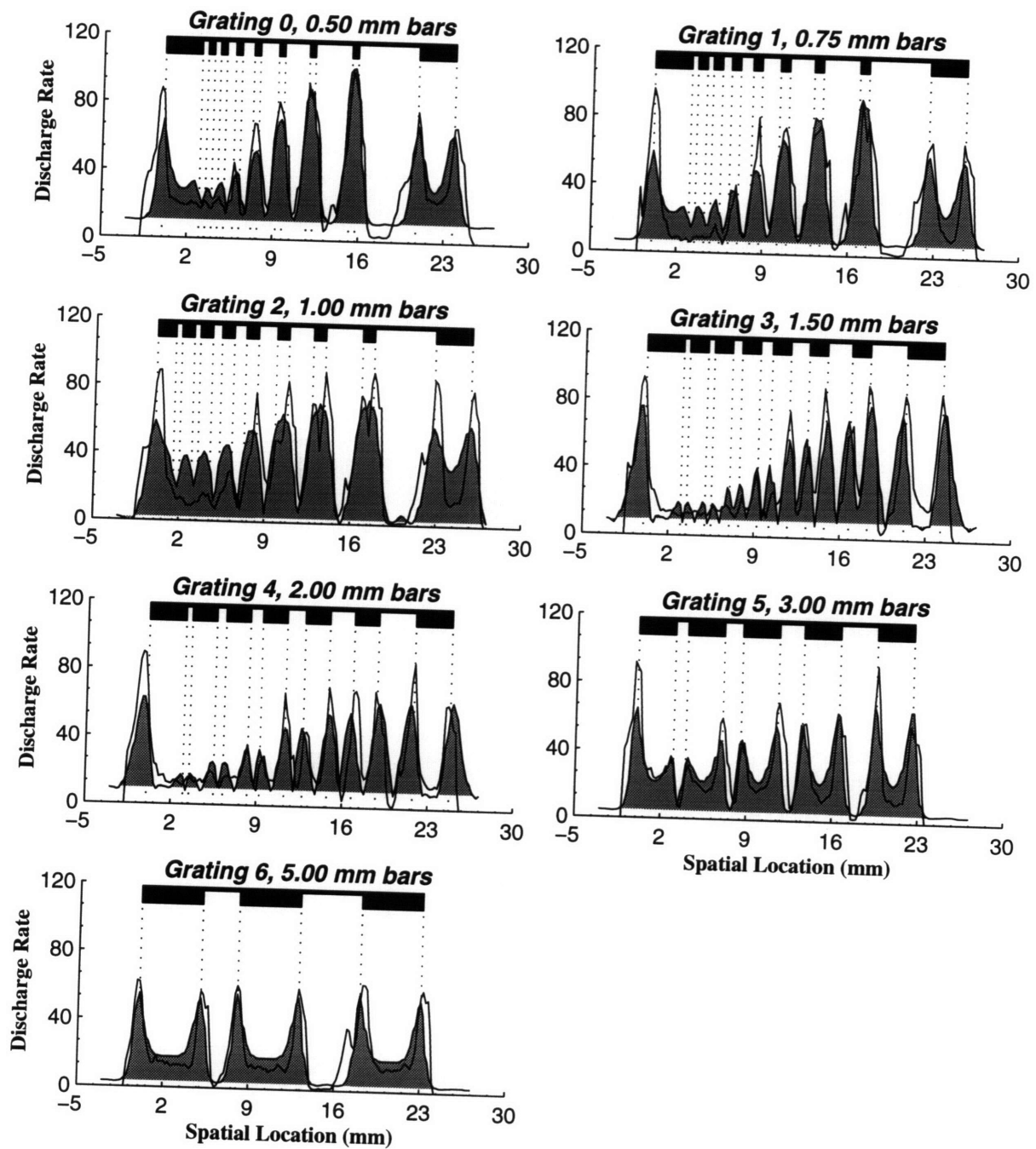


Figure 4-15: The experimental recorded observed spatial response profiles derived from a single SA-I afferent are shown by the solid line. The grating bars were aligned parallel to the axis of the fingertip. The strain measures, depth of the receptor and the diameter of the model were considered as free parameters in determining the best fit from the finite element simulations, which is shown by the filled trace. The strain measure, the depth of the receptor and the diameter of the model corresponding to the profiles shown are listed in Table 4.1.

Grating No.	Note	Strain Measure	R ²	Depth	Diameter
0	Best	Strain Energy Density	0.92	0.75	16.00
	2nd Best	Max. Compressive Strain	0.91	0.80	16.00
	Worst	Max. Tensile Stress	0.68	0.50	8.00
1	Best	Strain Energy Density	0.87	0.75	16.00
	2nd Best	Max. Compressive Strain	0.86	0.75	16.00
	Worst	Horizontal Stress	0.66	1.00	16.00
2	Best	Max. Compressive Strain	0.85	0.75	16.00
	2nd Best	Strain Energy Density	0.84	0.65	16.00
	Worst	Max. Tensile Stress	0.69	0.50	8.00
3	Best	Shear Strain	0.87	0.55	16.00
	2nd Best	Strain Energy Density	0.85	0.95	16.00
	Worst	Axial Stress	0.63	0.80	16.00
4	Best	Shear Strain	0.84	0.50	15.00
	2nd Best	Strain Energy Density	0.79	0.95	16.00
	Worst	Vertical Strain	0.62	0.70	16.00
5	Best	Strain Energy Density	0.85	0.85	16.00
	2nd Best	Max. Compressive Strain	0.84	0.95	16.00
	Worst	Max. Tensile Stress	0.61	0.50	8.00
6	Best	Strain Energy Density	0.85	0.80	16.00
	2nd Best	Max. Compressive Strain	0.84	0.95	16.00
	Worst	Max. Tensile Stress	0.55	0.50	8.00

Table 4.1: Summary of the comparison of the observed and predicted spatial response profiles. The best, second best and the worst fit between the observed and predicted data, along with the strain measures, the depth of the receptor and the diameter of the model are listed for each gratings. It can be observed that strain energy density is among the two best fits for all gratings.

the top 2 candidates in all the gratings and is, therefore, the top candidates for being the relevant stimulus for SA-Is. As noted before, for the plane strain models composed of an incompressible material, it can be shown that the strain energy density is proportional to the square of the magnitude of maximum compressive strain (see Appendix A). Based on their semi-infinite model of the fingerpad, Phillips and Johnson (1981b) also proposed maximum compressive strain magnitude as the relevant stimulus for slowly adapting receptors. It is of interest to note that Grigg and Hoffman (1984) in their study of Ruffini mechanoreceptors in the joint capsules concluded that the strain energy density had a high correlation with the receptor response.

Phillips and Johnson (1981a) have performed the series of indentations for grating bars placed perpendicular to the finger ridges (perpendicular to the axis of the finger). Figure 4-16 shows the comparison of the experimentally observed and predicted neural responses

Grating No.	Note	Strain Measure	R ²	Depth	Diameter
0	Best	Strain Energy Density	0.94	0.60	16.00
	2nd Best	Max. Compressive Strain	0.93	0.75	16.00
	Worst	Max. Tensile Stress	0.64	0.50	8.00
1	Best	Max. Tensile Strain	0.93	0.55	16.00
	2nd Best	Strain Energy Density	0.93	0.50	16.00
	Worst	Max. Tensile Stress	0.70	0.50	8.00
2	Best	Strain Energy Density	0.89	0.55	16.00
	2nd Best	Max. Compressive Strain	0.87	0.70	16.00
	Worst	Max. Tensile Stress	0.66	1.00	16.00
3	Best	Max. Compressive Strain	0.87	0.75	16.00
	2nd Best	Strain Energy Density	0.86	0.65	16.00
	Worst	Max. Tensile Stress	0.68	1.00	12.00
4	Best	Strain Energy Density	0.89	0.75	16.00
	2nd Best	Max. Compressive Strain	0.88	0.85	16.00
	Worst	Max. Tensile Stress	0.69	1.00	16.00
5	Best	Max. Compressive Strain	0.84	0.75	16.00
	2nd Best	Strain Energy Density	0.82	0.65	16.00
	Worst	Max. Tensile Stress	0.66	1.00	13.00
6	Best	Strain Energy Density	0.91	0.65	16.00
	2nd Best	Max. Compressive Strain	0.91	0.75	16.00
	Worst	Max. Tensile Stress	0.64	1.00	16.00

Table 4.2: Summary of the comparison of the observed and predicted spatial response profiles. The best, second best and the worst fit between the observed and predicted data, along with the strain measures, the depth of the receptor and the diameter of the model are listed for each gratings. The grating bars were aligned across the finger ridges (perpendicular to the axis of the fingerpad). It can be observed that strain energy density is among the two best fits for all gratings.

when the grating bars were oriented across the finger ridges. The fitting procedure was the same as described before.

Relevant stimulus is a property of the mechanoreceptor and does not depend on the mechanical stimuli on the surface. Hence, neural discharge rates for a given unit to a variety of mechanical stimuli can be combined and the candidacy of each of the strain measure for being the relevant stimulus can be examined. Neural data obtained from one SA-I afferent for all the 7 gratings was combined and compared with the subsurface strain measure. Depth of the receptor and model diameter were treated as variables within the acceptable ranges as described earlier. A perfectly linear relationship would imply that in a plot of discharge rate versus the strain measure the data points would lie along a straight line.

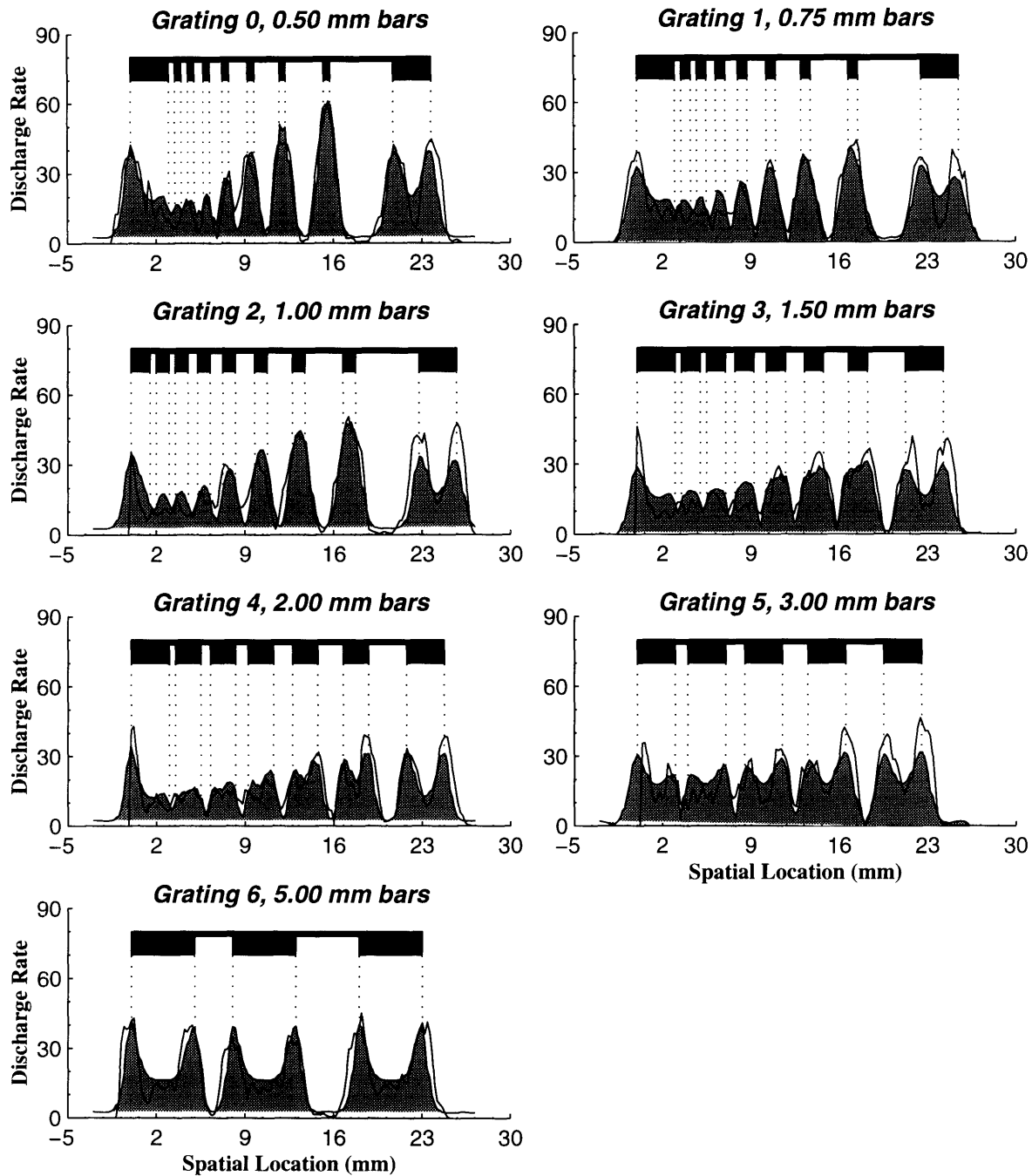


Figure 4-16: The experimental recorded observed spatial response profiles derived from a single SA-I afferent are shown by the solid line. The grating bars were aligned perpendicular to the axis of the fingertip. The strain measures, depth of the receptor and the diameter of the model were considered as free parameters in determining the best fit from the finite element simulations, which is shown by the filled trace. The strain measure, the depth of the receptor and the diameter of the model corresponding to the profiles shown are listed in Table 4.2.

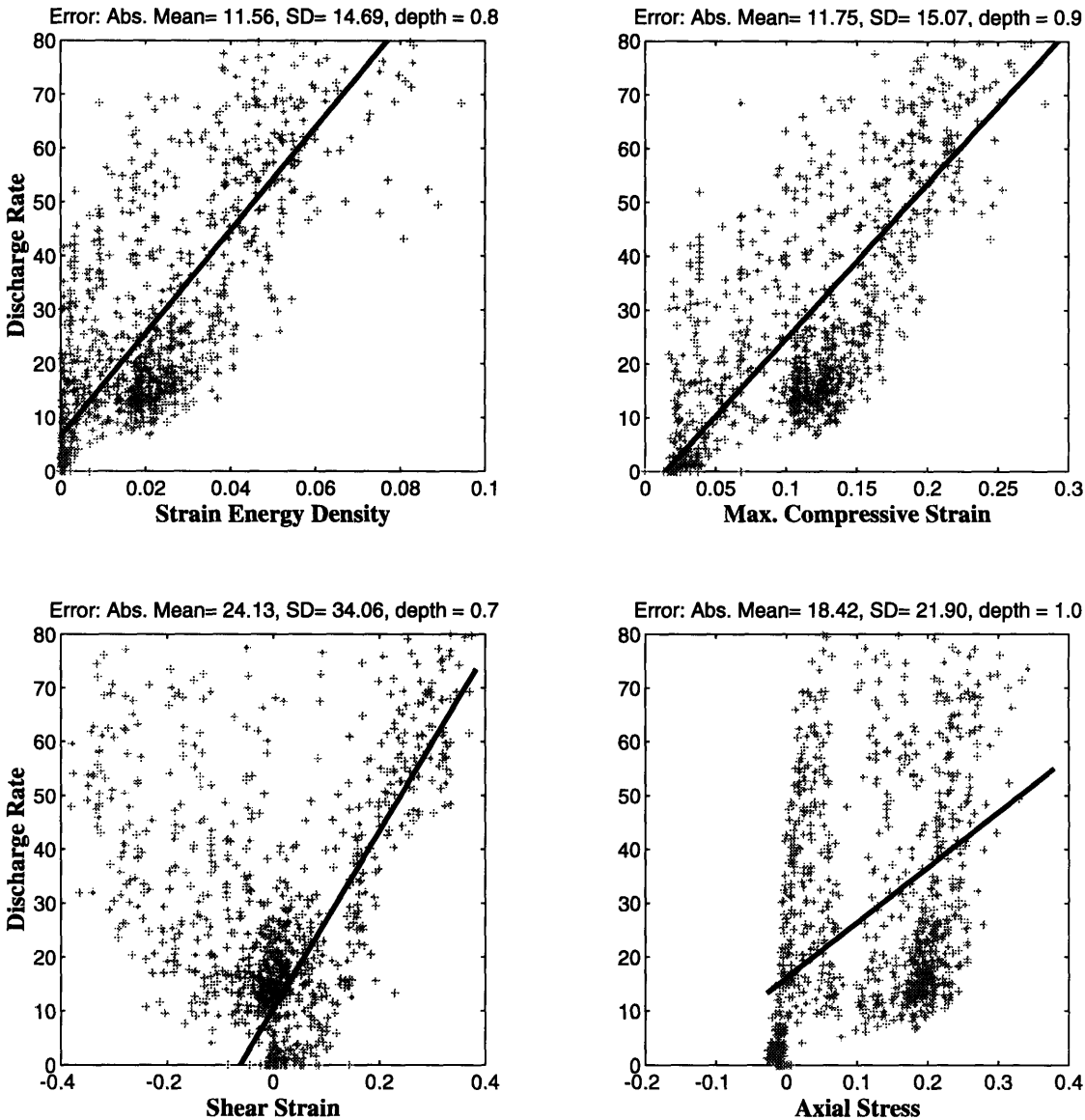


Figure 4-17: The experimentally observed neural discharge of a single SA afferent (Phillips and Johnson, 1981a) to all the gratings is plotted with respect to the strain measure at the receptor location. The straight line shows the best linear fit between the discharge rate and the strain measure.

Figure 4-17 is a plot of the neural discharge versus the various strain measures. It is evident that there is considerable scatter owing to the multiple values of discharge rate associated with each value of the calculated strain measure. The strain energy density and maximum compressive strain show minimum scatter about the best linear fit between the strain measure and the neural discharge. The goodness of fit in this data is very sensitive to the horizontal location of the stimulus. It is likely that by allowing the data set an additional degree of freedom in the lateral direction the goodness of fits could be increased

Strain Measure	Error	Depth	Diameter
Strain Energy Density	14.73	0.8	16.00
Max. Compressive Strain	15.10	0.9	16.00
Shear Stress	16.23	0.7	14.00
Shear Strain	16.23	0.7	14.00
Max. Tensile Strain	16.40	0.8	16.00
Max. Compressive Stress	19.84	0.9	16.00
Horizontal Strain	21.80	0.5	16.00
Vertical Strain	21.84	0.6	16.00
Vertical Stress	21.89	0.8	16.00
Axial Stress	21.93	1.0	16.00
Max. Tensile Stress	21.99	0.5	8.00
Horizontal Stress	22.13	1.0	16.00

Table 4.3: The goodness of linear fit between the strain measure and the neural response is summarized with data from all gratings combined, when the grating bars were aligned parallel to the finger axis. The error is the width of the error band in impulses per second. The results show that the strain energy density and maximum compressive strain emerge as the leading contenders to be the relevant stimuli for the slowly adapting receptors.

further. The duration of the neurophysiological experiments can be typically several hours and it is likely that the afferent fiber might have exhibited some time dependent adaptation, which cannot be modeled in the finite element model.

All the strain measures were considered in the comparison and the best linear relationship was examined. The RMS scatter from the best linear fit to the combined data set was considered as the error measures in comparing the candidate strain measures. The various strain measures are arranged in ascending order of error in Table 4.3 and 4.4 for grating bars aligned along the axis of the finger and perpendicular to the axis of the finger respectively.

Although maximum compressive strain and strain energy density are related by a simple nonlinear relationship in the finite element models considered here, there are inherent differences between them which affect their suitability as relevant stimuli. If it is assumed that a particular receptor is able to measure strain in a fixed direction, then, in order to measure the maximum compressive strain at a point, the receptor should be oriented to measure strain in the principal direction. However, the principal direction at a given location varies with the stimulus, and hence a receptor fixed in location and oriented in a particular direction cannot measure the maximum compressive strain for all the stimuli.

Strain Measure	Error	Depth	Diameter
Strain Energy Density	7.34	0.7	16.00
Max. Compressive Strain	7.34	0.8	16.00
Max. Tensile Strain	7.90	0.7	16.00
Max. Compressive Stress	9.29	0.8	16.00
Vertical Strain	10.38	0.5	16.00
Horizontal Strain	10.48	0.5	16.00
Vertical Stress	10.49	0.8	16.00
Axial Stress	10.58	0.9	16.00
Horizontal Stress	10.66	1.0	16.00
Shear Stress	10.74	0.8	15.00
Shear Strain	10.74	0.8	15.00
Max. Tensile Stress	12.53	1.0	16.00

Table 4.4: The goodness of linear fit between the strain measure and the neural response rate is tabulated with data from all gratings combined, when the grating bars were aligned across the finger ridges (perpendicular to the finger axis). The error is the width of the error band in impulses per second. The results show that the strain energy density and maximum compressive strain emerge as the leading contenders to be the relevant stimuli for the slowly adapting receptors.

If, on the other hand, it is assumed that receptors can measure maximum compressive strain at a certain location irrespective of their own fixed orientation, then what is being postulated is, in effect, an internal information processing mechanism that picks the maximum strain among the strains in all directions. There is no evidence at present for such a mechanism to operate within a receptor or even among the complex Merkel cells believed to be the endings of SAI fibers. In contrast to the maximum compressive strain, strain energy density is an invariant of the strain tensor that does not depend on the direction of measurement at a given point and, hence, is a natural candidate to be the relevant stimulus. In addition, this scalar quantity is a measure of the amount of distortion at that location and, therefore, is possibly related directly to the opening or closing of ionic channels in the receptor. If the Merkel cell receptors generate a neural impulse rate proportional to the strain energy density in their neighborhood, then the receptors can have a fixed location and orientation relative to the skin surface and yet code with high fidelity the different mechanical stimuli imposed on the skin surface.

4.5.4 Central vs off-center receptors

In spite of drastic differences in the geometry and resulting strain distributions under a single indentation by a grating (Figure 4-10) among the cylindrical and semi-infinite models, the calculated spatial profiles shown in Figure 4-11 are surprisingly similar to those obtained by Phillips and Johnson (1981b). This is because the influence of a load on the strain state at the receptor location decreases rapidly (exponentially in the semi-infinite model) with increases in the distance between the receptor and the loads. Only loads acting within a “region of influence” (which depends on the strain measure of interest, but is about the same for the two models) have a significant effect. Therefore, although the calculated strain fields and, hence, the predicted population responses are very different for cylindrical and semi-infinite models, the spatial profiles of a strain measure for the two models are similar at a central receptor location. However, the farther a receptor is from the central longitudinal section, the higher is the difference between the spatial profiles predicted by the two models (Srinivasan and Dandekar, 1995).

Due to the experimental difficulties, most of the reported neurophysiological recordings consist of responses of single afferent fibers. Phillips and Johnson (1981b) have used the recordings from a single fiber to construct the spatial response profiles. The spatial response profile would be the same as the population response *only* if the semi-infinite model of the fingertip truly represented its geometry. Clearly, the finiteness and the surface curvature of the fingertip violate the assumption of semi-infiniteness and flatness. For the semi-infinite model and at a given depth, the location of the receptors does not affect the spatial response profile of the strains. This “uniformity” is no longer applicable for a model of finite width or curved surface as the number of bars contacting the model and the loads imposed will be affected by the spatial location of the grating. Consequently, the spatial profile of strain measures is dependent on the location of receptors, even when the depth of the receptors is the same. The effect of a curved fingertip is two fold. Due to the curved contour the local stiffness of the fingerpad is different than its neighboring receptor for the same stimulus over its most sensitive spot, as discussed earlier. Secondly, for stimuli which are comparable in width to the fingerpad dimensions, like wide bars or flat plates, the indenter does not contact the fingerpad at all points on its surface in contrast to the semi-infinite model.

Figure 4-18 illustrates the effect of receptor location predicted by the cylindrical model

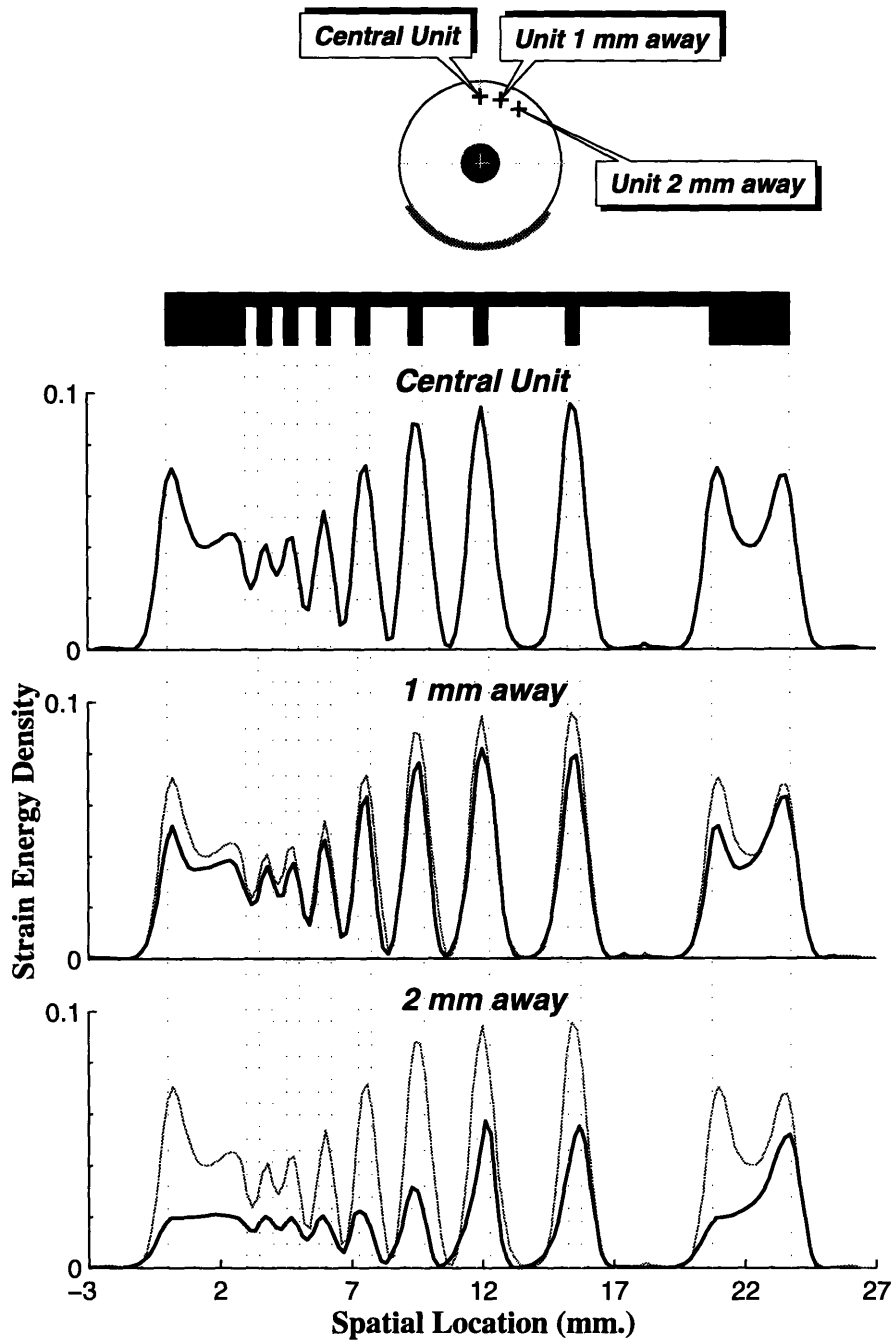


Figure 4-18: The strain energy density profiles at various receptor locations in response to indentations by an aperiodic grating of 0.5 mm wide bars (Phillips and Johnson, 1981a) are shown. The top trace is the profile for the central unit. The middle and the bottom traces are for receptors which are located at 1 mm and 2 mm away from the central unit respectively. The trace in faint gray in the middle and bottom trace is that of the central unit and is plotted for comparison.

with bone. The top trace shows the *spatial response profile* predicted by the central unit and the bottom two panels show the response of receptors which are off-center by 1 and 2mm. For a semi-infinite model, this would be identical to the population response and the response of any other receptor at the same depth irrespective of its lateral location. The middle and bottom traces in Figure 4-18 show the difference between the *spatial response profile* predicted by receptors which are off-center by 1 and 2 mm respectively. The responses are shifted by 1 and 2 mm respectively so that they can be compared with the response of the central unit which is shown as the gray trace. These profiles are different even when sensitivity and threshold are the same for all three units.

4.5.5 Human threshold of gap discrimination

Johnson and Phillips (1981) indented the fingertips of awake human subjects to determine the human threshold for gap discrimination. They observed that the d' values can be closely approximated by the two straight lines shown in Figure 4-20. To compare the correlation between the experimental results and the finite element simulations, the variation in the shear strain across gaps in the different gratings was examined. Figure 4-19 shows the variation in the shear strain at a depth of 0.75 mm. The two peaks across the gaps are joined by a straight line as shown in the figure and the slope of that line and the distance between the peaks of shear strain is calculated. It is hypothesized that the information used in the detection of edges of the bars is the spatial variation of the shear strain and more specifically the points of inflection of the shear strain. If this hypothesis is verified, similar algorithms can be used in robotic tactile sensors to identify either a gap or a bar, as the features that defines either a gap or a bar are the two edges that define its spatial extent.

If it is assumed that the spatial variation in the shear strain at the receptor location is used in determining the location of the edges of the stimulus and, hence, the width of a gap indented into the fingerpad, then, variation in the slope and the distance between the two peaks of the shear strain will be the cues used by subjects in detection and discrimination. In Figure 4-20, the experimental observed data for gap detection (Johnson and Phillips, 1981) is compared with the experimentally observed inter-peak distances. A linear relationship between the inter-peak distance and the d' values is assumed and the best fit between the experimentally observed and predicted data is shown in Figure 4-20. The straight line

Grating 4 with 2.0 mm bars

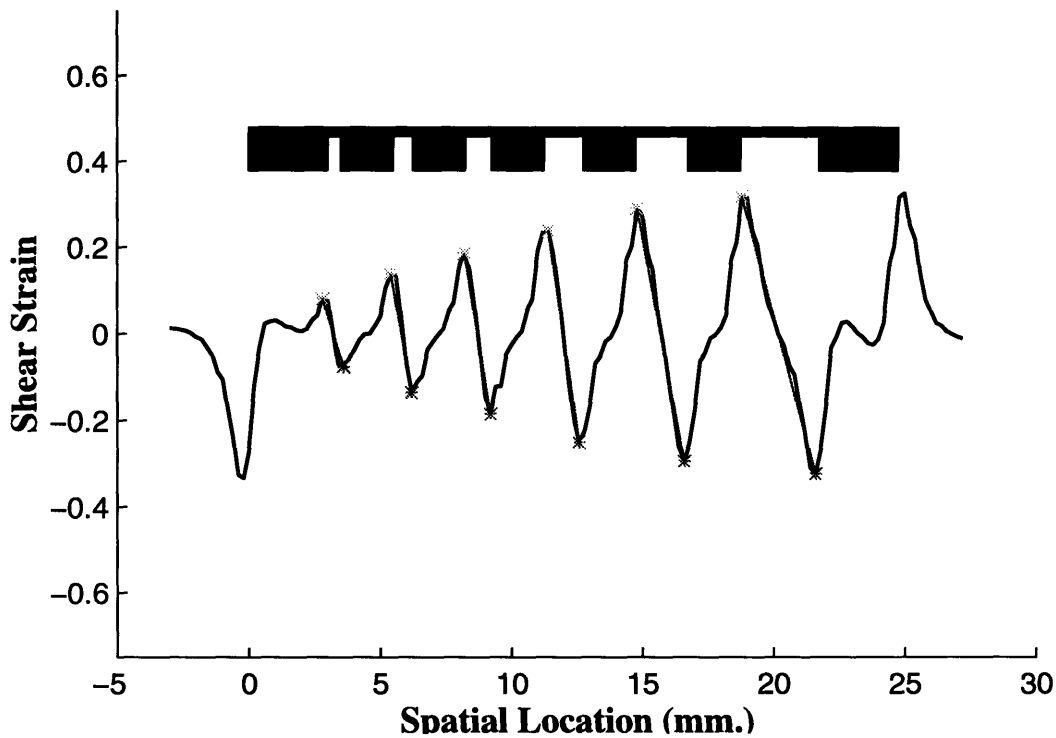


Figure 4-19: The shear strain at a depth of 0.75 mm is plotted for grating 4 with 2.0 mm wide bars. The line joining the peaks across each of the gaps in the grating is shown in light gray. The slope of this line is calculated and used in Figure 4-20.

relationship suggested by Johnson and Phillips (1981) is shown by the dashed lines. It should be noted that there are only 3 data points in the finite element simulations, owing to the fact that, this data was derived from the simulations of the grating experiment. However, some salient features can be observed in spite of the rather coarse sample. The knee in the variation of d' in the experimental and finite element data agree closely. The experimental data is available till 1.0 mm width and the simulation data predicts a settling trend in the variation of d' as against the linear extrapolation in the experimental data. In order to investigate the actual predicted threshold of human gap detection further, finite element simulations with various gaps used in the experiments should be carried out on the cylindrical model.

4.6 Indentation by Cylindrical Indentors

Two plane strain models of circular cross-section (8 mm diameter) were indented by a series of cylindrical indentors used in previous neurophysiological experiments (Srinivasan and

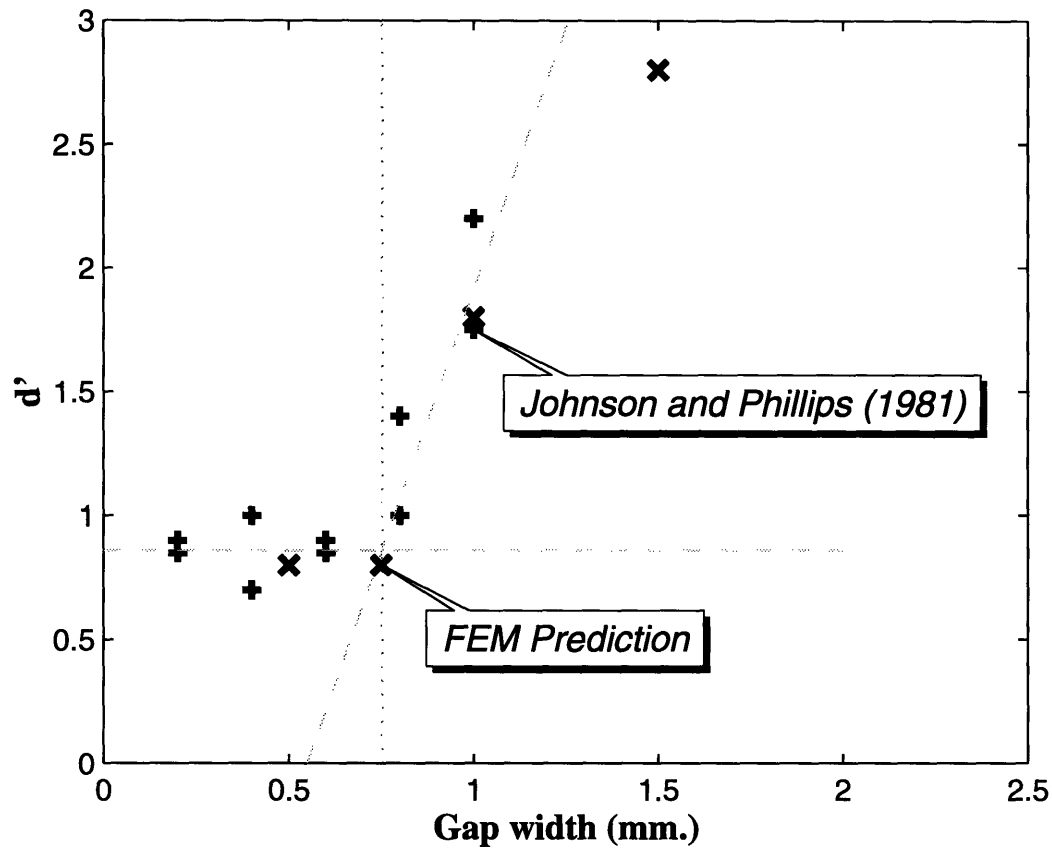


Figure 4-20: The d' values for human gap discrimination are shown as '+' marks (Johnson and Phillips, 1981). The distance between the peaks of shear strain seen in Figure 4-19 is scaled and plotted as the 'x' marks. The linear relationship suggested by Johnson and Phillips is shown by the dashed line (1981).

LaMotte, 1991). The first model consisted of a linear elastic and isotropic solid enclosing a central rigid bone of 2 mm diameter; the second model consisted of a 1 mm thick layer of the same solid enclosing an incompressible fluid (Dandekar and Srinivasan, 1994). The nodes on the bottom third of the circumference, which correspond to the fingernail in the model, were constrained in all the degrees of freedom. The models were analyzed under constant force indentations by a series of cylinders whose diameters were the same as those used to record SA responses in previous neurophysiological experiments (Srinivasan and LaMotte, 1991). Figure 4-21 shows the finite element mesh used in the two models. The mesh was identical in the solid and solid-fluid model, however, the material property definition was different in the two models. Interface elements were used to couple the pressure in the fluid elements with the solid elements.

The contact mechanics problem was solved iteratively using the ABAQUS finite el-

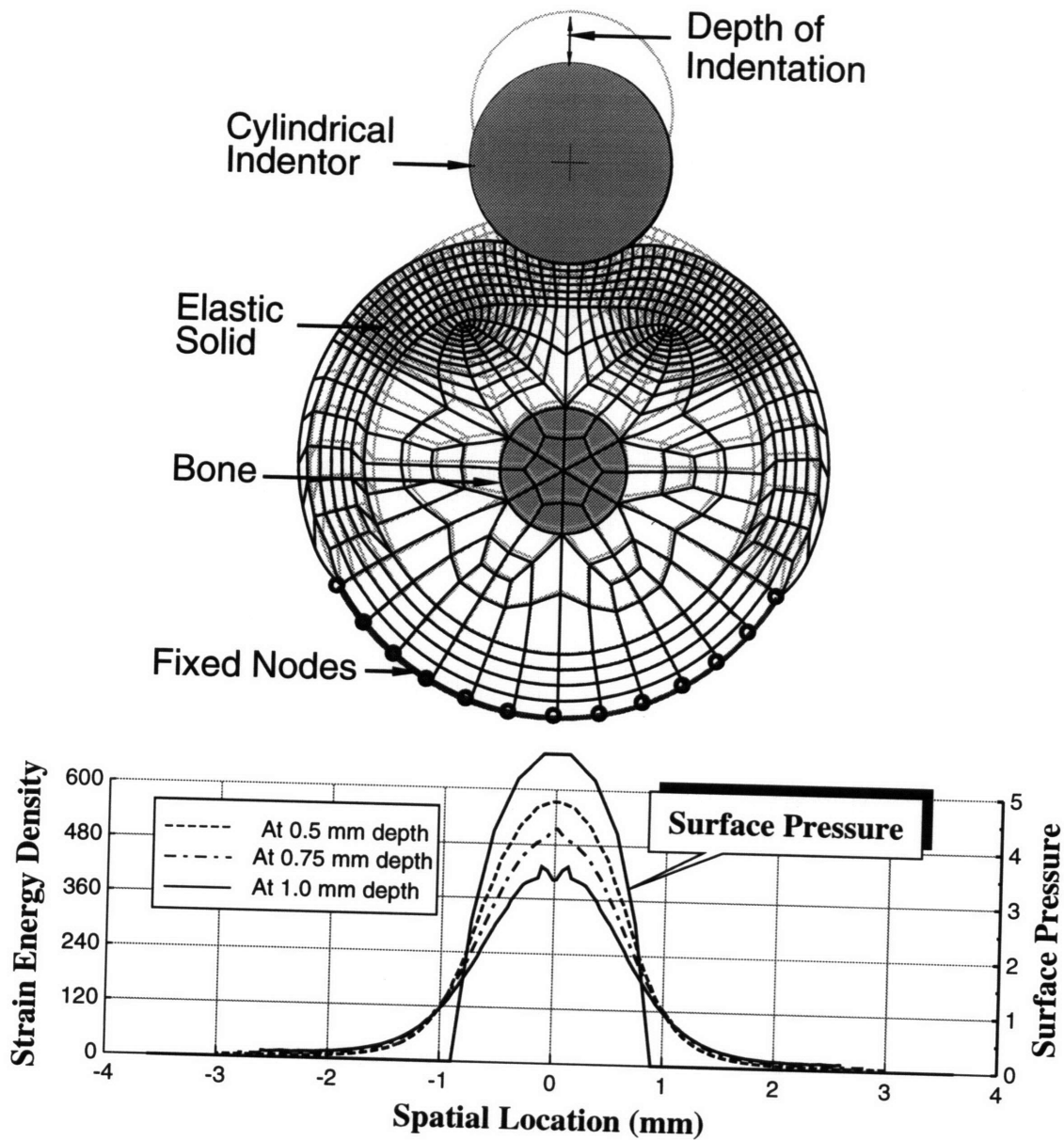


Figure 4-21: A cylindrical indenter of curvature $\frac{1}{16}$ inches indenting the cylindrical model. Also shown are the initial and deformed meshes in the finite element model. The surface pressure and the strain energy density at typical receptor locations is shown in the lower panel.

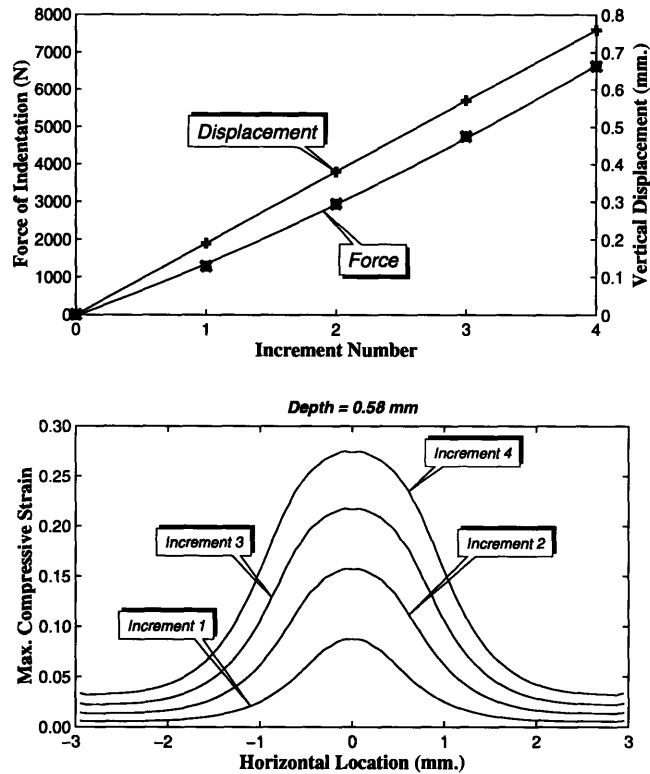


Figure 4-22: The cylindrical indenter of 2.3805 mm diameter was indented into the fingerpad to a depth of 0.76 mm in four equal steps. The prescribed depth of indentation and the corresponding force of indentation is shown in the top panel. The maximum compressive strain at a depth of 0.58 mm is shown for each step in the indentation.

ement software. In the neurophysiological experiment, the monkey fingertips were indented till a prescribed constant force was recorded in the stimulator controlling the indentation (Srinivasan and LaMotte, 1991). In the finite element simulation, the indenter was indented into the cylindrical model in steps. Figure 4-22 shows the variation in the force of indentation with four equal steps in the depth of indentation in the top panel. The maximum compressive strain at a depth of 0.58 mm is shown corresponding to the four steps of the finite element solution. It can be seen that the magnitude of the maximum compressive strain and the spatial extent increase non-linearly with the increase in the depth of indentation.

For each cylindrical indenter, the pressure distribution and the width of contact region at the skin-cylinder contact interface, as well as the stress and strain distributions at typical SA-I locations (0.5 to 1 mm below the skin surface) were calculated. The bottom panel in Figure 4-21 shows the surface pressure and the strain energy density at three typical depths at the end of the indentation, when the prescribed force was achieved.

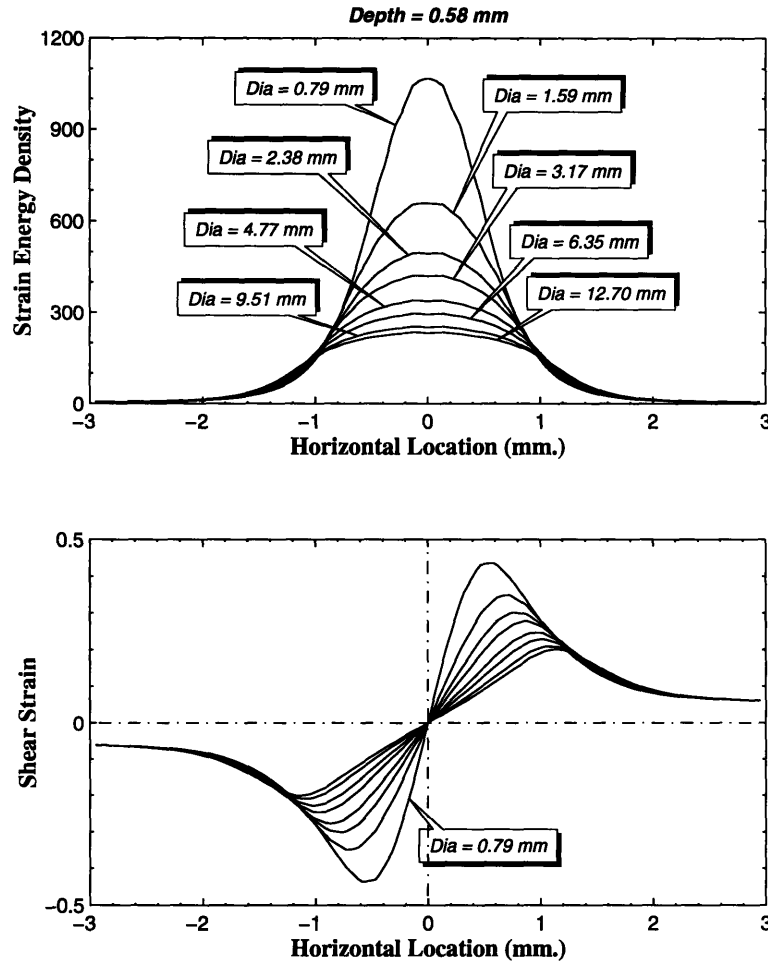


Figure 4-23: The solid model was indented by cylindrical indentors of various diameters. The variation in the strain energy density and the shear strain at a depth of 0.58 mm is shown for all the cylindrical indentors.

Strain measures at the typical receptor locations under indentation by various cylindrical indentors can be compared in Figure 4-23. In the top panel the strain energy density at a depth of 0.58 mm is shown, when the cylindrical model was indented by the various cylindrical indentors. The difference in the magnitude of the maximum strain energy density is clearly visible. In the bottom panel, the variation in the shear strain is shown. The magnitude of the maximum shear strain and the location of the maximum shear strain varies with the diameter of the cylindrical indenter. Various calculated strain measures were then correlated with the previously recorded SA-I responses to infer the *relevant stimuli* for SA-Is, i.e., the strain measures that possibly trigger the SA-I responses.

To attain the same prescribed force, each cylinder had to be indented to a higher depth in the solid-fluid model than in the solid model. The depth of indentations required to

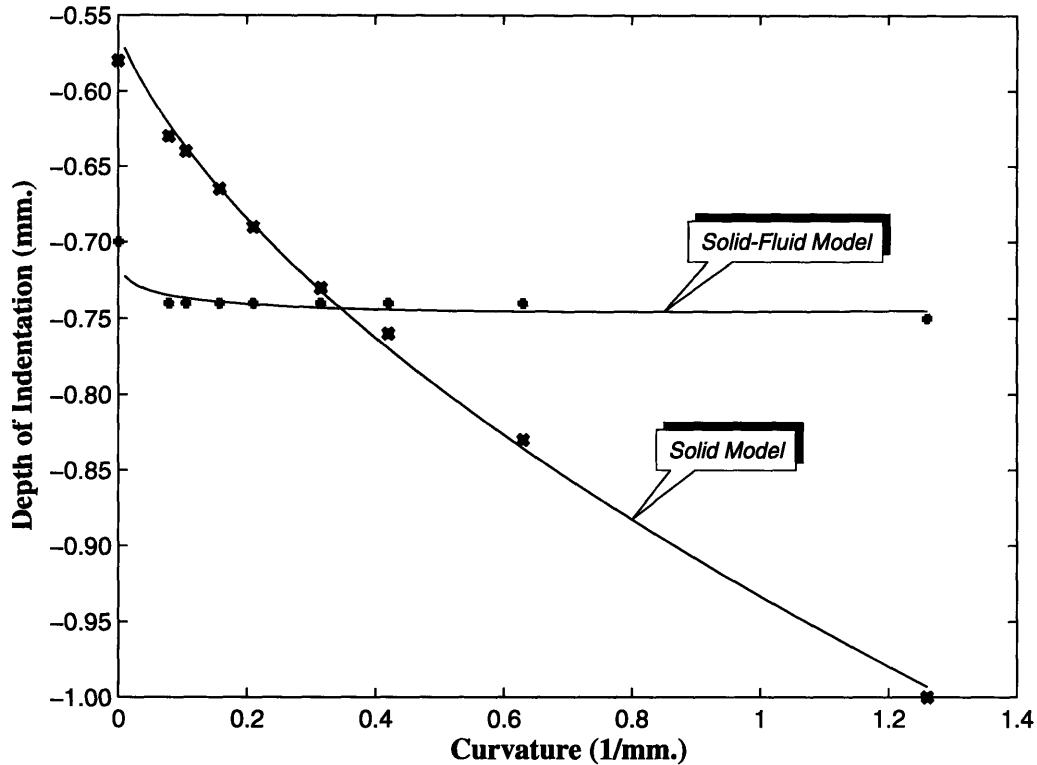


Figure 4-24: The depth of indentation required to attain the constant force of indentation for the solid and solid-fluid model for various cylindrical indentors is plotted. It can be observed that the variation in depth of required for the solid model was much higher than the variation in the solid-fluid model.

achieve the prescribed force for the solid and the solid-fluid model are plotted in Figure 4-24. It can be seen that, the depth of indentation to achieve the prescribed force increased in proportion to the square root of the cylinder curvature for the solid model whereas there was no appreciable change for the solid-fluid model. The variation in contact width and the maximum pressure in the region of contact between the indenter and the cylindrical model is shown in Figure 4-25. For each cylinder, the solid model had higher maximum pressure than the solid-fluid model and consequently had smaller contact widths. The contact width decreased with increase in curvature, and the reduction was more rapid for the solid-fluid model. These results agree with the intuitive expectation that the solid model is much stiffer than the solid-fluid model.

In order to correlate the strain measures with the neural response data, a relation of the form $I = a\epsilon + b$ was assumed (same as before, Equation 4.1), where I is the neural discharge rate in impulses per second, and ϵ is the strain measure; a and b are constants across all the data points and represent, respectively, the sensitivity and response threshold of the

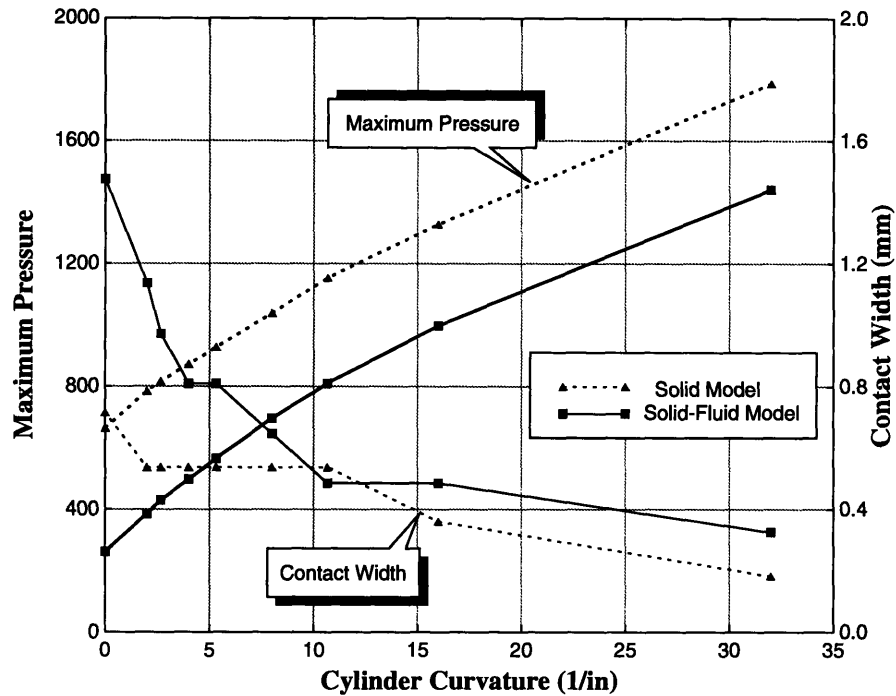


Figure 4-25: The variation in the contact area and maximum contact pressure for cylindrical solid and solid-fluid models is shown

receptor to ϵ . Except for 1 mm depth (interface of solid-fluid) in the solid-fluid model, all the strain measures in both the models correlated quite well with the neural discharge rate. The best matches at typical receptor locations from both models and all strain measures were absolute shear strain at 0.5 mm depth in the solid-fluid model together with strain energy density at 0.75 mm and absolute shear strain at 1.0 mm depths in the solid model (Figure 4-26).

Excellent correlations obtained between neurophysiological recordings and mechanistic calculations in Figure 4-26, other figures in this thesis, and in previous papers (Phillips and Johnson, 1981b; Srinivasan and Dandekar, 1992) imply that (1) Use of simplified fingertip models is a fruitful approach (similar to approximating cornea, lens and vitreous body of the eye by a simple lens), and (2) mechanoreceptor electrophysiological response is directly related to strain measures at receptor locations. More biomechanical and neurophysiological experiments involving static and dynamic indentations with various shapes, as well as corresponding dynamic analysis using the finite element models are required to fully explore the role of mechanoreceptors in the tactile recognition of shapes (Srinivasan

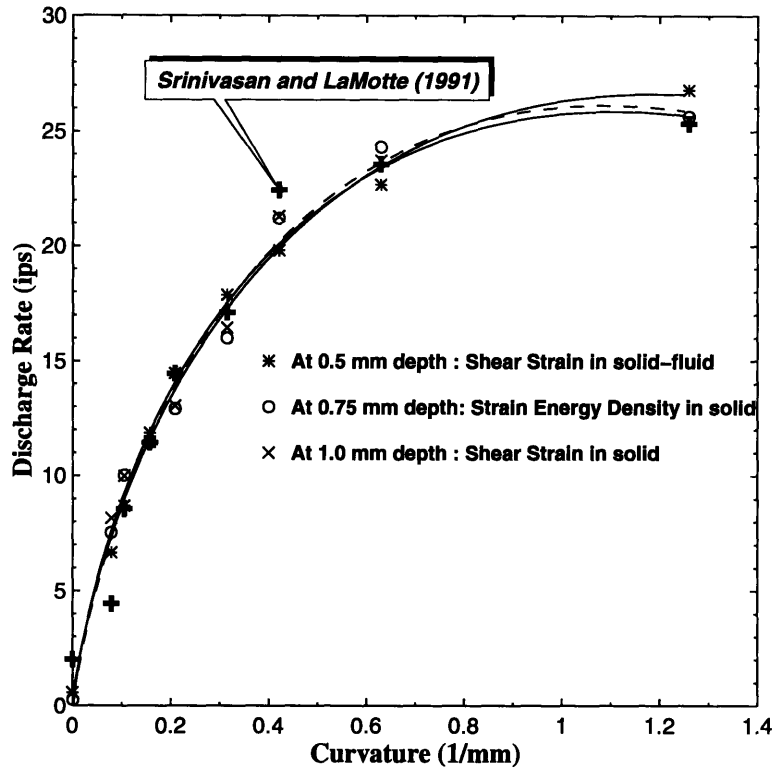


Figure 4-26: The comparison of the observed and the predicted discharge rate of SA afferents under indentations by cylindrical indentors of varying curvature. The neural data is from Srinivasan and LaMotte (Srinivasan and LaMotte, 1991). The best matches between strain measures and the observed discharge are shown at the depths of 0.5, 0.75 and 1.0 mm.

and Dandekar, 1995).

4.7 Surface Deformation Under a Line Load

The surface deflection of the fingerpad under a known loading provides a clue to infer the mechanical nature of its constituent materials. Therefore the experimentally observed surface deflection profiles of monkey and human fingerpads under 1 mm indentation by a single line load were compared with the corresponding predictions of each of the models. As explained earlier and shown in Figure 4-27, the Boussinesq solution does not match the experimental data points, whereas the waterbed model proposed by Srinivasan (1989) does predict the observed profile quite well. It should be noted that both of these analytical solutions have as a free parameter the horizontal distance from the load to the point where the deformed surface profile crosses the undeformed profile. In Figure 4-27, this distance has been chosen for both the models to be the same as the one observed in the

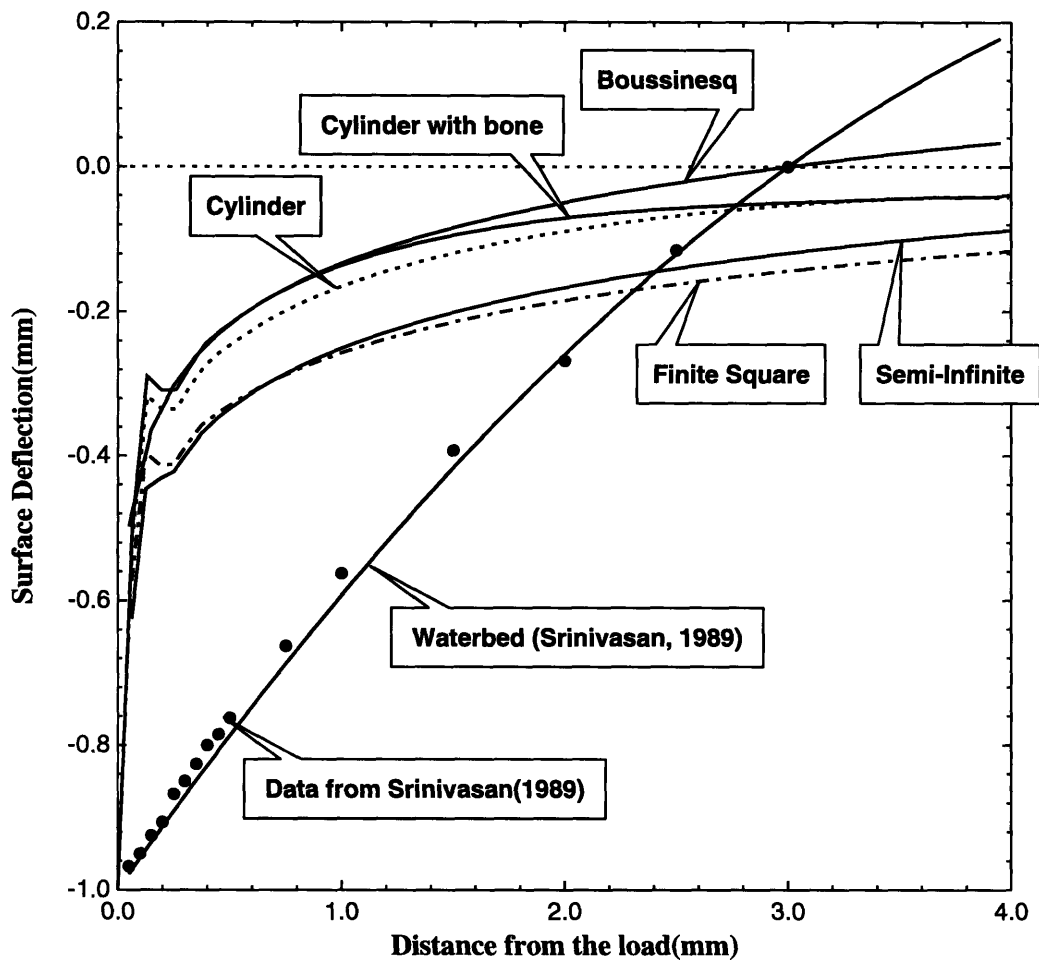


Figure 4-27: Deflection profiles of the skin surface under a line load perpendicular to the model cross-sections shown in Figure 4-1. Only half the profiles are shown due to symmetry. The experimental data points are the averages of the corresponding points on the left and the right side of a sharp wedge indenting a monkey fingerpad (Srinivasan, 1989). Calculated profiles are shown as continuous traces since the data points are only 0.05 mm apart.

experiments. Also shown in the figure are the profiles predicted by the four finite element models. In each of these profiles, the kink observed near the load is a numerical artifact and should be ignored. It occurred closer to the load as the element size was reduced and is due the singular nature of the concentrated load coupled with the plane strain and small deformation assumptions. An appropriate choice of the free parameter in the Boussinesq solution, different from the one shown in Figure 4-27, matched the analytical and numerical profiles for the semi-infinite medium quite well. It can be seen that the profiles for the semi-infinite and finite square models are close together, as are those for the

cylinder with and without the bone. If the vertical deflection, say at 2 mm from the load, is taken as a measure of the overall stiffness of the models, then the four finite element models in increasing order of stiffness are the finite square, semi-infinite, cylinder and cylinder with bone. It is clear from Figure 4-27 that, irrespective of their shape, the models composed of homogeneous linear elastic medium do not predict the experimental profile as accurately as the inhomogeneous waterbed model.

5

Biomechanical Experiments

No reliable biomechanical data on the geometry and material properties of the fingerpad and its constituents, which could be incorporated in finite element models, is available. This chapter describes the experiments performed to obtain accurate external geometry of the primate fingerpads. The external geometry obtained was used in the 3D reconstruction of the primate fingertips which was necessary in the generation of accurate finite element models. Also described are the experiments to study the *in vivo* deformation of the human fingertips under indentations by various indentors. The measured skin and surface deformations provide a way to check the biomechanical response of the finite element model.

5.1 3D Reconstruction of the Primate Fingerpads

The two dimensional model of the primate fingertip described in chapter 4, approximated the cross-section of the fingertip by a circle. The loading used in most of the neurophysiological and biomechanical experiments was constant along the axis of the fingertip and, thus, plane strain assumption could be used for the circular cross-section. Implicit in the assumption is the fact that, all the cross-sections are identical in geometry and loading. Beginning the 3D modeling with an idealized cylinder as the approximation of the fingertip is, thus, unlikely to enhance the accuracy of the model in simulating the biomechanical and neurophysiological experiments. The effort required in developing 3D models is much higher than the 2D models and refining the accuracy of geometrical representation in stages is not justified. The experiments described here are designed to extract accurate representation of the external geometry of the primate fingertips. As and when internal geometry of the fingertip becomes available, it can be seamlessly integrated with the

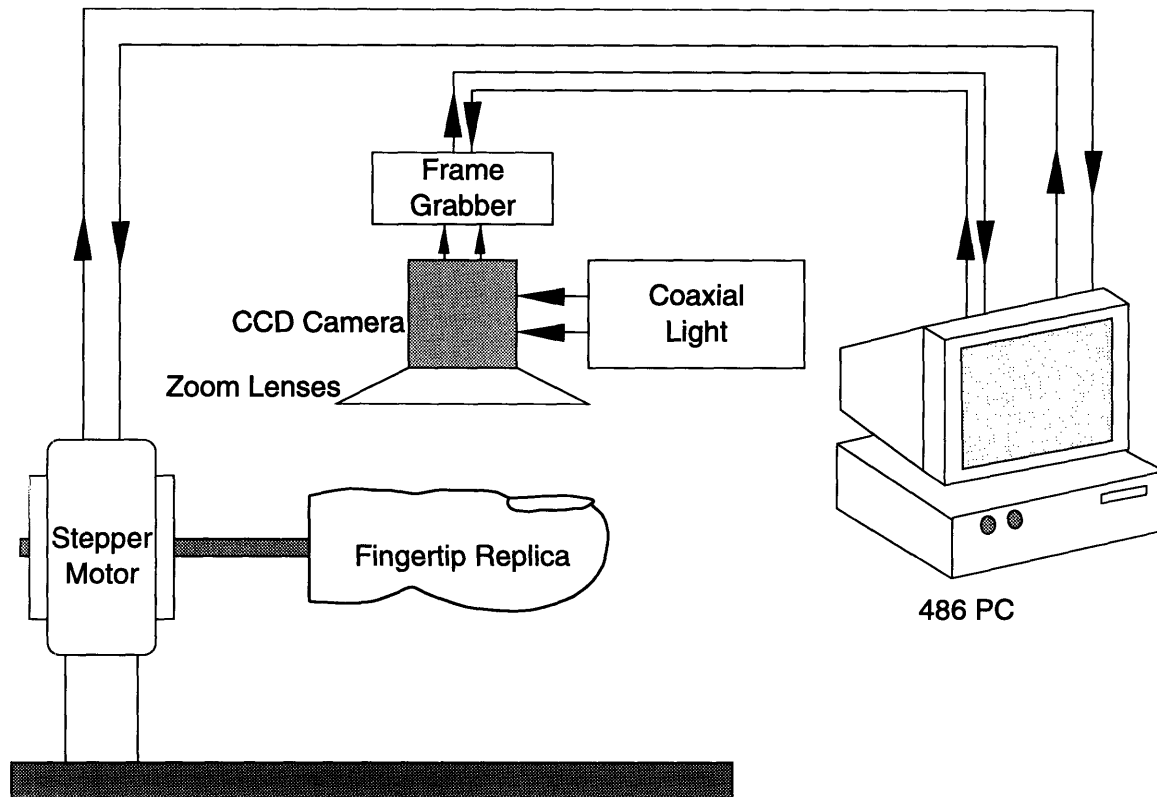


Figure 5-1: Experimental setup used for extracting borders from the epoxy replicas of monkey and human fingertips.

external geometry to refine the finite element models.

If accurate information about the external geometry of the fingertips is available, a 3D solid model can be generated, which in turn can be used to generate a 3D finite element model necessary to simulate biomechanical and neurophysiological experiments. A videomicroscopy setup¹ was used to acquire high contrast 2D images of primate fingertip replicas at various orientations. The border of the fingertip in each image was extracted and all such borders from different orientations were combined to reconstruct the 3D geometry of monkey and human fingertips.

5.1.1 Experimental setup

The experimental setup used to acquire high resolution images of the epoxy fingertip replicas is schematically shown in Figure 5-1. The videomicroscopy setup consisted of a

¹The videomicroscopy setup was built by Jyh-shing Chen and the author wishes to gratefully acknowledge his assistance in these experiments.

monochrome CCD camera with zoom lenses, co-axial and other lights, a frame grabber, and a 486 PC. Using the zoom lenses, the field of view of the camera could be adjusted such that the entire fingertip could be seen in the image for both monkey and human fingertip replicas. Co-axial lighting was necessary to obtain the high contrast images sought in this experiment. The frame grabber was capable of taking a snapshot of the video output of the CCD camera and digitize the image. The frame grabber was controlled by the PC and software was developed to save the acquired images to the hard drive of the computer.

The fingertip replicas were painted flat black to increase the contrast in the images which was necessary to extract the correct border from the image. A central hole was drilled in the epoxy replicas and a steel rod was inserted and glued in the replica, which then served as the axis of the fingertip. Using this rod, the fingertip replicas were mounted on a stepper motor, which was also controlled by the 486 PC. It was thus possible to rotate the replicas about the axis of the finger at desired angles. The stepper motor had a resolution of 400 counts per revolution and, thus, the replicas could be rotated about the axis in steps of 0.9° with each step of the stepper motor.

5.1.2 Experimental protocol

Similar experiments were attempted earlier with *in vivo* human fingertips and it was impossible to maintain the position of the fingertip fixed during the duration of the experiment. To obtain images of the fingertip from different orientations, the videomicroscopy setup had to be moved and re-calibrated before acquiring every image. This not only increased the time of the experiment, but also introduced errors in the angular position of the videomicroscopy setup and position of the fingertip due to involuntary motions of the subject. If the subject was allowed to rest the finger on a rigid surface, images could not be obtained from all angles about the axis of the finger. To solve these problems, precise epoxy replicas of primate fingertips were made and used in the experiment. Dental cement was used to make the mold for the replicas and human subjects were asked to insert their finger in a plastic tube containing the dental cement in liquid state. The hardening time of the cement was about 3 to 6 minutes and the subjects were asked to pull their finger out of the mold after 8 minutes. The fingers could be easily removed from the mold, as the dental cement was quite flexible in the hardened state. To obtain replicas of monkey fingertips tranquilized *Macaca fascicularis* monkeys were used and the same procedure

was followed. Epoxy resin was later poured in the molds and allowed to solidify. The replicas were obtained by removing the mold around the epoxy. The replicas were washed with water to remove any dental cement adhering to them. These casts were extremely accurate in reproducing the finger print ridges, details of the nail and wrinkles on the skin. The use of the rigid epoxy casts made it possible to use a stepper motor to accurately position the fingertip at the required orientation.

The fingertip replica was mounted on the stepper motor using the rod as shown in Figure 5-1 and the zoom lenses were adjusted such that the entire fingertip and a portion of the rod inserted in the replica was visible in the image. The replica was rotated at 10° intervals and the axial alignment of the shaft was checked. If the axis of the shaft was not parallel to the axis of the finger, the shaft was removed and a new hole was drilled in the replica after filling up the old hole with epoxy. Once the alignment of the rod was found to be correct, the lens setting was fixed and was maintained unchanged till the end of the experiment. The replica was removed from the stepper motor and a template of known size (typically 12.7 mm diameter circle), fixed to a shaft of the same diameter as the rod in the replica, was mounted on the stepper motor. An image was acquired which was used in deciding the scale factor and the aspect ratio of the images. The fingertip replica was mounted back on the stepper motor and images were acquired using a computer program. Software was developed such that images could be automatically acquired at the required orientations. The computer program could control the process of image acquisition in which an image was grabbed and saved to the disk, the stepper motor was then stepped through the required angle to attain the required orientation, and the process was repeated. Typically, 100 images at distinct orientations were obtained for each fingertip. The image acquisition was monitored to ensure that the change in orientation did not affect the contrast in the image.

The border of the fingertip in each image was extracted as shown in Figure 5-2. The raw image as acquired in the experiment is shown in the left panel. It can be seen that, due to the flat black paint on the replicas and the use of co-axial lighting it was possible to acquire high contrast images. In the central panel, this fact is shown graphically. On the Y-Z plane the same image as shown in the left panel is shown. The gray scale value at each point in the image is plotted on the vertical axis. This is an image with 256 gray scales (1 byte per pixel) and it can be seen that the border of the fingertip is clearly identifiable from

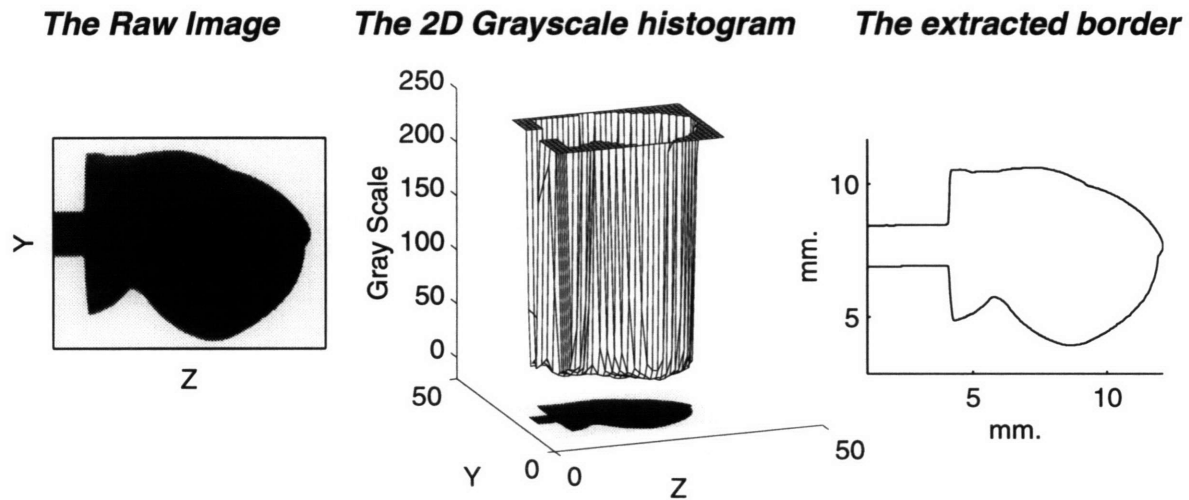


Figure 5-2: This figure shows the extraction of the borders from the computer images. The raw image shown in the left panel is the image as acquired by the frame grabber. The 2D histogram is shown in the middle panel and shows a clear distinction between the gray-scale values of the fingertip and the background. The extracted border is shown in the right panel.

the 2D histogram. Any gray scale value between 50 and 200 can be used as the threshold value in extracting the edges in the image. The border of the fingertip was defined as the transition point from the white pixel (gray-level greater than 250) to a non-white pixel. The extracted border is shown in the right panel. It can be seen by comparing the raw image and the extracted border that minute details of the image are also accurately represented in the extracted border.

5.1.3 Reconstruction algorithm

The lateral cross-sections obtained by extracting the border from the images can now be plotted in 3D as shown in Figure 5-3. The borders are plotted at the respective orientation at which they were acquired and as the rotation of the finger is defined about the axis of the finger, this angle is measured about the Z axis. Four sections are shown and the outline of the axial cross-section of the fingertip is shown for better understanding of the construction only.

Although it is possible to construct a 3D solid representing the fingertip from the lateral cross-sections, it is important to obtain axial cross-sections of the fingertip as the primate fingertips are more or less symmetric about the axis of the fingers. It would be easier to

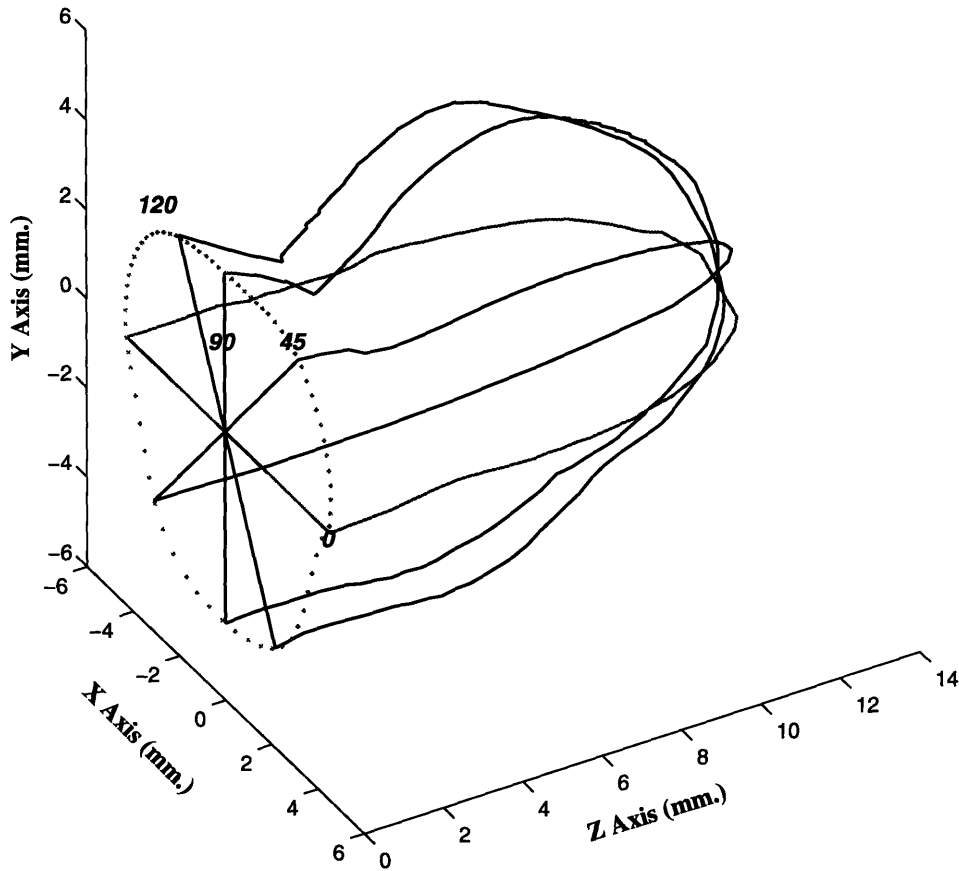


Figure 5-3: Lateral cross-sections of the monkey fingertip aligned at their respective orientations. Four sections at angles 0, 45, 90 and 120° are shown.

define the layers of the skin, epidermal and dermal ridges of the skin and diameter of the bone if such data is available. The data set consisting of lateral cross-sections can be converted to a data set consisting of axial cross-sections using the following algorithm.

The reconstruction algorithm is schematically shown in Figure 5-4. On the left side, three lateral cross-sections at angles 0, 45 and 90° are shown. The Z axis, which is the axis of the finger and the axis of the rod inserted in the fingertip replica, is shown by a dash-dot line. The figure shows the steps involved in reconstructing the axial cross-section at a Z location, shown by the gray vertical line. The vertical distances of the boundary points where the gray line intersects the border are measured perpendicular from the Z axis.

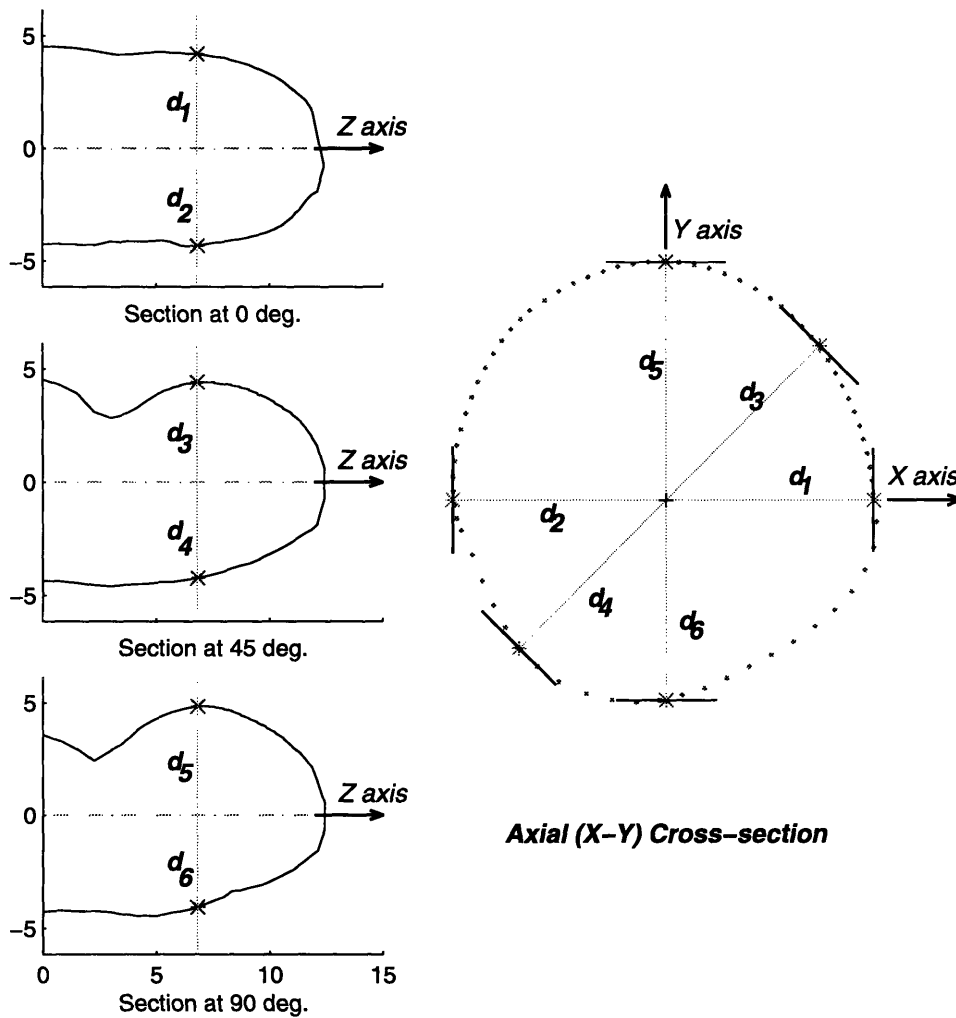


Figure 5-4: Three lateral cross-sections at 0, 45 and 90° are shown on the left. The steps involved in constructing the axial cross-section at an axial location (shown by the vertical line) are shown. The distances are measured from the Z axis shown by dash-dot lines.

These distances are plotted radially at the respective angles in the figure on the right side. Perpendicular lines are drawn to the segment joining the origin (Z axis) and the boundary point plotted at its orientation. The angle is measured about the Z axis with the counter-clockwise angles being positive. It can be seen that the distances d_1 and d_2 are plotted at an angle of 0°, d_3 and d_4 at an angle of 45°, and so on. To better visualize this transformation, assume that a camera is placed at the bottom of the cross-section shown on the right. The two points seen in that view would be d_1 and d_2 distances apart. If the cross-section is rotated clockwise, the points defined by d_3 and d_4 will be seen. Thus, the angle of rotation of the fingertip replica is inverted in plotting the points are their respective orientations in

the axial cross-section.

When an image is acquired using the method described above, each point on the extracted border defines a tangent to the fingertip. This can be visualized by considering a line parallel to the X-Z plane and perpendicular to the Y axis, as the projector of the point on the fingertip, projected onto the Y-Z plane. At a particular Z location, two such lines which are tangents to the fingertip on the top and bottom surface will define the two points in the extracted border. These lines are uniquely defined by their vertical distance from the Z axis, as it is already known that these lines are perpendicular to the Y axis and lie in a plane parallel to the X-Z plane. The X coordinate of the point of tangency of the tangents with the fingertip is not known. In most of the cases, it would be $x = 0.0$, but it is not necessarily true in all cases. Thus, each border provides two points in the X-Y cross-section and the line perpendicular to the line joining the origin and the point drawn at the point, defines a tangent to the cross-section of the solid at that angle. Thus each lateral cross-section essentially defines two tangents to the X-Y cross-section. The 6 tangents defined by the three lateral cross-sections are shown in Figure 5-4. The tangents defined by all the cross-sections are drawn in the X-Y plane and the section of the fingertip is generated by drawing a smooth curve inscribed in the polygon defined by the intersecting tangents, such that each side of the polygon is a tangent to the fingertip contour. It should be noted that the point of tangency of the fingertip contour and the tangent drawn from in the X-Y plane does not have to be the point used in drawing the tangent.

This method can be used for different biological structures that need to be reconstructed on a computer. A physical statement of the suitability of a cross-section to be reconstructed by this method can be stated as follows:

If a string is wrapped around a cross-section and it maintains contact with the cross-section at all points, then the cross-section can be reconstructed exactly using this method.

Errors will be introduced at the points where the string loses contact with the object cross-section. This will happen at points, where the curvature of the object is negative, i.e., the shape of the surface is concave. The fingertip passes this test at most of the points and the locations where this method would introduce errors are the intersection of the nail and the skin and in the reconstruction of the finger ridges. For the present purposes, such

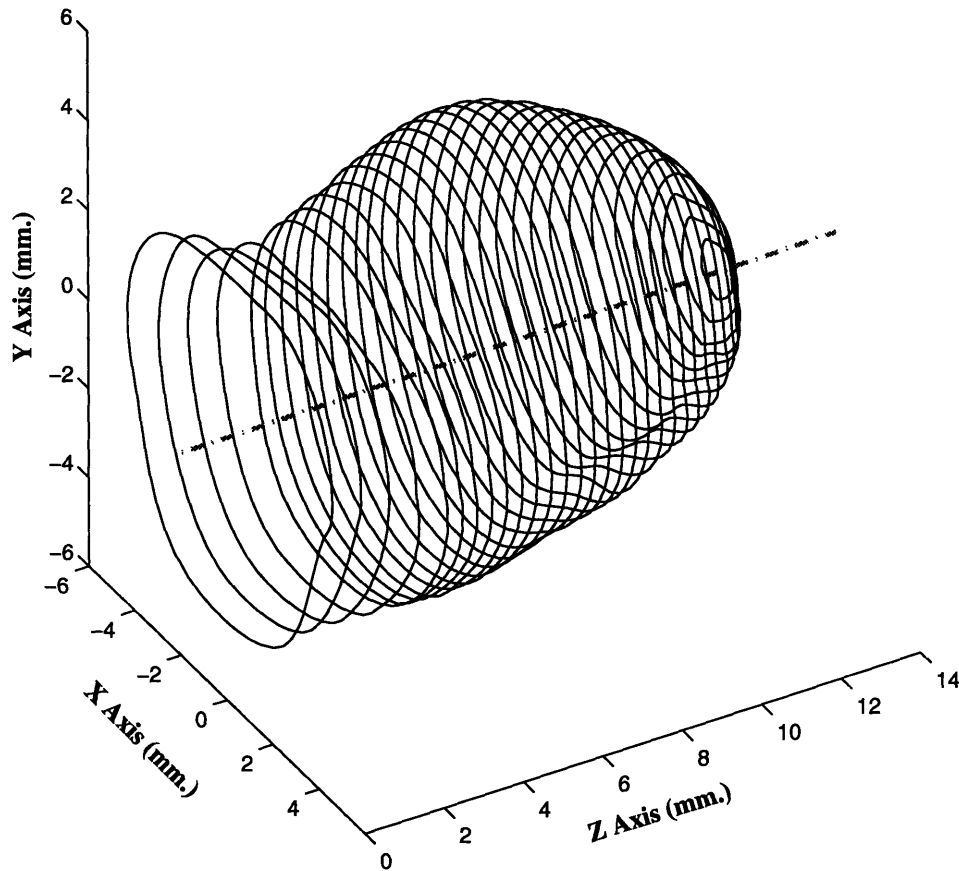


Figure 5-5: Axial cross-sections reconstructed from the extracted borders. These cross-sections define the external geometry of the monkey fingertip and a solid can be generated by generating a patch over the axial cross-sections.

errors do not significantly affect the finite element analysis of the whole fingertip.

The process of generating the axial cross-sections has to be repeated at all the desired Z locations. Depending on the curvature of the fingertip, axial cross-sections were generated at every 0.5 mm to 2.0 mm apart. Several axial cross-sections of the monkey fingertip generated using this algorithm are shown in Figure 5-5. It is not necessary to accurately model the hemispherical end of the distal phalanx and the sections were not generated in that region.

These 2D sections were imported into a solid modeler software (PATRAN) and 'patches'

were defined in each cross-section. Patches are 2D parametric surfaces, that form a primitive of the solid model. Five layers were defined in each of the cross-sections which was necessary to model different layers in the fingerpad. The dimensions of the layers were chosen from the available data on the thickness of the layers of skin and more layers were generated than the required minimum. The dimensions of the bone in the distal phalanx were extracted from X-ray images and the thickness of the bone as a percentage of the fingertip diameter was calculated at various locations along the Z axis. This was used in determining the size of the innermost layer of the cross-section which corresponded to the bone. Hyperpatches were generated using patches in the neighboring axial cross-sections and second order continuity was enforced between two hyperpatches. Hyperpatches is the three-dimensional equivalent of the patches and forms the 3D primitive of the solid model. The model was thus generated in five layers in each axial cross-section and several axial cross-sections along the axis of the finger. The boundary of the nail was extracted from the top and side views and a patch corresponding to the nail was generated and overlaid on the fingertips. It should be noted that, the geometry definition was completely distinct from the finite element mesh and hence the same geometry definition could be used to test different meshing schemes. The specification of the material properties can also be selected independent of the geometry and the mesh definition (Dandekar and Srinivasan, 1995b).

5.2 Surface Deformation of Human Fingertips *in vivo*

It is not possible to directly observe the sub-surface deformation or the stress-state *in vivo* because of the opacity of the fingerpad. The deformation of the surface, however, can be observed under a variety of stimuli. Experiments were designed to observe the deformation of the fingertip surface under a variety of indentors and the deformation data used in the biomechanical validation of the finite element model.

5.2.1 Experimental setup

The experimental setup for these experiments was very similar to the one used in the earlier experiments to reconstruct the 3D external geometry of primate fingerpads and is shown in Figure 5-6. The videomicroscopy component of this setup was identical to the

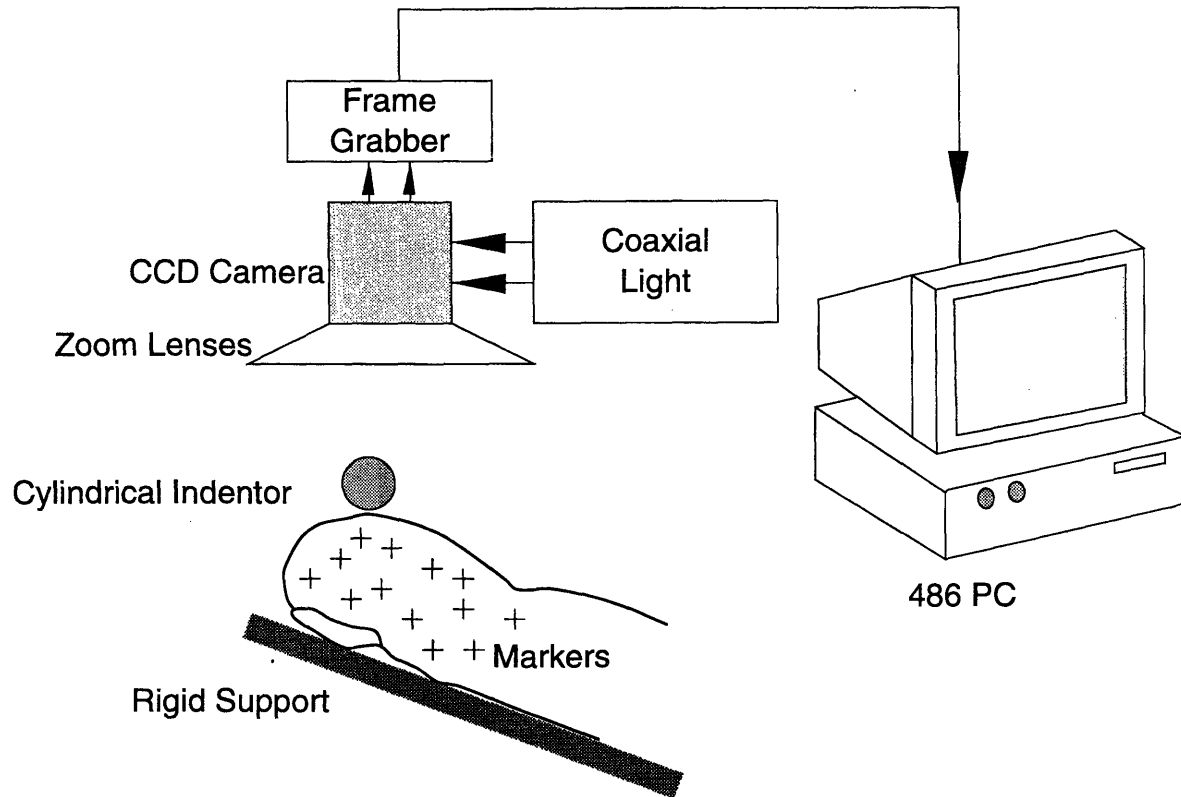


Figure 5-6: Experimental setup used for the fingertip deformation experiments. The cylindrical indenter is shown aligned perpendicular to the finger axis and the camera is positioned to acquire images for the top view.

one described earlier and shown in Figure 5-1. The zoom lenses were chosen such that the entire fingerpad could be viewed in the image.

A rigid platform at an angle of 30 degrees with the horizontal was fabricated. Subjects were asked to place their fingertips on this rigid support as shown in figure. This ensures that the region of the fingertip predominantly used in exploration tasks is indented by the indentors. The fingernail was glued to the support to avoid motions of the fingertip. The arm was further supported by an arm rest and an elbow rest to make the posture comfortable for the subject. A linear stage (not shown in the figure) was designed so that various indentors, like the cylindrical indenter shown in the figure, could be mounted on the stage. The stage had a micrometer screw which could be used to lower the indenter in the vertical direction with an accuracy of about $25 \mu m$???. The indenter could be mounted such that it was either perpendicular to the axis of the finger, as shown in figure, or parallel to the axis of the finger. About 100-150 markers were placed on the fingertip skin using

Indenter Code	Size		Type
	Diameter or width mm.	inches.	
R1	12.7	$\frac{1}{2}$	Rectangular
R2	38.1	$\frac{1}{2}$	Rectangular
C1	1.59	$\frac{1}{16}$	Cylindrical
C2	3.18	$\frac{1}{8}$	Cylindrical
C3	4.76	$\frac{3}{16}$	Cylindrical
C4	6.35	$\frac{1}{4}$	Cylindrical
C5	9.52	$\frac{3}{8}$	Cylindrical
C6	12.7	$\frac{1}{2}$	Cylindrical
C7	19.05	$\frac{3}{4}$	Cylindrical
C8	25.4	1	Cylindrical

Table 5.1: Indentors used in the study of fingertip deformation

a micro tip pen with waterproof ink. The diameter of the pen was 50 microns and it was thus possible to accurately position the markers on the finger ridges.

Adjusting the lighting to strike a balance between the contrast in the background and the border of the finger as well as the contrast between the markers and the rest of the finger posed one of the most difficult problem in the experiment. A combination of co-axial and other lighting was used along with strategically placed mirrors to eliminate unwanted shadows. To enhance the contrast under the indenter, the bottom half of the indenter was painted white and the top half of the indenter was painted black. This made it possible to obtain a sharp boundary of the indenter on the top and a clear border of the deformed fingertip under the indenter in the side view.

5.2.2 Experimental protocol

The subject was comfortably seated and the fingernail glued to the rigid platform as described earlier. Lighting was next adjusted with two or three indentors to attain the required contrast. The zoom lenses were adjusted such that the fingertip and the markers on the fingertip could be seen in the image and the lens setting was maintained unchanged for the rest of the experiment. For each setting, a calibration image with a template of known sizes was acquired before the start of the indentations, which was necessary to determine the aspect ratio and the scale factor of the image.

The sizes of the eight cylindrical indentors and two rectangular indentors used in the

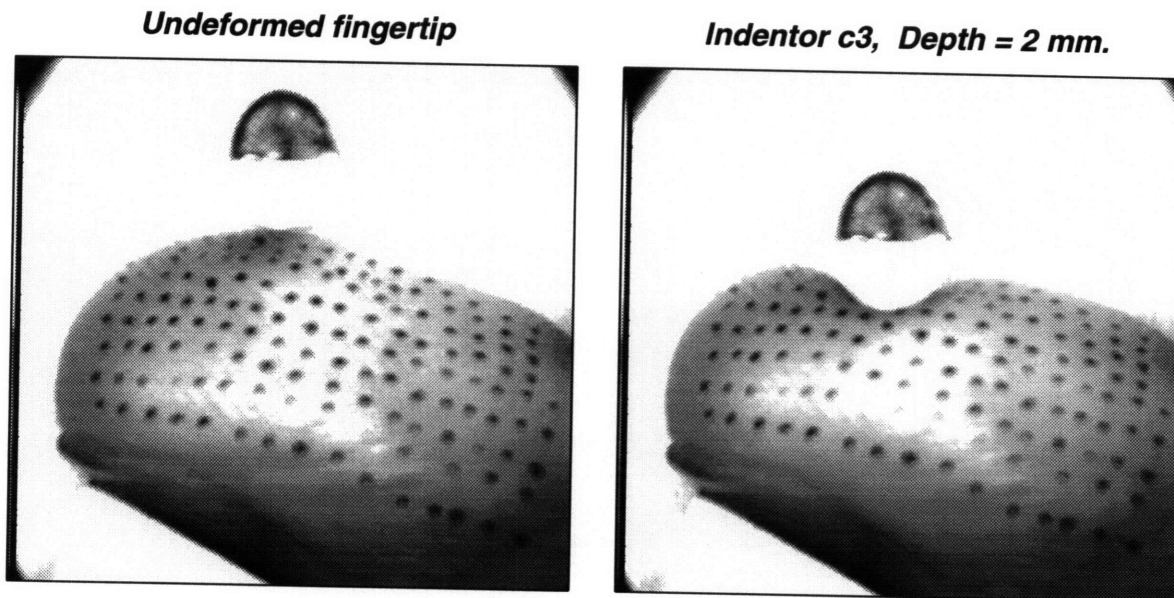


Figure 5-7: The side view of cylindrical indenter indenting the human fingertip are shown. The lower half of the indenter is painted white to clearly observe the surface of the deformed fingertip under the indenter. The indenter is indented into the fingertip to a depth of 2.0 mm in the right panel.

experiment are listed in Table 5.1. The choice of the diameters of the circular indentors and the widths of the rectangular indentors was made such that the neurophysiological data for indentation by these indentors on monkey fingertips was available (Srinivasan and LaMotte, 1991; Phillips and Johnson, 1981a).

The indenter was mounted on the linear stage and was gradually lowered till it just touched the fingertip. This was designated as the datum for the measurement of the depth of indentation. A computer program was written to run the experiment and images were acquired as the fingertip was indented in steps of 0.5 mm to a depth of 3.0 mm. The fingertip shows changes in deformation with time and it was observed that the changes are negligible after the first two minutes. Hence, the image corresponding to a particular depth of indentation was acquired 2 minutes after the completion of the indentation. In some cases, when the indenter was comparatively large and the subject expressed discomfort the maximum depth of indentation was limited to 2.0 or 2.5 mm. After acquiring the final image the indenter was brought to its original position and replaced with the next indenter.

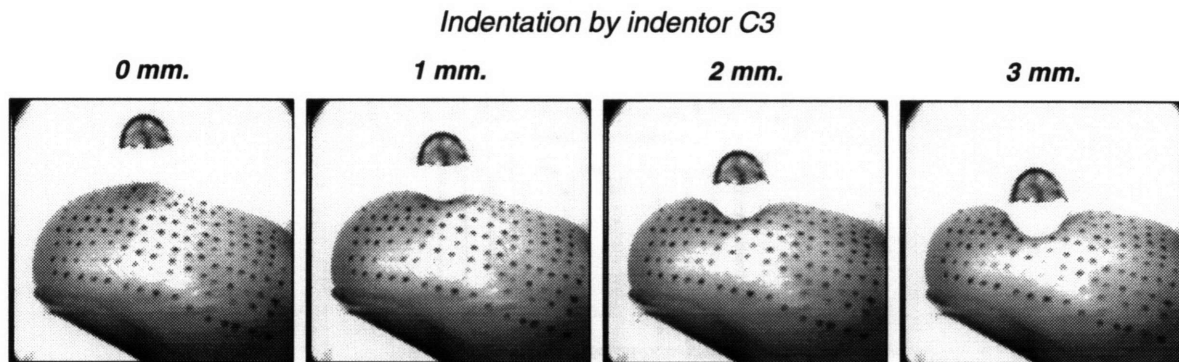
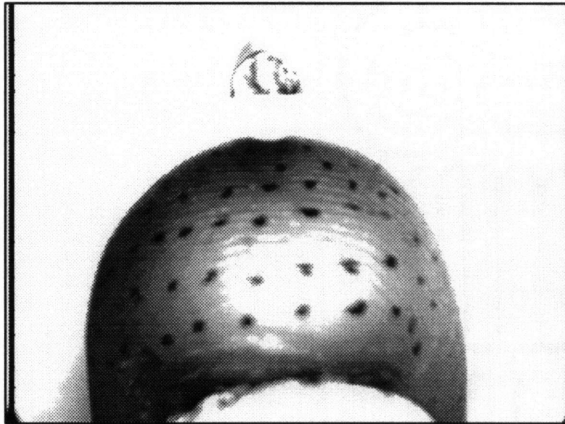


Figure 5-8: Side views of a cylindrical indenter placed perpendicular to the finger axis and indenting the human fingertip is shown. The left image shown the initial position of the indenter when it just touches the fingertip. The other three images were acquired at the depths shown.

The images of the undeformed and deformed fingertip under indentation by a cylindrical indenter C3 of 3.175 mm diameter ($\frac{1}{8}$ inch) are shown in Figure 5-7 and Figure 5-8. The images are not processed in any way and the figures were generated directly from the acquired binary images. The use of the combination of the co-axial and other lighting made it possible to obtain a satisfactory image that could be used in both determining the border of the deformed and undeformed fingertip and the location of the deformed and undeformed markers. The rigid support and the bottom half of the indenter was painted white, as was the bottom half of the indenter. It was, therefore, possible to obtain a clear border of the deformed fingertip under the indenter.

Each of the ten indentors were aligned perpendicular and parallel to the axis of the finger. For each orientation the side view, top view and the axial view was obtained. With the indenter aligned perpendicular to the finger axis, the side view is shown in Figure 5-8 and the top view is shown in Figure 5-11. No axial views were taken when the indenter was aligned perpendicular to the axis of the finger. With the indenter aligned parallel to the axis of the finger, the axial view is shown in Figure 5-9 and the top view is shown in Figure 5-10. Images from the side view were not acquired when the indenter was aligned parallel to the finger axis. A typical experimental session was limited to 1.5 hours and it was possible to complete indenting the fingertip with 5 or 6 different indentors to all the depths for a particular view. Three male and two female subjects between the age of 19 and 40 were used in the experiment.

Undeformed fingertip



Indenter c2, Depth = 2 mm.

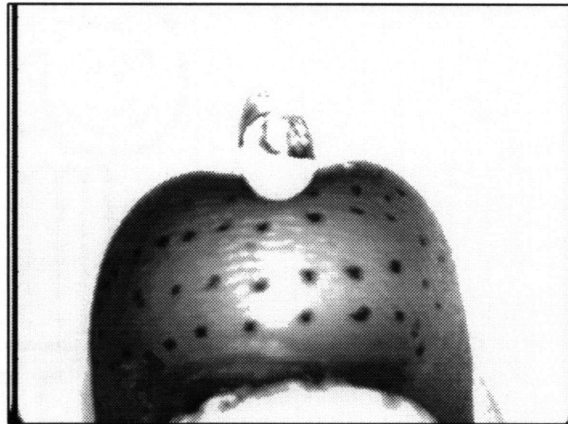
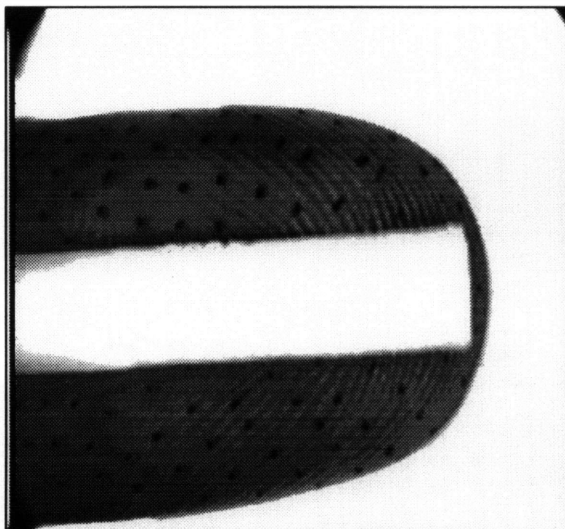


Figure 5-9: The axial view of a cylindrical indenter placed parallel to the finger axis, indenting the human fingertip is shown. The indenter is painted half white to improve the contrast under the indenter. The indenter is indented into the fingertip to a depth of 1.0 mm in the right panel.

Undeformed fingertip



Indenter c3, Depth = 3 mm.

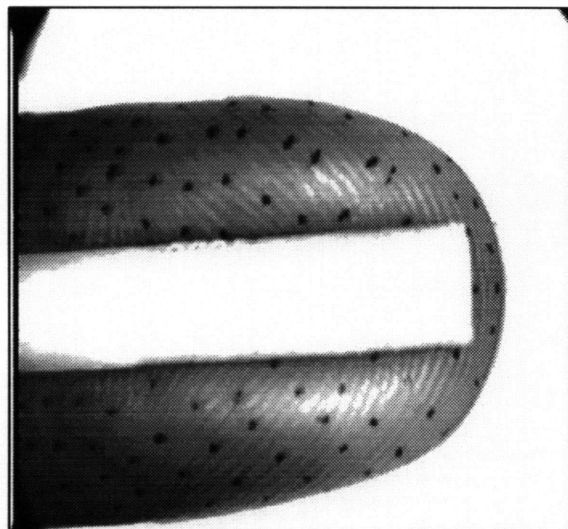


Figure 5-10: The axial view of a cylindrical indenter placed parallel to the finger axis, indenting the human fingertip is shown. The indenter is painted half white to improve the contrast under the indenter. The indenter is indented into the fingertip to a depth of 1.0 mm in the right panel.

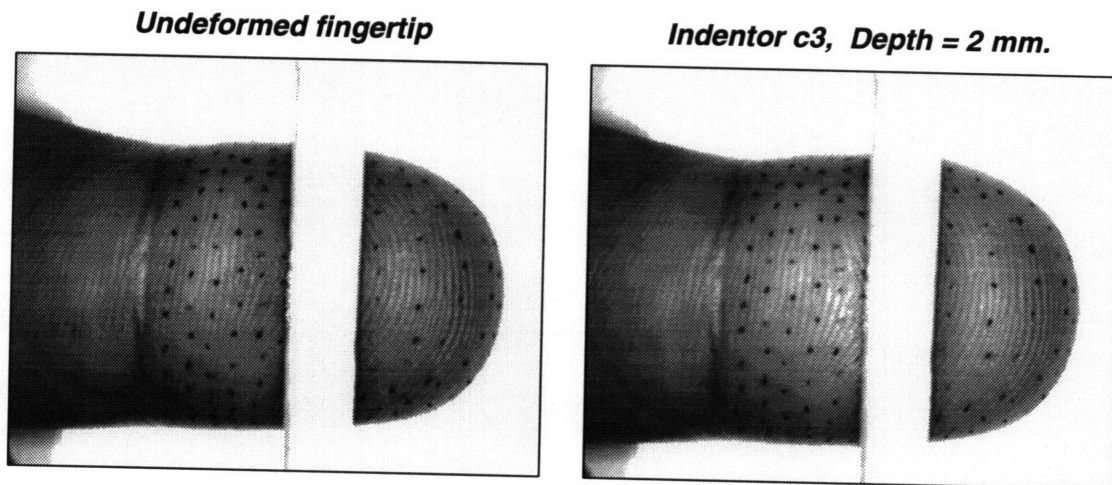


Figure 5-11: The axial view of a cylindrical indenter placed parallel to the finger axis, indenting the human fingertip is shown. The indenter is painted half white to improve the contrast under the indenter. The indenter is indented into the fingertip to a depth of 1.0 mm in the right panel.

5.2.3 Data analysis

The border of the fingertip was extracted from the images to compare the profile of the undeformed and deformed fingertips. The extracted border of the human fingertips under indentation by indenter C4 is shown in Figure 5-12. In the top panel, the border of the fingertip at all the depths of indentation is shown. A few points on the indenter are digitized and are used to determine the position of the indenter with respect to the extracted border. The points used to locate the indenter for the highest depth of indentation (3 mm), and the position of the indenter are shown in gray lines. Because of the non-uniform lighting on the top surface of the fingertip, the border appears to be jagged at some points. This can be smoothed out by filtering the data as shown in the middle panel. It is clear from the top two panels, that indentation to a depth of 3 mm on the glabrous side induces negligible deformations on the other side of the fingertip. This is to be expected since the nail is much stiffer than the rest of the tissues and it is glued to the rigid platform in this case. As the finger is resting on the rigid platform, the only relevant deformations are of the glabrous side which are shown in the bottom panel. These deformation can be compared with the deformations predicted by the finite element model, to check the biomechanical accuracy of the finite element model.

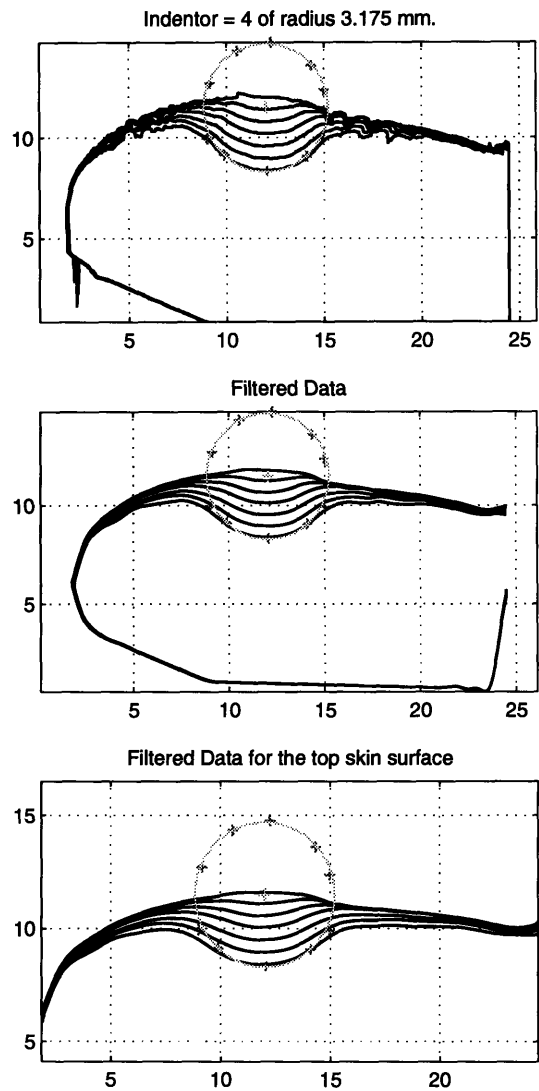
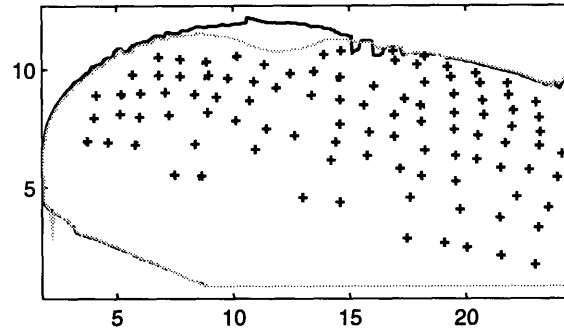
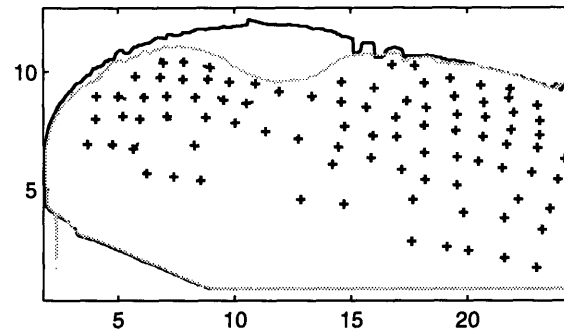


Figure 5-12: Experimentally observed surface deformation of the human fingertip under indentation by a cylindrical indenter of radius 3.187 mm ($\frac{1}{4}$ inch) at various depths are shown. The indenter is indented by 0.5 mm in each step. The position of the indenter in the deepest indentation is shown by the gray circle. The points extracted from the image used in determining the indenter location are shown as '+'s. The top panel shows the raw data, the middle panel has the filtered data and magnified surface deformation profiles are shown in the bottom panel.

Indenter = 4 of radius 3.187 mm. Depth of Indentation : 1 mm.



Depth of Indentation : 2 mm.



Depth of Indentation : 3 mm.

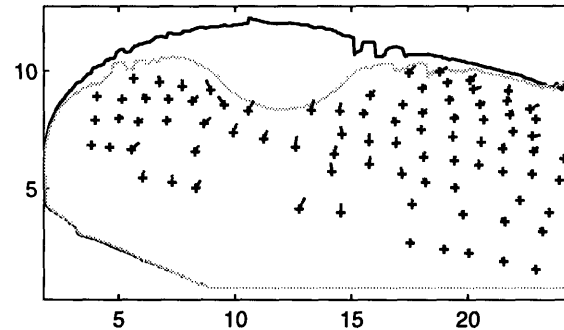


Figure 5-13: Experimentally observed surface deformations of the human fingertip under indentation by a cylindrical indenter of radius 3.175 mm ($\frac{1}{4}$ inch) at 3 depths (1, 2 and 3 mm) are shown. The position of the markers after indentation is marked by a '+'.

By observing the undeformed and deformed position of the markers placed on the fingertips, the overall deformation pattern of the fingertip under a specific indenter can be studied. The locations of the markers were manually extracted from the images in the undeformed and deformed fingertips. The original and final location of the markers on the fingertip under indentation by indenter C4 at various depths of indentation are shown in Figure 5-13. The undeformed profile of the fingertip is shown in a solid line and the

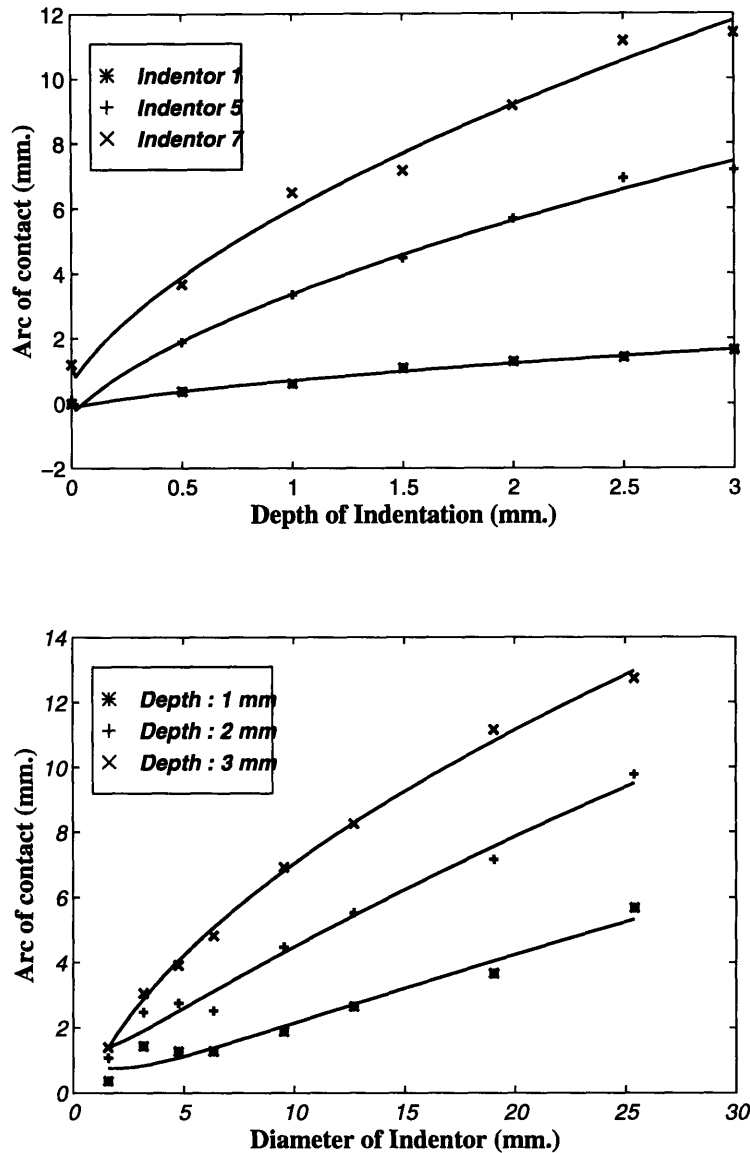


Figure 5-14: Variation in experimentally observed contact area between the cylindrical indentors and the human fingertips for one subject. The top panel shows variation in contact area with respect to depth of indentation for 3 indentors. Variation with respect to the diameter of the indenter for three different depths of indentation is shown in the bottom panel.

deformed profile is shown in gray. The '+' marks the final position of the marker and a line is drawn from the initial position to the final position to indicate the magnitude and direction of the displacement of the marker points. Although the overall pattern of deformation can be seen in these figures, it is necessary to summarize the deformation by expressing them as a algebraic function for a particular indenter.

Figure 5-14 shows the variation in the area of contact with depth of indentation and diameter of indenter for one subject. In the top panel, the variation of contact area is shown with respect to the depth of indentation for three indentors. The variation is more or less linear for the smaller indenter but increases rapidly for smaller depths of indentation for larger indentors. At higher depths of indentation the area of contact tends to flatten out. The bottom panel shows the variation with respect to the diameter of the indenter. It should be noted that the indentors were indented into the fingerpad to a fixed depth of indentation as shown in the legend. For smaller depths the area of contact varies linearly with the diameter of the indent ion.

6

3D Models

This chapter describes the modeling and simulations using the three dimensional (3D) models of the primate fingertips. The biomechanical verification of the models is presented followed by the results of simulating various neurophysiological experiments.

6.1 Construction of the Models

Construction of an accurate solid model using experimentally acquired external geometry of the primate fingertips was the first step in generating the 3D finite element models. The solid model consisted of a collection of patches and hyperpatches which are the 2D and 3D parametric primitives used in the algebraic representation of surfaces and solids respectively. The finite element mesh was constructed using the solid model by generating node points, which were used in the definition of elements. Assignment of material properties to all the elements and verification of the model using several standard tests was necessary before using the finite element models in the simulations of biomechanical and neurophysiological experiments.

High resolution images of the primate fingertips replicas were acquired at various orientations using the videomicroscopy setup as described in section 5.1. Each of these images represented the orthographic projection of a longitudinal section of the fingertip at that orientation. The primate fingertip is more or less symmetrical about the axis of the finger and hence use of axial cross-sections provides greater flexibility in the definition of salient geometrical features of the fingerpad. The longitudinal sections were, therefore, converted to axial cross-sections using the reconstruction algorithm described in section 5.1.3. The solid modeler PATRAN Plus was used to combine these axial cross-sections and reconstruct the 3D geometry of the fingertip.

In each axial cross-section, five concentric layers of patches were generated. Thickness of the bone relative to the width of the fingertip at all the axial locations was derived from X-ray images of the fingers and used to determine the dimensions of the innermost layer which corresponds to the bone. The skin of the fingertip was modeled as two outer layers of 0.5 and 1.0 mm thickness corresponding to the epidermis and dermis respectively. The bone was approximately 2 mm in diameter. Two more intermediate layers were generated between the skin and the bone to model the adipose tissues and the fibrous matrix. The bone in the distal phalanx is axially shifted towards the nail, away from the geometrical center of the axial sections of the fingertip, and this offset was taken into account in defining the bone location in each of the axial cross-sections. All the internal layers except the innermost layer corresponding to the bone were generated by scaling the profile of the cross-section. Scaling factors were defined as the ratio of the thickness of each layer and the thickness of the fingertip at three representative axial sections. The same factors were then used for all the axial sections and, therefore, in a given axial cross-section the exact thickness of individual layers was proportional to the size of the cross-section.

To facilitate definition and refinement of the finite element mesh in the solid model, each axial cross-section was divided into six equal slices in the θ direction. With 5 layers in the radial direction, each cross-section thus contained 30 patches. Bi-cubic hyperpatches were generated by combining corresponding patches from 4 neighboring axial cross-sections. The hyperpatches, therefore, followed the same pattern as the patches in maintaining the layered structure of the model. Four neighboring cross-sections containing 30 patches each were combined into an 'slice' of finite width containing 30 hyperpatches. C^1 continuity was imposed on any two adjacent hyperpatches to ensure a smooth geometry suitable for the generation of higher order finite elements.

Finite element mesh was generated in the hyperpatches and Figure 6-1 shows a perspective view of the monkey fingertip with the hidden lines removed. The nail is shown shaded gray on the top. The model shown contains 8 noded isoparametric elements for the fingertip and 4 noded membrane elements for the fingernail. It should be noted that, in all the simulations the fingernail is always glued to the table and hence the elements shown shaded gray should be treated as equivalent to the region where the fingertip is fixed to the table. The extension of the fingernail in the distal direction which overhangs the fingertip is solely for cosmetic reasons and none of the elements of the fingernail have

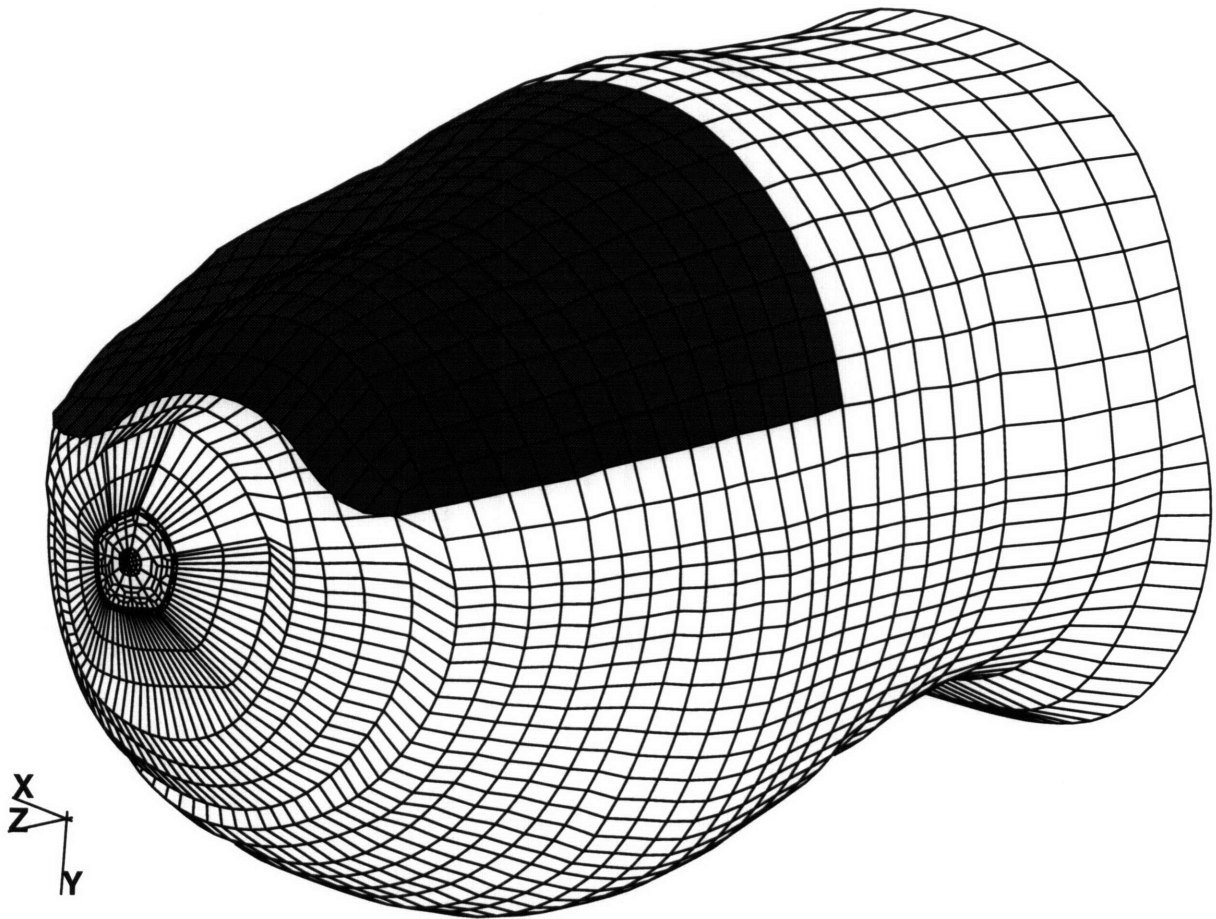


Figure 6-1: 3D view of the monkey fingertip showing the nail. The hidden lines are removed for clarity

any active degree of freedom in the solution.

Because of the irregular geometry of the fingertip and features that vary in size by orders of magnitude, together with the conflicting requirements of higher resolution and lower computational effort, choosing a meshing scheme was essentially a multi-variable optimization problem with several non-unique solutions. High spatial resolution was sought in the vicinity of the receptors (in the top 1.5 mm of skin on the fingerpad) so that spatial resolution finer than the receptor spacing in the actual fingertip could be obtained. The stimuli in all the biomechanical and neurophysiological experiments of interest to us are delivered on the fingerpad and, hence, finer mesh size is required on the glabrous skin

to accurately simulate the mechanistic interaction of the fingertip with various indentors used in the experiments. As in the case of 2D models, it is desirable to have elements with aspect ratio close to unity in the region where loads are prescribed and the region where stress-state is desired. For the stimulus of interest, a finer mesh size was deemed unnecessary on the dorsal side and towards the proximal end of the fingertip. Rather, using a finer mesh would significantly increase the computational effort required for the solution of the finite element problems.

The advantage of separating the solid model from the finite element model is that, several meshing schemes could be implemented in the same solid model. Refinement of the finite element model can be done irrespective of the solid model. Several different meshing schemes were considered and evaluated against the requirements listed above. Some form of transition in the mesh size from fine to coarse, however, was essential to limit the computational effort considering the fact that the model would be used in the solution of several iterative non-linear contact problems in the simulation of some neurophysiological experiments. The automatic meshing schemes provided in PATRAN Plus failed to generate a satisfactory mesh. Custom programs were written in the Patran Command Language (PCL) to test various meshing schemes that would allow the mesh to be varied in the radial and axial direction, while satisfying other requirements.

Figure 6-2 shows three different sections of the fingertip in relation to the entire monkey fingertip. The nail is not shown for clarity and the outline of the fingertip is shown in gray. In all the three cross-sections, the different layers are indicated by different shades of gray. It can be seen that smaller element size was used on the glabrous side (the bottom part in this figure) and on the surface of the glabrous skin. Two models with 8 and 20 noded isoparametric elements were generated and the number of nodes in the two models were 8500 and 17,000 respectively. For simulating monkey fingertips a typical diameter of approximately 8 mm was used and element size in the region of contact with indentors was approximately 500 microns and 250 microns for the 8 noded and 20 noded element monkey fingertip models respectively. It can also be seen that the size of the elements was increased in the proximal direction along the axis of the fingertip and, thus, the rightmost section has only one element in the axial direction, whereas the other two sections have two elements each for the same thickness. The transition scheme used increases the size of the elements by a factor of 2 in the radially inward direction with every layer of the transition

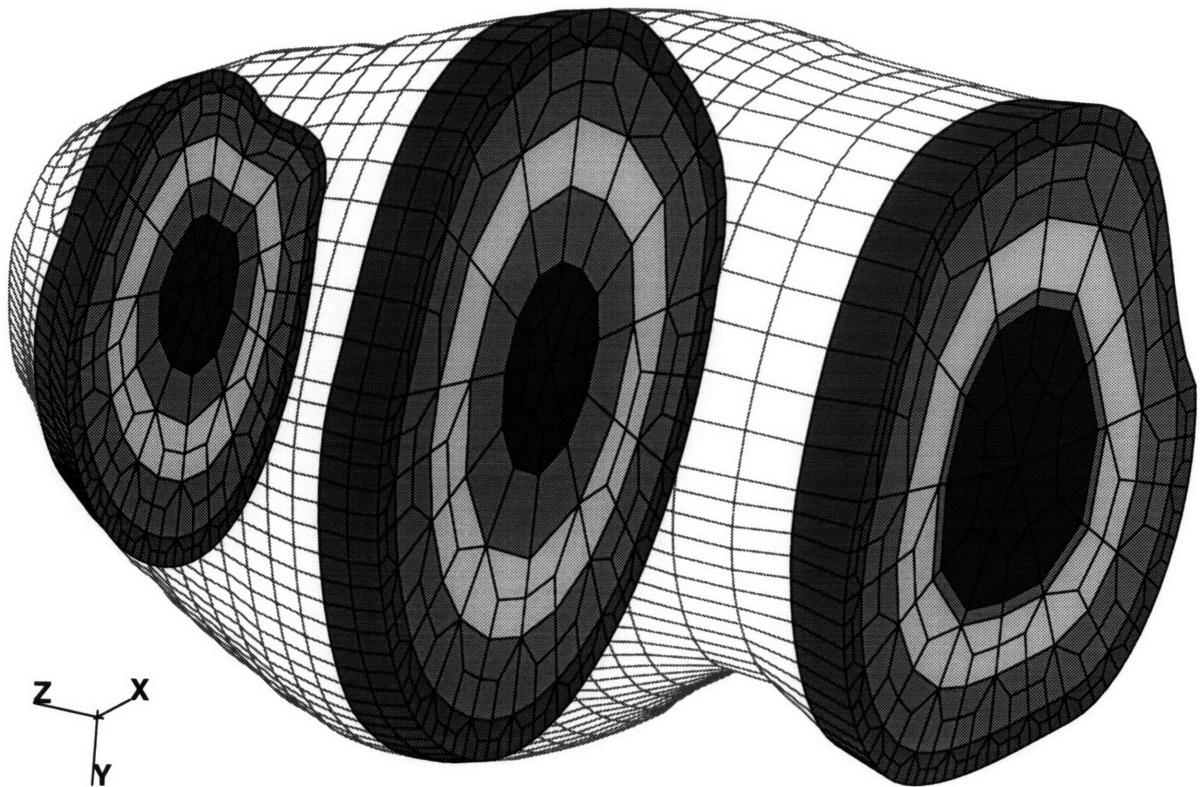


Figure 6-2: Three slices of the monkey fingertip are shown with reference to the boundary of the fingertip. The elements are shaded to show the layers used in the model.

elements. The geometry of the transition elements is suitable to model the epidermal and dermo-epidermal ridges with the proper assignment of material properties to distinguish between the layers of the skin.

Figure 6-3 was produced by clipping out the section of model by the Y-Z plane and plotting only the elements with positive X coordinated to generate the sagittal cross-section of the monkey fingertip. The various layers of the fingertip can be distinguished by the different shades of gray. The innermost layers is the bone and the shape of the bone can be clearly seen. It should be noted, however, that the model is not meshed symmetrically about the Y-Z plane and hence some elements that are partly on the positive X axis are not shown, causing the illusion of voids in the model. The tip of the fingertip is not fully modeled and hence the bone continues till the distal end of the model. When the hemispherical tip of the finger is accurately modeled, the various layers of the skin could be

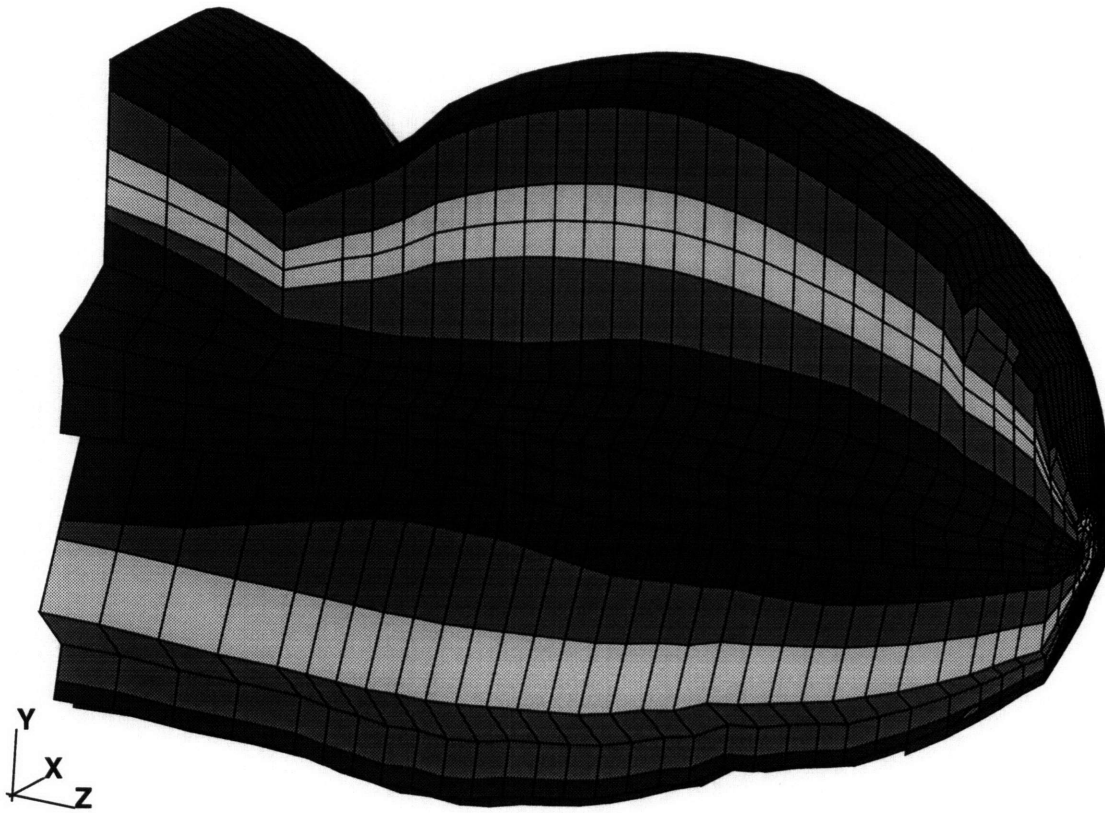


Figure 6-3: Longitudinal section of the monkey fingertip showing the layers of the model. The innermost layer is the bone, and the dimensions of the bone are derived from X-ray images of the distal phalanx.

wrapped around the bone at the distal end. In the previous model, mechanical properties can be assigned to each of the elements irrespective of each other. The layered construction of the model makes it very easy to change the material properties of all the elements in a layer with a single command. In all the biomechanical and neurophysiological experiments the fingernail is always glued to the table and that is simulated by suppressing all the degrees of freedom of the nodes on the fingernail.

To reduce the computational effort in iterative problems requiring matrix decomposition, the sub-structuring option was explored. By sub-structuring the model, it is possible to reduce the total degrees of freedom in the problem by eliminating the local degrees of freedom at the substructure level. This process is known as static condensation (Bathe, 1982) because a part of the solution is in effect, performed prior to the assembling the

structural matrices. The extra calculation increases the computation and the stiffness matrix of the substructure which is usually not banded, may affect the mean bandwidth of the stiffness matrix. The sub-structuring was found to be most effective in 20 noded element model, where large number of degrees of freedom could be eliminated by combining adjacent elements into a substructure.

6.2 Biomechanical Verification

The peripheral neural signals received and used by the brain to infer the properties of the object in contact with the human fingertips are the trains of neural impulses generated by the population of mechanoreceptors. The mechanoreceptors transduce the stress-state in their respective neighborhoods to generate these neural impulses. It is, thus, essential to verify that the mechanistic behavior of the fingerpad is accurately modeled by the finite element model which is used to estimate the sub-surface stress-state. The three inputs required for an accurate mechanistic model are the geometry of the fingertip, the boundary conditions along with the loading on the fingertip, and the material properties of the constituents that make up the fingertip. The experiments described in Chapter 5 were designed to obtain an accurate representation of the geometry of the fingertip, which also affects the specification of the boundary conditions and the loading. The behavior of the fingertip materials has to be understood to reliably predict the stress-state using the finite element model. Following the black-box approach described in Chapter 3 and Figure 3-1, the material behavior can be modeled by studying the biomechanical input-output relationship of the fingerpad. Once the biomechanics is successfully modeled, the model can be used to simulate neurophysiological experiments.

6.2.1 Surface deformation under line load

Surface deformation of the monkey and human fingertips under known loadings is one such biomechanical input-output relationship that can be experimentally observed *in vivo*. Srinivasan (1989) indented human and monkey fingertips with a sharp wedge and obtained photographic images of the undeformed and deformed fingertips. The fingertips were glued to the table and the sharp wedge was indented *in vivo* to a prescribed depth into the fingerpad. The surface deformations were determined by comparing the undeformed and

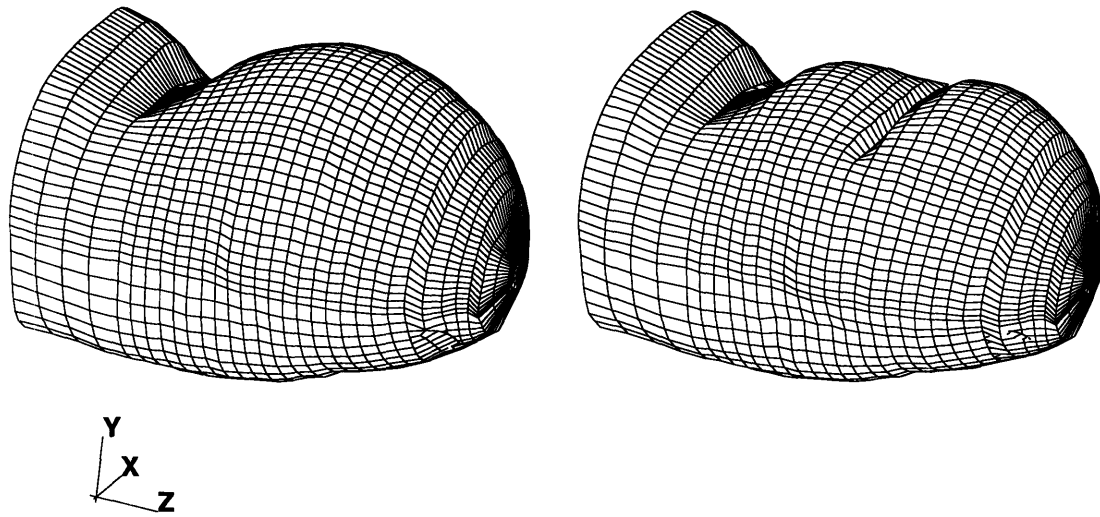


Figure 6-4: The model of a monkey fingertip is shown indented by a sharp wedge aligned perpendicular to the axis of the finger. The model was indented by a sharp wedge, which delivers a line load, to a depth of 2.0 mm in increments of 0.5 mm. The undeformed mesh is shown on the left and the deformed mesh when the depth of indentation was 2.0 mm is plotted on the right.

deformed profiles of the skin.

As described in Chapter 4, the two dimensional models failed to accurately predict the surface deformations under a line load and as shown in Figure 4-27, all the models predicted a characteristic “elastic” response characterized by extremely localized deformations. The 2D model was assumed to be in the ‘plane strain’ condition and, hence, any out of plane deformations were assumed to be zero. Modeling the cross-section as a plane-strain problem is equivalent to adding infinite stiffness in the axial direction. Could this modeling assumption affect the surface displacements predicted in the plane of the model? This question was addressed by simulating the same experiment on the 3D models.

Effect of geometry

Figure 6-4 shows the simulation of the same experiment using the finite element models. The undeformed monkey fingertip is shown on the left. In the experiments, the fingertip is fixed to the table by gluing the fingernail to the table, and that boundary condition is simulated by constraining all the degrees of freedom for all the nodes on the nail. The rigid backing provided by the table is simulated by suppressing the Y displacement for

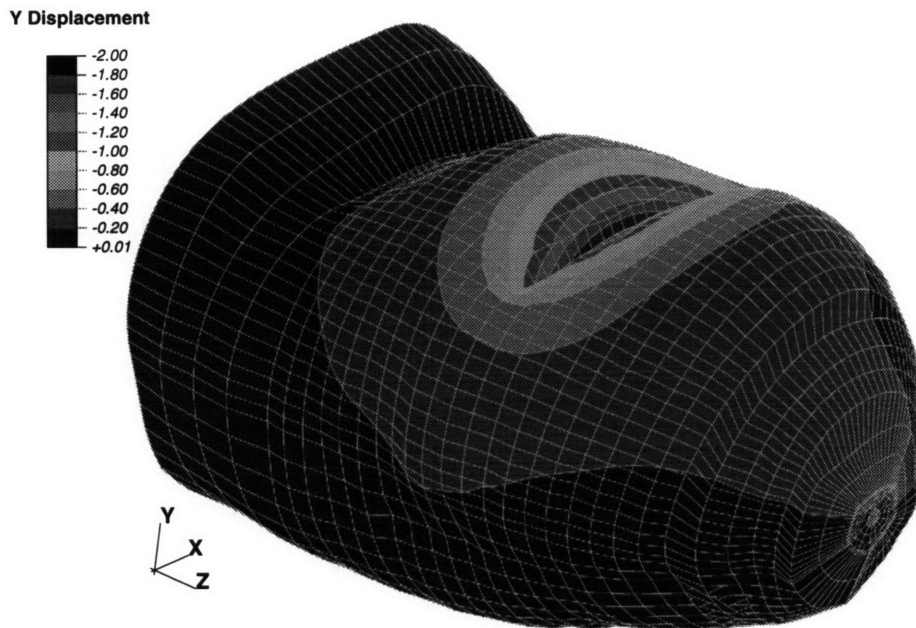


Figure 6-5: The contours of constant vertical displacement are plotted on the deformed monkey fingertip. The model is indented by a sharp wedge to a depth of 2.0 mm as in Figure 6-4.

the nodes on the dorsal surface of the fingertip model where the fingertip would touch the horizontal table. The fingertip is indented by a sharp wedge aligned perpendicular to the finger axis to a depth of 2.0 mm and the deformed mesh with the hidden lines removed is shown on the right in Figure 6-4. The indentation was carried out in steps of 0.5 mm. The wedge was generated in Matlab and displacement was prescribed on the nodes under the wedge to simulate the indentation. The finite element problem was solved using the large displacement formulation. The finite element solver Abaqus installed at the Pittsburgh Supercomputing Center Cray C-90 was used in the solution of the problems. The CPU time required in the solution of the problem was about 6 minutes.

The extent of the deformation can be estimated from the deformed mesh in Figure 6-4 and it can be seen that even at a depth of indentation of 2.0 mm the deformations rapidly decrease with distance from the line load. This fact is clearly illustrated in Figure 6-5 where contours of constant vertical displacement are shown overlaid on the deformed mesh, when the depth of indentation was 2.0 mm. The asymmetry in the spread of the deformations along the axis of the fingertip can be seen. This is to be expected since there is a marked difference in the boundary conditions at the proximal and the distal end of the

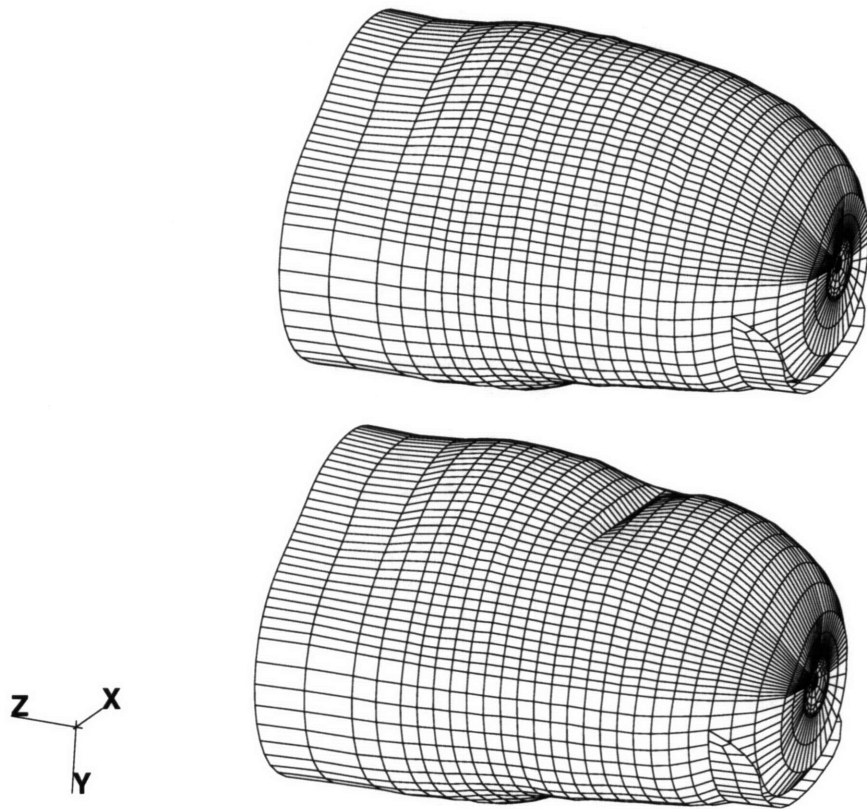


Figure 6-6: The model of a human fingertip is indented by a line load delivered through a sharp wedge aligned perpendicular to the finger axis. The top view shows the undeformed mesh and the bottom plot shows the deformed mesh, when a sharp wedge was indented into the fingertip to a depth of 2.0 mm.

distal phalanx, which affects the stiffness and hence the deformations in that region. The attrition in deformations is faster at the proximal end than the distal end, as can be seen by the contours of deformation. The local nature of the deformations can be understood from the contours shown in Figure 6-5. The entire dorsal half and the proximal end of the fingertip have less than 10% of the maximum deformations.

The same analysis was repeated on the human fingertip models and the deformed and undeformed meshes are shown in Figure 6-6. The contours of the vertical displacement are shown overlaid over the deformed human fingertip model in Figure 6-7. The material model for both the human and monkey fingertips models shown in Figures 6-4, 6-6, 6-5 and 6-7 is m43338 and the Poisson's ratio ν is 0.48. The explanation of the convention used in the material specification is deferred to the next section, where the effect of ma-

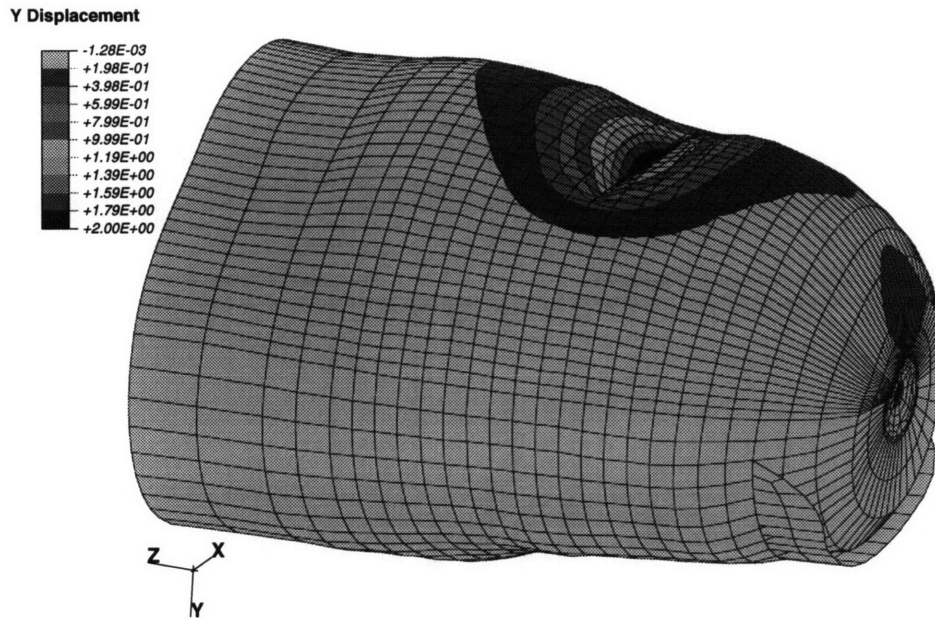


Figure 6-7: The contours of constant vertical displacement are plotted on the deformed human fingertip. The model is indented by sharp wedge to a depth of 2.0 mm as in Figure 6-6.

terial properties on the predicted surface deformations is discussed in detail. There is considerable difference in the dimensions of the monkey and human fingertips, the human fingertips being 16-20 mm in diameter whereas the monkey fingertips are typically 8-10 mm in diameter. There is also a difference in the curvature of the fingertips: it can be seen that the monkey fingertips are more ellipsoidal whereas the human fingertips are more cylindrical. In spite of the differences in the sizes of the fingertips, the overall shape and the internal structure of the primate fingertips is similar. The predicted vertical displacements are also similar to the displacements seen in the monkey fingertips. The local nature of the human fingertip deformations is seen from the contours of the vertical displacements shown in Figure 6-7.

Figure 6-8 shows the deformations predicted by the *homogeneous* 3D model of the monkey fingerpad. In this model, the bone was modeled as five orders of magnitude stiffer than the rest of the fingerpad and all the layers of the finite element model were assigned identical material properties. This model is, thus, the 3D counterpart of the 2D cylindrical model composed of homogeneous soft tissues with bone. In the figure, the distance from the line load is plotted on the X axis to logarithmic scale to emphasize the importance of

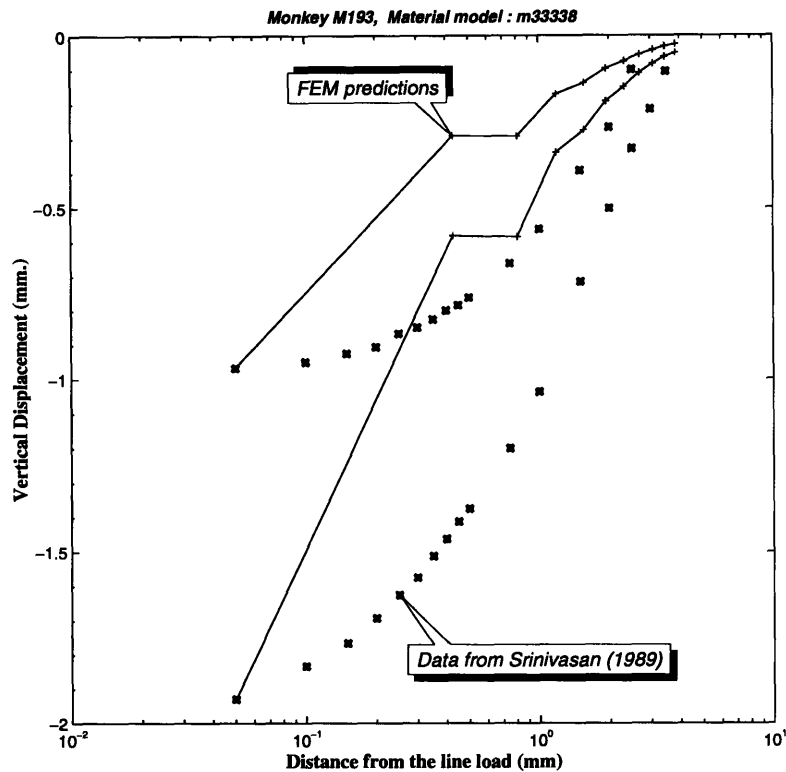


Figure 6-8: The surface deformations predicted by an homogeneous monkey fingertip model are compared with the experimentally observed deformation (Srinivasan, 1989). Vertical displacements are two depths of indentations viz., 1 mm and 2 mm are shown

the region close to the load over the region away from the load. It was shown in section 4.3, that loads more than about 3 mm distance from the point of interest do not significantly affect the stress-state at the point under consideration. At higher distances from the line load, the observed and predicted displacement are relatively close but improvement in accuracy is desired in the region close to the load. Similar deformations were observed in the homogeneous human fingertip model and are shown in Figure 6-9.

Figures 6-8 and 6-9 shows that, in spite of relaxing the plane strain assumption and calculating the displacements using the 3D model that is geometrically accurate, the predicted displacements do not match the experimentally observed displacements. Hence, it is certain that there is some biomechanical aspect of the primate fingertip which is responsible for the characteristic surface deformation observed under a line load, remains unmodeled in the 3D homogeneous model.

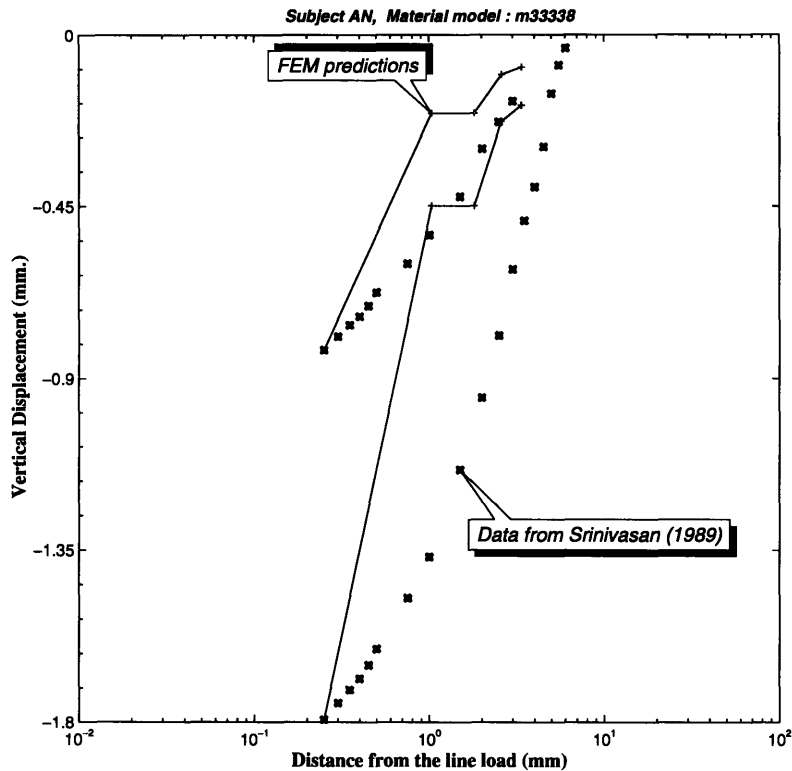


Figure 6-9: The surface deformations predicted by an homogeneous human fingertip model are compared with the experimentally observed deformation (Srinivasan, 1989). Vertical displacements are two depths of indentations viz., 1 mm and 2 mm are shown

Effect of multiple layers

Various layers of the skin and the differences in the mechanical properties of the constituents of the fingerpad are described in Chapter 2. Although, the exact mechanical properties of the layers of the skin are not known, there is general agreement about the relative strength and other mechanical properties of the constituents. Using the five layers of the finite element model, a parametric study was undertaken to study the effect of changing the stiffness of a particular layer on the overall surface deformation profile. The results of this study are summarized in Figure 6-10. In all the sub-plots, experimentally observed data for a monkey fingertip (Srinivasan, 1989) is used for comparison with the model predictions. The vertical displacements are plotted as a function of the distance from the line load. The material of all the elements in the finite element model was linear elastic and isotropic. Thus, only the Young's modulus and the Poisson's ratio are necessary and sufficient to completely describe the material behavior in the static problems. Models

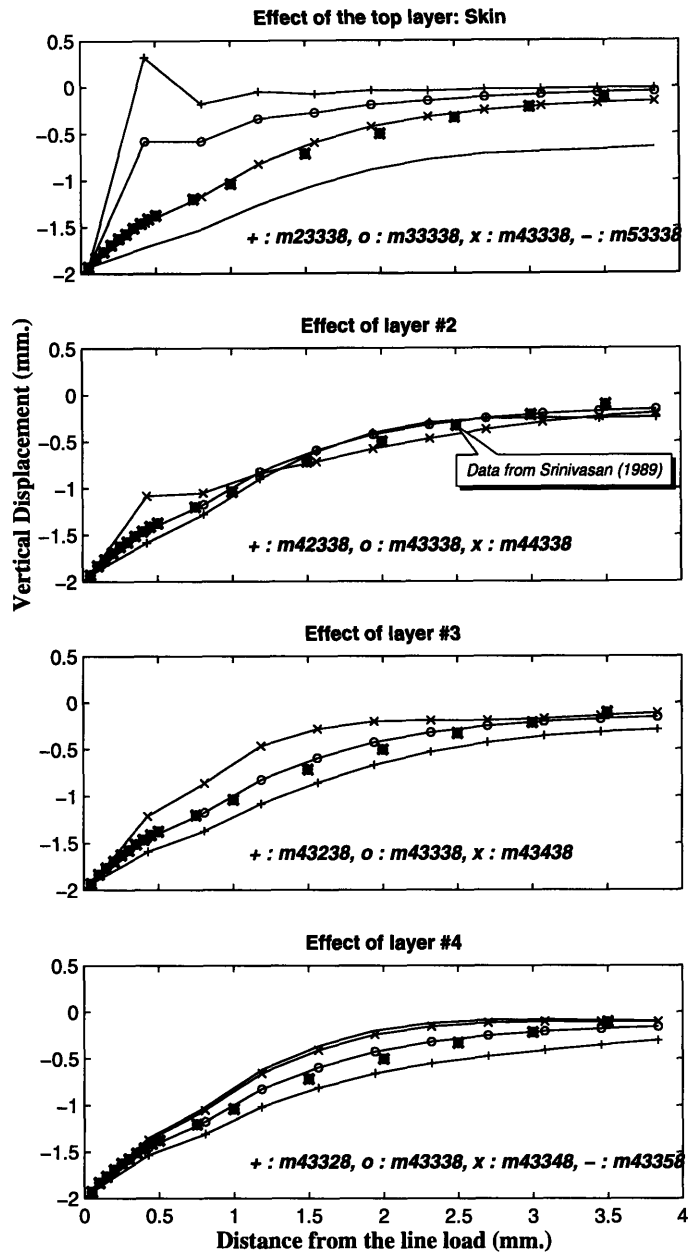


Figure 6-10: The effect of changing the stiffness of the various layers on the predicted surface deformation is studied. The stiffness of the bone was held constant at 10^8 Pa and stiffness of other layers was varied successively by a factor of 10. The predicted surface deformation is compared with the experimentally observed data for a monkey fingertip indented to a depth of 2.0 mm.

with different Young's moduli for each layer were analyzed under indentation by a sharp line load to a depth of 2.0 mm. The Poisson's ratio ν was assumed to be 0.48 in all the models. The Young's modulus of the layer corresponding to the bone is held constant at 10^8 Pa, which is at least 3 orders of magnitude higher than that for any other layer of the fingertip. The layers of the model are numbered radially inward and, therefore, outermost layer of the skin corresponds to layer #1 and the bone corresponds to layer #5. Layers #1 through #4 were assigned Young's moduli, in powers of 10 and, hence, it is possible to represent a model by collating the logarithms of the Young's moduli of all the layers. For example, a model designated by m43328 had the Young's moduli of 10^4 , 10^3 , 10^3 , 10^2 and 10^8 Pa for the layers of the model starting from the outer layer of skin and proceeding to the bone. The homogeneous model shown in Figure 6-8 is thus designated as m33338.

The top panel in Figure 6-10 shows the effect of changing the stiffness of the outermost layer, which corresponds to the epidermis. The trace corresponding to the model m33338 is identical to the uniform model described earlier in Figure 6-8 and shows a marked elastic valley near the line load. If the stiffness of the outermost layer is decreased (model m23338, symbol : +), the spatial extent of the deformation reduces and the deformation is more localized as compared to the homogeneous model, thereby, increasing the error between the observed and the predicted data. On the other hand, if the topmost layer is stiffened by increasing the Young's modulus of the layer (models m43338 and m53338), the predicted surface deformation approaches the observed deformations. The deformations predicted by these models have a larger spatial extent than the uniform model and the localized valley is not seen in both the profiles. From a stiffness standpoint, if we consider the surface deformation at a distance of 1.0 mm from the line load, we can observe that the predicted surface deformation reduces with reduction in the stiffness of the outer layer. Therefore, in the 4 models considered here, m23338 has the highest stiffness corresponding to the lowest overall deformation and m53338 has the lowest stiffness corresponding to the largest predicted deformation at all the points.

In the bottommost panel of Figure 6-10, the effect of changing the stiffness of layer #4, which circumscribes the bone is considered. The Young's modulus of the outer layer is held constant at 10^4 Pa and the Young's modulus of the bone is maintained at 10^8 Pa. At all distances away from the line load, as the Young's modulus of the layer is increased the predicted vertical displacement decreases. The horizontal location most affected by

the change in stiffness of this layer is at a point where the difference in the displacements predicted by the two models, with the extreme Young's moduli for the layer in question, is maximum. This location can be graphically determined by locating the point where the vertical distance between the two extreme traces is the maximum and is approximately around 2.0 mm away from the line load. The effect of changing the stiffness of layer #3 can be examined in the third sub-plot. As in the case of layer #4, an increase in the Young's modulus of layer #3 causes the increase in stiffness of the model at all points indicated by a decrease in the predicted vertical displacements. The horizontal location most affected by the changes is now around 1.3 mm from the line load as can be seen from the distance between the profiles corresponding to the models m43238 and m43438. The effect of increasing the stiffness of these two layers is exactly opposite to the effect observed for in case of the outermost layer. Increasing the Young's modulus of layer #3 or #4, increases the stiffness of the model, whereas, an increase in the Young's modulus of the outermost layer decreases the stiffness of the model. The behavior of layer #2 is intermediate between these two effects, which can be seen from the sub-plot for layer #2 in Figure 6-10. For all the points less than about 1.25 mm from the location of the line load, increasing the Young's modulus of layer #2 causes a decrease in stiffness of the model, similar to the behavior of the outermost layer. At all horizontal locations more than 1.25 mm away from the line load, increasing the Young's modulus of layer #2 causes an increase in the stiffness of the model, which is similar to the effect observed in case of layer #3 and #4. Interestingly, there exists a point at approximately 1.25 mm away from the line load, where the local stiffness is not affected by the changes in the Young's modulus of layer #2.

In summary, we can conclude that by changing the stiffness of the individual layers the overall stiffness of the model can be controlled. Depending on the depth of a layer from the surface, an increase in the Young's modulus of that layer may increase or decrease the stiffness of the model. There exists a point where the local stiffness is most affected by the changes in the Young's modulus of a particular layer. This point shifts away from the load as the depth of the layer being considered increases. This finding essentially provides us with a logical method of adjusting the model parameters to match the observed displacement data. Examining Figure 6-8, we can observe that the predicted displacements are lower than those experimentally observed and conclude that the finite element model is stiffer than the actual fingertip. Also, the errors in the model predictions and experimental

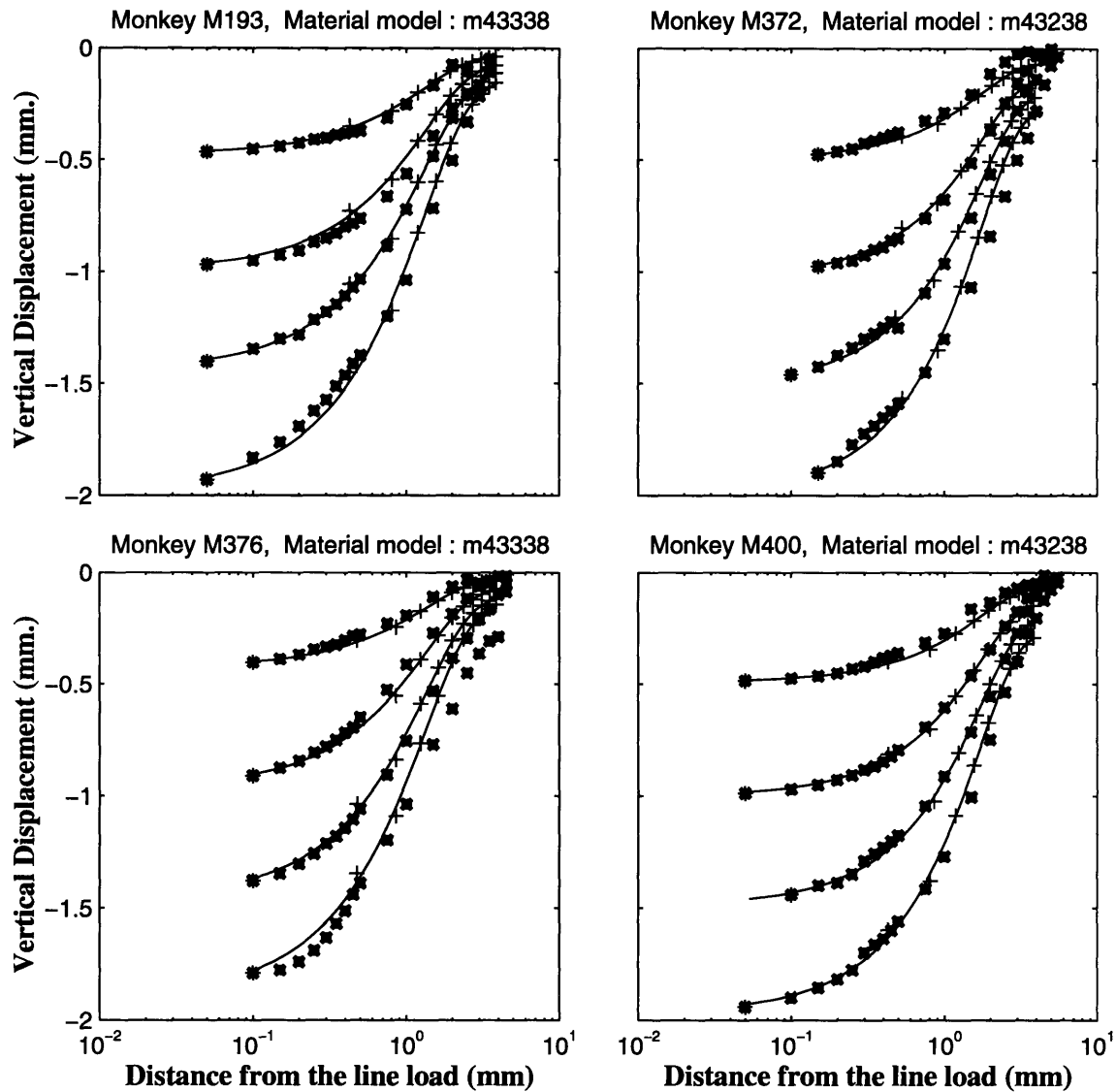


Figure 6-11: Comparison of the observed and predicted surface deformation data for four monkey fingertips. The experimentally observed data is from Srinivasan (1989) and the FEM predictions are shown by solid lines.

data are maximum at distances less than 1 mm from the line load. The parametric study revealed that the outermost layer has the maximum effect on the predicted displacements in the close vicinity of the load and an increase in the Young's modulus of the outermost layer decreases the stiffness of the model. Also from all panels in Figure 6-10 m43338 and m43238 show the most promise in accurately predicting the observed surface deformations. Therefore, the homogeneous model was modified by increasing the stiffness of the outermost layer to 10^4 Pa and the effect of layer #3 was analyzed in more detail.

The m43338 model was considered the datum in varying the material properties of the various layers in order to match the deformations predicted by the model with the experimentally observed deformations in monkey and human fingertips. For each human and monkey subject several material models were analyzed and the predicted surface deformations were compared with the observed deformation profiles. Matches and mismatches in the two along with the guidelines for changing the material parameters depending on the the region of the mismatch discussed earlier were used to successively modify the materials of the various layers. Figure 6-11 shows the comparison of the predicted surface deformation with the experimentally observed data for the best material model for each monkey units. The data shown in the figure by thick × marks was obtained from four different monkey fingertips and each of the fingertip was indented to a depth of 2.0 mm in steps of 0.5 mm (Srinivasan, 1989). For each monkey fingertip, the material model used in the finite element models is listed on the top of the plot and the finite element predictions are shown by the solid line. The excellent match between the observed and predicted data is clearly seen. In all the cases, the stiffness of the outermost layer was higher than the inner layers. In case of monkey M372 and M400, the best match was obtained with the middle layer being more compliant than layers #2 and #4. A three layer model consisting of a stiff outer layer, a complaint medium and a rigid bone is adequate to accurately predict the surface deformations under a line load. Because of the biological variability, individual differences are to be expected between subjects and between different fingertips of the same subject. There is evidence (Tregear, 1966) to suggest that the epidermis is stronger than the dermis in its mechanistic behavior. In the three layered model, the effects of the skin are lumped in the stiff outer layer, the adipose tissue and the ground substance are modeled as the middle layer, and the bone is modeled as the innermost layer which is several orders of magnitude stiffer than the rest of the fingertip and, hence, can be treated as rigid. Although the material properties were varied between the model, the geometry of all the models was identical. From the excellent matches with the experimental data in Figure 6-11, it can be concluded that the geometry of the fingertip does not play a dominant role in governing the displacements on the surface of the skin. Although, we have not accounted for the variability in the geometry of the various monkey fingertips, a single finite element model with different material properties was able to successfully predict the surface deformations.

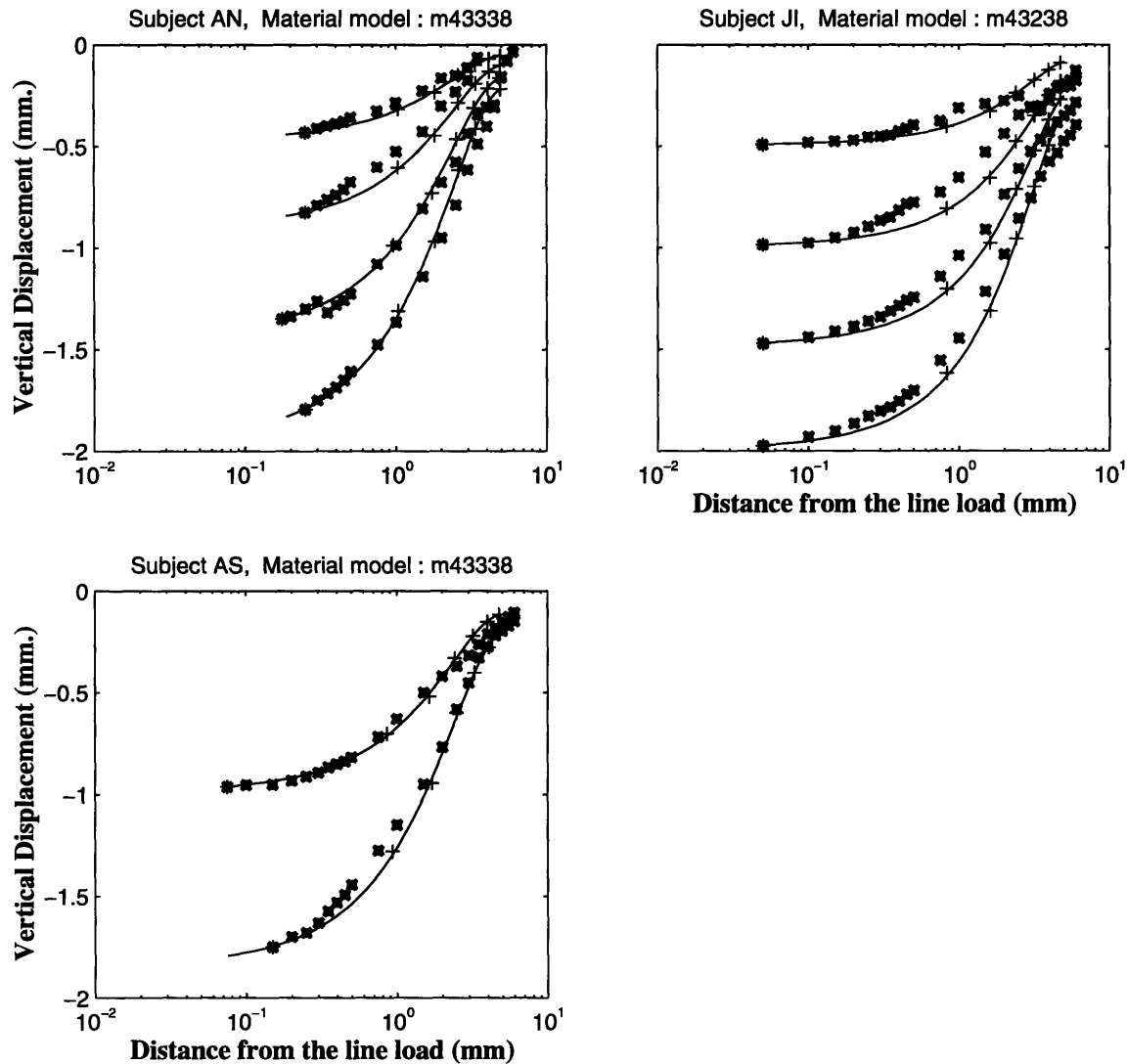
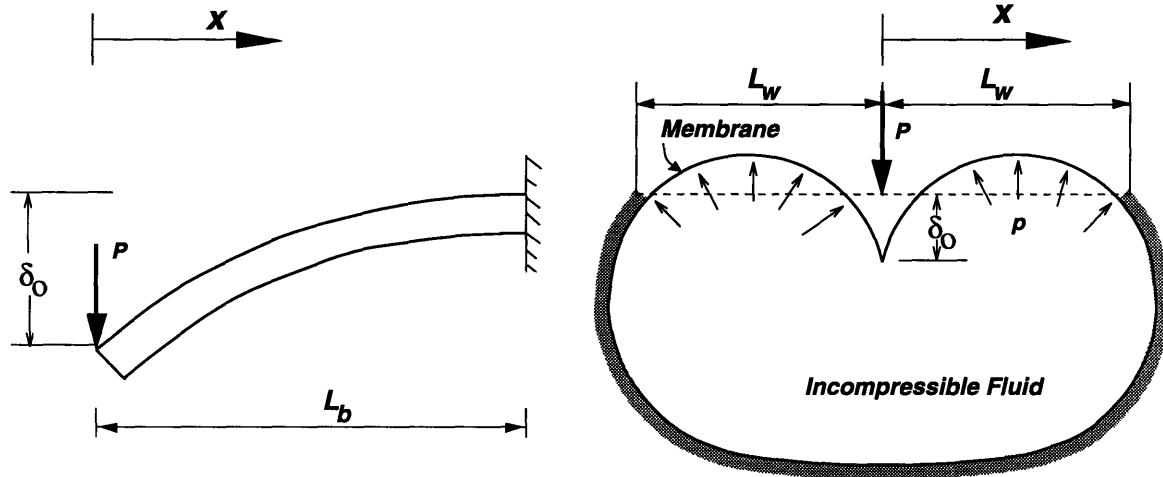


Figure 6-12: Comparison of the observed and predicted surface deformation data for three human subjects. The experimental data is obtained by indenting the fingertips of subjects *in vivo* in steps of 0.5 mm (Srinivasan, 1989). The finite element predictions are shown as solid lines.

A three layered model m43338 was developed for human fingertip geometry as well and used to predict the deformations under a line load for the human fingertips. The comparison of the experimentally observed and predicted deformations is shown in Figure 6-12. Data for 3 subjects at various depth of indentation (Srinivasan, 1989) is shown by thick \times marks and the finite element predictions are shown by solid lines. The finite element model predicts the surface deformations under the line load very well. As in the case of monkey fingertips, a three layered model is adequate to predict the surface defor-



The "Beam" Model

The "Waterbed" Model

$$\delta_b(x) = \delta_o \left[\frac{1}{2} \left(\frac{x}{L_b} \right)^3 - \frac{3}{2} \left(\frac{x}{L_b} \right) + 1 \right] \quad \delta_w(x) = \delta_o \left[3 \left(\frac{x}{L_w} \right)^2 - 4 \left(\frac{x}{L_w} \right) + 1 \right]$$

Figure 6-13: The solution of the waterbed model (Srinivasan, 1989) and the deflection predicted by a simple cantilever beam is compared.

mations of the human fingertips under a line load. Interestingly, as in the case of monkey fingertips, even though the human data is from three different subjects a single finite element model was used to predict the surface deformations. There is no free parameter in the model and no curve fitting was performed before plotting the data in Figures 6-11 and 6-12. The excellent agreement between the observed and predicted data confirms that the use of the accurate *material model* is of primary importance in predicting the surface deformation under a line load for monkey and human fingertips and the geometrical differences between the individual subjects have a secondary effect on the observed surface deformations.

The beam model

One question of considerable interest is then, the reason why the waterbed model (Srinivasan, 1989) predicted the surface deformations accurately. It is possible that two different models can predict an input-output relationship correctly, and, further experiments might become necessary to show which model is better. The uncertainty associated with the

non-unique representation of the input-output relationship can be resolved if one of the models can be shown to be a special case or a subset of the other model. This can be attempted by identifying the similarities and differences in the two models.

The waterbed model is schematically shown in Figure 6-13. In this 2D idealization, the fingertip is modeled as incompressible fluid enclosed by a membrane of infinitesimal thickness. The vertical deflection $\delta_w(x)$ at any horizontal location is given by the equation shown in figure (Srinivasan, 1989). The semi-width of the membrane L_w is a free parameter in the model.

$$\delta_w(x) = \delta_o \left[3\left(\frac{x}{L_w}\right)^2 - 4\left(\frac{x}{L_w}\right) + 1 \right] \quad (6.1)$$

The finite element model that best matches the experimentally observed surface deformations had a stiff outer layer covering the compliant inner layer. This can be idealized by a simple beam where the stiffness of the outer layer is approximated by the stiffness of the beam and the stiffnesses of the inner layers are neglected. When the fingertip is indented by a sharp wedge, owing to the symmetry in the geometry and the loading, we can model one half of the fingertip indented by a line load as a cantilever beam indented by a load at its free end as shown in Figure 6-13. The solution of this fundamental problem is usually sought when the load is prescribed. With the origin at the fixed end and the X axis pointing towards the free end of the beam L units long, the displacement $\delta(x)$ at any point x units away from the fixed end can be written as

$$\delta = \frac{P}{6EI} [3x^2L - x^3]$$

where, P is the point load on the beam and EI is the flexural rigidity. This solution can be re-written with the X axis as shown in Figure 6-13 and with a displacement δ_o prescribed at the free end. The deflection δ_b at any point x units from the free end for a beam L_b units long can be written as follows.

$$\delta_b(x) = \delta_o \left[\frac{1}{2}\left(\frac{x}{L_b}\right)^3 - \frac{3}{2}\left(\frac{x}{L_b}\right) + 1 \right] \quad (6.2)$$

The suffix 'b' on the δ indicates the displacement predicted by the "beam model" in which the length of the beam L_b is a free parameter in this model. A comparison of Equa-

tion 6.1 and Equation 6.2 reveals the similarity between the two expressions. In both the equations, the vertical displacement at any point is expressed in terms of the displacement under the line load and each term on the right hand side of the equation is normalized with respect to the characteristic length of the model and is, hence, dimensionless. Both the expressions on the right hand side are polynomials in x , have the same constant term, and the signs of the coefficients of the first order term are identical. In the region of interest x is always less than L_b or L_w and, hence, $\frac{x}{L_w}$ and $\frac{x}{L_b}$ are always less than 1. Neglecting higher order terms, to examine the relationship between the free variables of the two models, we can equate the expressions for the displacement, when $\delta_b = \delta_w = 0$. Thus,

$$-\frac{3}{2}\left(\frac{x}{L_b}\right) = -4\left(\frac{x}{L_w}\right)$$

Simplifying,

$$L_w = \frac{8}{3}L_b$$

In the waterbed model, the solution in the region where $0 < x < \frac{L}{3}$ was used to predict the surface displacements of the fingertip. The waterbed solution predicted bulging of the skin for $\frac{L}{3} < x < L$, whereas, no bulging was experimentally observed. Comparison of Equations 6.1 and 6.2 indicates that if $L_w = \frac{8}{3}L_b$, then neglecting higher order terms the displacements predicted by both the models will be very similar. Conversely, the beam solution in the region near the line load for the waterbed model where $0 < x < \frac{3}{8}L_w$ will be identical to the waterbed solution. Since, $\frac{3}{8}$ is approximately equal to $\frac{1}{3}$, both the beam and waterbed analytical solutions predict similar surface displacement profiles in the region of interest, which is near the line load.

The predictions of the beam model and the 3D finite element model m43338 are compared with the experimentally observed data and the predictions of the waterbed model in Figure 6-14. The experimentally observed data (Srinivasan, 1989) is shown as thick \times marks for monkey and human fingertips indented to a depth of 1.0 mm. The best fits were obtained by varying the free variables (the lengths L_w and L_b) in each of the beam and waterbed models and the values of these variables used are shown in each panel of the figure. It can be seen that the beam model also predicted the vertical deflections very well. Depending on the subject and the depth of indentation, the goodness of fit of the beam model was better than the goodness of fit for the waterbed model and can be seen in the

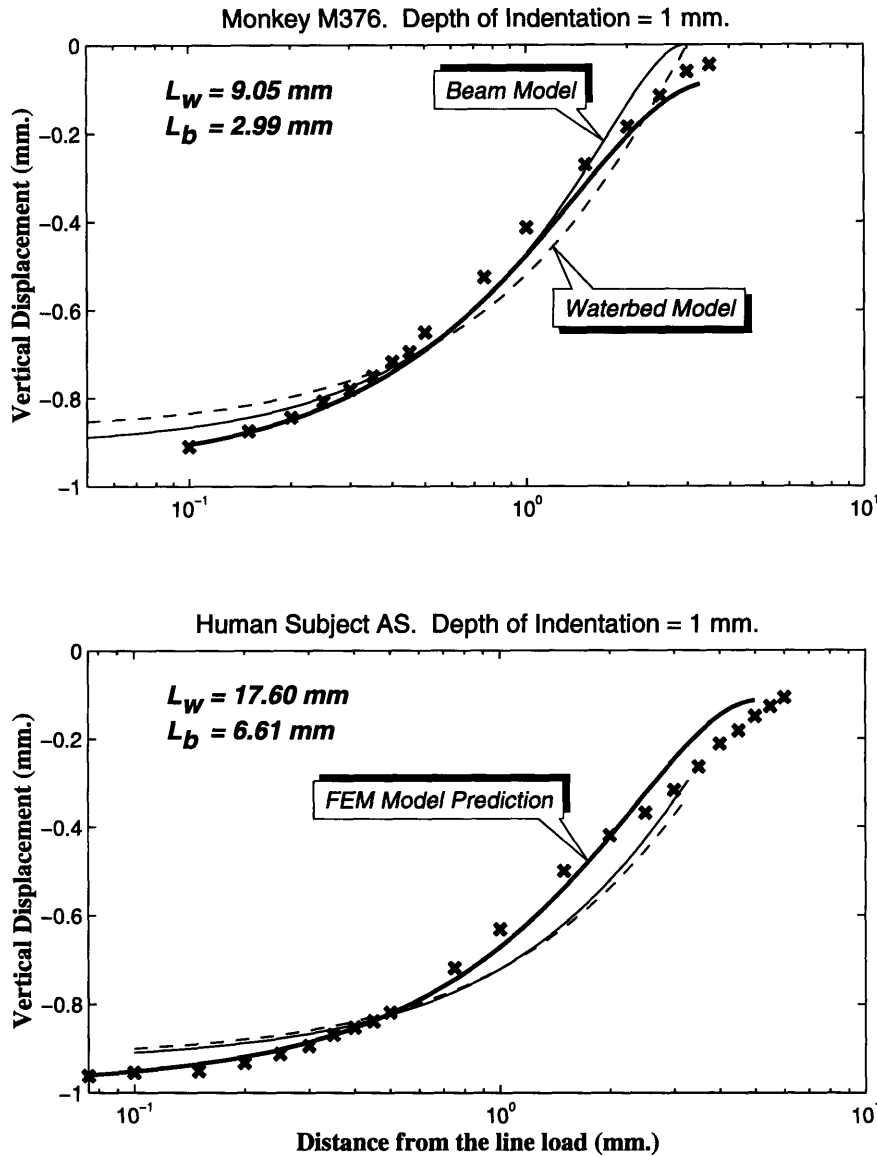


Figure 6-14: The surface deformation of the monkey fingertip predicted by the beam model are compared with the predictions of the waterbed model in the top panel. Experimentally observed data (Srinivasan, 1989) is shown as thick 'x' marks, whereas the predictions of finite element model m43338 are shown by a thick line. The lengths L_w and L_b used in obtaining these fits are listed. The predictions of both these models along with the vertical displacement predicted by the FEM model m43338 for human fingertip is shown in the bottom panel.

top panel comparison of the two models for the monkey fingertip. In the bottom panel, in addition to these two idealized model, the finite element model predictions using model m43338 are shown in a solid line. In this case, the finite element model predicts the vertical displacements better than both the idealized models.

We have, therefore, identified the significant factor in the waterbed model that was responsible for the excellent predictions of the surface displacements. It is the difference in the stiffness of the various layers that is responsible for the characteristic observed surface deformation profile. The difference in the stiffness could either be modeled by considering a membrane enclosing incompressible fluid or by modeling the fingertip as a cantilever beam. The relative stiffness of the layers of the fingerpad is reliably represented in the finite element model presented here. It should also be noted that both the beam and waterbed analytical solutions have serious limitations. As explained in section 2.2.1, the waterbed model fails to predict the spatial variation in the stress state at all sub-surface locations and cannot account for inhomogeneities like presence of bone and other solid tissues inside the fingertip. The beam model implies increase in stress and strain values at locations farther from the load. Both these idealizations are solutions for a single point load and lose their simplicity for real life loadings involving non-linear changes in the magnitude and contact area of the loading imposed. The finite element models for the monkey and human fingertips proposed here do not have any of the above limitations. These 3D models are based on actual fingertip geometry, can be refined as and when more data about the internal structure becomes available and can be used to simulate any physically realizable loading on the fingertip.

The stiffness of the layers of the model are expressed as ratios of their Young's moduli. For finite element problems with prescribed displacement the strains are independent of the Young's modulus in a homogeneous medium. If the Young's moduli of individual layers are expressed in terms of the Young's modulus of one layer, the strains in the model will depend only on the ratios of the Young's moduli of the constituent materials. The actual values of the Young's moduli can be determined if the force-displacement relationships of the fingerpads under a variety of indentors are known.

6.2.2 Surface deformation of human fingertips under cylindrical indentors

Human fingertips were indented by a variety of cylindrical and rectangular indentors as described in section 5.2 and images of undeformed and deformed fingertips were acquired using a videomicroscopy setup. The borders of the undeformed and deformed fingertip were extracted from the acquired images as explained in section 5.2.3. By comparing the deformed and undeformed profiles of the fingertip, the vertical displacements were calculated. Epoxy replicas of the same fingertip used in the experiment was made and a 3D finite element model was constructed by acquiring images of the replica in various orientations as described in section 5.1. This finite element model was used to simulate the indentation experiments performed on the fingertips.

The comparison of the *in vivo* indentation of the human fingertip and simulation of the same experiment using the 3D finite element model is shown in Figure 6-15. On the left side the the experimentally acquired images of the human fingertip when indented by cylindrical indenter C5 (diameter 9.52 mm) are shown. The undeformed fingertip is shown on the top and the fingertip indented to a depth of 2.0 mm is shown in the bottom panel. On the right side corresponding images from the finite element simulation are shown. The material model m43338 was used in the finite element model. The inclined support available to the fingertip in the experiment was modeled by suppressing the appropriate nodal degrees of freedom for the corresponding nodes.

Figure 6-16 shows the meshes of the undeformed and deformed fingertip under indentation by a cylindrical indenter aligned perpendicular to the axis of the finger. In the both the panels, the indenter is clipped to show the mesh on the glabrous skin below the indenter. In the actual finite element solution, the indenter was 20% longer than the largest width of the fingertip. The fingernail was fixed to the base by suppressing all the degrees of freedom of the nodes on the fingernail. As in the experiments, the indenter was gradually indented into the fingerpad model in steps of 0.5 mm to a depth of 3.0 mm. In this 'contact problem' the extent of the area of contact between the fingertip and the indenter and the magnitude of loads imposed on the fingertip is not known *a priori*. The associated finite element problem was solved using the Abaqus solver installed on the Pittsburgh Supercomputer Center C-90. The iterative solution required approximately 30 cpu minutes for indentation to a depth of 3.0 mm. In the right panel, in Figure 6-17 the deformations under the indenter are clearly seen. To emphasize the spatial extent of the

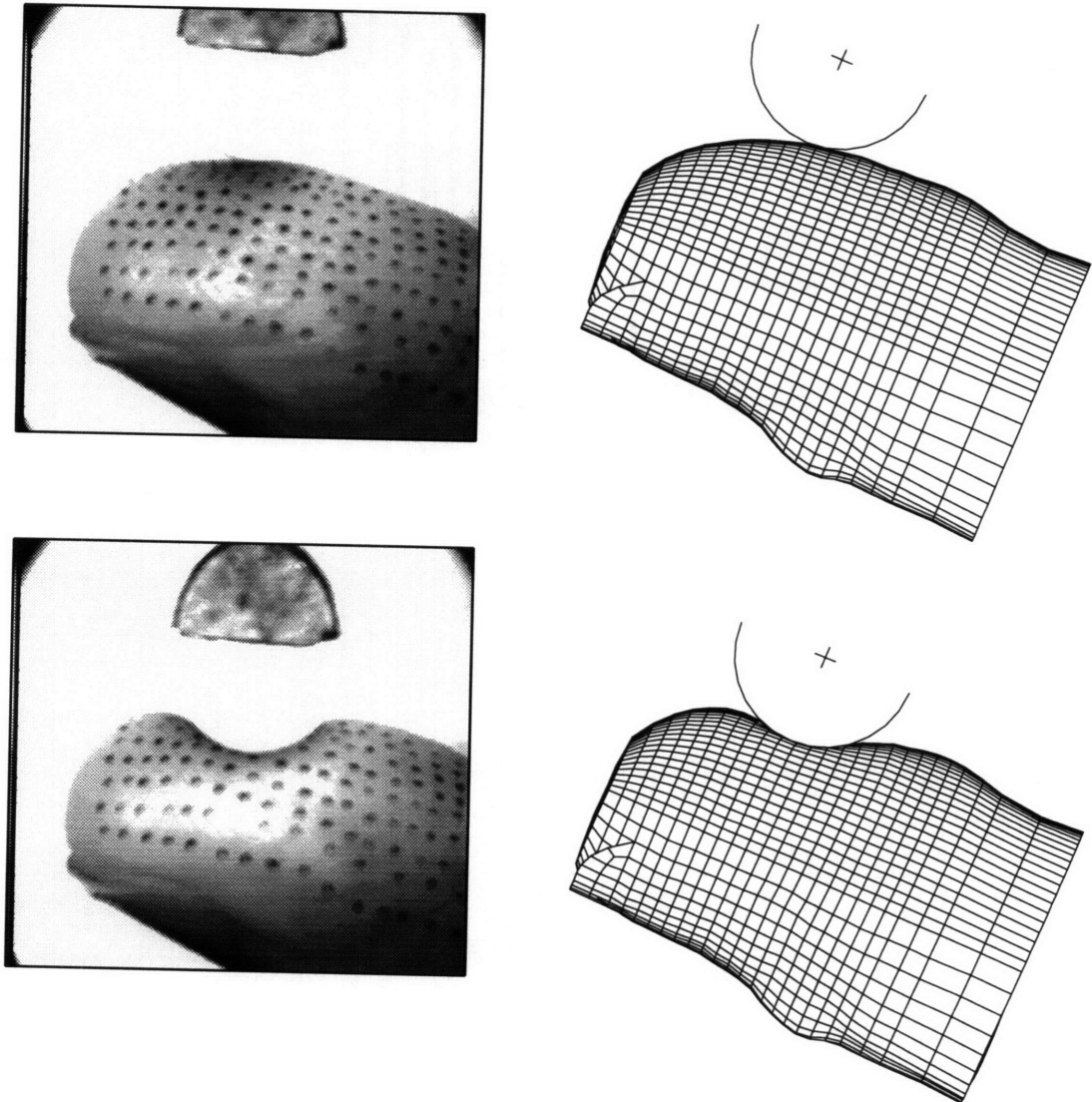


Figure 6-15: The experimentally observed images of the undeformed and deformed human fingertip are shown on the left. On the right is the FEM simulation of the experiment. Cylindrical indenter C5 (diameter 9.52 mm) is placed perpendicular to the axis of the finger and indented to a depth of 2.0 mm into the fingertip.

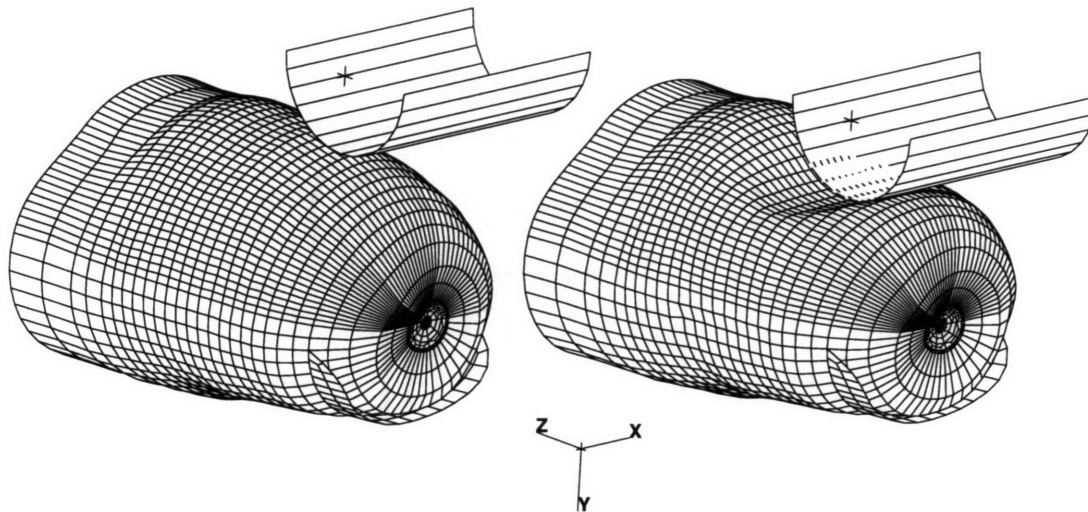


Figure 6-16: The undeformed and deformed meshes of the human fingertip under indentation by a cylindrical indenter are shown. Cylindrical indenter C5 (diameter 9.52 mm) is placed perpendicular to the axis of the finger. The part of the indenter in the positive X plane is not shown to illustrate the deformation under the indenter as seen in the right panel.

deformations, contours of constant vertical displacement are shown over the deformed mesh in Figure 6-17. As seen earlier in Figure 6-7 for a line load, the deformations are localized and the entire dorsal half and the proximal end of the fingertip have less than 10% of the maximum vertical displacement.

The border of the finite element model was extracted from the side view. By calculating the vertical displacements of the nodes corresponding to this border, the deformed and undeformed profiles of the fingertip model generated. Figure 6-18 shows the comparison between the experimentally observed deformations and the deformations predicted by the finite element model. Results for the cylindrical indenter C5, which was 9.52 mm in diameter, are shown for indentations in steps of 0.5 mm upto a depth of 3.0 mm. The experimentally observed profile is shown un-filtered by a solid line and the finite element predictions are shown by plus marks. True scale is maintained on the plots so that the actual shape of the deformed fingertip can be visualized. It can be seen that the finite element model predicts the surface deformations very well (Dandekar and Srinivasan, 1995e). The spacing of the points available in the finite element data is governed by the size of the elements on the surface of the fingertip. Finer resolution can be obtained by using a model with finer mesh. Use of the 20 noded element model will also effectively

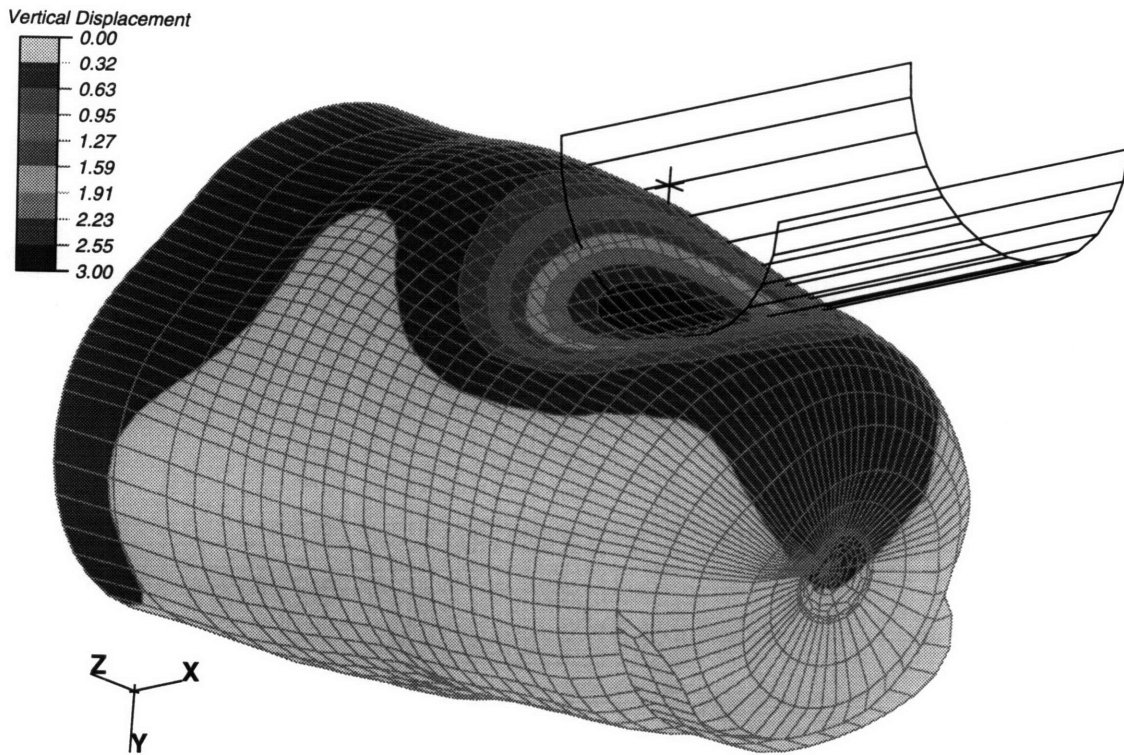


Figure 6-17: The deformed meshes of the human fingertip under indentation by a cylindrical indenter are shown. Cylindrical indenter C5 (diameter 9.52 mm) is placed perpendicular to the axis of the finger. The contours of constant vertical displacements are shown over the deformed fingertip.

double the sampling points available on the surface. At higher depths, there is a small disagreement between the experimental and model data on one side of the indenter. This may be due to an experimental error in maintaining the indentation path. It should be noted that, the experimental data is not filtered and the finite element data is not processed in any way and no fitting was performed before plotting the data.

A closer examination of the experimentally observed displacements and the model predictions can be performed if the displacements are plotted to a enlarged scale as shown in Figure 6-19. Displacements of the same fingertip as in Figure 6-18 and indenter C5 are shown for the depths of 2.5 and 3.0 mm. The scale on the Y axis is enlarged to facilitate a finer comparison of the observed and predicted data. The excellent agreement between the two is clearly apparent from the figure.

Comparison of the experimentally observed and predicted surface displacements for

Cylindrical Indentor C5 (diameter 9.52 mm)

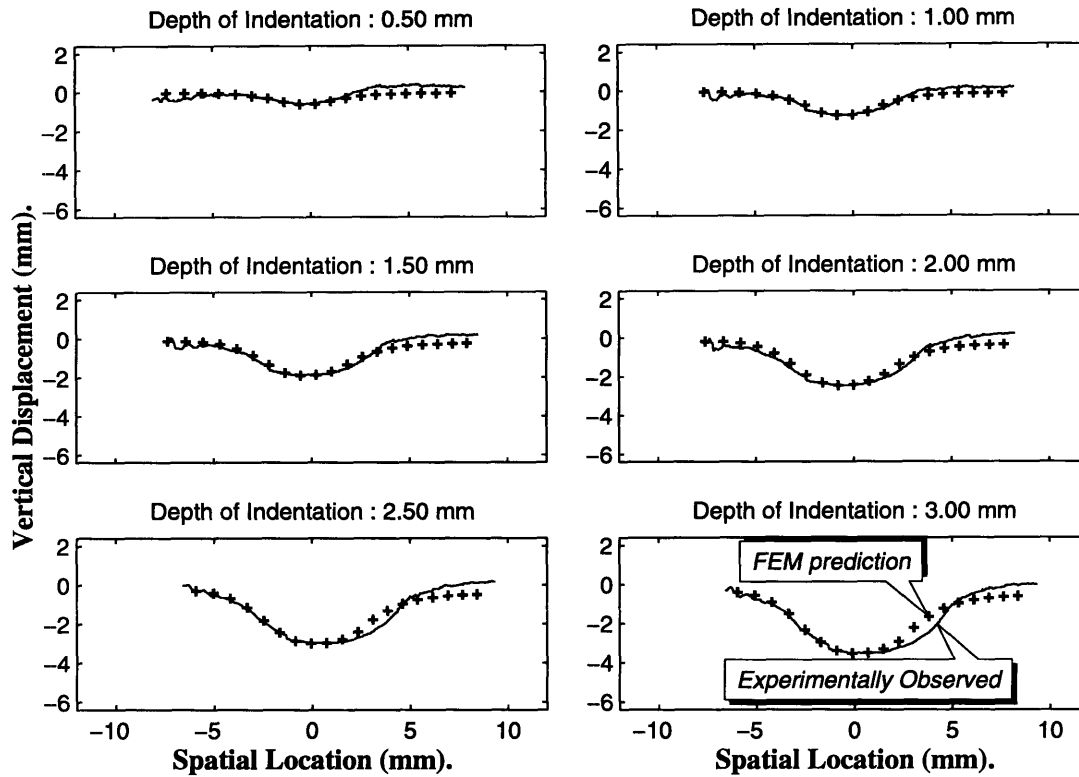


Figure 6-18: The human fingertip model is used to predict the deformations observed under the indentation of the human fingertip by cylindrical indentor. The experimentally observed displacements are shown in solid lines and model predictions are shown with + markers for depths of indentation upto 3.0 mm in steps of 0.5 mm.

the cylindrical indentor C2 with a diameter of 3.17 mm is shown in Figure 6-20. The observed displacement shown by a solid line and is not filtered or processed in any way. This indentor is considerably smaller in diameter as compared with indentor C5 and the agreement between the experimental and observed data continues to be excellent (Dandekar and Srinivasan, 1995c). The displacements for the depths of 1.0 mm and 3.0 mm are shown magnified in Figure 6-21. Thus, the finite element model m43338 is successful in predicting surface deformations under cylindrical indentors as well as line loads (section 6.2.1). As compared to the idealized solutions proposed for predicting surface deformations earlier (i.e., waterbed and beam model described in section 6.2.1), there are no free parameters and no need for fitting the data to the observed displacements.

Natural differences between fingertips of different individuals might affect the match

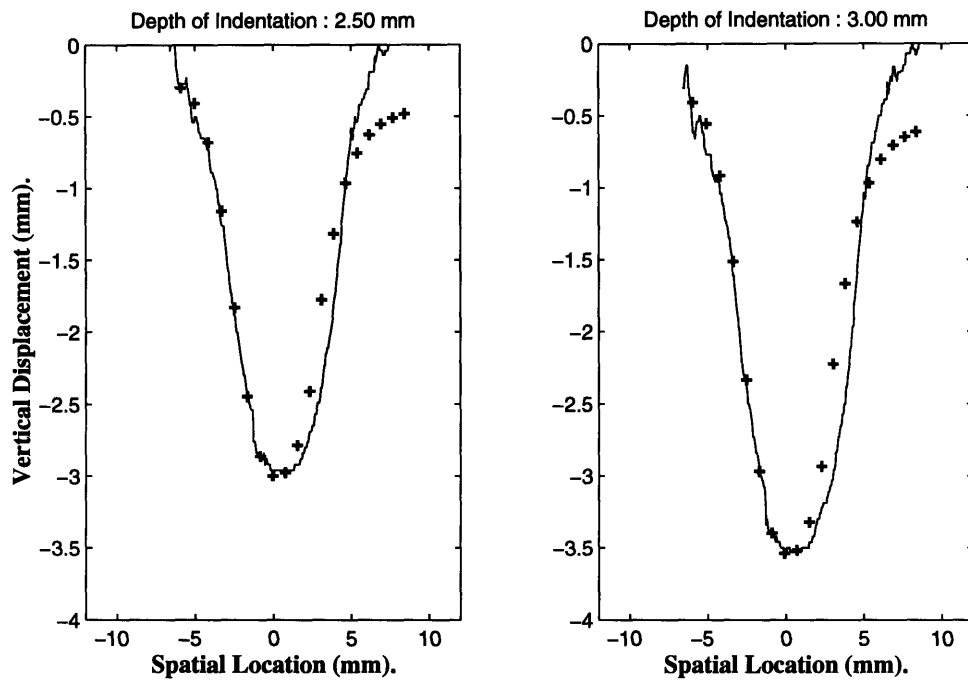


Figure 6-19: The human fingertip model is used to predict the deformations observed under indentation of the human fingertip by indenter cylindrical indenter C5 (diameter 9.52 mm). The experimentally observed displacements are shown in solid lines and model predictions are shown with + marks for depths of indentation of 2.5 and 3.0 mm. In contrast with Figure 6-18, scale on the vertical axis is enlarged to closely observe the displacements.

between the observed and predicted data. A parametric study of the effect of changing the stiffness of a layer on the predicted surface displacements (as described in section 6.2.1) can be used to further refine a specific model if the application requires better accuracy in the predicted displacement response.

6.2.3 Force displacement relationships for human fingertips

To study the force displacement relationship of the fingerpad as a whole, human fingertips was indented by various indentors and the force required for indentation measured at each depth of indentation. The fingertips were supported and restrained using a fixture to prevent involuntary motions. The fingernail was glued to the rigid support and the volar surface of the fingertips was indented by various shaped indentors mounted on a tactile stimulator. The fingertips were pseudo-statically indented by a point, circular and a flat plate indentors the force required for the indentation was measured using a force sensor

Cylindrical Indentor C2, (diameter 3.17 mm)

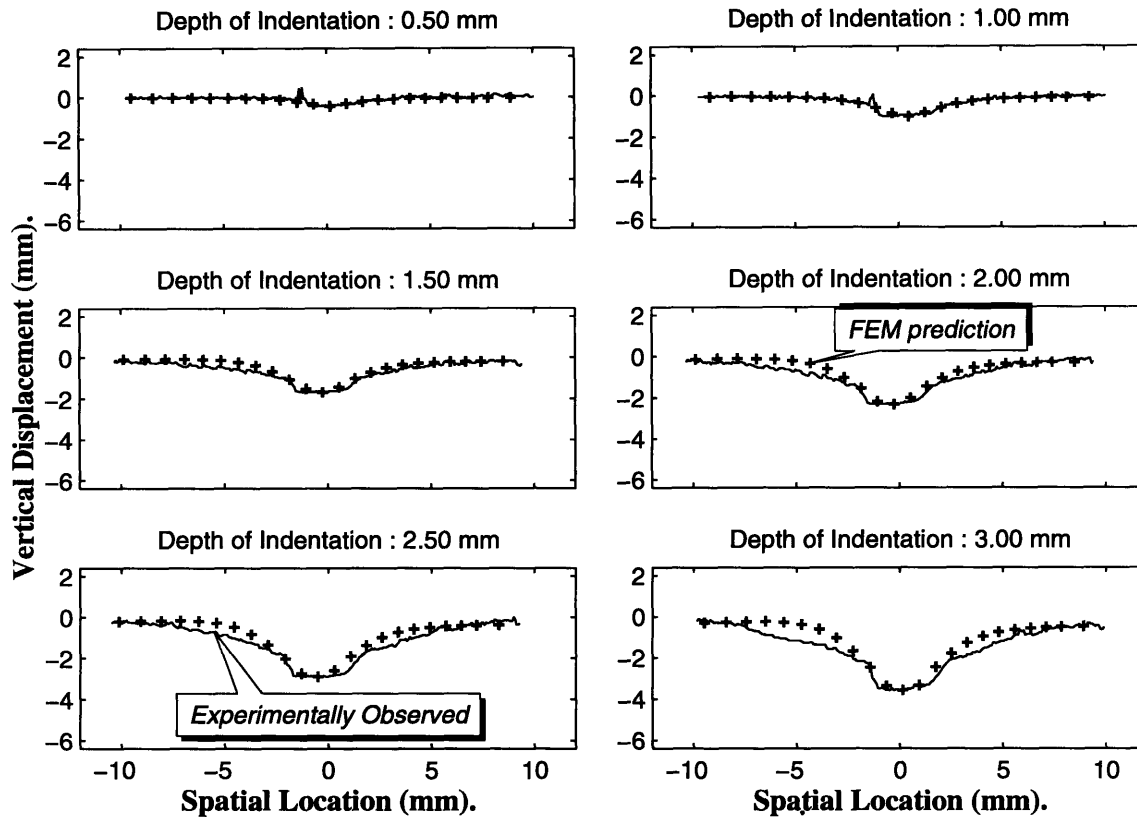


Figure 6-20: The human fingertip model is used to predict the deformations observed under indentation of the human fingertip by cylindrical indentor C2 (diameter 3.17 mm). The experimentally observed displacements are shown in solid lines and model predictions are shown with + marks for depths of indentation upto 3.0 mm in steps of 0.5 mm.

mounted on the tactile stimulator (Gulati, 1995; Gulati and Srinivasan, 1995). A non-linear relationship between the depth of indentation and the force of indentation was observed for all the indentors. The force required for a given displacement was dependent on the indentor used and varied from subject to subject.

The 3D finite element model of the human fingertip (m43338) used to simulate these indentation experiments is shown in Figure 6-22. In the experiment, the conical indentor was used to simulate point load and was machined out of a cylinder of radius 3.175 mm. The height of the conical part of the indentor was 2.4 mm. The cylindrical flat indentor was also 3.175 mm in radius and the flat plate was 20 mm × 20 mm in size. The same dimensions were used in defining the indentors used in the finite element simulations

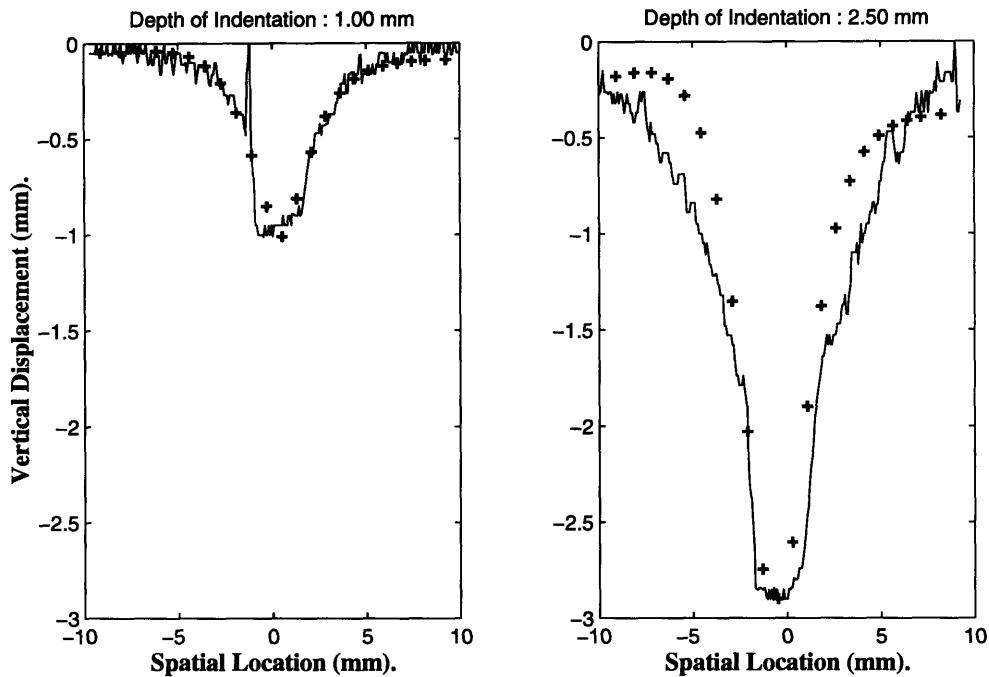


Figure 6-21: The human fingertip model is used to predict the deformations observed under indentation of the human fingertip by cylindrical indenter C2 (diameter 3.17 mm). The experimentally observed displacements are shown in solid lines and model predictions are shown with + marks for depths of indentation of 1.0 and 2.5 mm. In contrast with Figure 6-18, scale on the vertical axis is enlarged to closely observe the displacements.

and are shown in Figure 6-22. In the experiments, to ensure that the indenter indents the portion of the fingertip most frequently used in exploration tasks, the fingertips were inclined with the axis of the indenter. Identical orientation was used for the indentation in the finite element simulations and appropriate boundary conditions were prescribed to simulate the rigid support provided by the inclined surface. The indentors were indented in steps of 0.25 mm into the finite element model and the resulting contact problem was solved at each step. The force required for the indentation was measured and Figure 6-23 shows the variation in the force of indentation with the depth of indentation for four different subjects.

For each subject the experimentally observed data is shown by dashed lines for all the indentors. The finite element predictions are shown by solid lines. The forces predicted by the finite element models are scaled such that the experimentally observed force and the force predicted by the finite element simulation at the maximum indentation by the flat plate indenter (2.0 mm) are the same. In the experimental and simulation data, the data

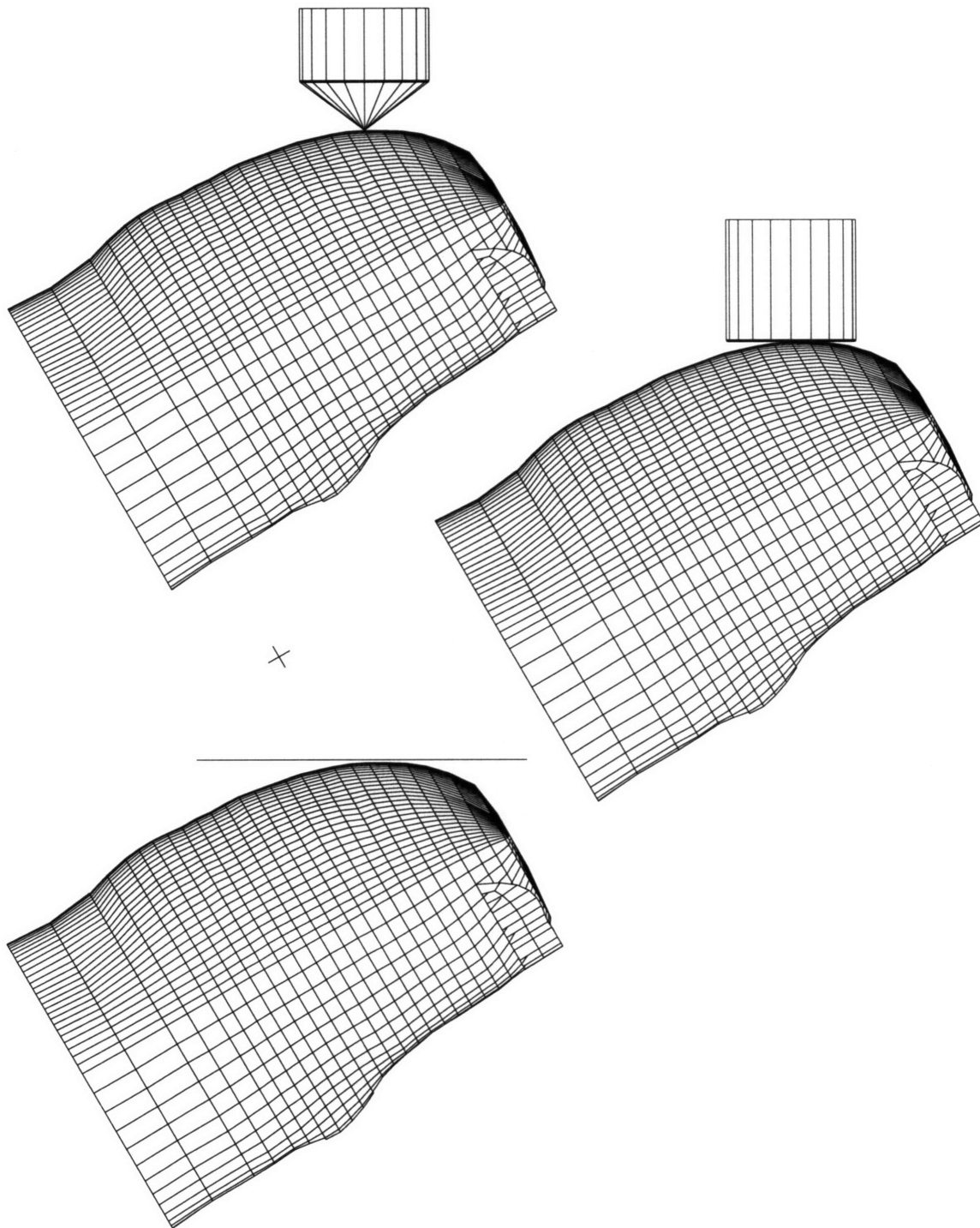


Figure 6-22: The indentors used in the study of force-displacement relationship of the human fingertip are shown. The conical indenter simulated the sharp point, the flat circular indenter has a diameter of 6.35 mm and the flat plate (20 mm × 20 mm) was much larger than the fingerpad.

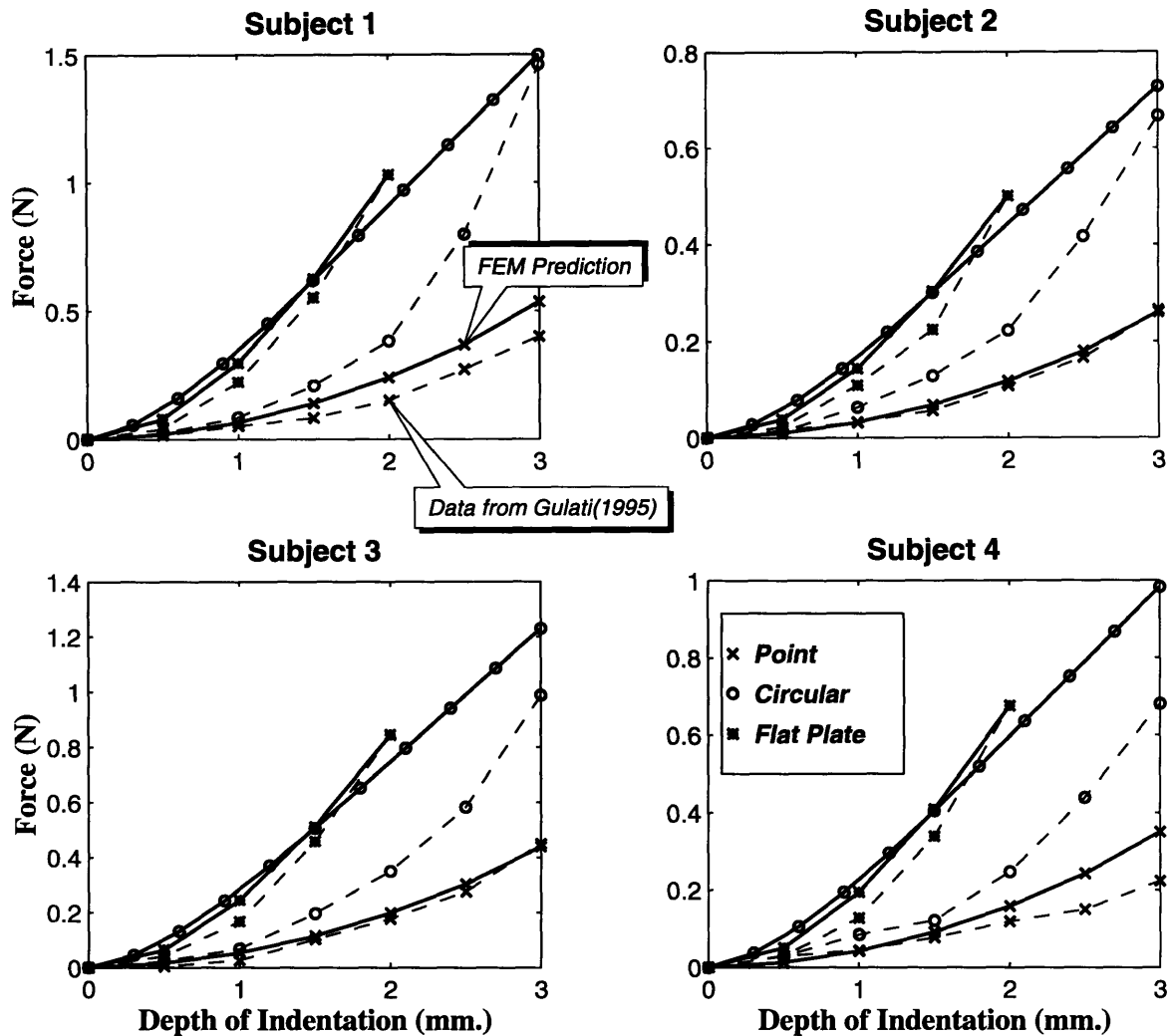


Figure 6-23: The multi-layered 3D model of the human fingertip (m43338) was indented incrementally by several indentors and the force required for the indentation is plotted against the depth of indentation for four subjects. The forces predicted by the model were scaled such that the force at 2 mm indentation by the flat plate was identical in the experimental data and the model predictions.

points are joined by straight lines. It can be seen that the finite element model predicts a non-linear relationship for point and flat plate indentors. The model predictions and experimentally recorded forces agree very well for the point and flat plate indenter for subjects 2 and 3. But for the all the subjects the force profile corresponding to the circular indentors is non-linear upto a depth of about 1.3 mm and linear thereafter.

The non-linearity in the experimentally observed force-displacement relationship could be because of a variety of reasons. As the indenter is indented into the fingertip, the area

of contact and the magnitude of loads imposed varies non-linearly with the depth of indentation. It can be recalled that in a classical contact problem of a sphere pressed on a flat plate, the area of contact is proportional to the square root of the depth of indentation (Johnson, 1985). Secondly, the material of the skin and the fingertip can be inherently non-linear in its constitutive behavior. The finite element models used in the simulations have a linear material model and thus will not be able to simulate the non-linearity due to the material behavior. It can be seen that, the contribution of the non-linear change in contact area and loads to the overall force-displacement response is modeled by the finite element models. However, once the indenter is fully in contact with the fingertip (as in the case of circular flat indenter) the response of the model to any further indentation is linear. There is no change in the area over which loads are imposed after full contact is established and the increase in the magnitude of loads is linear with respect to the depth of indentation because of the linear material model.

The linear model can successfully predict the overall non-linear force displacement relationships of the human fingertips if the effect of non-linear strain-displacement relationship does not dominate the overall non-linearity in the response. It should also be noted that, one finite element model was used to predict the force profile obtained from different subjects. The external geometry was, therefore, not accurately modeled in the simulations. In predicting the surface deformations, a single model was able to accurately predict the deformations observed in different subjects (section 6.2.1). In predicting the force profiles, however, the role of variations in geometry of the fingertips in the overall force-displacement profiles needs to be investigated by simulating the experiment on the finite element models of the actual fingertips used in the experiment. If the simulations with the actual fingertip models do not accurately predict the force profiles, further improvement in the ability of the models to accurately predict the non-linear force displacement relationship can be achieved by modeling the material of the layers of the finite element models as non-linear.

6.3 Neurophysiological Verification

As the models of the fingertip are refined, attempt should be made to retain all the desirable qualities of the earlier model in the refined version. Increase in the complexity of the

models can be justified only if the new model is better than the earlier model in predicting the system response. Ideally, the new models should be a superset of the earlier models retaining all the desirable properties of the previous models. Comparing the 3D models with the 2D models, we notice that the geometry of the fingertips is accurately modeled in the 3D models. As shown in Figures 6-11 and 6-12, the 3D multi-layered models predict the observed surface deformations very well and much better than the 2D models. The 2D models, however, predicted the experimentally observed neurophysiological spatial response profiles very well as discussed in Chapter 4. It is thus necessary to check the ability of the 3D models to predict the neurophysiological response and compare it with the 2D models. In all the following sections the multi-layered model is used for the finite element simulations. The effect of the stiff outer layer on the spatial variation of subsurface strain measures is discussed in section 7.1.2 and the influence of the change of the model geometry from 2D to 3D on the subsurface strains is discussed in section 7.1.1.

6.3.1 Indentation by rectangular bars

Figure 6-24 shows the undeformed and deformed meshes of the monkey fingertip model indented by a 1.5 mm wide rectangular bar aligned parallel to the axis of the finger and indented to a depth of 1.0 mm in the fingertip. The undeformed mesh is shown on the top and the deformed mesh without the indenter is shown on the bottom. In the hidden line removal, the post-processor (Abaqus-Post) was not able to correctly render the fingernail because of the curvature singularities due to an out of plane membrane. This is why the fingernail appears broken and some of the elements appear to be missing from the tip of the fingernail in both the undeformed and deformed mesh plots. The nail was glued to the table in the neurophysiological experiments and that was simulated by suppressing all the degrees of freedoms of all the nodes on the fingernail.

Using the three dimensional model, the response of the receptor population can be estimated from the stress-state at various receptor locations. The magnitude of strain energy density at depths of 0.75 mm and 1.0 mm from the skin surface is shown in Figure 6-25. Each of the profiles shown by a continuous line was calculated at a constant z location, which represents the receptors in an axial cross-section of the model. It can be seen that the profiles of strain energy density at different z locations are not identical.

The curvature of the fingertip in the X and Z direction is clearly seen in the undeformed

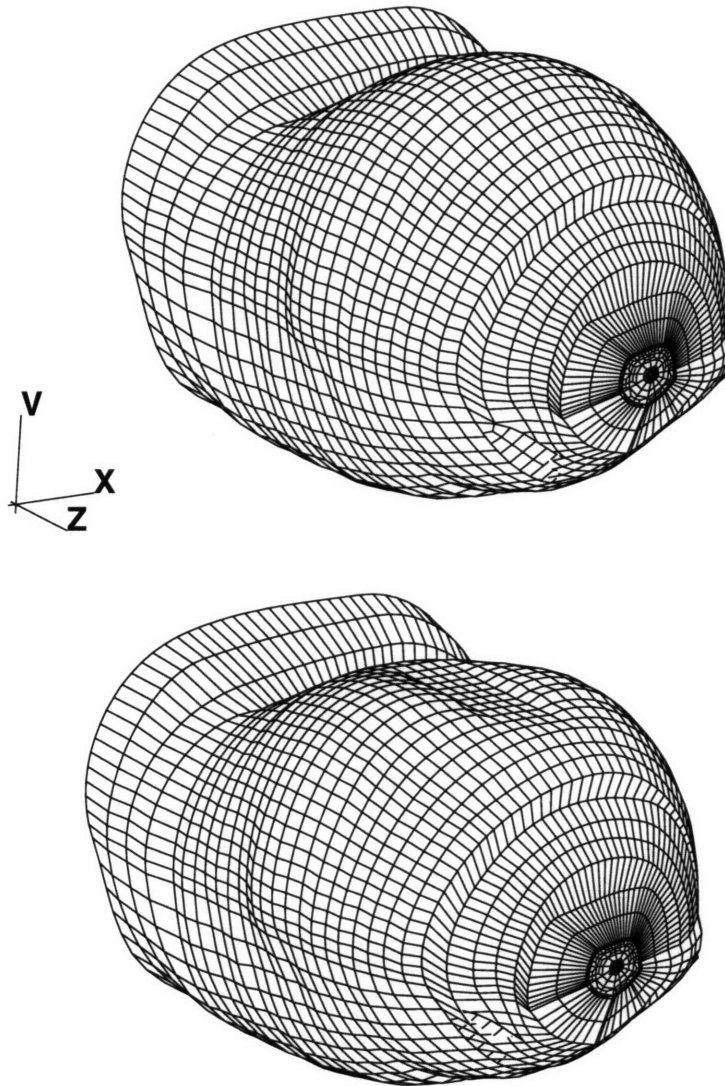


Figure 6-24: The monkey fingerpad model (m43338) is indented by a 1.5 mm wide rectangular bar. The axis of the bar is parallel to the axis of the finger and is indented into the fingertip to a depth of 1.0 mm. The undeformed and deformed meshes are shown in the top and bottom panel respectively.

mesh shown in Figure 6-24. The point on the skin that first contacts the indenter will be indented to a depth of 1.0 mm. Because of the curvature of the fingertip, all other points which are under the indenter in the deformed mesh shown in Figure 6-24, are indented by less than the maximum indentation (1.0 mm in this case). From analytical solutions to loads imposed on the elastic half space discussed in section 2.2.1 (Timoshenko and Goodier, 1982), it is known that the influence of a load on the stress-state at a point is

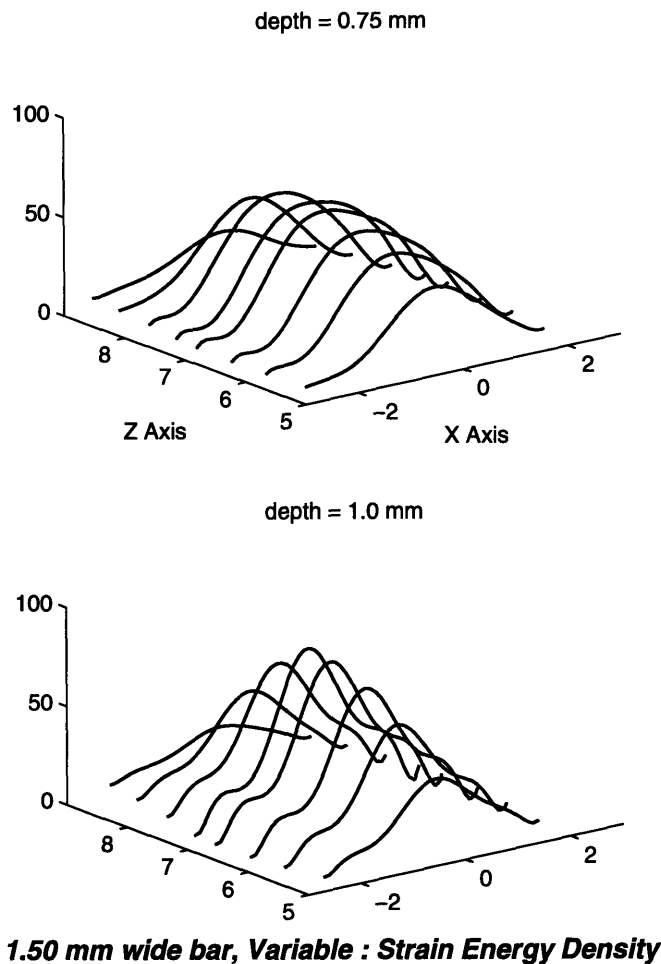


Figure 6-25: The spatial variation of strain energy density for a 1.5 mm bar indenting the monkey fingertip (as shown in Figure 6-24). The magnitude of strain energy density at depths of 0.75 mm (top panel) and 1.0 mm (bottom panel) from the skin surface are shown.

inversely proportional to the distance between the point of application of the load and the point where the stress-state is evaluated. The dominance of any load applied on the surface on the strain energy density at a sub-surface location is, therefore, inversely proportional to the distance between the point and the load. The strain energy density profiles at the two depths reflect the magnitude of loads imposed by the rectangular bar on the surface of the fingertip skin.

In the 2D models, characteristic low-pass filtering of the stress-state, by the elastic medium resulted in a population response that decreased in magnitude and lost high spatial frequency components. The material model in the 2D models was homogeneous, but a multi-layered model was used in the 3D models. What is seen in Figure 6-25 is the

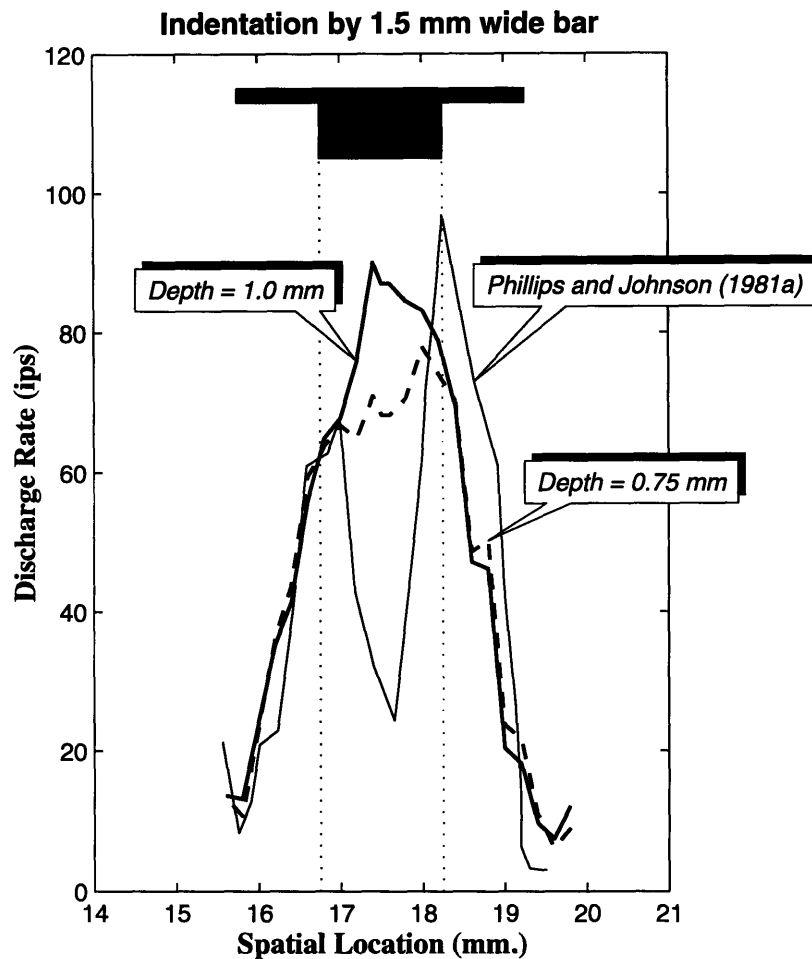


Figure 6-26: The spatial response profile predicted by the 3D model for indentation by 1.5 mm wide bar is shown. Data from Phillips and Johnson (1981a) is shown in by the thin line. Strain energy density at 0.75 mm and 1.0 mm depth is scaled and is shown in the dashed line and the solid line respectively.

“beam-like” effect in the variation of strains with depth. It can be recalled that strains in the classical beam solution are proportional to the distance of the point from the neutral axis. In this case, as the depth increases from 0.75 to 1.0 mm the distance from the neutral axis increases, resulting in higher magnitudes of strains at a depth of 1.0 mm. The magnitude of the strains at the receptor locations can be significantly higher in the multi-layered model than an uniform model. Various neurophysiological implications of the multi-layered model are discussed in section 7.1.2 in Chapter 7.

Phillips and Johnson (1981a) indented the monkey fingertip with a several rectangular bars and used the response of a single peripheral afferent fiber to construct the spatial

response profile. The experimentally observed spatial response profile is shown by a thin line in Figure 6-26. The same experiment was simulated using the 3D monkey fingertip model (m43338) and the corresponding spatial profiles of strain energy density at 0.75 mm and 1.0 mm depth in the skin are shown by dashed and solid lines respectively in Figure 6-26. A linear relationship is assumed between the strain energy density and the discharge rate given by Equation 4.1. It can be seen that the finite element model cannot predict the neural data very well. In particular, the decrease in the discharge rate near the center of the bar cannot be reliably simulated. It should be noted that the element size on the surface of the model is about 500 μm square to limit the problem size and other factors discussed in section 6.1. Thus for a 1.5 mm wide bar, the resolution of load specification on the surface is 0.5 mm or one-third the width of the bar. To predict a reliable spatial response, the element size on the surface will have to be refined to accurately define the loading on the model.

If the model is limited by the mesh resolution on the surface of the skin, the spatial response profile should improve for wider bars. Figure 6-27 shows a similar comparison for a 3.0 mm wide bar. As in Figure 6-26 the neural data is recorded from a SA-I afferent fiber with the rectangular bar moved laterally by 0.2 mm between successive indentations. The spatial response profile predicted for the 3.0 mm bar shows the reduction in the strain energy density near the center of the bar as observed in the experiment. Comparing Figure 6-26 and 6-27, we can conclude that the fine spatial features of a given spatial response profile can be predicted by the model if the resolution for specification of the loads on the surface is increased.

In Chapter 4, various strain measures at the receptor location were compared with the corresponding neural data and it was concluded that maximum compressive strain and strain energy density are the candidates most likely to be the relevant stimuli to the SA-I receptors (section 4.5.3). Maximum compressive strain and strain energy density at 1.0 mm depth are compared with the experimentally recorded neural response in Figure 6-28. The data points in the neural data and the finite element predictions are joined by straight lines. The neural data (Phillips and Johnson, 1981a) is shown by the thin line and maximum compressive strain and strain energy density are shown in a dashed and solid line respectively. A linear relationship was assumed between the strain measures and the neural discharge as given in Equation 4.1. It can be seen that both maximum compressive

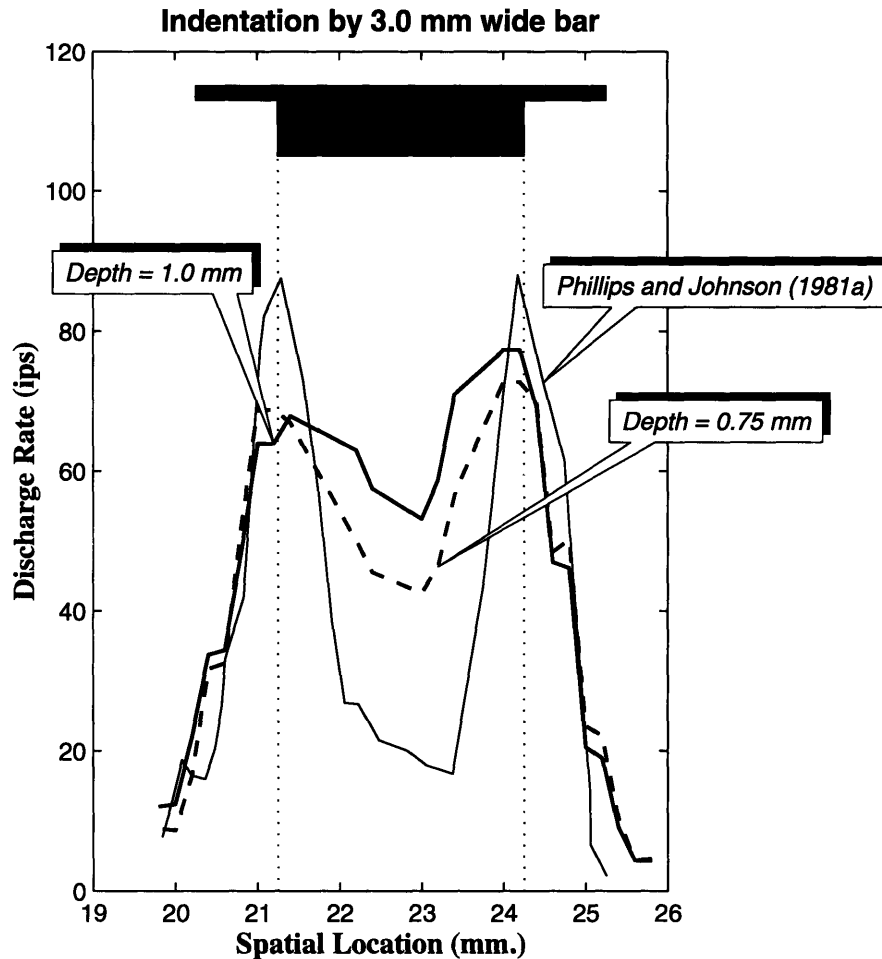


Figure 6-27: The spatial response profile predicted by the 3D model for indentation by 3 mm wide bar is shown. Data from Phillips and Johnson (1981a) is shown in by the thin line. Strain energy density at 0.75 mm and 1.0 mm depth is scaled and is shown in the dashed line and the solid line respectively.

strain and strain energy density predict the peak and valleys in the response at the correct spatial location although the magnitudes are exactly predicted. The strain energy density is slightly better in predicting the sharp slopes at the end of the bars, whereas, the reduction in the magnitude of the maximum compressive strain does not follow the neural response. It should be noted that, a finer element size will certainly improve the spatial details in the predicted strain measures and will improve the fit between the predicted and the experimentally observed neural data. With the given model, maximum compressive strain and strain energy density continue to closely predict the neural discharge experimentally observed under similar mechanical stimuli on the monkey fingertip.

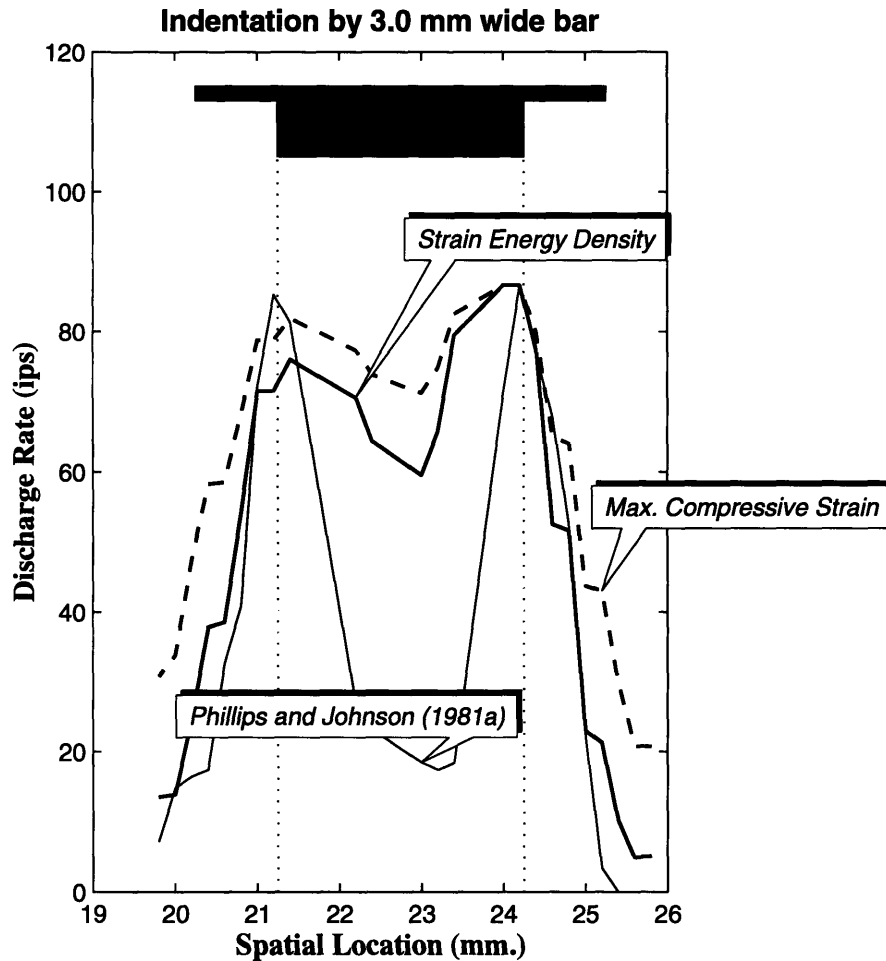


Figure 6-28: The spatial response profiles predicted by the maximum compressive strain and strain energy density at 1.0 mm depth in the 3D model for indentation by 3 mm wide bar are shown. Data from Phillips and Johnson (Phillips and Johnson, 1981a) is shown in by the thin line. Strain energy density and maximum compressive strain are shown in solid and dashed line respectively.

6.3.2 Indentation by cylinders

In the neurophysiological experiment by Srinivasan and LaMotte (Srinivasan and LaMotte, 1991), the monkey fingertips were indented by cylinders of varying curvature and the response of SA-I afferent fibers was recorded. The recorded response was found to be related to the skin curvature and hence, the sensitivity of the SA-I afferents to curvature of the object in contact was established. To eliminate any intensive cues, all the indentors were indented into the fingertip until a prescribed force was imposed on the fingertip. This experiment was simulated on the monkey fingertip model and the finite element

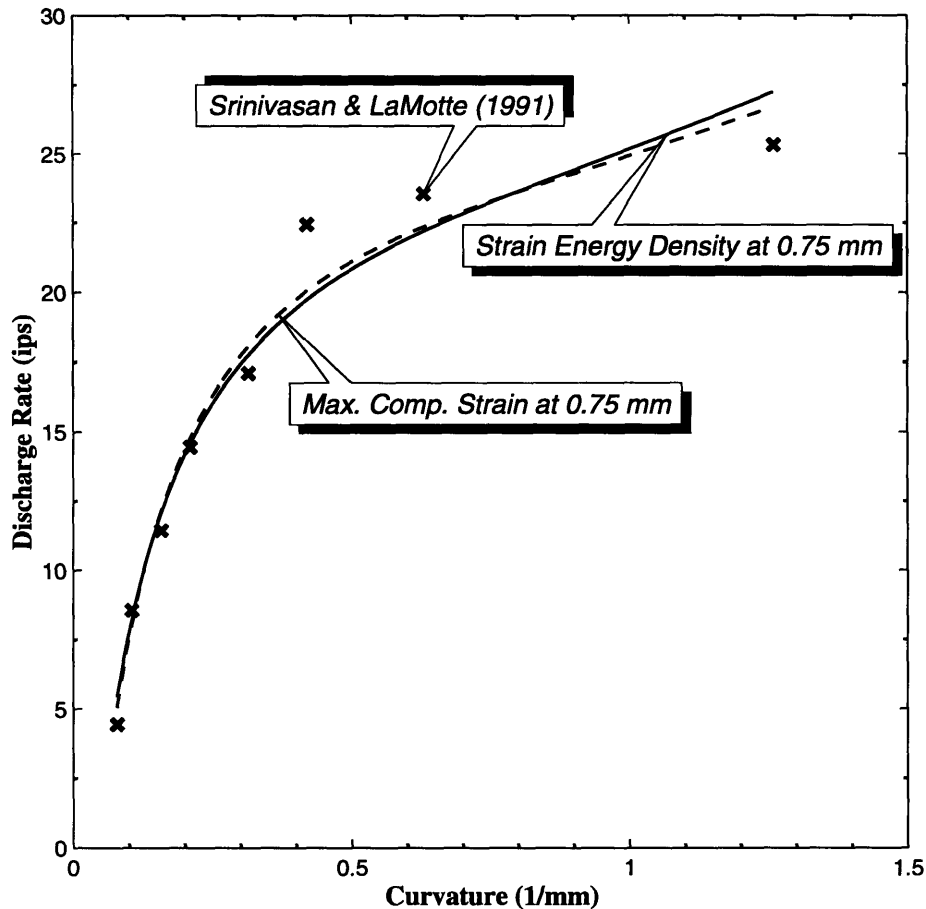


Figure 6-29: The predictions of the multi-layered 3D finite element model (m43338) are compared with experimentally recorded responses from monkey SA-I afferents under constant force of indentations by cylinders of varying curvature (Srinivasan and LaMotte, 1991).

model was indented by cylindrical indentors of varying diameters listed in Table 5.1. The problem of determining the gradual increase in the region of contact as the indentation proceeded was iteratively solved on the Cray C-90 and the approximate solution time for each indentation was approximately 14 cpu minutes. Various stress and strain measures were calculated at the receptor locations and compared with the recorded SA neural discharge rate from LaMotte and Srinivasan (1991). The linear receptor model given by equation 4.1 was used to predict the neural discharge rate. Our previous work (Srinivasan and Dandekar, 1994a) has shown that strain energy density and maximum compressive strain are the strain measures that are linearly related to the SA responses, and therefore, are the leading contenders to be the *relevant stimulus* of the SA receptors. Figure 6-29 shows the comparison of the experimentally recorded steady state SA discharge rate and the best

fits of calculated strain measures at the typical receptor locations, 0.75 mm and 1.0 mm below the skin surface. The experimental data is shown by thick × marks (Srinivasan and LaMotte, 1991). The excellent fit between the experimental and calculated data supports the validity of the multi-layered 3D model and indicates that the strain energy density and the maximum compressive strain are linearly related to the discharge rate of SA-Is. In our earlier work, the mean stress also provided a good fit if the stress-fields were interpolated over material discontinuities (Dandekar and Srinivasan, 1995a). In calculating the stress-state at a point in the model, if no integration points is found at the required location, the stress-state has to be interpolated from the neighboring integration points. In the monkey model, the outer layer was stiffer than the inner layer and this material discontinuity could be either ignored or accounted for in interpolating the results. If the material discontinuity is ignored, the predicted mean stress at the depth of 0.75 mm also provides a good fit to the experimental data. In plotting the matches in Figure 6-29 the strain measures were interpolated in the regions of identical material properties and points lying in layers of the model that have different material properties were not used to interpolate the strains at an intermediate point.

At present, it is not possible to experimentally observe or record the contact region and the spatial distribution of the contact pressure under an indenter. Using the finite element model, we can determine the contact region and the spatial distribution of contact pressure under the indenter. Figure 6-30 shows the variation in the contact area and maximum pressure in the region of contact as a function of the indenter radius. In the top panel, the radius of the contact circle is plotted. The total area of contact is calculated and the radius of the circle with the same area is plotted for each indenter. The indentors are indented into the fingertip till a prescribed force is achieved and, hence, if the contact area increases with increase in indenter radius, the mean pressure would be expected to decrease. It can be observed that the maximum pressure also reduces with increase in radius of the indenter. This information is important in hypothesizing the response of a population of receptors because, the contact region defines the area over which loads are imposed on the skin and the spatial distribution of pressure provides the necessary input for calculating the stress-state at the receptor location. This information can also be used to analyze the results of psychophysical experiments as the spatial extent of contact area under the indenter is a measure of the spatial cues available to the subject, which the

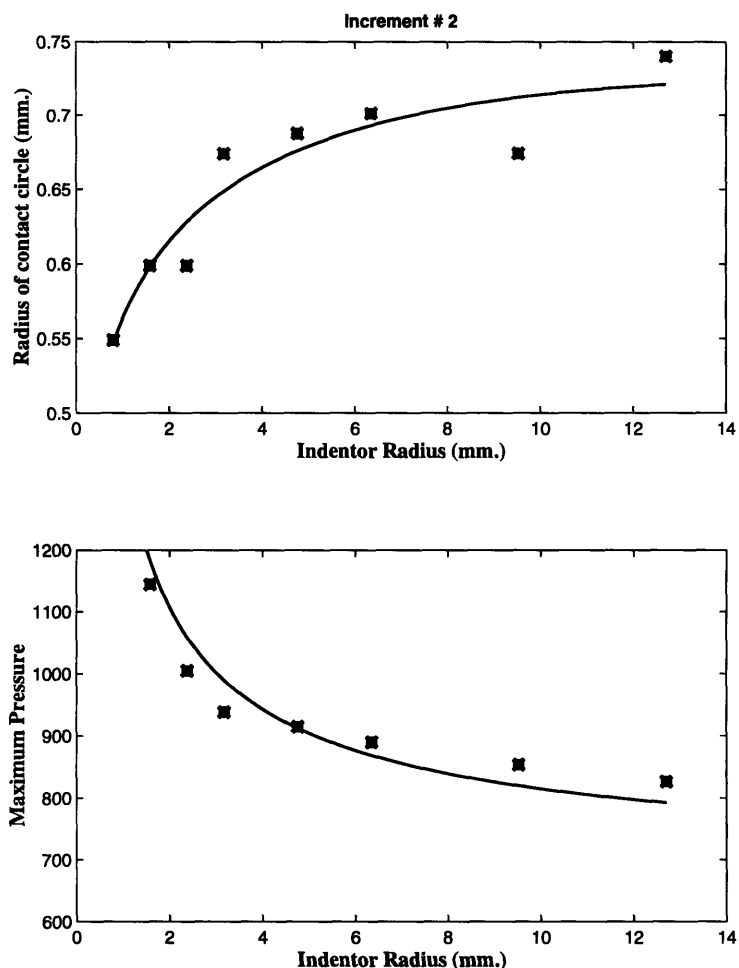


Figure 6-30: The variation in contact area and the maximum pressure under indentations by various cylindrical indentors is plotted with respect to the radius of the indentors. The data points shown by thick \times marks are the finite element predictions and a smooth curve fitted to these points is shown by the solid line.

subject may or may not use in the detection or discrimination experiments. Knowledge of these parameters can be helpful in planning future experiments with better control over the cues available to the subject.

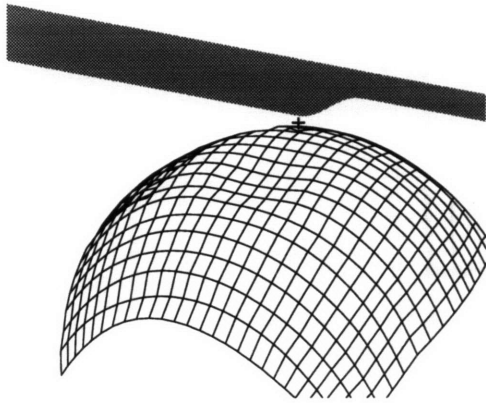
6.3.3 Indentation by step shapes

Monkey fingertips were indented by step shapes of varying curvatures to investigate the relationship between the SA-I response and the curvature of the object in contact with the skin (Srinivasan and LaMotte, 1987). Step shapes were machined out of clear plastic and the two flat portions of the step were separated in height by 0.5 mm. The transition from

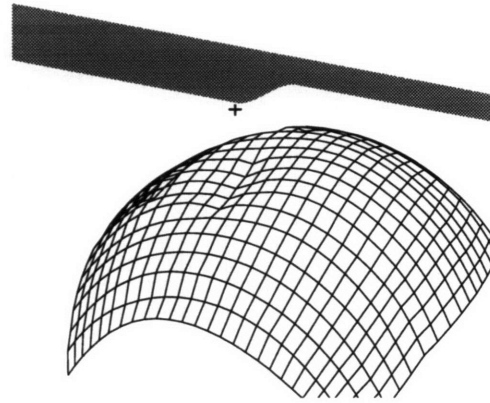
the lower part to the upper part of the step was accomplished by machining the step in the shape of a half sinusoid. The wavelength of the sinusoid was varied to generate different step shapes. Six different step shapes of varying wavelengths of the sinusoids were used in the simulations (Srinivasan and LaMotte, 1987). Steps 0, 1, 2, 3 with half-wavelengths 0, 450, 1195 and 1230 μm respectively were designated as “steep” steps, whereas, steps 4 and 5 with half wave-lengths 3038 and 3134 μm respectively were designated as gradual steps. The steps were indented into the fingertip until a prescribed force was imposed on the fingertip. The steps were then lifted off the skin, laterally moved in air across the fingerpad and indented into the fingerpad. This procedure was repeated until the entire step passed over the monkey fingertip restrained on the table. Each of the indentation was solved as a contact problem in which the step was assumed to be perfectly rigid. It was incrementally indented into the fingerpad till the prescribed force was achieved. Solution of each of the problem required about 15 CPU minutes on the PSC C-90 running ABAQUS 5.3. The steps were stepped across by 0.1, 0.25 or 0.5 mm depending on the curvature of the step and typically the simulation of each step consisted of about 40 static problems.

Figure 6-31 shows the deformed surface of the monkey fingertip under indentation by step 3 which had a sinusoid of half wavelength 1230 μm between the two flat portions 0.5 mm apart. The four panels in the figure show the deformed surface profile at four positions of the step relative to the monkey fingertip. The ‘+’ mark shown at the bottom of the step in all the four panels is used as the datum in locating the position of the step with respect to the fingerpad. The fingertip is indented by the lower flat portion of the step in the top left panel when the step is located at spatial location -0.75 mm. For all negative locations the flat part of the step indents the fingertip. The top right (0.6 mm) and the bottom left (1.4 mm) panels show the indentation of the fingerpad when the sinusoidal part of the step indented the fingerpad. In the bottom right panel (1.75 mm) the sinusoid has passed over the center of the fingerpad. In all the indentations the force of indentation was held constant and hence the variation in the area of the contact region and the spatial distribution of contact pressure in the area of contact is directly related to the curvature of the portion of the step contacting the fingerpad. In all the panels, the deformations are magnified by 50% to highlight the areas of deformation and therefore, when the flat portion of the step is indenting the fingertip the surface of the deformed fingertip does not appear flat.

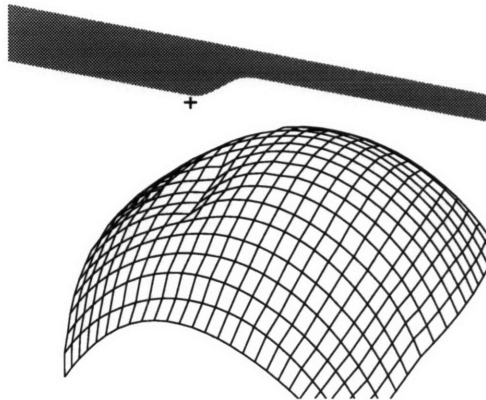
Step at -0.75 mm.



Step at 0.6 mm.



Step at 1.4 mm.



Step at 1.75 mm.

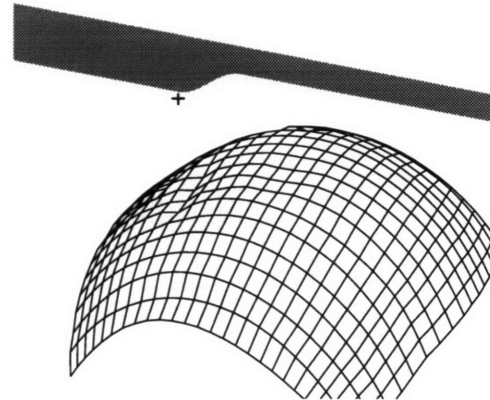


Figure 6-31: The surface deformations of the monkey fingertip under indentation by step 3 are shown in the four panels. The position of the step is measured with respect to the datum point on the step indicated by a '+' mark.

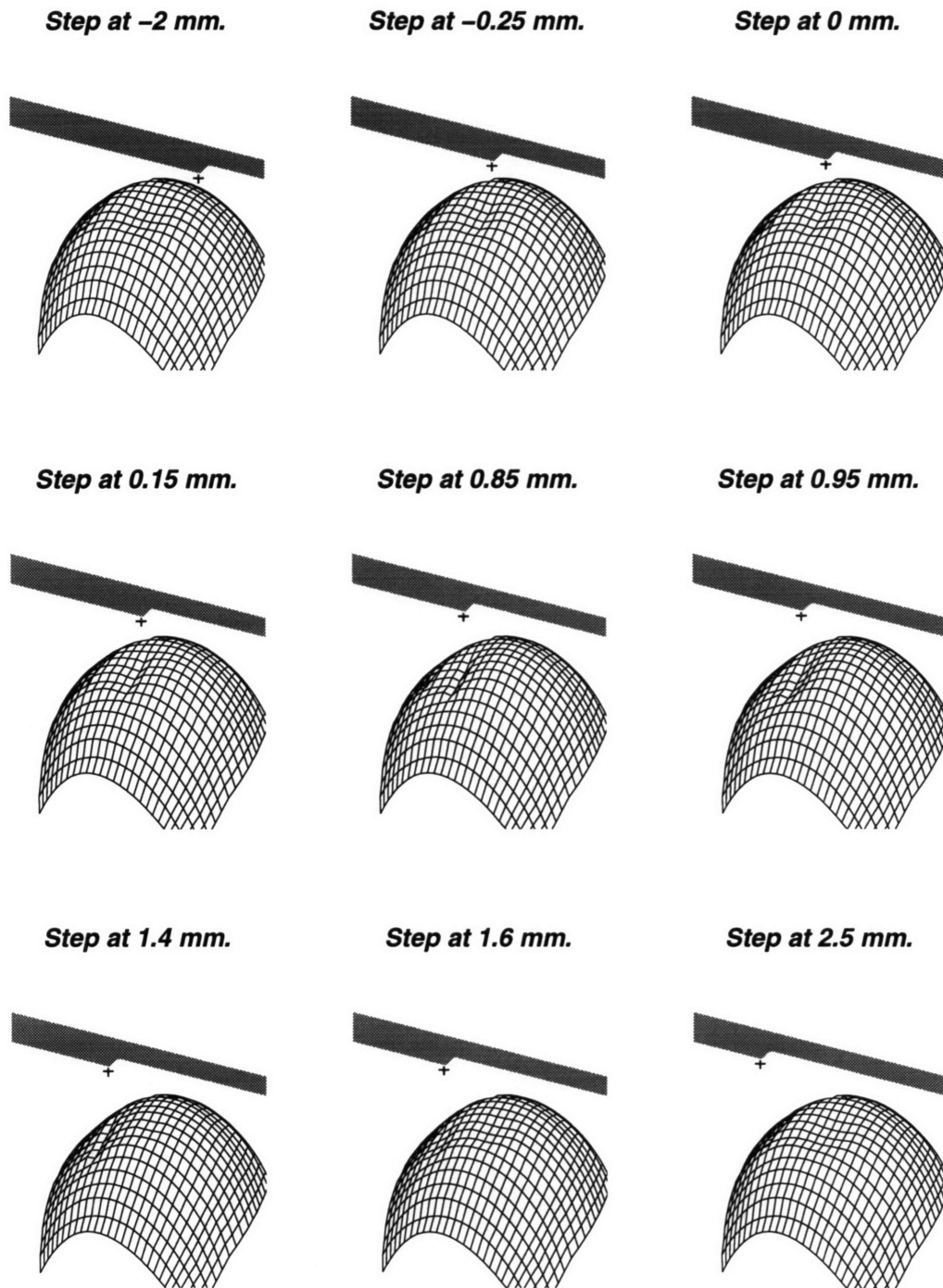


Figure 6-32: The surface deformations of the monkey fingertip under indentation by step 1 are shown for various position of the step. The position of the step is measured with respect to the datum point on the step indicated by a '+' mark. The displacements are magnified by 50% to emphasize the areas of contact between the step and the fingertip.

Figure 6-32 shows the deformed surface of the monkey fingertip under indentation by step 1 which had a sinusoid of half wavelength $450 \mu m$ between the two flat portions 0.5 mm apart. As in Figure 6-31, the deformations are magnified by 50 % to highlight the areas of contact between the fingertip and the step. In the top left panel the step is at -2 mm and the lower flat portion of the step is indenting the fingerpad. As the step is moved leftwards, which is indicated by the increase in the location of the step, the curved part of the step indents the fingertip. At -0.25 and 0 mm the contact region is shifting from the flat part to the curved part. The region of the fingerpad undergoing maximum deformation shifts leftwards as seen in the panel corresponding to locations 0.15 mm. From the panels corresponding to 1.4 mm and 1.6 mm, it can be seen that the contact area between the fingertip and the step is not contiguous. The curved part of the step contact the fingerpad at the off-center location and the lower flat part of the step contacts the fingerpad near the center of the fingertip. When the step is displaced further to the left to 2.5 mm, the lower flat part of the step contacts the fingertip and this is identical to the indentation at -2 mm.

Figure 6-33 shows the loads imposed on the fingerpad when step 3 was indented into the fingerpad. The locations of the steps are the same as shown in Figure 6-31. The magnitude of the surface pressure is shown by vertical lines at the spatial location of the nodes in the X-Z plane where the contact was established. The location of the step is measured with respect to the datum point on the step shown by a '+' mark on the top of the step. In the top left panel the lower flat portion of the step is in contact with the fingerpad. The change in the region of contact and the magnitude of the loads imposed can be observed in relation with the location of the step. It can be observed that the magnitude of the loads increase when the region of contact moves from the flat part of the step to the curved part of the step. It can also be observed that the curvature of the monkey fingertip plays an important role in determining the magnitude of the loads imposed. The curvature of the fingertip in the X and Z direction can be seen in Figure 6-1. This geometry is clearly reflected in the magnitude of the loads seen in panels corresponding to step positions of 0.6 and 1.4 mm. For a constant X locations, the variation in the magnitude of the loads in the Z direction is similar to the variation in the Y coordinate of the surface, which can also be seen in Figure 6-31. The point on the surface of the fingerpad with the maximum Y coordinate, is the first point where contact is established between the step indenter and the fingertip. Consequently, the vertical deformation of the points in the region of contact

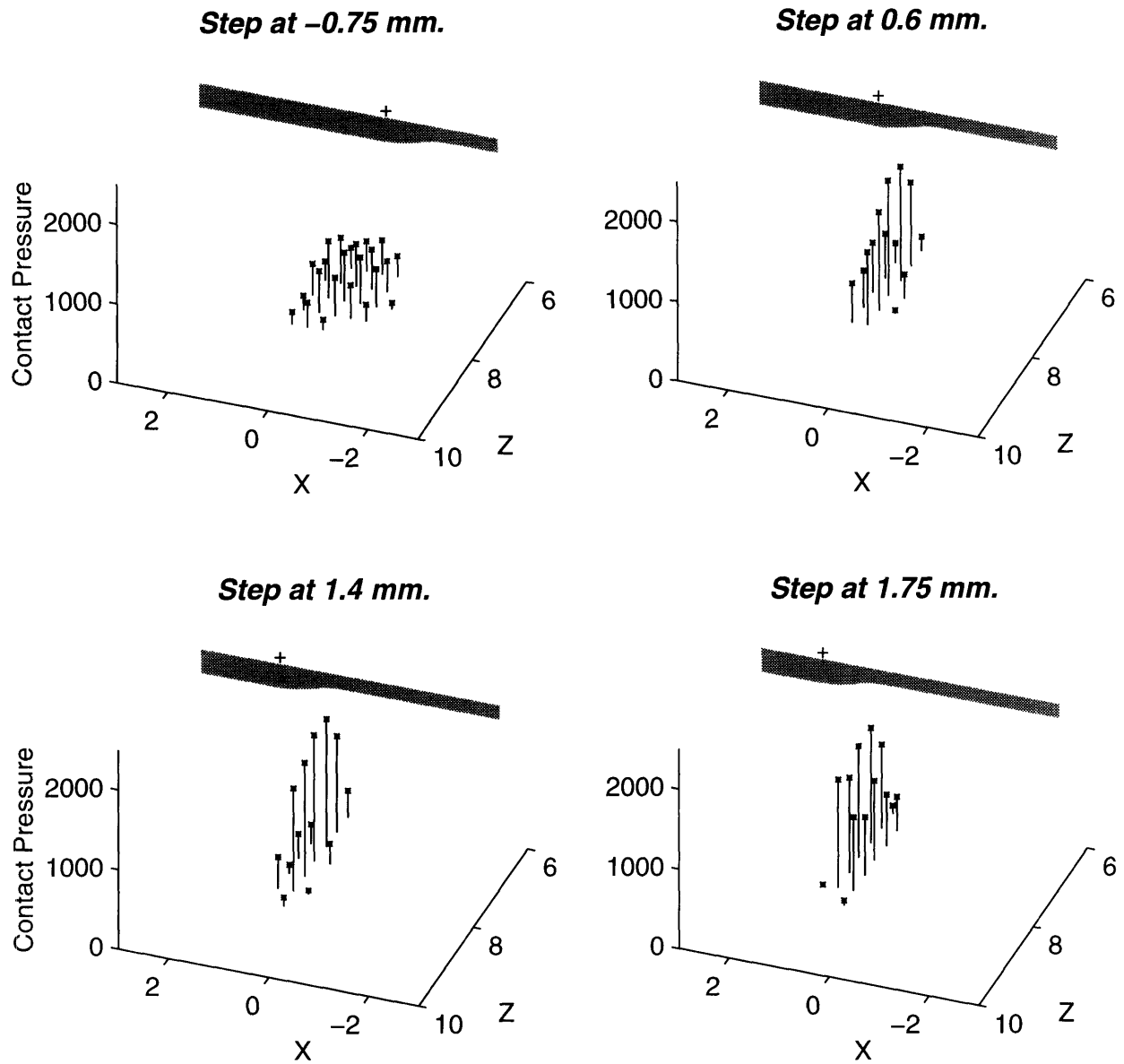


Figure 6-33: The contact pressure on the surface of the monkey fingertip under indentation by step 3 are shown in the four panels. The position of the step is measured with respect to the datum point on the step indicated by a '+' mark. Four different positions of the step are shown in the figure.

and hence, the loads imposed also depend on the Y coordinate of the points on the surface of the fingerpad. Similar variation is also seen in the X direction for points with the same Z coordinate.

The variation in the contact area and the magnitude of the contact pressure under indentations by step 1 is shown in Figure 6-34. In all the panels the surface pressure imposed on the fingerpad is plotted with respect to the spatial locations of the point of contact. A non-zero surface pressure is imposed only when contact is established between the indenter and the fingerpad and to simplify the figure only non-zero surface pressure is shown. The locations of the step are same as in Figure 6-32 and the axis limits and the scale in all the panels is identical, thereby enabling a visual comparison of the magnitude of the surface pressure. In the top left panel corresponding to the position of -2 mm, the lower flat portion of the step indents the fingertip. When the step is located at 2.5 mm, the upper flat portion of the step indents the fingertip and it can be seen that as expected, the spatial extent and the spatial variation in magnitude of the surface pressure is identical in the top left and bottom right panel. As more curved portions of the step indent the fingerpad, the magnitude of the surface pressure increases. As the step is indented to a constant force, the total force exerted on the fingerpad is the same in all the panels. An increase in magnitude of the surface pressures is accompanied by a decrease in the contact area as clearly seen in the panels corresponding to step positions of 0.15 mm through 0.85 mm. The maximum contact pressure at a point in all the indentations occurs at the this location and it can be seen that the contact between the fingertip and the step is reduced to a line contact. As the step is stepped further to the left, the concave part of the step is above the center of the finger and it results in non-contiguous contact regions as seen in the panels corresponding to step locations 1.4 and 1.6 mm. Examining the load profiles under the curved part of the step and the flat part of the step reveal the difference between the loading imposed on the fingertip, even though the step shape is indented into the fingerpad with the same force.

The variation in the surface pressure is reflected in the sub-surface variation of strain measures. The spatial variation of strain energy density at typical receptor location (0.75 mm depth) is shown in Figure 6-35. The locations of the step are the same as the locations used in Figure 6-32 and 6-34. The magnitude of the strain energy density is plotted in the X-Z plane and the same scale is used on the vertical axis enabling the comparison of the magnitude of the strain energy density corresponding to the different locations

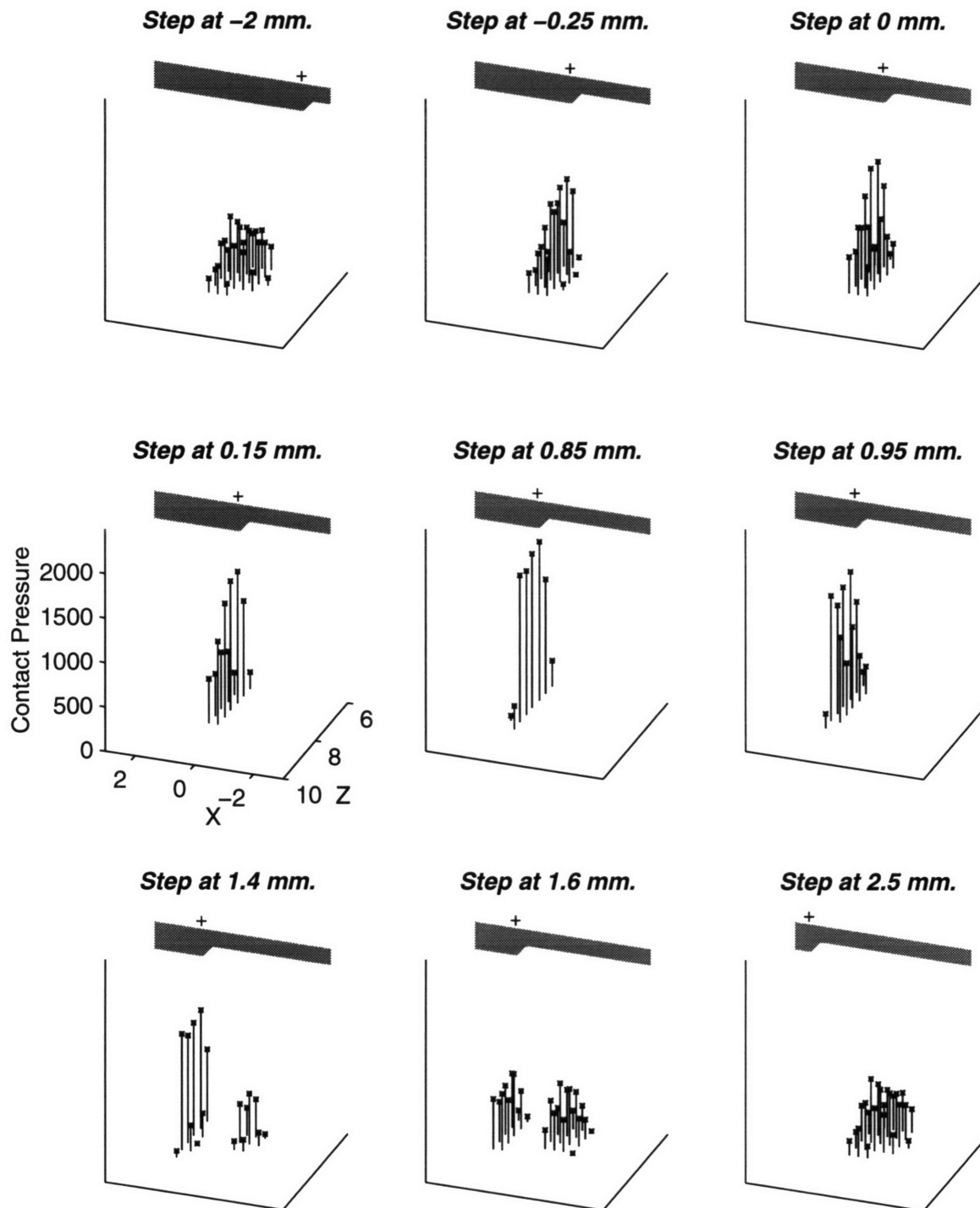


Figure 6-34: The contact pressure on the surface of the monkey fingertip under indentation by step 1 are shown in the four panels. The position of the step is measured with respect to the datum point on the step indicated by a '+' mark.

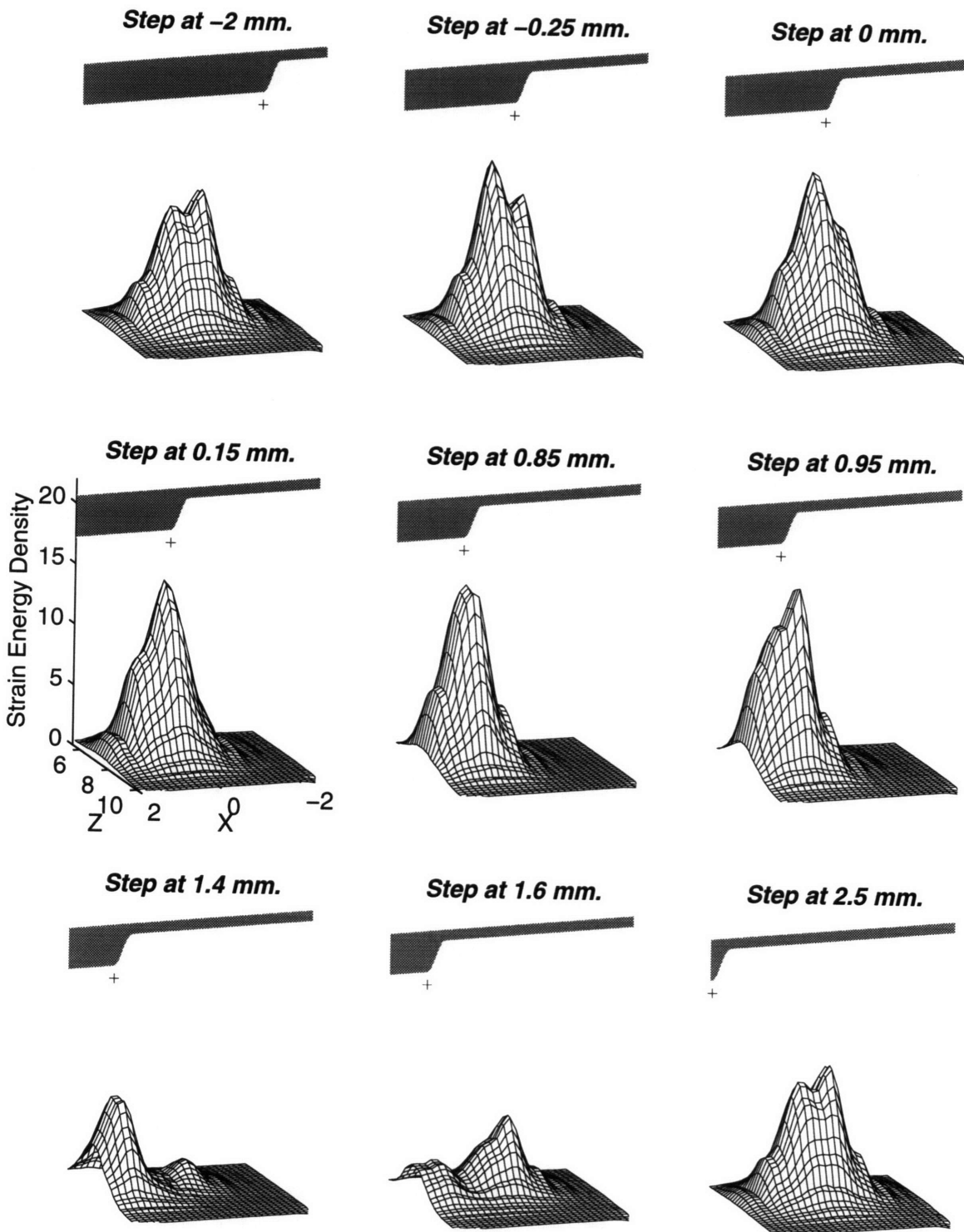


Figure 6-35: The spatial variation in strain energy density at the receptor location is plotted for various positions of step 1 which indents the fingertip is shown. The step is moved from left to right starting from the top left panel. The variation in strain energy density is heavily dependent on the location and the extent of the contact region between the step and the fingertip.

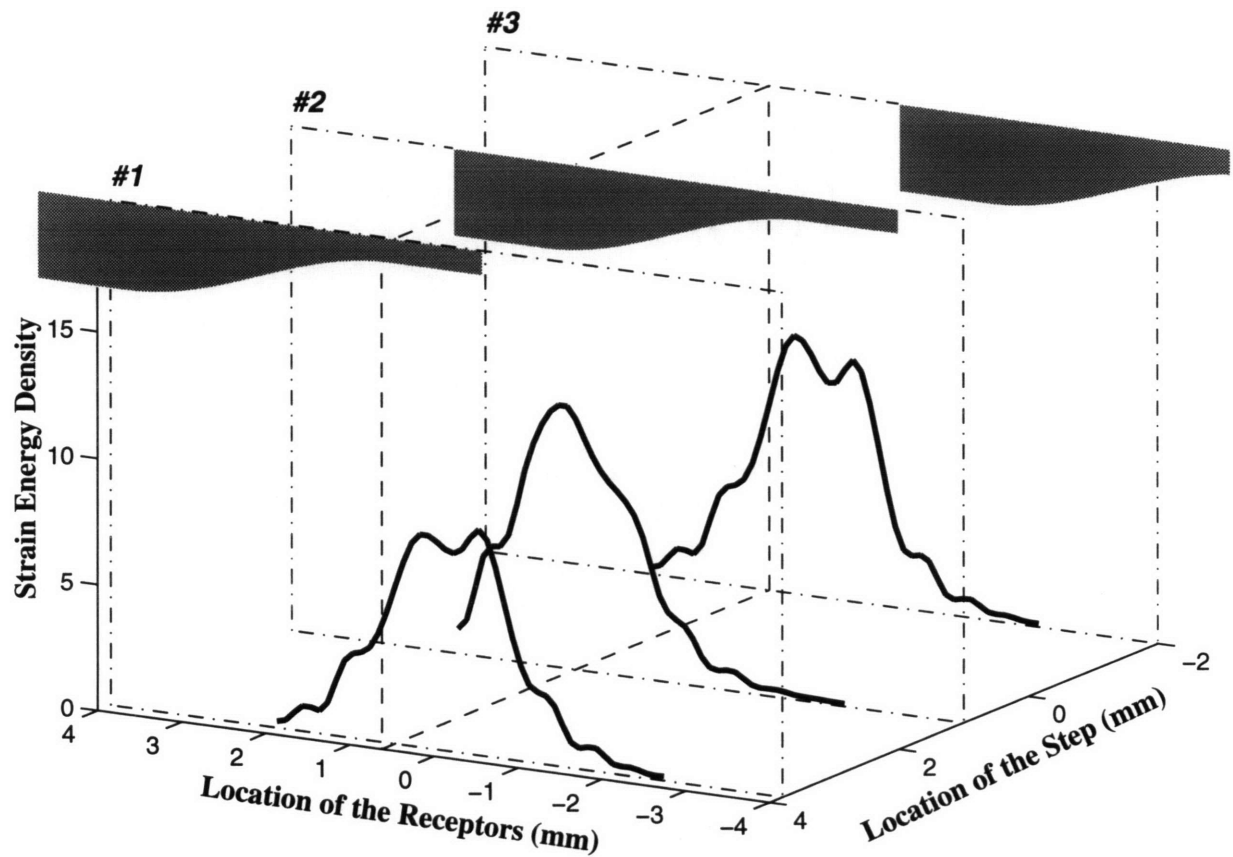


Figure 6-36: The spatial variation in strain energy density at the receptor location in an axial cross-section for three different step locations is shown. The three different positions of the step are shown in #1, #2 and #3. The plane of the cross-section in the three positions is shown by the dash-dot lines. A plane used to construct the spatial response profile is shown by the dashed line.

of the step. The mesh shown in the figures was generated by fitting a smooth surface to the data points where the strains were evaluated. If the slowly adapting receptors are assumed to be coding the strain energy density then these mesh plots essentially represent the response of a population of receptors. Such a response cannot be empirically observed at present, but it is used by the CNS in the decoding of shape. In order to hypothesize and test the hypotheses about coding of shape, it is necessary to consider the response of a population of receptors as shown in the Figure 6-35. For such simulations, a model with higher spatial resolution in load definition on the surface and result evaluation at the receptor location should be used (section 8.1).

Current experimental techniques can be used to record the response of a single afferent

fiber and construct a spatial response profile from the recorded data. The influence of various factors such as the location of the most sensitive spot of the receptor on the predicted spatial response profile can be studied as the true population response of the receptor population can be estimated using the finite element model. Figure 6-36 shows the spatial variation of strain energy density in an axial cross-section for three positions of the step. If the receptors were responding to the strain energy density in the the close vicinity of the mechanoreceptors, this would be the true response of the population of receptors in this cross-section. The spatial response profile is generated by recording the neural data from a single receptor and plotting the response versus the spatial location of the stimulus. This is equivalent to considering the response of a receptor in the cross-section of the 3D model shown in the figure, under indentation by the step in different positions of the step. A possible choice for the receptor is shown by the plane shown by dashed lines. The response of the receptor in the plane, if plotted versus the the location of the step as the spatial coordinate, would generate the spatial response profile.

Several population responses for an axial cross-section when the monkey fingertip model was indented by step 5 are shown in Figure 6-37. As explained in Figure 6-36, each trace represents the population response of the receptors in the cross-section at a particular location of the step. The location of the receptor that can be used to generate the spatial response profile is arbitrary and one such location is shown by the dashed plane in the figure. The response of the receptor from each of the traces is joined by the thick line which lies in the plane. As the axial sections correspond to a unique location of the step, the thick line is essentially the response of a single receptor plotted versus the spatial location of the stimulus, and hence is the spatial response profile.

As explained earlier, the choice of the receptor used in the reconstruction of the spatial response profile is arbitrary. For an identical stimulus, the spatial location of the mechanoreceptor can influence the form of the spatial response profile. Figure 6-38 illustrates the different spatial response profiles that could be generated by choosing a different receptor in the reconstruction of the spatial response profile from the population response. This means, that if such profiles are observed experimentally, the difference in the form of the spatial response can be attributed to the difference in the spatial location of the receptors, as the same strain measure is used in predicting these different spatial response profiles. The curvature of the fingertip and other factors discussed earlier, affect the stress-

Step 5, Section at $x = 0.62$

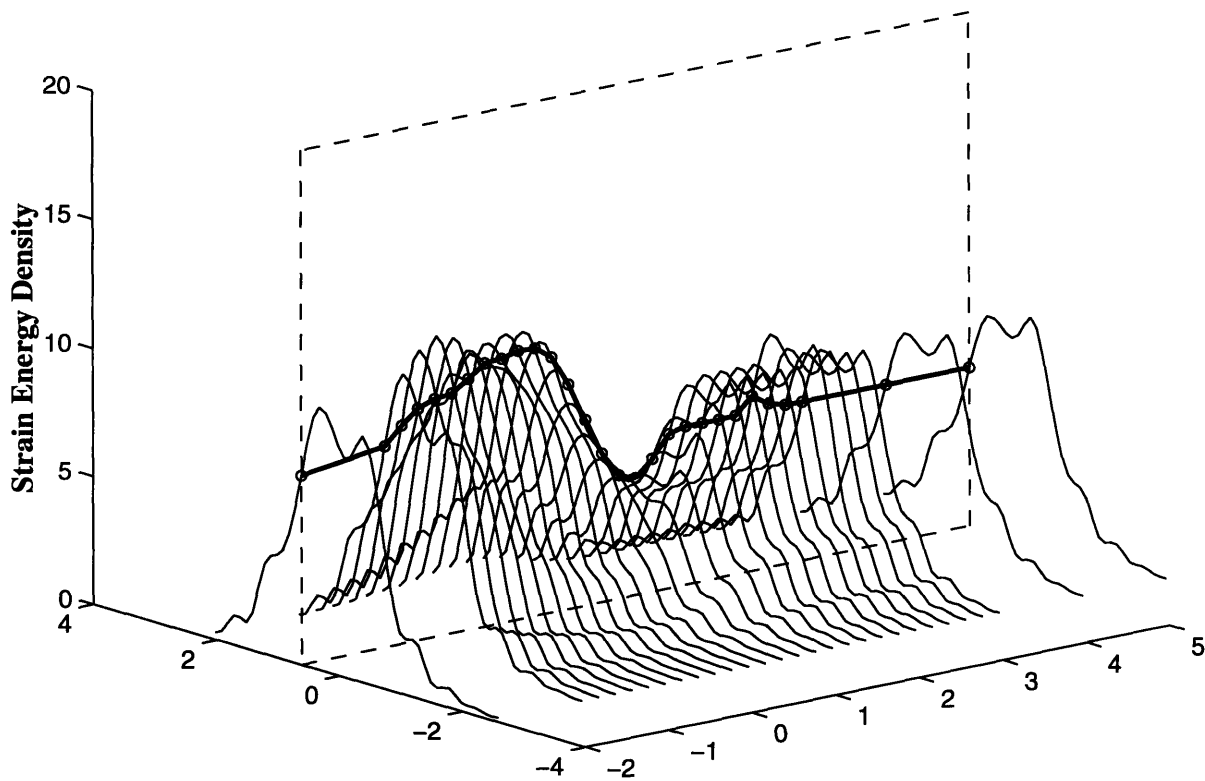


Figure 6-37: The spatial variation in strain energy density at the receptor location in an axial cross-section for different step locations is shown. The plane representing the location of the receptor is shown by the dashed lines. The spatial response profile generated using the receptor in this plane is shown by the dark line in the dashed plane.

state in the vicinity of the receptors resulting in different spatial response profiles as shown in Figure 6-38.

The indenter corresponding to step 5 is shown in the top panel of Figure 6-39. The two flat surfaces, and the half sinusoid between the two flat regions of the step are clearly seen. The step was generated in Abaqus and indented into the fingerpad model. The force required for the indentation was monitored and the indentation was continued until the required force was imposed on the fingertip. The solution of the contact problem was obtained iteratively and each indentation required about 14 cpu minutes on the PSC Cray C-90. The indenter was laterally shifted by 0.1 or 0.2 mm depending on the curvature of the step, and the process of indentation continued till the entire step passed over the fingertip model. Although it is not experimentally possible to record the area of contact

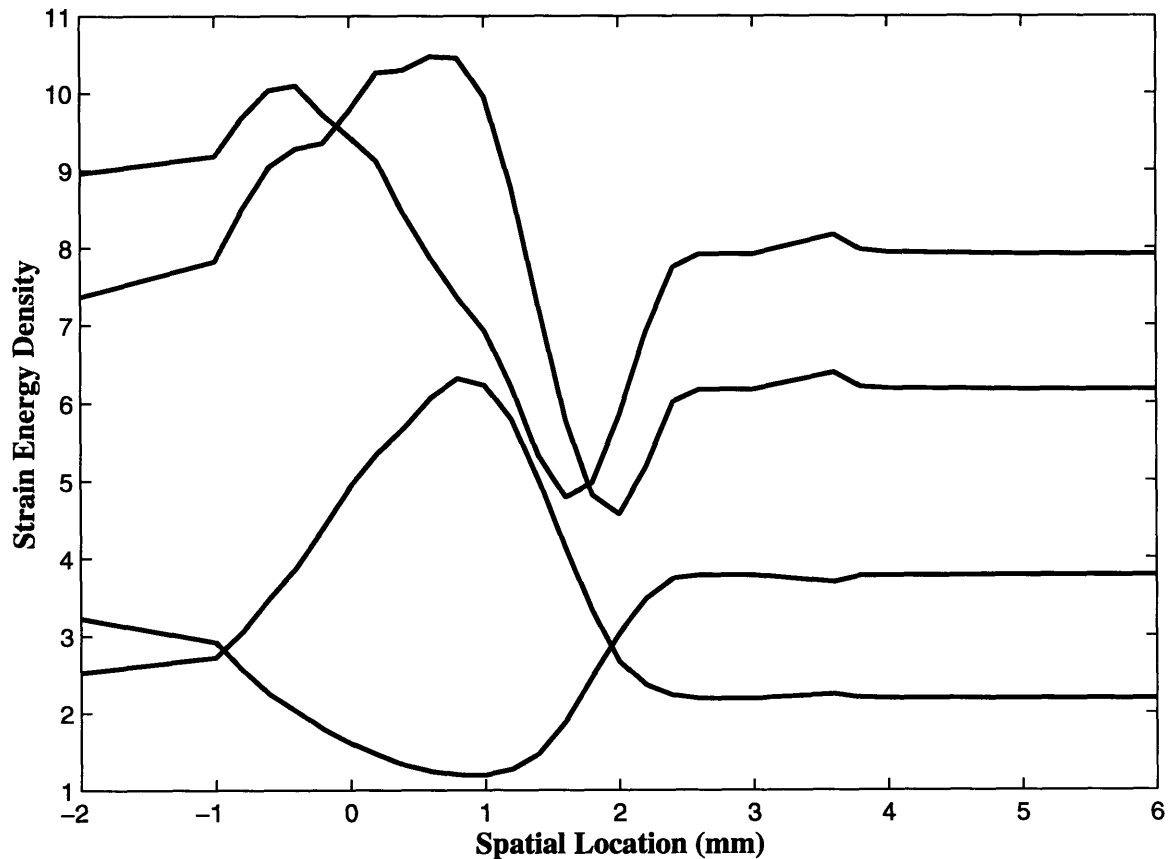


Figure 6-38: Different spatial response profiles based on the receptor selected are shown. All the spatial response profiles were generated from the data shown in Figure 6-37 but different locations of the receptor were selected for each profile.

between the step and the fingertip and the maximum contact pressure in the contact region, finite element analyses enables us to predict these variables as the step is indented across the fingertip. The variation of the contact area and the maximum contact pressure in the contact region with the spatial location of the step is shown in Figure 6-39. As in the case of cylindrical indentors indented with constant force, it can be seen that an increase in the contact area is always accompanied by a decrease in the maximum contact pressure and vice-versa. The contact area is minimum under the regions of the step that have high convex curvature. When the concave part of the step is over the fingertip model, the contact area is the highest and is accompanied by the lowest magnitude of the maximum pressure in the contact region.

Neurophysiological data from one SA-I afferent (Srinivasan and LaMotte, 1987) was

Step No 5

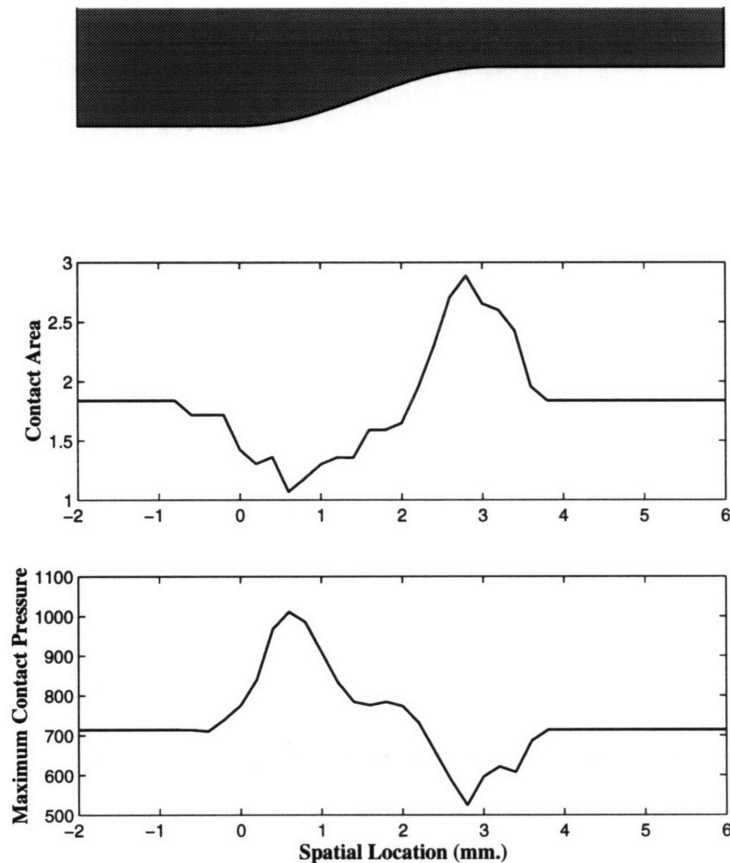


Figure 6-39: The variation in contact area and maximum contact pressure for constant force of indentation of step #5 across the monkey fingertip are shown in the two bottom panels. The step is shown in the top panel.

compared with strain energy density at the receptor location using a single set of scaling and thresholding parameters. If the strain energy density is the strain measure coded by the mechanoreceptors, then for the experimental data from a single afferent, a single set of scale and threshold parameters should be able to predict the neural response of the mechanoreceptor under all the stimuli. Figure 6-40 shows the comparison between the experimentally observed and the predicted data. The experimentally observed data (Srinivasan and LaMotte, 1987) is shown with the '*' marks and the finite element predictions are shown by a solid line. The spatial response profile of the SA is generated by plotting the evoked impulses as a function of the step position and the finite element predictions are also plotted as a function of the step position. The experimental data for step 1 was

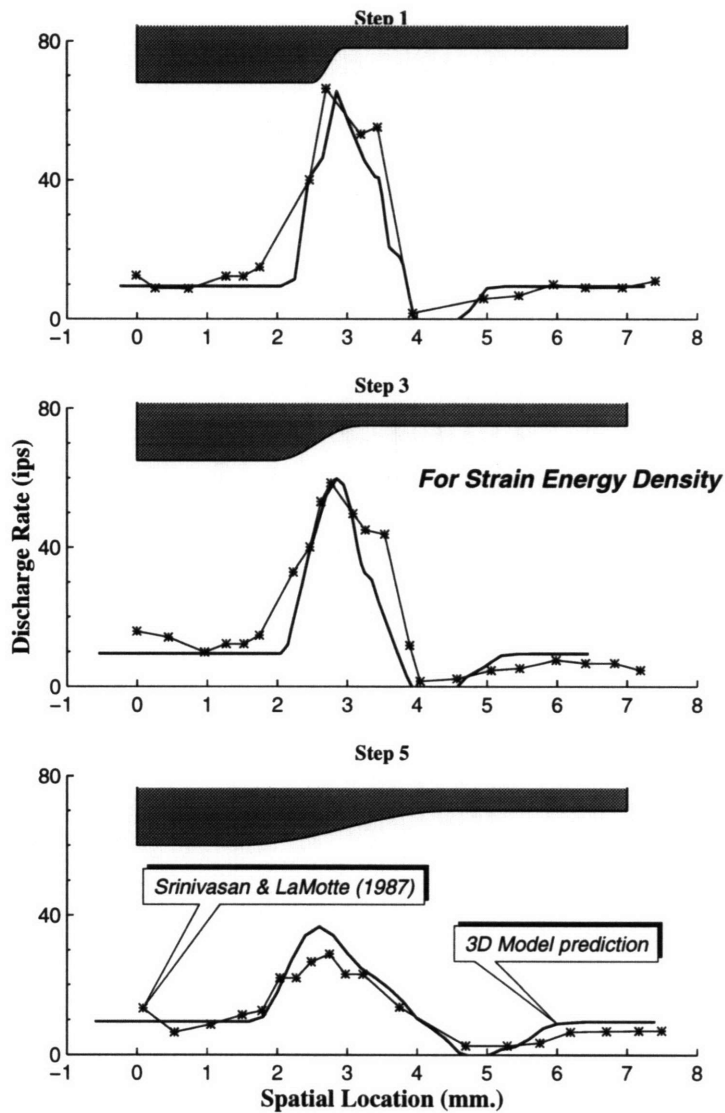


Figure 6-40: Assuming strain energy density to be the relevant stimulus and using a single threshold and scale parameters, the response of the mechanoreceptor to indentations by three step shapes is predicted. It agrees very well with the experimentally observed neural discharge rate shown in thin lines.

compared with the finite element predictions of strain energy density at the receptor location 0.75 mm below the skin surface and the fitting parameters were derived to obtain the best fit. The same parameters were used to predict the response when the fingertip was indented by steps 3 and step 5. By comparing neural data from one afferent unit, with the stress-state at a unique receptor location along with the same set of fitting parameters, we are verifying the combination of the biomechanical and neurophysiological models.

The agreement between the experimental and predicted data indicates the reliability of the model in predicting results of future neurophysiological experiments (Dandekar and Srinivasan, 1995d). One of the differences in the observed and predicted data is the flat response in the predicted data at the two extreme spatial locations. At these locations the flat part of the step contacted the fingertip. As the loading was a prescribed force, the stress-state in the model was identical regardless of the position of the step when the entire contact region was on the flat portion of the steps. In the experimental data, however, it is likely that the adaptation of the receptors caused the response under the flat portions of the step to be different on both sides of the step shape. The adaptation and other temporal effects influencing the dynamics of the receptor response are not taken into account by the single receptor model proposed here.

7

Discussion

In the 3D finite element models, the material properties of the layers of the models were inferred by using the empirically observed surface deformations under line load as discussed in Chapter 6. The finite element model of the monkey fingertip with the same material properties predicted the neurophysiological data for a variety of stimuli quite well. In this chapter, the mechanical behavior of the finite element models is discussed. The salient similarities and differences in modeling the fingertip as a cylindrical 2D model with a concentric bone (Chapter 4) and a realistic 3D model of equivalent material properties are examined and the limitations of the 2D models are discussed. The unique mechanistic properties of the fingerpad owing to its non-homogeneous material constitution are explained. Some possible biomechanical experiments required for unequivocal determination of the relevant stimuli, which could also be used in the determination of relevant stimuli for other mechanoreceptors, are presented. The implications of the research reported in this thesis to neurophysiology, robotics and virtual environments are summarized.

7.1 Mechanical Behavior of Models

7.1.1 Effect of geometry

The 3D model is compared with its precursor: the 2D cylindrical model with bone in Figure 7-1. The deformed mesh of the monkey fingertip under indentation by a 1.5 mm wide bar is shown in gray lines and an axial section of the model is shown in solid dark lines. A typical section like the one shown in Figure 7-1 was modeled by the 2D circular cylindrical model with bone discussed in Chapter 4.

For the cross-section shown in Figure 7-1, the undeformed boundary of the cross-

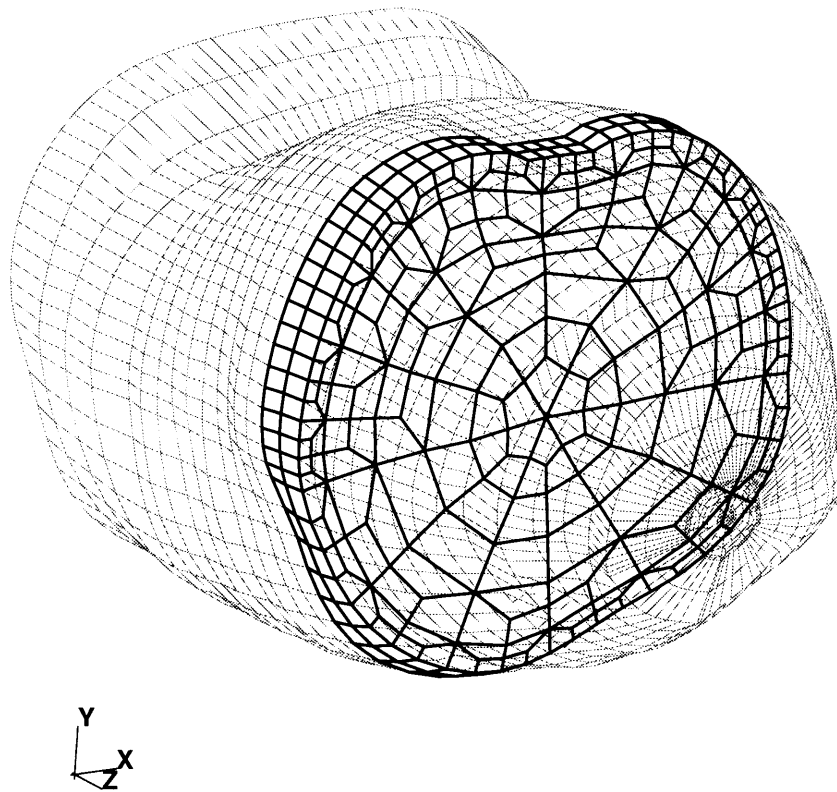


Figure 7-1: A typical cross-section of the 3D model shown in dark lines is compared with the 2D cylindrical model with bone discussed in Chapter 4.

section as seen in the X-Y plane can be approximated by the circular cross-section of the 2D models. Due to the local nature of the deformations, unmodeled curvature changes in the undeformed geometry of the cross-section more than about 3 mm away from the region of contact between the indenter and the fingertip will not affect the predicted spatial variation in the vicinity of the mechanoreceptors (Chapter 4). In the neurophysiological experiments the fingernail is glued to the table to avoid any motion of the fingertip relative to the table. This boundary condition is modeled by suppressing all the degrees of freedom of all the nodes corresponding to the fingernail in the 3D model. In the 2D model this boundary condition was modeled by suppressing all the degrees of freedom for the boundary nodes on the bottom third of the circumference which is an acceptable representation of the extent of the fingernail. One major modeling decision in modeling the fingertip as a 2D model was to model the section of the fingertip as a plane strain problem. By assuming the cross-section to be in the *plane strain* condition, all the non-zero strains restricted to lie

in the plane of the model and all out of plane deformations are ignored. This is effectively equivalent to constraining the cross-section between two rigid walls and restricting the deformations under the influence of in-plane loads to the plane of the section. The cross-section shown in Figure 7-1 is similar to its neighboring cross-sections in shape, size, internal geometry, material properties, and the boundary conditions and, therefore, *plane strain* is a reasonable assumption as long as the analysis is restricted to sections that are in the central glabrous region and away from the distal end of the fingertip and the loading and boundary conditions are identical in the axial direction. It was shown in section 4.5.2 that the diameter of the 2D cylindrical model had a significant effect on the loading imposed on the model. Consequently, the 2D model will not be able to predict the variation in loading along the axial (Z) direction due to the change in the diameter of the finger in the X-Y plane, for stimuli that do not vary in the Z direction such as bars, gratings used in the neurophysiological experiments. The curvature of the fingertip in the Z direction cannot be modeled by the 2D models, which is an important factor in predicting the response of a population of mechanoreceptors for truly 3D stimuli like ellipsoids or spheres.

All the neurophysiological data available and used in the simulations discussed earlier was recorded from single peripheral afferent fibers. The 3D finite element models were meshed to simulate these experiments involving single fiber recordings and, hence, the mesh size and the spatial resolution in the interior of the model was chosen to be rather coarse to minimize the computational effort required in the solution of the finite element solutions. If the models are to be used to predict the response of a population of receptors finer mesh is required inside the fingertip. In the following comparisons with the 2D models it should be noted that the spatial resolution in the 2D models was about $60 \mu m$, whereas, the spatial resolution of the 3D models was approximately $500 \mu m$.

In modeling the fingertip as a 2D cross-section, the plane-strain assumption was used and the all the sections of the fingertip were assumed to be identical in the geometry, loading and boundary conditions. Therefore, the predicted stress-state in the various cross-sections was identical as the variations in fingertip diameter and loading observed in the real fingertip could not be modeled in the 2D model. The strain energy density and maximum compressive strain at a depth of 0.75 mm predicted by the 2D model and the 3D model (m33338) are compared in Figure 7-2. The axial cross-section at $z = 7.495$ is

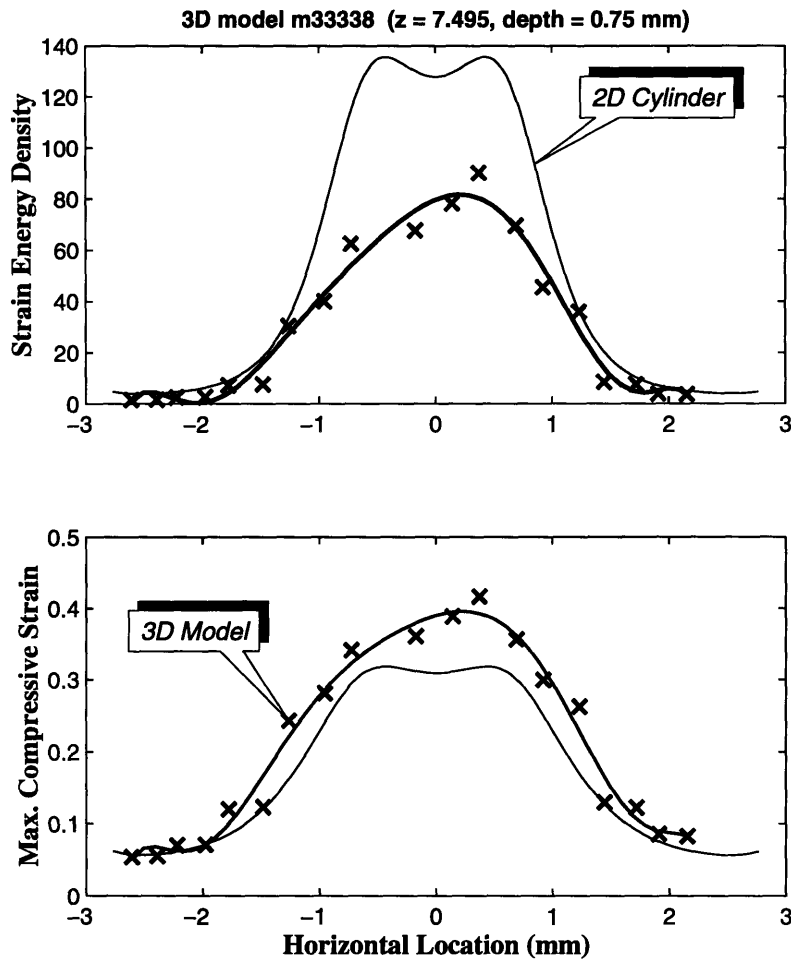


Figure 7-2: A section of the 3D model at $z = 7.495$ is compared with the 2D cylindrical model. This is a central section of the distal phalanx which was about 16 mm long. The strain energy density and maximum compressive strain at a depth of 0.75 mm in both the models are shown in the top and bottom panel respectively.

chosen for the comparison. When the bar is lowered onto the fingerpad, the first point of contact between the indenter and the fingertip occurs on this cross-section and, hence, the maximum prescribed vertical displacement for the nodes in this cross-section is 1 mm which is equal to the maximum prescribed vertical displacement in the 2D models. The 2D model had a stiff concentric bone and uniform material properties for the rest of the finger. In the 3D model m33338 similar material properties are chosen and the bone is several orders of magnitude stiffer than the rest of the fingertip. The 3D model is limited by spatial resolution of the integration points where the stress state is evaluated and data evaluated at only the integration points is shown by cross marks. These points are joined by a smooth

curve shown by the thick line in both the panels of Figure 7-2. The predictions of the 2D models are shown by the thin line generated by joining the data points by straight lines. The data points are not shown because they were very close to each other. The maximum compressive strain shown in the bottom panel is approximately equal in magnitude and form in the two models. By comparing these two models with identical material properties under similar mechanical stimuli, any differences in the strain measures at the given depth can be attributed solely to the difference in the geometry of the two models. The maximum compressive strain in the 3D model is slightly higher than the 2D model, indicating that the 2D model is stiffer than the 3D model, which is to be expected since the plane strain assumption is used in the analysis of the 2D model. There is a difference in the magnitude of maximum strain energy density predicted by the 2D and the 3D models. In the 2D models, constraining of the deformations to the plane is equivalent to assuming the stiffness in the axial direction to be infinite. Consequently, when the bar is indented to a depth of 1.0 mm into the fingertip regardless of the force required for the indentation, the 2D model being stiffer predicts a higher strain energy density. We can see that the overall form of the strain energy density in the 2D and 3D models is similar. In the 2D models it can be analytically shown that the strain energy density is directly proportional to the square of maximum compressive strain (Appendix A). Observing the differences in the profiles for the 2D models and the 3D models, this relationship does not hold for the 3D models. As a scaling parameter is used in the receptor model that relates the strain measure to the neural response (Equation 4.1), the difference in the magnitude of the strain measures will not affect the results of the neurophysiological predictions based on the 2D models.

Figure 7-3 shows a comparison of the strain measures from the 2D model and an axial section of the 3D model at $z = 9.17$, which is about 2 mm away from the node with the maximum prescribed displacement. The strain energy density and maximum compressive strain at a depth of 0.75 mm in both the models are shown in the top and bottom panel respectively as in Figure 7-2. From the spatial variation of strain energy density at a depth of 0.75 mm in the 3D model shown in Figure 6-25, it can be seen that the strain energy density profile is not the same for all axial cross-sections in the 3D model, whereas, the 2D model predicts the same spatial variation of the strain measures regardless of the axial location of the cross-section. Therefore, the strain measures for the 2D models shown in Figures 7-3 and 7-2 are identical, whereas, the spatial variations of the strain measures

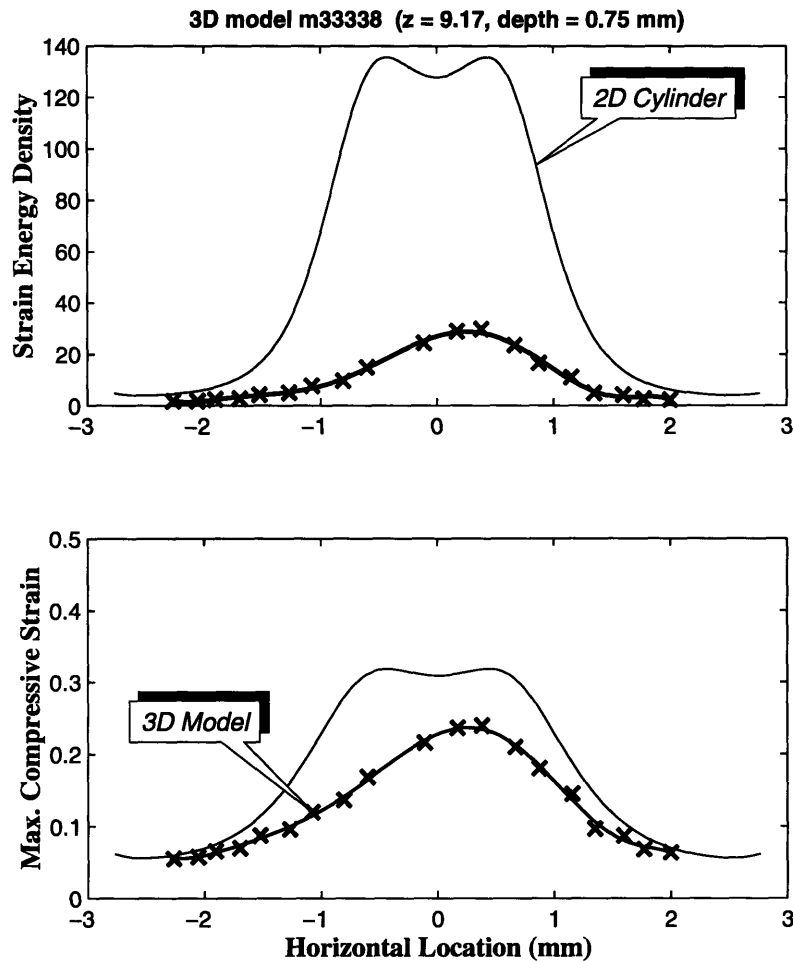


Figure 7-3: A section of the 3D model at $z = 9.17$ is compared with the 2D cylindrical model. The strain energy density and maximum compressive strain at a depth of 0.75 mm in both the models are shown in the top and bottom panel respectively.

predicted by the 3D model are not. The magnitudes of the maximum compressive strain in the 2D and 3D models are not equal at $z = 9.17$, and, all the strain measures in this cross-section are lower than the section at $z = 7.495$. This is to be expected because the curvature of the finger in the YZ plane causes the maximum depth of indentation for the nodes in this cross-section to be less than 1.0 mm, which was the corresponding maximum in the section at $z = 7.495$. By comparing Figure 7-2 and Figure 7-3, we can see that the 2D model approximates the 3D fingertip only for a limited range of the axial cross-sections. Although the stimulus is the same for both the cross-sections, difference in the diameter of the fingertip at the cross-sections and the curvature of the fingertip in the Y-Z plane result in a different loading for the two cross-sections. If a 3D population response of receptors at

a given depth is desired, the 3D model should be used in the simulations as the stress-state changes along the axis of the fingertip can be more accurately modeled by the 3D model as seen from Figure 6-25.

Such a comparison between a slice of the 3D model and the 2D model is possible for mechanical stimuli that do not vary along the axis of the finger and are aligned such that the axis of the stimulus and the axis of the finger are parallel. For a true 3D stimuli such as ellipsoids or irregular textures, it is necessary to use a 3D model of the primate fingertip to predict the stress-state at a receptor location and the response of a population of receptors.

7.1.2 Effect of multiple layers

The biomechanical basis of selection of the material model m43338 for simulations of the neurophysiological experiments on the monkey fingertips was its excellent match with the observed skin surface deformation under various mechanical stimuli. The comparison of experimental data with the model predictions under line load for monkey and human fingertips and cylindrical indentors for human fingertips is discussed in Chapter 6. Having discussed the effect of model geometry on the predicted stress-state at the receptor locations in the previous section, the effect of properties of the constituent material on the stress-state at the receptor location is discussed in this section.

A cross-section from the 3D model of the monkey fingertip with material model m33338 is shown in the left panel in Figure 7-4. The fingertip is indented by a rectangular bar 1.5 mm wide and aligned parallel to the axis of the finger as shown in Figure 6-24. Contours of constant strain energy density are shown over the deformed mesh and the hidden lines are removed for clarity. The same cross-section from the monkey model m43338 is shown in the right panel. The loading in this case is also indentation by a 1.5 mm wide rectangular bar to a depth of 1.0 mm. Some salient similarities and differences in the two cross-sections can be observed. In both the sections, the localized nature of the deformations is clearly seen from the contour plots. The deformation has a negligible effect on the magnitude of strain energy density about 3 mm from the edges of the bar. A large portion (85%) of the cross-section has less than 10 % of the maximum strain energy density indicating the local nature of spatial variation of strain energy density. All other strain measures also show a similar local distribution. Local distribution of deformations is desirable from the spatial acuity requirements of the mechanoreceptors because acuity suffers if stimuli contacting

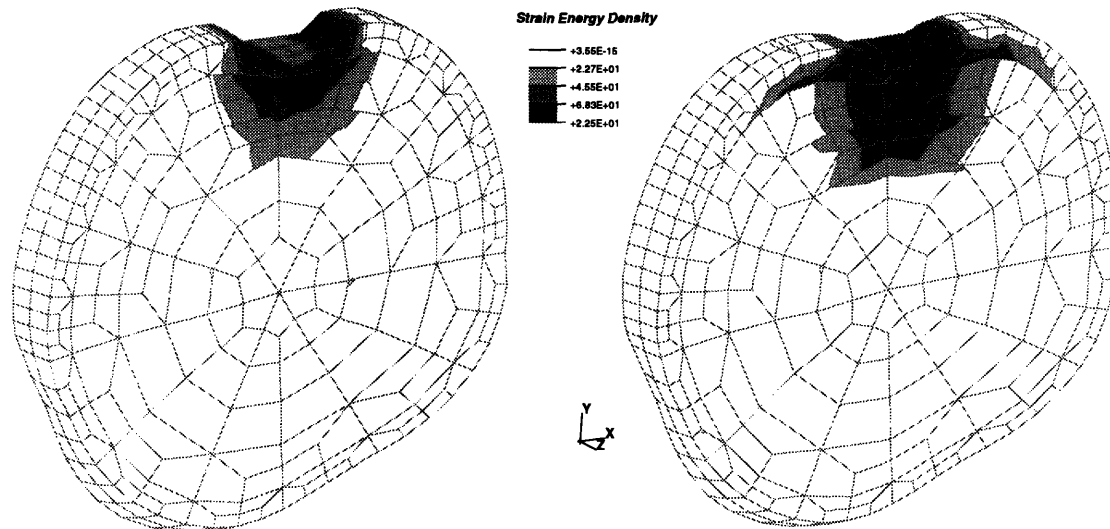


Figure 7-4: Sections of the the monkey models m33338 and m43338 at the identical location in the 3D model are shown. Contours of constant strain energy density when the 3D models were indented by a 1.5 mm wide bar to a depth of 1.0 mm are shown on the deformed mesh in both the sections.

the skin at a location far away from the mechanoreceptor affect the response.

The surface deformation profile under the bar predicted by the two models, however, is quite different. Model m33338 shows an “elastic” deformation characterized by sharp changes in the magnitude of vertical displacements similar to the localized deformation observed in the 2D models (See Figure 4-27). The surface deformation of the m43338 model is more gradual as discussed in section 6.2.1 and can be seen in the right panel of Figure 7-4. In extracting maximum tactile information from the object in contact with the skin, it is desirable to increase the contact area between the fingertip and the object. With a larger contact area a larger population of the receptors is stimulated, thus providing the CNS with sampled data from a wider region of the fingertip to decode the characteristics of the object in contact. The same is true in robotic manipulators used to perform manipulation tasks. Increase in the stiffness of the outer layer of the fingertip results in a wider area of contact and this counterintuitive phenomenon is discussed in detail in section 6.2.1. In addition to obtaining tactile information from a larger region, increase in contact area also improves the stability in manipulation tasks. The higher stiffness of the external layer provides these desirable attributes to the fingertip.

The location of the maximum strain energy density is the same in both the models, occurring under the edges of the bar which corresponds to the location of maximum pressure in the area of contact. The magnitude of the maximum strain energy density, though, is slightly higher in m43338 model due to the higher stiffness of the outer layer. The most interesting difference in these two models is the spatial variation in the magnitude of strain energy density at subsurface locations. In model m33338 the same spatial filtering characteristic as all the homogeneous models discussed in section 4.2 can be seen. Because of the higher stiffness of the outermost layer in the m43338 model, however, a “*beam like*” phenomenon is observed.

In the classical slender beam, the bending strain and deformation is zero for all points on the neutral axis and increases linearly with increase in distance from the neutral axis (Timoshenko and Goodier, 1982). A similar phenomenon is observed here, which causes the magnitude of strains to *increase* for depths beyond half the depth of the outer layer. This is seen by the higher magnitude of strain energy density in the lower part of the outermost layer indicated by darker contours in the right panel of Figure 7-4. The beam analogy, however, should be used with caution because although the variation of the magnitude of strains with distance along the thickness direction in the 3D model is similar to the corresponding variation in the classical beam, the expressions for stress, strain and displacements from the beam solution cannot be used. This is due to the difference in the boundary conditions between the finite element model and the classical beam solution and other simplifying assumptions used in deriving the analytical solution for the slender beam. Because of the difference in the stiffness of the two outer layers, the increase in strain energy density in layer #1 at the boundary of layers 1 and 2 does not propagate to layer #2. Although, the strains are continuous across element boundaries, difference in Young’s modulus implies discontinuous magnitude of stresses and, therefore, the strain energy density. Spatial low-pass filtering results in the loss of spatial information both in magnitude and the spatial frequency content. All the strain measures in homogeneous models plotted at subsurface locations show similar attrition of fine spatial details seen in the surface pressures (Figure 4-7). Because of the stiff upper layer in model m43338 the magnitude of the strain measures can actually increase with increase in depth as seen in the right panel of Figure 7-4. This property has both desirable and undesirable attributes. As the mechanoreceptors are at a sub-surface location in the fingertip, it is desirable to

have the strain measures (i.e. the *relevant stimulus*) at the receptor location to be as high as possible in magnitude to reduce the noise to signal ratio. A direct analog of this situation occurs in the robotic tactile sensing where it is not possible to place the tactile sensors on the surface of the robotic manipulator and are typically covered by protective material. As in a classical beam the strains in the stiff outer layer increase with distance from the neutral axis *and* with the distance (in the circumferential direction) from the load. The increase in magnitude of strains in circumferential direction is undesirable from the spatial acuity standpoint, contrary to the desirability of the increase in magnitude of the strains with increase in the depth of receptors from the signal processing standpoint. If amplified signals are produced in the vicinity of the receptor away from the load, the receptor at a larger distance from the stimulus would respond and thus the overall spatial acuity of the system will be degraded.

It is always possible to choose an optimum solution that will satisfy to the extent desired both the contradictory requirements. Towards this end, if the thickness of the outermost layer and the ratio of the stiffness of the material outermost layer to the material of the inner layers is varied, an optimal solution can be sought in this parameter space. Has the process of evolution led the development of the primate fingertip to such a point? This question needs to be addressed in the future work in this field.

7.2 Comparison of the competing relevant stimuli

In all the simulations of neurophysiological experiments, strain energy density and maximum compressive strain match the experimentally observed data quite well. The neurophysiological experiments used in these comparisons were designed with different objectives such as investigating the sensitivity of the receptors to curvature of objects indented into the fingertip. It is, therefore, necessary to perform experiments which are based on the biomechanical findings of the analysis aimed at resolving some of the unresolved issues in tactile neural coding of shape. Some of the possible experiments based on simple mechanical stimuli to uniquely identify the relevant stimulus are presented below. The mechanistic explanation is provided using the analytical solutions available, primarily to examine the effectiveness of the approach. Similar experiments can be simulated using the finite element models and stress-state at the receptor locations can be calculated,

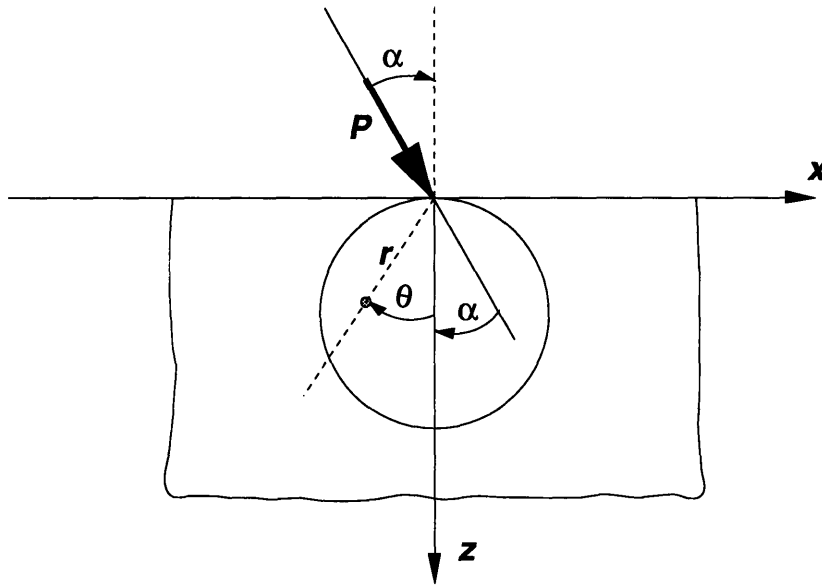


Figure 7-5: Schematic representation of a line load imposed on a semi-infinite plane. The angle which the line load makes with the semi-infinite plane α is varied.

which can be compared with the empirically observed neural discharge rate under similar mechanistic loadings.

As a first step in this direction, simple mechanical loadings on 2D semi-infinite medium can be considered. The loading should be chosen such that the maximum compressive strain and the strain energy density have different profiles with respect to the variable defining the loading. As an example let us consider a semi-infinite plane loaded by a point load as shown in Figure 7-5 and the variable defining the loading is the angle α , the inclination of the load with respect to the vertical axis.

A closed form solution for the stress-state inside the semi-infinite 2D medium indented by a line load is available (Timoshenko and Goodier, 1982). In polar coordinates,

$$\begin{aligned}\sigma_r &= \frac{-2P}{\pi r} \cos(\alpha + \theta) \\ \sigma_\theta &= 0 \\ \tau_{r\theta} &= 0\end{aligned}$$

As evident from the equations, the state of stress at all points in the medium is similar and the one of the principal stresses is always zero. The effect of rotating the point load on the surface by changing the orientation (α) of the load while maintaining the magnitude

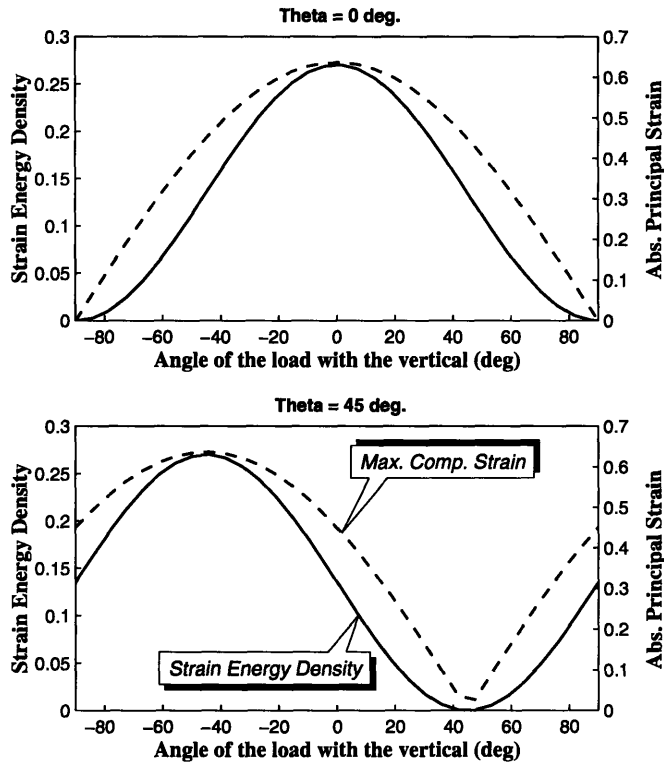


Figure 7-6: The strain energy density and absolute principal strain at typical receptor location is shown in the two subplots. In the top plot the receptor is located at $r = 1$ and $\theta = 0$, whereas, in the bottom panel the receptor is at $r = 1$ and $\theta = 45^\circ$.

constant can be examined. The profiles of the strain energy density and maximum compressive strain at a point in the medium as the angle α is varied from -90 to 90 degrees are shown in Figure 7-6.

From Figure 7-5, it can be seen that the orientation of the point load can be varied between -90 and 90 degrees only. In Figure 7-6 the profile of strain energy density is shown by a solid line whereas the principal strain is shown by a dotted line. Because of the stress-state in the 2D medium, the principal strain is equal to maximum compressive strain for most of the profile. In the top panel the receptor is located at $\theta = 0$. It can be seen that, although the magnitudes of the maximum compressive strain and strain energy density are different, the overall form is similar. Specifically, the α locations where the strain energy density and the principal strain are maximum are identical. In the bottom panel, the variation of the strain measures in a receptor at $\theta = 45$ is shown.

The absolute principal stress is equal to the maximum compressive stress for $-90 <$

$\alpha < 45$. For $45 < \alpha < 90$, the principal stress is tensile. Because of the incompressible medium the principal strains are equal in magnitude and opposite in sign. As in the top panel the overall form of the two strain measures including the locations of the extremums are identical. If the neural response in a peripheral afferent is recorded when the most sensitive spot of the fiber on the surface of the skin is indented by a point load that is oriented at different angle α s, the experiment cannot distinguish between maximum compressive strain and strain energy density as relevant stimuli. This example shows that using the 2D analytical models, the relevant stimuli cannot be uniquely determined. The 2D analytical idealization was chosen for the simplicity in the expressions for various strain measures. The proposed loading schemes should be simulated on the 3D finite element models to obtain accurate predictions of the stress state at the receptor locations.

Mechanical stimuli can be carefully selected such that the profiles of the two competing relevant stimuli are significantly different. The proposed loadings can be simulated on the finite element model and the profiles can be studied *a priori*. The same stimuli can be used in neurophysiological experiments and the comparison of the empirical and simulation data will uniquely determine the relevant stimulus. This technique is not restricted to the study of slowly adapting receptors and can be used to study rapidly adapting receptors if the viscoelasticity is modeled in the finite element models.

7.3 Implications

7.3.1 Neurophysiology

This results presented here further our understanding of the tactile neural coding of shape. The finite element model provides a numerical tool that can be used to predict the stress-state at the receptor location in previously reported neurophysiological experiments. By using the model presented in this thesis, response of a population of receptors can be estimated and testable hypotheses about the processing of the neural information by the central nervous system can be generated.

Reliable and predictive models of the fingertip biomechanics and receptor responses are also useful in the construction of the receptor population response (not only SAs and RAs, but also PCs and SAIIs) to a given stimulus, and in the development of hypotheses for the peripheral and central coding of such diverse sensory qualities as softness or mechanical

pain. As the reliability of the models improve, they may effectively reduce the need for many invasive neurophysiological experiments and suggest alternative approaches. The determination of the relevant stimuli for the receptors would provide an important link between the macroscopic mechanistic phenomena and the molecular mechanisms of nerve-impulse generation (for example, stretch-activated ionic channels). Similar results in vision and audition have given rise to rapid advances in those fields.

7.3.2 Rehabilitation

A deeper understanding of the mechanisms of the tactile sense is beneficial in (1) the development of tests for evaluation of tactile sensibility during diagnosis or monitoring of progress in rehabilitation, (2) the design of tactile communication devices, (3) the development of artificial tactile sensors for 'intelligent' prostheses or robotic assistants, (4) the development of human-machine interfaces for interaction with virtual realities or teleoperation systems, such as for telediagnosis or microsurgery.

7.3.3 Clinical simulation tool

The mechanistic model is an ideal simulating tool in clinical evaluation of impairments for studying the effects of size and shape of the fingertip (even monkey vs. human), the effects of hydration and elasticity, and separating the role of biomechanics from neural malfunctions.

7.3.4 Virtual environments and teleoperation

A thorough understanding of the various sensory systems is necessary to successfully introduce a human operator in a virtual environment. The finite element model presented here can be used as a simulation tool to estimate the deformations of the fingertips in the virtual environment. The finite element model combined with the receptor model can be used to calculate the response of a population of mechanoreceptors in the fingerpad. For force reflecting master-slave systems in teleoperation, the finite element model can be used to set the gains in the forward and feedback path to efficiently convey the haptic information from the master unit to the slave unit and vice-versa.

7.3.5 Robotics

One of the active area in robotics research is the development of compact array of tactile sensors. The findings of the analysis of this thesis can be used as guidelines in the development of the sensors. Although, strain energy density is identified as the relevant stimulus of the SA receptors, it poses a problem in the practical implementation because of the difficulty in measuring strain energy density without any local processing. The exquisite sensitivity of the shear strain can be utilized in developing a specialized sensor for detecting the edges in contact with the robot.

If a sensor needs to be designed to detect the edges in contact with the sensor, the absolute shear strain is an excellent candidate strain measure that could be used in the design of an edge detecting sensor. As seen from Figures 4-13 and 4-14, shear strain is very sensitive to the edges of the gratings in contact with the skin. Shear strain sensors should not pose the difficulty in designing sensors to measure the strain energy density which is a quantity derived from the stress and strain tensors.

8

Suggestions for Future Work

The work presented here is an important step in the direction of completely understanding the role of mechanics in the human sense of touch, but is far from complete. This is a list of various suggestions that could be implemented to further refine the models and authenticate the predictions to be used in biomechanical and neurophysiological experiments.

8.1 Limitation of the Current Models

As explained in Chapter 6, the mesh in the current 3D models was generated to adequately simulate the reported neurophysiological experiments. In all the neurophysiological experiments the neural response was recorded from a single peripheral afferent fiber. Considering the size of the finite element problem and the computation effort involved, the size of the elements on the surface of the fingertip was chosen to be around $500 \mu m$. This poses a limitation on the resolution available on the surface of the fingerpad in specifying the loading. The shape stimuli used in the simulations were of millimeter length scale. A finer mesh size is highly desirable if smaller stimuli have to be used. Similar refinement is necessary in the subsurface mesh before using the models in predicting the population response of receptors. It should be pointed out that, refinement of the mesh results in an exponential increase in the computational effort required in the solution. The resource requirement will further increase if solutions of the sought using an iterative scheme such as contact formulation or if time dependent behavior is modeled in the finite element model. A fair estimate should be obtained before redefining the mesh in the model. Viscoelasticity of the fingerpad is not modeled in the current model and the damping properties of the fingerpad need to be accounted for before using the model in simulating dynamic loadings used in the neurophysiological experiments.

8.2 Neurophysiological and Psychophysical Experiments

Receptive Fields

The different receptive fields predicted based on three strain measures are shown in Figure 4-4. It was pointed out, that the current experimental techniques were not adequate to distinguish between the three different receptive fields. As shown in section 4.2, these experiments should be performed using stimuli of smaller diameters.

Two Point Limen Experiment

The two point limen experiments was simulated using the finite element models as described in section 4.3. The difference in the cues available to the subject in deciding the response to the stimulus was examined. As discussed in section 4.3, two point load experiments to determine spatial acuity should be performed with two loads of constant force and not constant displacement. To examine the effect of the additional intensive cues available to the subject in prescribed displacement experiments, similar load spacings can be used and the results of the prescribed displacement and prescribed force paradigms can be compared.

Human Threshold of Gap Detection

Section 4.5.5 describes the correlation of shear strain with the width of the gap indented on human fingertips. The hypothesis relating the slope of the shear strain and the gap width can be experimentally examined by indenting the fingertips with gaps of different width at different forces. The correlation between the slope of the shear strain across the bars and gaps observed in the gratings (Figure 4-19) can be experimentally verified for different forces of indentation. In Figure 4-20, it was pointed out that the data points in the graph were limited and more data needs to be experimentally obtained to reliably explain the correlation in the gap width and shear strain.

8.3 Anatomical Studies

The Merkel discs are associated with the slowly adapting peripheral afferent fibers studied in this thesis. Information about the shape and size of the Merkel cells is well known and

is summarized in Table 2.2. It is likely that there is considerable mechanistic significance in the structure of the Merkel discs. Several unanswered questions should be investigated. Why are the Merkel receptors in the form of disks stacked together? Can we mechanically prove that measuring strains in several 2D circular plates of negligible dimensions, to be algebraically related to the strain energy density in the receptor? This result could be important not only in better understanding the human tactile sensing system, but will be invaluable for the robotics community where designing reliable tactile sensors with a wide bandwidth is an active area of research. The reason why numerous Merkel discs are lumped together can be investigated. By “sampling” a strain measure in the close vicinity of the receptor, does the system gain in any of the desirable properties like robustness, bandwidth, spatial acuity? Or could it be that by sampling strains at various locations and various orientations, the strain energy density could be accurately estimated by gating the samples together?

8.4 Receptor Silence in the Stimulus Withdrawal Phase

In a typical neurophysiological experiment involving ramp and hold stimulus, the receptors are classified as slowly adapting or rapidly adapting based on their response to the stimulus in the ramp and the hold phase. In almost all the cases, the receptors do not respond to the stimulus when the indenter is withdrawn from the skin. During withdrawal the skin is indented from its rest position, but even the slowly adapting receptors which respond to the displacement of the skin do not respond in the withdrawal ramp phase of the indentation.

This behavior can be explained by a very simple lumped parameters model of the receptor proposed here and shown in Figure 8-1. The receptor is modeled as a spring connected through a dashpot in parallel with a weak spring as shown in the figure. The dark rectangle shown in the figure, could either be connected to the skin or the model can be thought of as a “local” receptor model. The displacement of the skin is measured along the X axis as shown in figure. The direction of the skin displacement can be reversed and the model will remain unchanged for skin displacement in the opposite direction. For simplicity all the arguments will be presented for a displacement in the positive X direction as shown in Figure 8-1. In a typical ramp and hold stimulus as shown in Figure 2-4, the

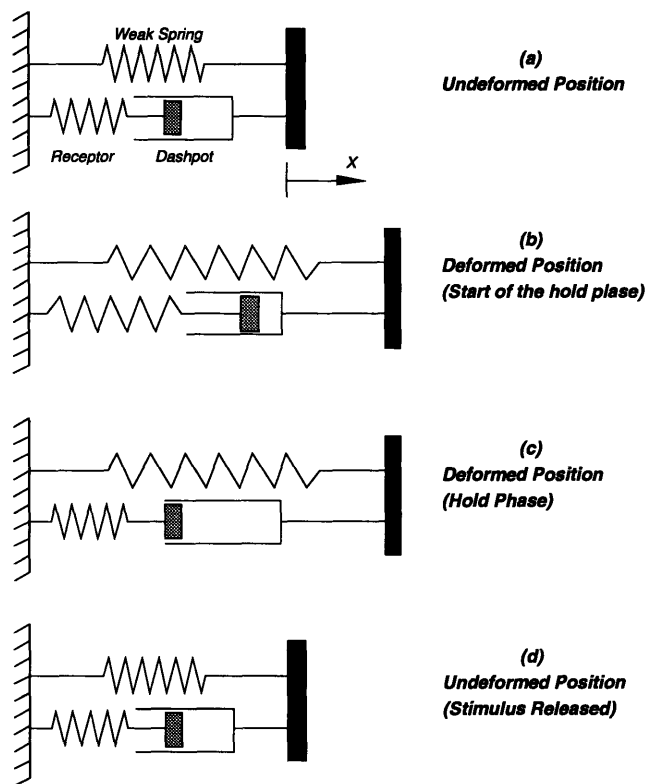


Figure 8-1: A lumped parameter model for mechanoreceptors is proposed. The receptor is modeled in the form of a spring, which is connected to the skin through a dashpot. A weak spring connecting the skin and the datum is shown. The sub-figures (a) through (d) schematically represent the deformations in the two springs at various instances during a ramp and hold stimulus.

skin is displaced from its datum and the plot of the skin displacement versus time is shown in the top panel of Figure 2-4. The schematic displacements in the elements of the receptor model at four salient instances in the ramp and hold stimulus are shown in Figure 8-1. The undeformed position of the receptor is shown in sub-plot (a). There is no force exerted on the skin and hence the force in the weak spring and the receptor is zero. The instance at the end of the ramp phase of the stimulus is shown in sub-plot (b). The skin is displaced from its datum position and the receptor as well as the weak spring are extended. Due to the difference in the stiffness of the two springs, the magnitude of the force in the receptor is much higher than the force in the weak spring. The displacement of the skin is maintained constant during the “hold” phase of the stimulus and sub-plot (c) shows the positions of the springs schematically when a steady state is obtained in the “hold” phase of the stimulus. As the weak spring is rigidly connected to the skin, its deformation remains the

same as in sub-plot (b). However, as the receptor is not directly connected to the skin, the energy stored in the receptor is discharged in the dashpot and it attains the undeformed configuration attaining its rest length as in sub-plot (a). The time required to attain the original length is directly related to the stiffness of the receptor spring and the coefficient of viscosity of the dashpot. In sub-plot (d), the stimulus is withdrawn and the receptor is shown to attain its original undeformed configuration which is same as sub-plot (a).

The question now is two-fold: 1) How does this model explain the adaptation of the receptors and 2) How does the model explain the silence of the receptors during the stimulus withdrawal phase? The receptor spring is connected to the skin through a dashpot. Therefore, the limb of the model containing the receptor will have a zero force in the steady state, as the dashpot is unable resist any static force. The extended receptor spring as in sub-plot (b), will dissipate the energy stored in the spring during extension into the dashpot. When the energy stored in the receptor spring is completely dissipated the receptor spring will attain its original length as shown in sub-plot (c), even though the skin is deformed from its original position. The speed at which the deformed receptor spring attains its original position is dependent on the time constant of the system and is directly proportional to the stiffness of the spring and inversely proportional to the damping ratio of the dashpot. Thus, by choosing appropriate values of the model parameters, we can model receptors that have different adaptation properties. If we assume that the receptor response is proportional to the length of the receptor spring then a slowly adapting receptor can be modeled by using a very high value of damping ratio of the dashpot. On the other hand, choosing a smaller value of the damping coefficient would result in a rapidly adapting receptor that responds only to the transient component of the stimuli applied to the skin.

In the case of a linear spring, the strain in the spring, strain energy in the spring are all related to the length of the spring. Hence, assuming the receptor response to be related to the length of the spring is equivalent to assuming the receptor response to be related to the strain energy stored in the spring or the linear strain in the spring. There are two possible explanations for why the receptors do not respond in the withdrawal of the stimulus. If we assume that in the rest position the spring is fully compressed, then the only possible deformation of the receptor is an "extension". When the skin is indented, the receptor is extended. During the hold part the receptor attains its original length.

When the stimulus is released, the receptor has already attained its undeformed length and even though the energy stored in the weak spring is dissipated into the dashpot, the receptor spring cannot be further compressed. Therefore, the receptor does not respond during stimulus withdrawal. Alternatively, we can assume that the receptor responds only during tension in the receptor spring. In that case, the receptor will be compressed when the stimulus is withdrawn as a result of the weak spring discharging into the dashpot, degree of compression depending on the ratio of the stiffness of the two springs. But as we have assumed the receptor to be responsive only to the tension in the spring, it will not respond during the withdrawal phase of the ramp and hold stimulus.

This is a very simple first order model that can be used in explaining both the adaptation and the lack of response in the withdrawal phase of the receptors. More work needs to be done in developing this idea and comparing the model predictions with some experimental observations.

8.5 Reduced Order Model for Surface Deformations

With the current experimental trend of recording from single peripheral fibers likely to continue in the near future, a reduced order model that can be used by neurophysiologists to predict the surface deformations under a limited mechanical stimuli would be extremely useful. Towards this end, if the stimuli are invariant in an axial direction (e.g., bars, cylinders, step shapes), a 2D model with multiple layers could be used to predict the deformation in a plane of the fingertip. This model could also be used in predicting the forces imposed in the prescribed displacement experiment and vice-versa. The mechanical parameters like width of contact and distribution of contact pressure in the region of contact which cannot be measured experimentally at present, can be predicted.

Appendix A

Strain Energy Density in Plane Strain Problems

This document details the derivation of strain energy density for a plane strain problems. The conventional approach, which fails in this case, is described first. The derivation of the relationship between the strain energy density and maximum compressive strain is presented next.

For a general problem, strain energy density, $sden$ is defined as,

$$sden = \frac{1}{2} \sigma_i \epsilon_i$$

For plane strain problems, $\epsilon_3 = 0$ and hence,

$$sden = \frac{1}{2} (\sigma_1 \epsilon_1 + \sigma_2 \epsilon_2)$$

For incompressible materials, $\nu = 0.5$ and $\sum \epsilon_i = 0$. Thus, with $\epsilon_3 = 0$, $\epsilon_1 = -\epsilon_2$. Using this in the expression for $sden$, we have:

$$sden = \frac{1}{2} \epsilon_1 (\sigma_1 - \sigma_2) \tag{A.1}$$

The strain-stress relationships have a factor of $(1 - 2\nu)$ in the denominator as shown and thus for incompressible models in finite element formulations stresses cannot be determined from strains. The following formula would need to be used to calculate σ_x from the strains in a plane strain problem ($\epsilon_y = 0$).

$$\sigma_x = \frac{E}{(1 + \nu)(1 - 2\nu)} [(1 - \nu)\epsilon_x + \nu\epsilon_z]$$

Boussinesq Problem

If we consider the Boussinesq problem as a special case of plane strain problems with incompressible materials, it is known that in the medium, $\sigma_1 = \sigma_r$ and $\sigma_2 = \sigma_\theta = 0$. Thus the strain energy density can be written as,

$$sden = \frac{1}{2}\epsilon_1\sigma_1$$

One cannot, however, calculate the stresses from the strains due to the incompressibility constraints.

Alternative Approach

Let us start with the general statement of the Hooke's law. The stress-strain relationships (Hooke's Law) for plane strain problems, $\epsilon_3 = 0$ are

$$\begin{aligned}\epsilon_1 &= \frac{1}{E}[\sigma_1 - \nu(\sigma_2 + \sigma_3)] \\ \epsilon_2 &= \frac{1}{E}[\sigma_2 - \nu(\sigma_1 + \sigma_3)] \\ \epsilon_3 &= \frac{1}{E}[\sigma_3 - \nu(\sigma_1 + \sigma_2)] = 0\end{aligned}\tag{A.2}$$

Therefore,

$$\sigma_3 = \nu(\sigma_1 + \sigma_2)$$

Substituting this in equations A.2, and eliminating σ_3 , we have:

$$\epsilon_1 = \frac{1 + \nu}{E} [(1 + \nu)\sigma_1 - \nu\sigma_2]\tag{A.3}$$

$$\epsilon_2 = \frac{1 + \nu}{E} [(1 + \nu)\sigma_2 - \nu\sigma_1]\tag{A.4}$$

Subtracting equation A.3 from A.4 we have,

$$\sigma_1 - \sigma_2 = \frac{E(\epsilon_1 - \epsilon_2)}{1 + \nu}$$

Introducing the incompressibility constraint and using $\epsilon_1 = -\epsilon_2$ we have,

$$\sigma_1 - \sigma_2 = \frac{2E\epsilon_1}{1 + \nu}$$

Instead of calculating the individual principal strains, what we have here is an analytical expression for the difference of the principal strains. We can substitute this in equation A.1 to obtain the strain energy density.

$$sden = \frac{1}{2}\epsilon_1 \frac{2E\epsilon_1}{1 + \nu}$$

with $\nu = \frac{1}{2}$,

$$\boxed{sden = \frac{2}{3}E\epsilon_1^2}$$

To summarize, starting from the Hooke's law, the following assumptions were required to show that the strain energy density is proportional to the square of maximum compressive strain.

- Plane Strain ($\epsilon_3 = 0$)
- Incompressibility ($\nu = 0.5$)

Appendix B

Strain calculations for finite element models with prescribed displacements

The finite element formulation for the static case reduces to

$$\mathbf{KU} = \mathbf{R}$$

where

\mathbf{K} is the stiffness matrix,

\mathbf{U} is the displacement vector,

\mathbf{R} is the load vector.

Loads and displacements can be prescribed at any node in the model, but both displacement and forces cannot be prescribed at the same node. Thus, we can separate the total number of nodes into two sets - one that has forces prescribed and the other which has displacements prescribed. Let \mathbf{R}_a be the prescribed forces and \mathbf{U}_a the corresponding unknown displacements and let \mathbf{U}_b be the prescribed displacements and \mathbf{R}_b the corresponding unknown reaction forces. The finite element equation can be rewritten in terms of the two sets of nodes as follows:

$$\begin{bmatrix} \mathbf{K}_{aa} & \mathbf{K}_{ab} \\ \mathbf{K}_{ba} & \mathbf{K}_{bb} \end{bmatrix} \begin{Bmatrix} \mathbf{U}_a \\ \mathbf{U}_b \end{Bmatrix} = \begin{Bmatrix} \mathbf{R}_a \\ \mathbf{R}_b \end{Bmatrix}$$

The problem now reduces to finding the unknown displacements U_a which can be used to determine the unknown reaction forces R_b . Rewriting, we have:

$$K_{aa}U_a = R_a - K_{ab}U_b$$

$$R_b = K_{ba}U_a + K_{bb}U_b$$

In the problems we have attempted, the loading is defined only by prescribing displacements and no forces are prescribed. Thus, $R_a = 0$ and the first equation above reduces to

$$K_{aa}U_a = -K_{ab}U_b \quad (\text{B.1})$$

The generic stiffness matrix is defined as

$$K = B^T E B$$

where

E is the elasticity matrix,

$$B = DN,$$

D is the differential operator,

N is the shape function matrix.

Matrix B consists of derivatives of shape functions of the element and does not depend on the material properties. E for isotropic materials is a function of the Young's modulus E and the Poisson's ratio ν . E for two-dimensional plane strain analysis can be written as:

$$E = \frac{E}{(1 + \nu)(1 - 2\nu)} \begin{bmatrix} 1 - \nu & -\nu & 0 \\ -\nu & 1 - \nu & 0 \\ 0 & 0 & \frac{1-2\nu}{2} \end{bmatrix}$$

The Young's modulus appears as a multiplying constant and can be extracted out as follows:

$$\mathbf{E} = E\mathbf{P}$$

where

$$\mathbf{P} = \frac{1}{(1 + \nu)(1 - 2\nu)} \begin{bmatrix} 1 - \nu & -\nu & 0 \\ -\nu & 1 - \nu & 0 \\ 0 & 0 & \frac{1-2\nu}{2} \end{bmatrix}$$

Equation B.1, used to determine the unknown displacements, can be rewritten as

$$\mathbf{B}_{aa}^T \mathbf{P}_{aa} \mathbf{B}_{aa} \mathbf{U}_a = -\mathbf{B}_{ab}^T \mathbf{P}_{ab} \mathbf{B}_{ab} \mathbf{U}_b$$

It can be seen that, as \mathbf{P} depends only on ν and \mathbf{B} is a function of the element shape functions, the above equation is independent of E , the Young's modulus. Hence, displacements and strains in a uniform plane strain finite element model with prescribed displacements and no prescribed forces are independent of the Young's modulus. Stresses are dependent on the Young's modulus, as they are obtained by multiplying strains by the elasticity matrix \mathbf{E} which depends on E .

References

- Aidley, D. J., *The Physiology of Excitable Cells*. Cambridge University Press, third ed., 1989.
- Bathe, K. J., *Finite Element Procedures in Engineering Analysis*. Prentice-Hall, 1982.
- Cauna, N., "Nature and functions of the papillary ridges of the digital skin," *Anat. Rec.*, vol. 119, pp. 449–468, 1954.
- Chouchkov, C., "Cutaneous receptors," *Adv. Anat. Embryol. Cell Biology*, vol. 54, no. 5, pp. 1–62, 1978.
- Cook, T. H., *The mechanical characterization of human skin in vivo*. PhD thesis, Stevens Institute of Technology, Castle Point, Hoboken, NJ, 1975.
- Dandekar, K. and Srinivasan, M. A., "Tactile coding of object curvature by slowly adapting mechanoreceptors," *Advances in Bioengineering*, vol. 28, pp. 41–42, 1994.
- Dandekar, K. and Srinivasan, M. A., "A 3 dimensional finite element model of the monkey fingertip for predicting responses of slowly adapting mechanoreceptors," *to be presented at the Summer Annual Meeting of the ASME*, 1995a.
- Dandekar, K. and Srinivasan, M. A., "3D finite element models of human and monkey fingertips," *to be submitted to the Journal of Biomechanics*, 1995b.
- Dandekar, K. and Srinivasan, M. A., "Mechanics of tactile sense I: 3D models of the primate fingertips," *to be submitted to the Journal of Neuroscience*, 1995c.
- Dandekar, K. and Srinivasan, M. A., "Mechanics of tactile sense II: Prediction of the peripheral neural response to static shapes using a 3D multilayered model of the monkey fingertip," *to be submitted to the Journal of Neuroscience*, 1995d.

- Dandekar, K. and Srinivasan, M. A., "Predicting the response of a population of mechanoreceptors using 3D finite element models of primate finger tips," *Society of Neuroscience Abstracts*, 1995e.
- Danielson, D. A., "Human skin as an elastic membrane," *J. Biomechanics*, vol. 6, pp. 539–546, 1973.
- Darian-Smith, I., "The sense of touch: Performance and peripheral neural processes," *Handbook of physiology - The nervous system -III*, pp. 739–788, 1984.
- Darian-Smith, I. and Kennis, P., "Innervation density of mechanoreceptive fibers supplying glabrous skin of the monkey's index finger," *Journal of Physiology (London)*, vol. 309, pp. 147–155, 1980.
- Darian-Smith, I., Davidson, I., and Johnson, K. O., "Peripheral neural representation of spatial dimensions of a textured surface moving across the monkey's fingerpad," *Journal of Physiology (London)*, pp. 135–146, 1980.
- Dellon, A. L., *Evaluation of Sensibility and Re-education of Sensation in the Hand*. Williams and Wilkins, Baltimore, 1981.
- Fung, Y. C., *Biomechanics*. Springer, New York, 1981.
- Fung, Y. C., *Biomechanics : Mechanical Properties of Living Tissues*. Springer-Verlag, second ed., 1993.
- Gibson, T. and Kenedi, R. M., "The structural components of the dermis and their mechanical characteristics," in *The Dermis. Advances in Biology of Skin* (Montagna, W., Bentley, J. P., and Dobson, R. L., eds.), vol. 10, pp. 19–38, Proc. Symp. on Biology of Skin, 1968.
- Grigg, P. and Hoffman, A. H., "Ruffini mechanoreceptor in isolated joint capsule: Responses correlated with strain energy density," *Somatosensory Research*, vol. 2, no. 2, pp. 149–162, 1984.
- Gulati, R. J., "Force displacement response of human fingertips," Master's thesis, Boston University, 1995.
- Gulati, R. J. and Srinivasan, M. A., "Human fingerpad under indentation I: Static and dynamic force response," *submitted to the Summer Annual Meeting of the ASME*, 1995.

- Halata, Z., "The mechanoreceptors of mammalian skin- ultrastructure and morphological classification," *Adv. Anat. Embryol. Cell Biol.*, vol. 50, no. 5, pp. 1–77, 1975.
- Jabaley, M. E., "Recovery of sensation in flaps and skin grafts," in *The Hand* (Tubiana, R., ed.), vol. 1, ch. 56, pp. 583–601, W. B. Saunders and Co., 1981.
- Johansson, R. S., "Tactile sensibility in the human hand: Receptive field characteristics of mechanoreceptive units in the glabrous skin area," *Journal of Physiology*, vol. 281, pp. 101–123, 1978.
- Johansson, R. S. and Valbo, A. B., "Tactile sensibility in the human hand: Relative and absolute densities of four types of mechanoreceptive units in glabrous skin," *Journal of Physiology (London)*, vol. 286, pp. 283–300, 1979.
- Johansson, R. S. and Vallbo, A. B., "Tactile sensory coding in the glabrous skin of the human hand," *Trends in Neuroscience*, vol. 6, pp. 27–32, January 1983.
- Johnson, K. L., *Contact Mechanics*. Cambridge University Press, Cambridge, 1985.
- Johnson, K. O. and Phillips, J. R., "Tactile spatial resolution - I. Two point discrimination, gap detection, grating resolution and letter recognition," in *J. Neurophysiol.* (Phillips and Johnson, 1981b), pp. 1177–1191.
- Knibestol, M. and Valbo, A. B., "Single unit analysis of mechanoreceptor activity from the human glabrous skin," *Acta Physiol. Scand.*, vol. 80, no. 6, pp. 178–195, 1970.
- Lamb, G. D., "Tactile discrimination of textured surfaces: Peripheral neural coding in the monkey," *Journal of Physiology (London)*, vol. 338, pp. 567–587(a), 1983a.
- Lamb, G. D., "Tactile discrimination of textured surfaces: Psychophysical performance measurements in humans," *Journal of Physiology (London)*, vol. 338, pp. 551–565, 1983b.
- LaMotte, R. H. and Mountcastle, V. B., "Capacities of humans and monkeys to discriminate between vibratory stimuli of different frequency and amplitude: A correlation between neural events and psychophysical measurements.," *J. Neurophysiol.*, vol. 38, pp. 539–559, 1975.

- LaMotte, R. H. and Srinivasan, M. A., "Tactile discrimination of shape: Responses of rapidly adapting mechanoreceptive afferents to a step stroked across the monkey fingerpad," *Journal of Neuroscience*, vol. 7, no. 6, pp. 1672–1681, 1987b.
- LaMotte, R. H. and Srinivasan, M. A., "Tactile discrimination of shape: Responses of slowly adapting mechanoreceptive afferents to a step stroked across the monkey fingerpad," *Journal of Neuroscience*, vol. 7, no. 6, pp. 1655–1671, 1987a.
- LaMotte, R. H. and Srinivasan, M. A., *Surface microgeometry: Tactile perception and neural encoding*. Information Processing in the somatosensory system, eds: O. Franzen and J. Westman, Wenner-Gren Intl. Symposium series, Macmillan Press, London, 1991.
- LaMotte, R. H. and Srinivasan, M. A., "Responses of cutaneous mechanoreceptors to the shape of objects applied to the primate fingerpad," *Acta Psychologica*, vol. 84, pp. 41–51, 1993.
- LaMotte, R. H. and Srinivasan, M. A., "Neural encoding of shape: Responses of cutaneous mechanoreceptors to wavy surfaces stroked across the monkey fingerpad," *submitted to the Journal of Neuroscience*, 1995.
- LaMotte, R. H. and Whitehouse, J., "Tactile detection of a dot on a smooth surface," *J. Neurophysiol.*, vol. 56, pp. 1109–1128, 1986.
- LaMotte, R. H., Srinivasan, M. A., Lu, C., and Klusch-Petersen, A., "Cutaneous neural codes for shape," *Canadian Journal of Physiology and Pharmacology*, 1993.
- Lanir, Y., "Skin mechanics," in *Handbook of Bioengineering*, ch. 11, pp. 11.1–11.25, McGraw-Hill, 1987.
- Lanir, Y., Dikstein, S., Hartzshtark, A., and Manny, V., "In vivo indentation of human skin," *J. of Biomechanics*, vol. 112, pp. 63–69, 1990.
- Lederman, S. J. and Taylor, M. M., "Fingertip force, surface geometry, and the perception of roughness by active touch," *Perception & Psychophysics*, vol. 12, pp. 401–408, 1972.
- Lighthill, J., "Biomechanics of hearing sensitivity," *Journal of Vibration and Acoustics*, vol. 113, pp. 1–13, 1991.

- Lockhart, R. D., Hamilton, G. F., and Fyfe, F. W., *Anatomy of the Human Body*. J P Lippincott Co., Philadelphia, 1965.
- Loomis, J. M., "An investigation of tactile hyperacuity," *Sensory Processes*, vol. 3, pp. 289–302, 1979.
- Morley, J. W., Goodwin, A. W., and Darian-Smith, I., "Tactile discrimination of gratings," *Experimental Brain Research*, vol. 49, pp. 291–299, 1983.
- Mountcastle, V. B., LaMotte, R. H., and Carli, G., "Detection thresholds for stimuli in humans and monkeys: Comparison with threshold events in mechanoreceptive afferent nerve fibers innervating the monkey hand," *J. Neurophysiology*, vol. 35, pp. 122–136, 1971.
- Mountcastle, V. B., LaMotte, R. H., and Carli, G., "Detection threshold for stimuli in humans and monkeys: comparison with threshold events in mechanoreceptive afferent nerve fibers innervating monkey hand," *J. Neurophysiol.*, vol. 35, pp. 122–136, 1972.
- North, J. F. and Gibson, F., "Volume compressibility of human abdominal skin," *J. Biomechanics*, vol. 11, pp. 203–207, 1978.
- O'Rahilly, R., "Skin, hair, and nails," in *Anatomy: A Regional Study of the Human Structure* (Gardner, E. and O'Rahilly, D. G. R., eds.), W. B. Saunders and Co., 1969.
- Phillips, J. R. and Johnson, K. O., "Tactile spatial resolution - II. Neural representation of bars, edges and gratings in monkey afferents," in *J. Neurophysiol.* (Phillips and Johnson, 1981b), pp. 1192–1203.
- Phillips, J. R., Johnson, K. O., and Browne, H. M., "A comparison of visual and two modes of tactual letter recognition," *Perception and Psychophysics*, vol. 34, pp. 243–249, 1983.
- Phillips, J. R. and Johnson, K. O., "Tactile spatial resolution - III. A continuum mechanics model of skin predicting mechanoreceptor responses to bars, edges and gratings," *J. Neurophysiol.*, vol. 46, no. 6, pp. 1204–1225, 1981b.
- Quilliam, T. A., "The structure of fingerprint skin," in *Active touch - The mechanism of Recognition of Objects by Manipulation: A Multidisciplinary Approach* (Gordon, G., ed.), Oxford: Pergamaon, 1978.

- Srinivasan, M. A., "Surface deflection of primate fingertip under line load," *J. Biomechanics*, vol. 22, no. 4, pp. 343–349, 1989.
- Srinivasan, M. A. and Dandekar, K., "Role of fingertip geometry in transmission of tactile mechanical signals," *Advances in Bioengineering*, vol. 22, pp. 569–572, 1992.
- Srinivasan, M. A. and Dandekar, K., "An investigation of the mechanics of tactile sense using two dimensional models of the primate fingertip," *to appear in the Journal of Biomechanical Engineering*, 1994a.
- Srinivasan, M. A., Gulati, R. J., and Dandekar, K., "In vivo compressibility of the human fingerpad," *Advances in Bioengineering*, vol. 22, pp. 573–576, 1992.
- Srinivasan, M. A., "Haptic interfaces," in *Virtual Reality. Scientific and Technological Challenges* (Durlach, N. I. and Mavor, A. S., eds.), National Academy Press, Washington, D.C., 1994.
- Srinivasan, M. A. and Dandekar, K., "Role of mechanics in cutaneous mechanoreceptor response," *Society of Neuroscience Abstracts*, 1991.
- Srinivasan, M. A. and Dandekar, K., "Mechanistic models for tactile neural coding of shape," *Society of Neuroscience Abstracts*, 1994b.
- Srinivasan, M. A. and Dandekar, K., "Prediction of peripheral neural response to static stimuli using 2d finite element models of the monkey fingertip," *to be submitted to the Journal of Neuroscience*, 1995.
- Srinivasan, M. A. and LaMotte, R. H., "Tactile discrimination of shape: Responses of slowly and rapidly adapting mechanoreceptive afferents to a step indented into the monkey fingerpad," *Journal of Neuroscience*, vol. 7, no. 6, pp. 1682–1697, 1987.
- Srinivasan, M. A. and LaMotte, R. H., "Encoding of shape in the responses of cutaneous mechanoreceptors," in *Information Processing in the Somatosensory system* (Franzen, O. and Westman, J., eds.), Wenner-Gren Intl. Symposium series, pp. 59–69, Macmillan Press, 1991.
- Srinivasan, M. A. and LaMotte, R. H., "Tactual discrimination of softness," *submitted to Journal of Neurophysiology*, 1994.

- Sussman, T. and Bathe, K.-J., "A finite element formulation for nonlinear incompressible elastic and inelastic analysis," *J. Computers and Structures*, vol. 26, no. 1/2, pp. 357–409, 1987.
- Thacker, J. G., *The Elastic Properties of Human Skin in vivo*. PhD thesis, University of Virginia, January 1976.
- Timoshenko, S. P. and Goodier, J. N., *Theory of Elasticity*. McGraw-Hill, New York, 1982.
- Tregear, R. T., *Physical Functions of Skin*. Academic Press, New York, 1966.
- Valbo, A. B. and Hagbarth, K. E., "Activity from skin mechano-receptors recorded percutaneously in awake human subjects," *Expl. Neurol.*, vol. 21, pp. 270–289, 1968.
- Valbo, A. B. and Johansson, R. S., "Properties of cutaneous mechanoreceptors in the human hand related to touch sensation," *Human Neurobiology*, vol. 3, pp. 3–14, 1984.
- van Doren, C. L., *Measurement and Modeling of spatiotemporal tactile sensitivity*. PhD thesis, Syracuse University, 1987.
- Veronda, D. R. and Westmann, R. W., "Mechanical characterization of skin - finite deformations," *J. Biomechanics*, vol. 3, pp. 111–124, 1970.
- Vierck, C. J., "Video images of monkey fingertip cross-sections - undeformed and under surface stimuli." Unpublished video images.
- von Gierke, H. E., Oestreicher, H. L., Franke, E. K., Panrack, H. O., and von Hittern, W. W., "Physics of vibrations in living tissues," *J. Appl. Physio*, pp. 886–900, 1952.